OBSERVATIONS AND GAS DYNAMICS OF EXTRAGALACTIC RADIO JETS

Thesis by

Kevin Robert Lind

In Partial Fulfillment of the Requirements

for the Degree of

Doctor of Philosophy

California Institute of Technology

Pasadena, California

1987

(Submitted November 20, 1986)

Acknowledgments

I have an awful lot of people to thank for helping me to this point, both professionally and personally. One of the things that first attracted me to radio astronomy and theoretical astrophysics was the generally helpful and friendly nature of the astrophysics community, and I have not been disappointed. I have received advice and encouragement from so many people that I would like to give all of you a blanket "thank you."

My advisors deserve particular thanks. Marshall Cohen and Roger Blandford are two of the best advisors I could imagine working under. They both care a great deal for their students and are almost always available for advice and help, but are also wise enough to avoid watching over their charges too closely. I have learned a great deal about science and how it is really done by being allowed to do it on my own, and then having it gently but thoroughly evaluated by one or both of them. They both have a sense for what is good and what is sloppy in their respective areas, and I cannot recall a piece of sloppy thinking that got past either of them. At the same time, they were always willing to ask questions about things that I might happen to know that they didn't, and so I always felt like a coworker. As people, they have been sympathetic and gracious to me in every way. They have always treated me with respect, and would always do what they could if I had a problem. Thank you both for a good, productive, and mostly happy five years.

I also owe a lot to my collaborators in both theory and observation. David Payne and Dave Meier have spent many hours laboring on our code, and have taught me a lot about code development and testing. In fact, the algorithm and many if not most of the test problems originated with David Payne, and

the philosophy of testing and debugging — and much if not most of the actual work involved in debugging — came from Dave Meier. Only after working with them did I really have a feel for how a code is really designed and tested. I would also like to thank Joan Wrobel and Dayton Jones, who were involved in the VLBI observations. Joan figured out the requirements for the phased-array VLA observations, so that the data could be used for polarization mapping, and was a great help in integrating the VLA into the network, as well as being on-site at the VLA during the observations. Dayton helped me design the experiment, since he had made similar observations previously, and was essential to the global fitting phase of the data analysis. I profited greatly from the experience and knowledge they contributed. I would also like to thank Mike Norman for his helpful comments and suggestions during the code development.

Among the Caltech community, past and present, there are a few people who deserve special mention. Steve Unwin, Dayton Jones, and Richard Simon were all instrumental in getting me started in VLBI, and they continue to be helpful whenever I have a question or a problem. John Biretta has been a friend since my days as a summer student at NRAO, and was one of the people who helped me settle in at Caltech and feel comfortable. Alain Porter and David Hough have also been good friends, and have made my stay here very pleasant. Among the theorists, it is hard to sort anybody out, since we have always been a rather close-knit group, but Lonnie and Lauren Western deserve recognition for assistance and encouragement above and beyond the call of duty, especially during the last haul of thesis writing. Jens Villumsen and Chris Kochanek have also been exceedingly kind and understanding, and have both, in their own ways, done a lot to calm me down these last few weeks. Sam Finn has also been a good friend over the past few years, and has kept things calm in the face of considerable difficulty as

system manager for our group. And, of course, I owe a debt of gratitude to John Hawley for spending so much time helping me get started on supercomputing, and for being a nice, mellow influence in the group atmosphere. Finally, I would like to single out the secretaries and administrative assistants for recognition. They have sorted out more bureaucratic tangles than I can imagine. All of them have gone out of their way to make Caltech pleasant, and have received little thanks for it. Consider yourselves appreciated.

I could list a page or more of people outside of Caltech, so I reiterate my blanket thanks. However, I would like to single out the Brits and the Swedes for a brief special mention. I do not see Peter and Althea Wilkinson, Ian Browne, or Lars Bååth very often, but I am always very happy when I do, as they are all good friends and good scientists. I gained a lot of respect for the European astrophysical community during my travels, and am happy I got to know the people there.

Finally, I would like to thank my wife, Janel, and both of our families, Mom, Dad, Will, LaRae, Beth, Paul, and Michelle, for being so loving and supportive. My parents weren't too sure about this astronomy thing, but they respected my decision and gave me the love and support I needed, and have always been interested in what I was doing, no matter how incomprehensible. They also love, who only smile and nod. Also, I was pleasantly surprised when I married Janel and got a whole new family as a bonus. Its not easy being a graduate student, and two sets of parents/brothers/sisters is none too many. And, of course, I must thank Janel. She has pushed me, comforted me, counseled me, and prayed with me, but above all else, she has loved me and shared what I have done, even if it didn't seem to make much sense at the time. Fortunately, she is one person who goes with me when I leave Caltech. Since I am thanking family, I should also include

Marty and Leah who, while not blood relatives, have been our brother and sister while we have been here. Thank you, all of you.

Abstract

This thesis is a combined observational and theoretical study of extragalactic radio jets. Jets are defined observationally as extended, center-brightened features, which are observed in radio images at all resolution scales. They are defined theoretically as momentum-dominated, well-collimated plasma flows. There is now little debate as to the basic interpretation of radio jets as actual plasma outflows, but the detailed dynamics of the jets, or even whether the kiloparsec-scale jets are relativistic, are still uncertain. The resolution of the details of the physics of jets requires improved radio images, especially at the base of the jet, and detailed models of jets. Maps of the base of the radio jet can only be obtained with VLBI observations; detailed jet models require numerical simulations on a supercomputer.

The observational work was a large global VLBI observation of the N galaxy 3C371. The goal was to detect and, if possible, map the underlying jet. This was done, and the results compared with a previous VLBI map, and with maps from other interferometers at lower resolution. No conclusions could be drawn regarding the nature of the jet, although it was clear that the jet was active, and appeared to vary on short time scales.

The theoretical work was in two parts, both of which were directed toward refining existing theories. The first part was to calculate the emission for relativistically moving patterns which themselves contain relativistic flows, to determine how much the flux as a function of viewing angle may vary between realistic models of the knots in relativistic jets. It was found that considerable variation was possible, and that superluminal expansion rates were not necessarily good determiners of the bulk flow rate. The second part was to develop a code to simulate

axisymmetric magnetized jets propagating into a uniform medium. This was implemented for the case of toroidal field only, and run for a moderately magnetized injected jet. It was found that, although most of the jet dynamics was determined by the nonmagnetic forces, the influence of the magnetic tension focused the flow sufficiently to significantly increase the speed of advance of the jet.

Table of Contents

CHAPTER 1

INTRODUCTION

The study of extragalactic radio jets has advanced rapidly in recent years. Improvements in instrumentation, observing techniques, and data reduction have increased both resolution and sensitivity for the imaging of jets, especially in radio interferometry. Optical, ultraviolet, and X-ray observers have continued to study the central engines of active galactic nuclei through spectral analysis and the monitoring of flux and polarization variability. Infrared and millimeter radio observations have begun to fill in some of the gaps in the broad-band spectra of these sources. Observations using a wider range of frequencies with improved resolution and sensitivity have both extended our knowledge of present classes of objects and introduced new classes of objects.

1. Jets

Jets are defined observationally as long, extended, center-brightened structures or trains of emitting regions with an axial ratio of at least 4:1, and with the major axis aligned with the core and lobes within the source (Bridle 1984a). They have been observed in both galactic and extragalactic radio sources and at both arcsecond and milliarcsecond resolutions. Galactic jets appear to be related to star formation (*e.g.*, bipolar outflows from young stars) and compact objects (*e.g.*, SS433). Extragalactic jets all appear to originate in compact regions, which suggests that they are associated with large black holes at the centers of galaxies and quasars. The extragalactic radio jets are found in both strong and weak sources, and are associated with spirals (*e.g.*, Seyferts), normal ellipticals (*e.g.*, M87), peculiar ellipticals (*e.g.*, NGC5128), and quasars (*e.g.*, 3C273). The presence of these features in so many different types of objects at so many different size and luminosity scales suggests that they are caused by robust physical mechanisms which are scale invariant. Observations of superluminal motion at VLBI scales (Porcas 1984; Cohen *et al.* 1984), which has been observed in extragalactic radio sources,

and the need for transport of energy to power the lobes of bright radio sources reinforce this model, and it is generally assumed that the observationally defined jets are associated with continuous plasma outflows. Except for the ejection of discrete packets of matter, or plasmoids (Pacholczyk 1982)— which could be thought of as highly irregular jets — there have been few serious alternatives to the jet model. Therefore, for the remainder of this thesis, I will assume this viewpoint.

The basic concepts of jets and associated phenomena have been well-established in theory for many years (Scheuer 1974; Blandford and Rees 1974; Blandford and Rees 1977) but theory is now hard-pressed to keep pace with observation. Before jets could be clearly resolved, and only the brightest details could be observed, it was sufficient to establish that there was sufficient energy and momentum in the jet to provide the observed luminosity and power the lobes, that ram pressure bending appeared to be sufficient to explain the head-tail sources (Jones and Owen 1979; Begelman *et al.* 1977), and that relativistic motion near the line of sight could explain observed superluminal motion (Scheuer 1984). The quality of the observations generally justified no further detail. Recent observations, which can resolve even faint features and delineate surrounding filamentary structure, allow consideration of details such as turbulence, the dynamical importance of magnetic fields, the development of axisymmetric and nonaxisymmetric instabilities, and the nature of the patterns observed in jets, especially those associated with superluminal motion. These considerations have implications, not only for the jet itself, but for the nature of the central engine in extragalactic radio sources and the ambient medium in which the flows propagate.

2. Radio Source Classification

The most basic characteristic of extended extragalactic radio sources, apart from their existence, is their division into two well-defined classes, the Fanaroff-

Riley class I and II sources (Fanaroff and Riley 1974). This classification is based on whether the extended emission is edge-darkened (class I; henceforth FRI) or edge-brightened (class II; henceforth FRII). The differences between these objects are more fundamental than this simple criterion would suggest; with few exceptions, the two classes exhibit marked differences in luminosity and jet structure which imply that there are fundamental physical differences between these two types of sources.

The FRI (edge-darkened) sources have low radio luminosity, characterized by a radio luminosity at 1.4 GHz of $P_{\rm tot}^{1.4} \leq 10^{24.5-25}$ W/Hz. The jets in these sources are two-sided over most of their length, where two-sided is defined by a jet to counterjet brightness ratio of less than 4:1. The one-sided jet region is typically restricted to the 10% of the jet nearest the nucleus. One exception is the jet in M87, which is one-sided along its entire length (fig. 1). However, its total physical length is roughly that of the one-sided jet region in a typical FRI source, and may be an example of a jet which has stagnated before forming large-scale two-sided structure (Bridle 1984b; Biretta *et al.* 1983; Charlesworth and Spencer 1982; Owen *et al.* 1980). The two sides are not identical; the brighter jet tends to remain brighter than the fainter jet, or counterjet, over the entire length of the jets. Many normal ellipticals fall into this class (fig. 2).

The FRII (edge-brightened) sources have high radio luminosity, with $P_{\rm tot}^{1.4} \geq 10^{25}$ W/Hz. The jets in these sources are one-sided over all or most of their length, although the sources themselves typically possess two edge-brightened lobes of emission located more or less symmetrically about the nucleus, with the brighter lobe associated with the jet. Most classical double radio galaxies and radio quasars fall into this class (fig. 3).

There are a number of FRI sources with distorted jets. The narrow angle tail sources (or NATS) are associated with non-dominant cluster ellipticals, and are characterized by symmetric bending of their jets to form a "U" shape (O'Dea 1984)(fig. 4). They can be explained by ram-pressure bending of a symmetric jet as the source sweeps through the intergalactic medium (Jones and Owen, 1979; Begelman *et al.* 1977). Another class of symmetrically-distorted source, the wide angle tail sources (or WATS), are associated with dominant cluster ellipticals; the radio jet is swept into a shallow "U" of large physical extent (Burns 1982). (fig. 5). These are generally interpreted as classical double radio sources which are not distorted by ram pressure, but by asymmetric density and pressure gradients, asymmetric distributions of cool, dense clouds, or large-scale magnetic fields in the inter-cluster medium (ICM)(Eilek *et al.* 1984). There are a number of mirror- and inversion-symmetric radio sources, which have large-scale wiggles rather than continuous bends. They can be modeled using the precession or orbit of the radio core about the center of the host galaxy (van Breugel and Miley 1977; Blandford and Icke 1978; Gower *et al.* 1982)(fig. 6). Finally, a few extended extragalactic radio sources appear to be more or less unique, such as the double-double jet in 3C75 (Owen *et al.* 1985)(fig. 7) or the starburst galaxy M82 (Kronberg and Clark 1982)(fig. 8); it is assumed that these sources are due to rare but energetic processes near the galactic nucleus, or unusual conditions in the surrounding medium which then distort the jets into unusual patterns. The appearance of distortions in the jets of FRI sources indicates that either the jets are intrinsically slow, which would allow interactions with the surrounding medium to influence the large-scale structures of the jets, or are embedded in such a dense medium that they are slowed by entrainment before reaching arcsecond scales. The low luminosity of these sources suggests either that the FRI jets have lower kinetic energy fluxes

than the FRII jets, or that an inordinate percentage of the kinetic energy flux in these jets is converted to gas motions in the intergalactic medium with little evidence of radiation. The bending of the FRI jets suggests that the low radio luminosities of FRI sources are due to low kinetic luminosities in the jets.

Another class of source, of particular interest to VLBI, is the compact source. Compact sources may be embedded in the core of an extended source such as a radio quasar, embedded in the core of a relatively unextended source such as an N galaxy, or totally isolated as a "point" source such as a blazar (*e.g.*, BL Lac). These compact cores are often highly variable at optical and X-ray wavelengths and somewhat variable at radio wavelengths, with the more compact sources generally the more variable. Many of these isolated cores have a small radio halo and a short arcsecond-scale jet. This appearance, as well as the relative brightness of the compact core and the rapid variability, can be explained by the beaming model (Readhead *et al.* 1978; Scheuer and Readhead 1979). This model assumes that the material in at least the compact core is moving relativistically. The Doppler effect shortens the time interval between outbursts as viewed by the observer, accounting for the rapid variability, and the Doppler boosting of the radiation accounts for the relative brightness of the core, and the one-sided nature, at milliarcsecond scales. There should be a larger number of such sources oriented in the plane of the sky, but these will be fainter than sources aligned directly with the observer (using a simple optically thin jet for the source model) by a factor of roughly $0.5(1-\beta)^{-(2+\alpha)} \sim 10^4 - 10^{5.5}$, where $\Gamma \equiv (1-\beta^2)^{-1/2} \approx 5 - 10$ is the bulk Lorentz factor and $\alpha \approx 0.5$ is the negative spectral index. This ratio is too large to be totally consistent with the classical double sources being identified with the compact sources, but oriented in the plane of the sky (Orr and Browne 1982). This suggests either that the two classes are intrinsically different, or that more

realistic source models must be used (Lind and Blandford 1985). Two other classes of phenomena support the idea of bulk relativistic flow in these sources. One is apparent superluminal motion, and the other is the ratio of X-ray to radio flux in the compact core.

3. Compact Jets

The observation of apparent superluminal motion in compact cores was the first real evidence that bulk relativistic motion was involved (Cohen *et al.* 1971). This phenomenon is related to the shortening of the variability time scales; the wave fronts received from an isolated emitter moving away from the core at a small angle toward the observer are compressed in time, but the angular separation observed between the core and the emitter is not; hence, the apparent angular velocity of separation can be increased to give an inferred physical separation velocity greater than the speed of light. As expected, this tends to occur in bright, one-sided milliarcsecond scale jets. There are, however, a number of exceptions, which include 3C179 (Porcas 1981), 3C245, and 3C263 (Hough 1986), which may be statistically acceptable if superluminal motion is common in compact sources. The ratio of X-ray to radio flux in these sources is lower than would be inferred for a source which is stationary relative to the observer, and which is radiating radio synchrotron and X-ray self-Compton radiation (Jones *et al.* 1974a; Jones *et al.* 1974b; Marscher 1983). If the source is moving relativistically, the density of relativistic electrons required to provide the observed synchrotron radiation in a given volume is reduced; since the X-ray flux is proportional to the intensity of radio synchrotron radiation and the density of relativistic electrons, the ratio of intrinsic X-ray to radio flux is reduced by the reduction in density. This has been used as evidence for relativistic motion in NRAO 140 and NRAO 150 (Marscher and Broderick 1981; Marscher and Broderick 1985) and other sources.

The various classes of compact cores can be accounted for by the beaming model (Blandford and Rees 1974; Scheuer and Readhead 1979; Pearson and Readhead 1984). The very compact cores, which are unresolved by VLBI, tend to be the most variable, and can be identified with jets pointed almost directly toward the observer. The steep spectrum compact (SSC) sources, as their name implies, have exceptionally steep spectra, with the compact jets apparently complex and often misaligned with the arcsecond scale jets. Since optically thin synchrotron radio flux is more highly beamed because of the dependence on spectral index of the beaming, the SSC sources are inferred to be pointing very close to the line of sight, with the complexity and misalignment of the jet due to the projection of small bends viewed almost along the line of sight (Readhead *et al.* 1978; Gower *et al.* 1982). The compact core-jet sources tend to be well-aligned with the large-scale structure, somewhat less variable than the very compact core sources, and often exhibit superluminal motion. These sources are believed to be oriented close to the line of sight, near the angle $\theta_{\rm obs} = \sin^{-1}(1/\Gamma)$ at which the apparent angular separation (superluminal motion) is a maximum, and inside of which the flux is strongly enhanced. Weaker cores tend to be one-sided, but are so faint that the flux cannot be traced out more than a milliarcsecond or so; these are interpreted as relatively unbeamed jets, directed at larger angles to the line of sight than the compact core-jet sources (Hough 1986; Ulrich and Meier 1984). The compact doubles tend to be nonvariable and do not exhibit superluminal motion; these are not believed to be part of this sequence in orientation angle, but are modeled as young twin jets which have not yet propagated far through the ISM (Phillips *et al.* 1984). They also show no extended structures, which agrees with the contention that the jets have as yet been confined to the central regions of the host (Pearson

and Readhead 1984). The extent of the large-scale structure associated with compact sources other than compact doubles tends to increase from the very compact cores to the weak asymmetric cores, reinforcing the interpretation of these sources in terms of the orientation of a relativistic jet (Perley 1982).

The physics of relativistic jets is difficult, and there are few attempts to deal with the detailed structure of milliarcsecond scale jets other than kinematically (Blandford and Königl 1979; and Königl 1980). This has been more than adequate given the observations, as the only imaging technique which can presently obtain milliarcsecond resolution is VLBI, which is difficult to do with sufficient sensitivity to image more than bright knots. While bright knots are excellent for measuring superluminal motions, they do not provide much information regarding the underlying extended flow field, if any, of the inferred relativistic jet. Two approaches used to attempt to circumvent this problem are the survey approach (Pearson and Readhead 1984) and the multi-frequency observing approach. The survey approach images a carefully selected sample of compact sources and examines the statistics of their structures, fluxes, etc. to find correlations which may indicate the underlying phenomena. These surveys strongly support the concepts of bulk relativistic flow and the different classes of objects being due to observing angle, but the VLBI morphology is so strongly influenced by beaming and projection that it is difficult to deduce more. Multi-frequency flux monitoring (Worrall *et al.* 1984) has been used to construct broadband spectra of the compact cores of radio sources, from which one can obtain information regarding the electron energy distribution and other parameters related to the microphysics of the emitting regions. Variability and flux ratios can also be used in some model-dependent but still useful ways to estimate the average relativistic flow speed (Blandford and Königl 1979). They are limited in their effectiveness by resolution; the fluxes which

can be obtained are integrated fluxes for the entire core, and cannot differentiate between different physical regions within the source.

The solution to this dilemma is to get better images of the flow field in VLBI jets. The limited dynamic range of VLBI, coupled with the sparseness of the sampling of the interferometer and the relative brightness of the knots in these sources, makes this difficult, and it has only been within the past few years that more telescopes and improvements in equipment and data analysis techniques have even made it possible. There have been several intense studies on individual sources, designed to produce highly sensitive maps. The galaxy 3C120 (Walker *et al.* 1984) has been observed at several epochs over several decades of resolution, which has produced a complete record of emission knots traced very far out along the jet. NGC6251 (Jones *et al.* 1986), on the other hand, is a very smooth, straight jet over many jet radii. 3C273 and 3C345 have been monitored with limited sensitivity for many epochs (Moore *et al.* 1984; Unwin *et al.* 1985; Biretta *et al.* 1985), giving a complete record of superluminal activity for several years, and 3C273 has recently been imaged to sufficiently high sensitivity to reveal underlying continuous flux (Davis and Unwin 1986). The second chapter of this thesis describes high dynamic range imaging of the VLBI jet in the N galaxy 3C371 and discusses the results in terms of previous VLBI maps, MERLIN and VLA maps, and multifrequency observations (Browne, private communication; Worrall *et al.* 1984; Staubert *et al.* 1986).

Apart from detailed images of VLBI jets, which require high sensitivity, the most important quantitative results obtainable from VLBI are apparent superluminal expansion rates. These have traditionally been interpreted as tracers of the bulk relativistic velocity of the fluid; the speed of the jet and the speed of the observed pattern are assumed to be the same. This is consistent in general with

the observed ratios of core to extended flux in extragalactic radio sources, but some discrepancies seem to indicate a somewhat slower, although still relativistic, velocity. These can be removed by decoupling the velocity of the patterns from the velocity of the emitting fluid, by noting that the fluid in the patterns may itself be moving relativistically relative to the pattern. This is the case for relativistic shocks, which have the additional advantage of providing an obvious site for transferring energy of bulk motion into radiation. The third chapter of this thesis analyzes this effect for several kinematically reasonable flow models, and demonstrates the degree to which the beaming and the apparent superluminal motion can be dissociated.

4. Large-Scale Jets

The compact jet is the base of the extended jet, and so the physics of jets at VLBI scales should have implications for the physics of jets at arcsecond scales. The most basic observation is the relative alignments of the compact and extended structure: the structure in extragalactic radio sources tends to be aligned within a few degrees between the milliarcsecond and arcsecond scales, with the one-sided jets on the same side in all cases (except for the steep-spectrum compact cores discussed previously). This supports the contentions that the jets observed at both resolution scales are part of the same physical jet, and that the emission in the large-scale jet is also beamed. The ratio of brightnesses for two identical jets with spectral index α oriented at an angle θ from the observer is $F^+/F^- = [(1 + \beta\cos\theta)/(1-\beta\cos\theta)]^{2+\alpha}$ ($3+\alpha$ for unresolved knots)(Scheuer and Readhead 1978; Perley 1984). Unfortunately, the best dynamic range attainable allows measured limits for jet to counterjet brightness ratios of no greater than about 50:1 or so. This gives $\beta\cos\theta > 0.62$ for $\alpha = 0.7$, implying that the jet is at least mildly relativistic. The best criterion would be direct measurement of the motion, either

by optical emission lines (which still leaves the question of whether that really relates to the jet velocity) or by proper motion of knots, which requires very precise measurements of position. This work is in progress, and should be able to measure relativistic motion in large-scale jets if the noise in the map can be reduced to near the thermal limit (Perley 1984).

A related measurement would be the observation of periodic structure in a jet (if present), coupled with some estimate of the precession rate of the central engine; the wavelength of the periodic structure (or "wiggles") and the rate of precession gives an inferred flow velocity for a given viewing angle, assuming that the wiggles propagate ballistically. The primary uncertainty is in determining the precession rates; these are unknown and, given anticipated time scales of 10^4 to 10^5 years, probably unmeasurable. A more likely technique is to look at the positions of bright features along jets and counterjets (which requires, of course, that the counterjets are observable), and compare their distances from the core; the Doppler effect would then give different apparent separations for identical physical separations. This gives $\beta \cos\theta < 0.05$ for NGC6251, which contradicts results from observed brightness ratios indicating that $\beta \cos\theta > 0.6$; either the knots are paired relativistic shocks in a nonrelativistic flow — which would be very difficult to explain physically — or there is indeed some physical asymmetry in the large-scale jets (Perley 1984).

The opposite extreme to one-sided large-scale jets being perfectly symmetric and beamed is that they are intrinsically asymmetric and unbeamed; the jets are actually one-sided, and the large-scale jet "flip-flops" across the source axis on some fairly long time scale (Rudnick and Edgar 1984). This model has several difficulties. Firstly, if VLBI jets are relativistic, then there should be as many large-scale jets without cores as with cores, since roughly half should be beamed below

the limit of detection. Secondly, there should be a number of cases where the jet has just flipped, and the VLBI jet is perfectly misaligned with the large-scale jet, which is not observed. Finally, the more compact hotspot in the classical double radio sources is generally associated with the brighter jet. Since the hotspot is the jet terminus, then the hotspot on the side from which the jet has flipped should remain more compact for at least the travel time for the jet material to reach the hotspots, since energy transport to the hotspot will be maintained for at least that time; the last material emitted from one side and the first material emitted from the other side must reach the lobes for them to change in relative compactness, even ignoring the time scale for diffusion in the starved lobe. If the time scale for the "flip-flop" is short enough to guarantee that both lobes will remain fairly bright, then it should also be short enough that a considerable number of weaker jets should be associated with more compact hotspots, which is not observed. In the beaming model, differences between the lobes can be explained by beaming of the hotspot emission (although the hotspot itself need not move relativistically), and the higher column density of material through which emission from the farther lobe must pass.

The properties of the lobes themselves can be used to obtain crude estimates of flow velocities in jets, by estimating the kinetic energy fluxes into the lobes from the lobe luminosities, the momentum fluxes into the lobes from the pressures in the lobes, and the mass flux into the lobe from depolarization and the estimated age of the source (Perley 1984). These arguments give a lower bound for the flow speed of the jet material of roughly 0.1c, which is consistent with the large brightness ratios between jets and counterjets (Dreher 1984).

The final arguments for large-scale one-sided jets being somewhat relativistic are physical. It is very difficult to slow a relativistic jet without totally disrupting

it; a minor reduction in the speed results in a large amount of energy and momentum dissipation, destroying the momentum-dominated nature of the flow. A gradual entrainment of ambient material could possibly slow a relativistic jet without disrupting it, but even this is questionable. On the other hand, the contradictory evidence for NGC6251 suggests that not all differences are due to relativistic motion. A reasonable hypothesis for the nature of the large-scale one-sided jets in FRII sources is that they are supersonic, mildly relativistic, and well-collimated. The jets in FRI sources exhibit neither one-sidedness nor lobes; their appearance is that of turbulent nonrelativistic subsonic or transonic flows, as evidenced by weak collimation, center-brightened structure, and generally plumed appearance (Bicknell 1984).

Despite the evidence for relativistic flow in large-scale jets, theoretical models have generally been based on nonrelativistic flow. There are a number of good reasons for this. Firstly, relativistic fluid flows are very difficult to calculate either analytically or numerically because of the Lorenz factors involved; they are very nonlinear in velocity, especially in the mildly relativistic limit where neither $\beta \approx 1$ nor $\Gamma = 1$ is an adequate approximation, and give very large gradients at shocks. Secondly, most of our intuition is based on nonrelativistic flows, and so it is easier to understand nonrelativistic flows first and then find out how they differ from relativistic flows than to jump directly to the relativistic case. Thirdly, there is a large body of experimental data on nonrelativistic flows, but nothing regarding relativistic bulk fluid flow. Finally, many of the qualitative features observed in nonrelativistic flows should also be present in relativistic flows, and thus a careful treatment of the nonrelativistic case could be considered the first stage of a fully relativistic understanding of these jets. In fact, if it could be demonstrated that nonrelativistic flows were inadequate to explain the pressure and density contrasts

inferred in these jets, it would be strong evidence for the relativistic nature of these flows, but such a demonstration would require a thorough knowledge of the behavior of nonrelativistic jets.

The behavior of nonrelativistic shocks includes both local and global phenomena. Local phenomena include reacceleration of synchrotron-emitting, relativistic electrons in shocks and turbulence, the development and structure of shocks and other localized flow instabilities, and the development and stability of knots of enhanced pressure and density. Global phenomena include collimation of the jet, the development of nonlinear modes of instability, and the effects of entrainment and other interactions with the ambient medium. Considerable analytical work has gone into the study of various dynamical and kinematical aspects of supersonic flow, such as global constraints on mass, energy, and momentum transport (O'Dea 1985), ram pressure bending of jets (Jones and Owen 1979; Begelman *et al.* 1977; O'Dea 1984), and the development of instabilities (Hardee 1984; Cohn and Payne 1985). Unfortunately, this leaves the theorist in much the same situation as the observer faced in the early days of interferometry; some global parameters and structural characteristics can be determined at the cost of considerable effort, just as fluxes and separations could be measured with only limited sensitivity and resolution using early radio interferometers.

5. Numerical Simulations of Hydrodynamic Jets

Observational advances were based largely on the development of instruments such as the VLA, MERLIN, Westerbork, and the global VLBI array; the theoretical analogy is the supercomputer, and the NSF Supercomputer Centers could well be called the "Theorist's VLA". The equations of hydrodynamics and magnetohydrodynamics are highly coupled and nonlinear, and detailed solution of these equations, showing the relative importance and nonlinear growth of all the modes

in a jet over the entire length of the jet, is analytically intractable. Detailed physical jets must be modeled numerically, and the observed features broken down and analyzed in terms of analytically understood instabilities and gas interactions, to provide explanations for features observable with modern radio interferometers. In fact, computer simulations are more closely analogous to classical observing than classical theory; rather than observing different regions of physical space, the numerical (magneto)hydrodynamicist observes different regions of parameter space, but the results must be interpreted in terms of physical processes in precisely the same way. The advantage of the numerical observation is that there is much greater knowledge of the parameters describing the flow, and the data are much more complete; the disadvantage is that there is no guarantee that the parameters chosen describe anything observed in the physical universe. Numerical observations do provide insight into processes which can be expected to occur in physical sources, but it is crucial to avoid the temptation to make a one-to-one correspondence between a numerical and a physical source. They are simply all part of some ensemble of sources, some of which are far better defined in terms of theory, and some of which are observed to exist.

Considerable numerical modeling has already been carried out for hydrodynamic jets (Norman *et al.* 1982a; Norman *et al.* 1982b; Williams and Gull 1984; Williams and Gull 1985; Wilson and Falle 1985; Arnold and Arnett 1986). This research has demonstrated that supersonic hydrodynamic jets are stable to axisymmetric instabilities over lengths of many jet radii. The Kelvin-Helmholtz reflection mode instability, which dominates in these jets, is saturated through the formation of oblique shocks, which could correspond to bright emission knots in physical jets. The characteristic wavelength of this mode is of order 5-10 jet radii, propagating downstream at one-quarter to one-half the flow speed in the jet, and

permitting overpressures in the knots of up to a factor of five over the pressure in the ambient medium. A more general result of these calculations is that transonic jets, which are subject to the ordinary Kelvin-Helmholtz instability, do tend to break up and become fully turbulent. This agrees with the observed differences between the FRI and FRII sources, in which the weaker jets become turbulent (FRI) and the stronger jets remain well-collimated but develop bright emission knots (FRII) (Norman *et al.* 1984).

6. Magnetohydrodynamic Jets

Unmagnetized outflow is insufficient to explain all of the features of extragalactic radio jets. These jets remain highly collimated over hundreds of jet radii, which implies that some mechanism in addition to oblique shock focusing must be responsible for the containment of the jet. A natural candidate for this would be toroidal magnetic fields. Magnetic confinement is also required to explain inferred overpressures of fifty or more in some sources (Bridle and Perley 1984). Since oblique shocks dissipate energy and momentum into the surrounding medium, magnetic confinement should be more efficient than shock confinement at transporting energy to the lobes without dissipating excessive amounts of energy and momentum, and thus reducing the energy and momentum flux requirements at the base of the jet. Finally, the observation of polarized radio flux from jets indicates that ordered fields are present in at least a statistical sense, and may be dynamically important.

The fourth, fifth, and sixth chapters of this thesis describe the development, testing and verification, and application of a two-dimensional, axisymmetric MHD code designed to simulate the behavior of magnetized jets.

Over the past two years, David Payne and David Meier of the Jet Propulsion Laboratory and I wrote and tested an explicit, two-dimensional, one-fluid, ideal

MHD code under the scientific supervision of Roger Blandford. In this code, a perfectly conducting jet with embedded toroidal field is injected into a perfectly conducting unmagnetized uniform medium. It is second-order accurate in both space and time. Operator splitting is used to reduce the two-dimensional flow equations to a series of one-dimensional flow equations. In carrying out the spatial differencing of the flow equations, which have been written in a conservative form, the transport terms are differenced via a modification of van Leer's monotonic upwind differencing scheme, while the Lagrangian terms are center-space differenced. Temporal differencing is done by a predictor-corrector scheme, where the time step is determined by selection of a maximum Courant number over the entire computational grid. No adaptive gridding or interface tracking is employed in the code. This code has been tested on a variety of one-dimensional flows, including the standard Riemann shock tube problem and several analytic solutions to Burger's equation, with excellent results. Tests have also been carried out on two-dimensional solutions of Burger's equation. Hydrodynamic simulations run with this code were compared in detail with older codes of proven reliability, *cf.*, with Norman (Norman *et al.* 1982a). The goal of this work is to determine the stability and collimation of magnetized jets, explain large pressure overdensities in knots in terms of magnetic pinches, and determine ways in which magnetized and unmagnetized flows differ morphologically, so that they can be distinguished by radio imaging.

7. Evidence From Radio Polarization

The most obvious way of distinguishing between magnetized and unmagnetized plasmas is to look for polarized flux in the radio synchrotron emission. However, the interpretation of observed polarization in terms of a physical description of the emitting region is not straightforward. The emitting gas is not the only influence

on the polarization vector; an intervening magnetized plasma — such as would be present in a cocoon surrounding a magnetized jet — would contribute Faraday rotation, and unmagnetized or weakly magnetized plasma would tend to depolarize the radio flux. For example, the weaker lobe in a classical double radio source should be depolarized relative to the stronger lobe in the beaming theory, even though the lobes are assumed to be physically identical, because the weaker lobe points away from the observer and hence its emission passes through a higher column density of foreground plasma. Observed polarized emission is a function of both emitting and foreground regions; the effects of the foreground must be estimated by analysis of radio polarization maps at several frequencies with similar resolution before any solid statements may be made regarding the polarization of the emitted radiation (Laing 1984; Laing 1986).

Even given the intrinsic polarization of the emitting region, there are a number of considerations involved in linking the polarization vectors to the magnetic field configuration. Firstly, the direction of the polarization vectors depend on the optical depth for synchrotron emission; the electric vectors are perpendicular to the underlying magnetic field for optically thin emission, but parallel for optically thick emission. Secondly, the polarized flux is proportional to the strength of the magnetic field and the density of relativistic electrons; since high magnetic fields and charged particle reacceleration occur primarily in regions of strong shear or compression (such as shocks), the polarization may be more characteristic of local disturbances in the field than the general magnetic configuration. Finally, highly polarized emission can originate from compressed or sheared regions of tangled field as well as from regions of ordered field; high polarization does not imply highly-ordered fields.

While the correlation between Fanaroff-Riley class and polarization properties of jets need not be due to dynamically important large-scale magnetic fields, confinement arguments strongly suggest that they have some influence in the jets associated with FRII sources. There are three types of magnetic configurations seen in extended jets: magnetic field parallel to the jet axis, magnetic field perpendicular to the jet axis, and magnetic field initially parallel but becoming perpendicular at some point along the jet. The first is characteristic of the one-sided jets found in FRII sources, whereas the latter two are found in the two-sided jets of FRI sources (Bridle 1984b).

The field configuration in the FRI sources is that expected from a subsonic or transonic turbulent flow with tangled fields; indeed, turbulence would be suppressed if the field were dynamically dominant, or would rapidly tangle any ordered field if it were not, so if these jets are turbulent, the field must be tangled. Since the jets are two-sided, they must be moving nonrelativistically. If the flow is actually subsonic or transonic (indicated by the low luminosity and poor collimation), then it should be relatively easy to compress as it enters the ambient medium, which would amplify the tangled field perpendicular to the jet. However, a subsonic turbulent jet would be subject to considerable buoyant and viscous interactions with the surrounding medium. These interactions, as well as the turbulent velocity field within the jet itself, would amplify the parallel component of the tangled field through velocity shearing, and turbulent motions would carry reaccelerated electrons and amplified fields throughout the body of the jet. Such a jet would also be easily bent by ram pressure; changes in field orientation observed at bends are consistent with a longitudinal compression of the gas at the bend, which amplifies the field component parallel to the jet. Luminosity, collimation, polarization properties, and general appearance support the contention that the jets in FRI sources

are turbulent with embedded tangled fields, and are at most mildly momentum dominated; supersonic jet models with large-scale ordered fields are not relevant to these jets, and should be compared to the jets in FRII sources.

Large-scale collimation and high overpressures in the knots of one-sided jets indicate magnetic confinement, but polarization measurements suggest that the field is poloidal rather than toroidal (except at knots, where shocks would amplify the toroidal field). However, much if not all of this could be explained by the generation of relativistic electrons and amplification of the parallel component of tangled field by axial velocity shear in the body of the jet; it need not be representative of the nature of the ordered field, or of the field in cooler, but possibly dynamically dominant, parts of the jet. The radiation from jets is akin to a leak in a pipe, in which energy and momentum is diverted from its original course to power instabilities and shears which reaccelerate particles on the microphysical level, and the appearance of the leak is due to the nature of the leak as well as the nature of the pipe. Despite the need for caution, the prevalence of parallel magnetic field in arcsecond scale jets as inferred by the direction of the polarization suggests that there may be a significant amount of poloidal field in these jets.

It is likely that the real magnetic field consists of all three components. The toroidal field would confine the flow, but may appear to dominate primarily near shocks and pinches. The poloidal field would stiffen or kink the jet, and may appear to dominate over most of the length of the jet. The tangled field would provide a more or less isotropic pressure and magnetic viscosity, and would have some anisotropic contribution to the pressure in regions of strong compression or shear. Ideally, this is what should be calculated for a complete numerical model of a supersonic extragalactic radio jet. In practice, it is far easier to develop a limited code and upgrade it, and the most basic field configuration to develop

initially is toroidal. This has the conceptual advantage of demonstrating confinement, the nonlinear development of pinch instabilities, and the generation of large-scale poloidal currents without complications arising from the tangled and poloidal fields. The jet model described in this thesis is acknowledged to be far simpler than the physical jet it is designed to explain, but is illustrative of the characteristics arising from a limited range of phenomena within the jet, which can be expanded upon by improvements to the model. Once this simpler model is understood, it will be easier to go on to an understanding of more complicated models.

8. Observational and Theoretical Study of Jets

The detail available theoretically through analysis of parameterized numerical simulations of jets is beginning to approach the detail available observationally through radio interferometry and multi-frequency flux monitoring. In many ways, this is the most efficient state for the production of scientific results, as theoretical developments can be considered in terms of presently available observations, and observational results can be considered in terms of presently available theoretical concepts. Our knowledge of jets is being advanced on both fronts simultaneous, by the development of higher resolution with greater sensitivity and polarization imaging capability on the observational side, and numerical and analytical study of relativistic and magnetized flows on the theoretical side. The coordination of these efforts requires that jet researchers, whatever their specialization, develop an appreciation and understanding of both the observations and the theory, and it is goal of this thesis to present a combined observational/theoretical study of jets to further this understanding.

References

Arnold, C.N. and Arnett, W.D. 1986, *Ap. J. (Letters),* **305**, L57.

Begelman, M.C., Rees, M.J., and Blandford, R.D. 1977, *Nature,* **279**, 770.

Bicknell, G.V. 1984, in *Physics of Energy Transport in Extragalactic Radio Sources* ed. A.H. Bridle and J.A. Eilek (NRAO: Green Bank, West Virginia), p. 229.

Biretta, J.A., Cohen, M.C., Hardebeck, H.E., Kaufmann, P., Abraham, Z., Perfetto, A.A., Scalise, E. Jr., Schaal, R.E., and Silva, P.M. 1985, *Ap. J. (Letters),* **292**, L5.

Biretta, J.A., Owen, F.N., and Hardee, P.E. 1983, *Ap. J. (Letters),* **274**, L27.

Blandford, R.D. and Icke, V. 1978, *M.N.R.A.S.,* **185**, 527.

Blandford, R.D. and Königl, A. 1979, *Ap. J.,* **232**, 38.

Blandford, R.D., McKee,C.F., and Rees, M.J. 1977, *Nature,* **267**, 211.

Blandford, R.D., and Rees, M.J. 1974, *M.N.R.A.S.,* **169**, 395.

Blandford, R.D., and Rees, M.J. 1977, *Phys. Scr.,* **17**, 265.

Bridle, A.H. 1984a, in *Physics of Energy Transport in Extragalactic Radio Sources* ed. A.H. Bridle and J.A. Eilek (NRAO: Green Bank, West Virginia), p. 1.

Bridle, A.H. 1984b, in *Physics of Energy Transport in Extragalactic Radio Sources* ed. A.H. Bridle and J.A. Eilek (NRAO: Green Bank, West Virginia), p. 135.

Bridle, A.H. and Perley, R.A. 1984, *Ann. Rev. Astr. Ap.,* **22**, 319.

Burns, J.O. 1982, in *Astrophysical Jets* ed. A. Ferrari and A.G. Pacholczyk (Reidel: Boston), p. 67.

Charlesworth, M. and Spencer, R.E. 1982, *M.N.R.A.S.*, **200**, 933.

Cohen, M.C., Cannon, W., Purcell, G.H., Shaffer, D.B., Broderick, J.J., Kellerman, K.I., and Jauncey, D.L. 1971, *Ap. J.*, **170**, 207.

Cohen, M.H. and Unwin, S.C. 1984, in *IAU Symposium 110: VLBI and Compact Radio Sources* ed. R. Fanti, K. Kellerman, and G. Setti (Reidel: Boston), p. 95.

Davis, R.J. and Unwin, S.C. 1986, unpublished map.

Dreher, J.W. 1984, in *Physics of Energy Transport in Extragalactic Radio Sources* ed. A.H. Bridle and J.A. Eilek (NRAO: Green Bank, West Virginia), p. 109.

Eilek, J.A., Burns, J.O., O'Dea, C.P., and Owen, F.N. 1984, *Ap. J.*, **278**, 37.

Ekers, R.D., in *IAU Symposium 97: Extragalactic Radio Sources* ed. D.S. Heeschen and C.M. Wade (Reidel: Boston), p. 465.

Fanaroff, B.L. and Riley, J.M. 1974, *M.N.R.A.S.*, **167**, 31p.

Gower, A.C., Gregory, P.C., Hutchings, J.B., and Unruh, W.G. 1982, *Ap. J.*, **262**, 478.

Hardee, P. 1984, in *Physics of Energy Transport in Extragalactic Radio Sources* ed. A.H. Bridle and J.A. Eilek (NRAO: Green Bank, West Virginia), p. 144.

Hough, D.H. 1986, Ph.D. thesis, California Institute of Technology.

Jones, D.L., Unwin, S.C., Readhead, A.C.S., Sargent, W.L.W., Seielstad, G.A., Simon, R.A., Walker, R.C., Benson, J.M., Perley, R.A., Bridle, A.H., Pauliny-Toth, I.I.K., Romney, J., Witzel, A., Wilkinson, P.N., Bååth, L.B., Booth, R.S., Fort, D.N., Galt, J.A., Mutel, R.L., and Linfield, R.P. 1986, *Ap. J.*, **305**, 684.

Jones, T.W. and Owen, F.N. 1979, *Ap. J.*, **234**, 818.

Jones, T.W., O'Dell, S.L., and Stein, W.A. 1974a, *Ap. J.*, **188**, 353.

Jones, T.W., O'Dell, S.L., and Stein, W.A. 1974b, *Ap. J.*, **192**, 735.

Königl, A. 1980, *Phys. Fluids*, **23**, 1083.

Kronberg, P.P. and Clarke, J.N. 1978, *Ap. J.*, **224**, L51.

Laing, R.A. 1984, in *Physics of Energy Transport in Extragalactic Radio Sources* ed. A.H. Bridle and J.A. Eilek (NRAO: Green Bank, West Virginia), p. 90.

Laing, R.A. 1986, private communication.

Lind, K.R. and Blandford, R.D. 1985, *Ap. J.*, **295**, 358.

Marscher, A.P. 1983, *Ap. J.*, **264**, 296.

Marscher, A.P. and Broderick, J.J. 1981, *Ap. J.*, **249**, 406.

Marscher, A.P. and Broderick, J.J. 1985, *Ap. J.*, **290**, 735.

Moore, R.L., Biretta, J.A., Readhead, A.C.S., Bååth, L. 1984, in *IAU Symposium 110: VLBI and Compact Radio Sources* ed. R. Fanti, K. Kellerman, and G. Setti (Reidel: Boston), p. 109.

Norman, M.L., Smarr, L., Winkler, K.-H.A., and Smith, M.D. 1982a, *Astr. Ap.*, **113**, 285.

Norman, M.L., Winkler, K.-H.A., and Smarr, L. 1982b, in *Astrophysical Jets* ed. A. Ferrari and A.G. Pacholczyk (Reidel: Boston), p. 227.

Norman, M.L., Winkler, K.-H.A., and Smarr, L. 1984, in *Physics of Energy Transport in Extragalactic Radio Sources* ed. A.H. Bridle and J.A. Eilek (NRAO: Green Bank, West Virginia), p. 150.

O'Dea, C.P. 1985, Ph.D. thesis, University of Massachusetts.

O'Dea, C.P. 1985, *Ap. J.*, **295**, 80.

Orr, M.J.L. and Browne, I.W.A. 1982, *M.N.R.A.S.*, **200**, 1067.

Owen, F.N., Hardee, P.E., and Bignell, R.C. 1980, *Ap. J. (Letters)*, **239**, L11.

Owen, F.N., O'Dea, C.P., Inoue, M. and Eilek, J.A. 1985, *Ap. J. (Letters)*, **294**, L85.

Pacholczyk, A.G. 1982, in *Astrophysical Jets* ed. A. Ferrari and A.G. Pacholczyk (Reidel: Boston), p. 291.

Payne, D.G. and Cohn, H. 1985, *Ap. J.*, **291**, 655.

Pearson, T.J. and Readhead, A.C.S. 1984, in *IAU Symposium 110: VLBI and Compact Radio Sources* ed. R. Fanti, K. Kellerman, and G. Setti (Reidel: Boston), p. 15.

Perley, R.A. 1982, *A.J.*, **87**, 859.

Perley, R.A. 1984, in *IAU Symposium 110: VLBI and Compact Radio Sources* ed. R. Fanti, K. Kellerman, and G. Setti (Reidel: Boston), p. 153.

Perley, R. and Cornwell, T. 1984, in *Physics of Energy Transport in Extragalactic Radio Sources* ed. A.H. Bridle and J.A. Eilek (NRAO: Green Bank, West Virginia), p. 39.

Phillips, R.B., Hodges, M.W., and Mutel, R.L. 1984, in *IAU Symposium 110: VLBI and Compact Radio Sources* ed. R. Fanti, K. Kellerman, and G. Setti (Reidel: Boston), p. 63.

Porcas, R.W. 1981, *Nature*, **294**, 47.

Porcas, R.W. 1984, in *Active Galactic Nuclei* ed. J. E. Dyson (Manchester University Press: Manchester, England), p. 20.

Readhead, A.C.S., Cohen, M.H., Pearson, T.J., and Wilkinson, P.N. 1978, *Nature,* **276**, 768.

Rudnick, L. and Edgar, B.K. 1984, *Ap. J.,* **279**, 74.

Scheuer, P.A.G. 1974, *M.N.R.A.S.,* **166**, 513.

Scheuer, P.A.G. 1984, in *IAU Symposium 110: VLBI and Compact Radio Sources* ed. R. Fanti, K. Kellerman, and G. Setti (Reidel: Boston), p. 197.

Scheuer, P.A.G. and Readhead, A.C.S. 1979, *Nature,* **277**, 182.

Staubert, R., Brunner, H., Worrall, D.M. 1986, preprint.

Ulrich, M.-H. and Meier, D.L. 1984, *A.J.,* **89**, 203.

Unwin, S.C., Cohen, M.C., Biretta, J.A, Pearson, T.J., Seielstad, G.A., Walker, R.C., Simon, R.S., and Linfield, R.P. 1985, *Ap. J.,* **289**, 109.

van Breugel, W.J.M. and Miley, G.K. 1977, *Nature,* **265**, 315.

Walker, R.C., Benson, J.M., Seielstad, G.A., and Unwin, S.C. 1984, in *IAU Symposium 110: VLBI and Compact Radio Sources* ed. R. Fanti, K. Kellerman, and G. Setti (Reidel: Boston), p. 121.

Wardle, J.F.C. and Potash, R.I. 1984, in *Physics of Energy Transport in Extragalactic Radio Sources* ed. A.H. Bridle and J.A. Eilek (NRAO: Green Bank, West Virginia), p. 30.

Williams, A.G. and Gull, S.F. 1984, *Nature,* **310**, 33.

Williams, A.G. and Gull, S.F. 1985, *Nature,* **313**, 34.

Wilson, M.J. and Falle, S.A.E.G. 1985, *M.N.R.A.S.,* **216**, 971.

Worrall, D.M., Puschell, J.J., Bruhweiler, F.C., Miller, H.R., Rudy, R.J., Ku, W.H.-M., Aller, M.F., Aller, H.D., Hodge, P.E., Matthews, K., Neugebauer,

G., Soifer, B.T., Webb, J.R., Pica, A.J., Pollock, J.T., Smith, A.G., and Leacock, R.J. 1984, *Ap. J.*, **278**, 521.

Figure Captions

Figure 1. M87.

This contour map of M87 shows the one-sided jet. The jet broadens and brightens at the point marked "A." This may be indicative of dissipation, which could cause the jet to stagnate before escaping from the core of the ISM (Biretta *et al.* 1983).

Figure 2. Example of an FRI Source (M84).

M84 is an example of an FRI source. It is center-brightened, its jet is clearly two-sided, and it is strongly distorted (Laing 1984).

Figure 3. Examples of FRII Sources.

This collection of FRII sources are edge-brightened, their jets are clearly one-sided, and they are very straight (Wardle and Potash, 1984).

Figure 4. Narrow Angle Tail Source NGC1265.

NGC1265 is a narrow angle tail source (NAT), in which the radio-emitting gas is swept back by motion through the surrounding medium. The twin ridges near the core (where the jet is bent by ram pressure) and the extended tail are typical of this class of objects (O'Dea 1984).

Figure 5. Wide Angle Tail Source 3C465.

3C465 is a wide angle tail source (WAT), in which the radio-emitting gas is bent by pressure, density, or magnetic gradients in the surrounding medium. The

bend is less pronounced than for the NATs, but the extensions are similar in appearance to the tails of NATs (Eilek *et al.* 1984).

Figure 6. Symmetric Source 3C449.

While 3C449 is symmetric, like the NATs, its jets are not swept back, but appear to wiggle symmetrically. A similar class of objects, the antisymmetric sources, are typified by M84 (fig. 2) (Perley and Cornwell 1984).

Figure 7. Double-double Source 3C75.

3C75 has twin nuclei. Two-sided jets emerge from each nuclei, and merge on one side of the source (Owen *et al.* 1985).

Figure 8. Starburst Galaxy M82.

It is not clear whether the jet in M82 is truly a jet, is the result of widespread energetic activity associated with the galaxy-wide burst of star formation, or both (Kronberg and Clarke 1978).

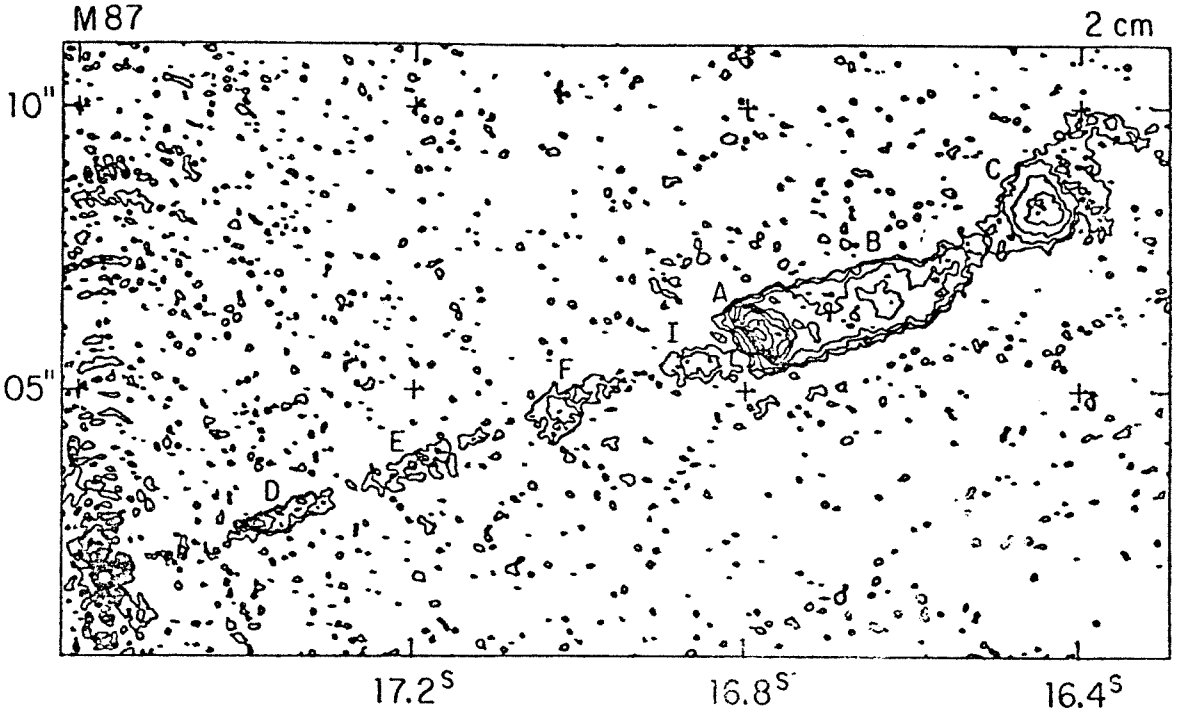

Figure 1

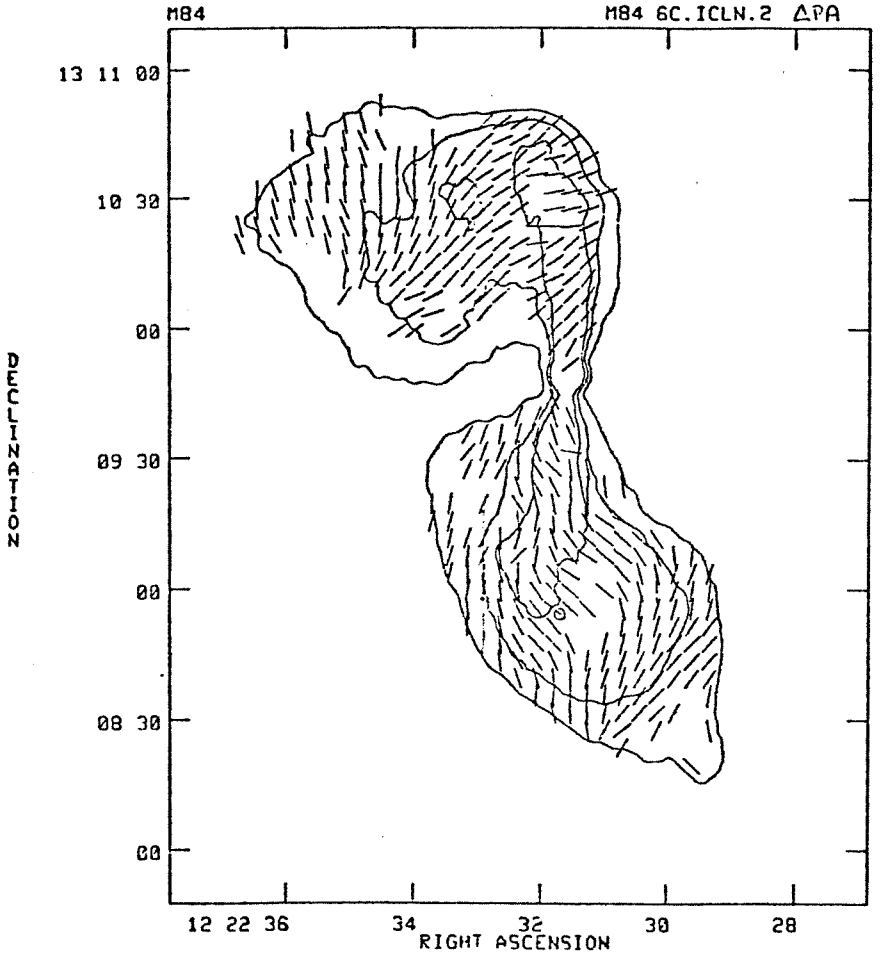
M84
M84 6C.ICLN.2 ΔPA
13 11 00
10 30
00
09 30
00
08 30
00
DECLINATION
12 22 36
34
32
30
28
RIGHT ASCENSION

Figure 2

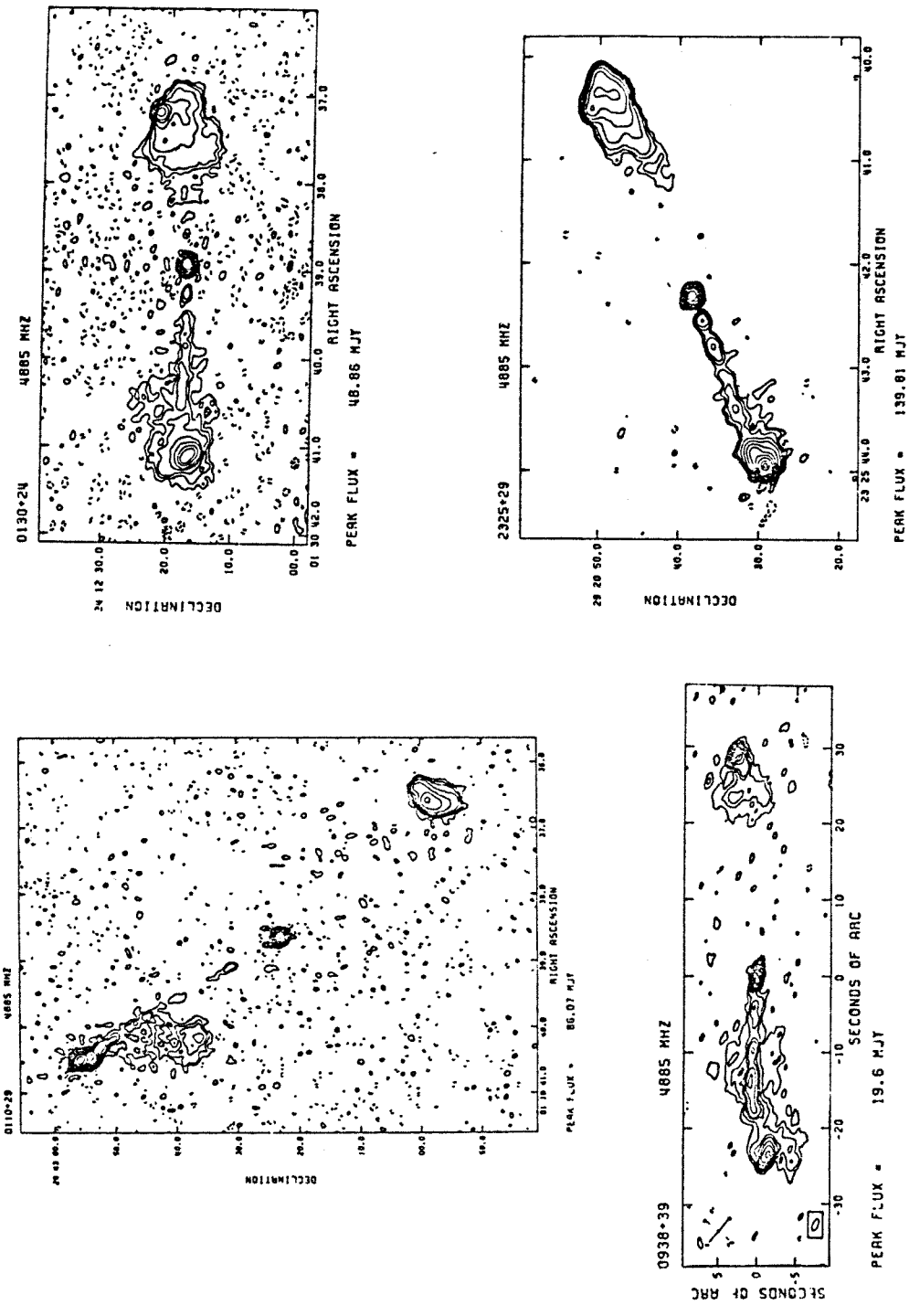
0130+24
4885 MHZ
RIGHT ASCENSION
DECLINATION
PEAK FLUX = 48.86 MJY
2325+29
4885 MHZ
RIGHT ASCENSION
DECLINATION
PEAK FLUX = 139.81 MJY
0110+29
4885 MHZ
RIGHT ASCENSION
DECLINATION
PEAK FLUX = 86.07 MJY
0938+39
4885 MHZ
SECONDS OF ARC
SECONDS OF ARC
PEAK FLUX = 19.6 MJY

Figure 3

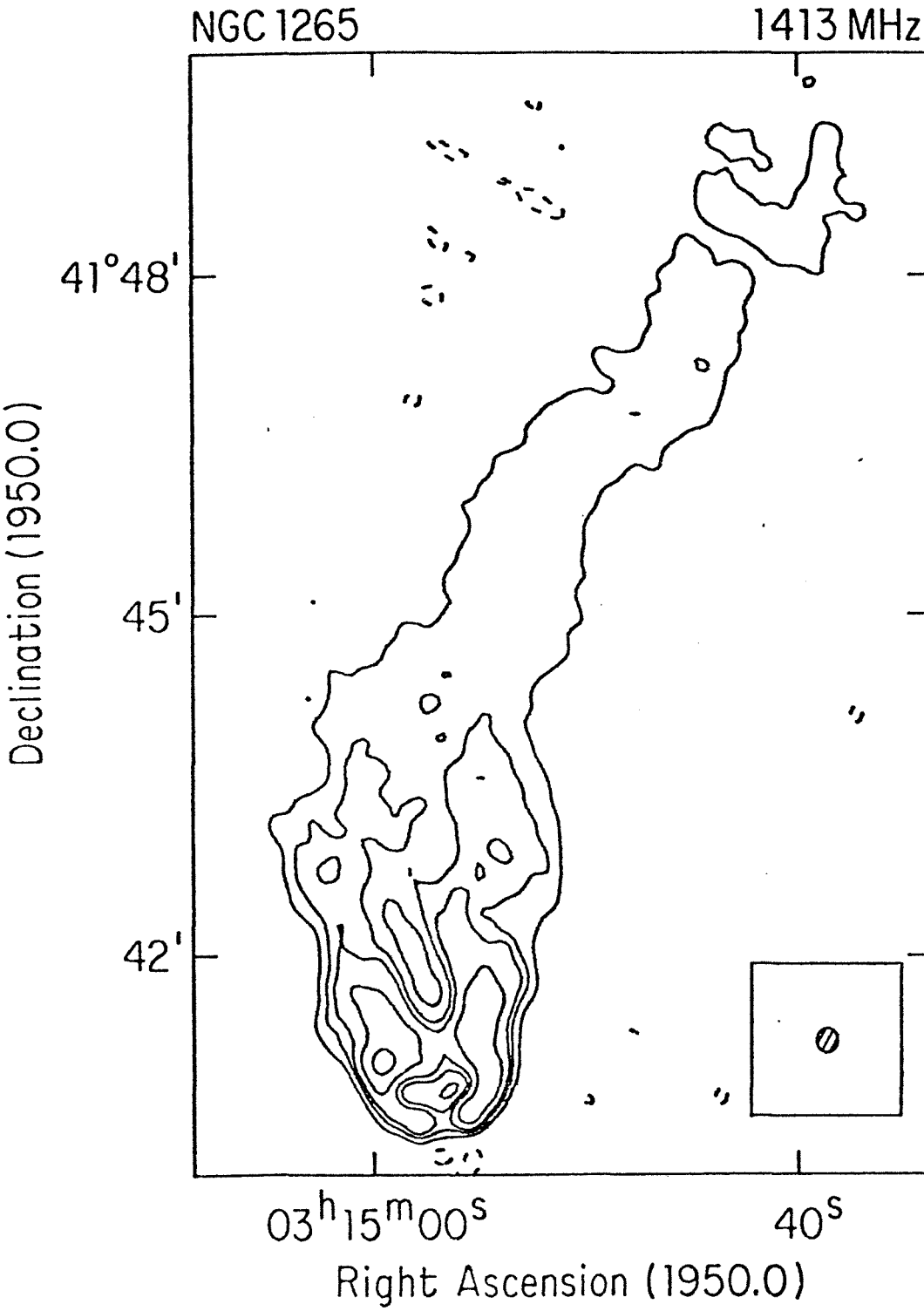
NGC 1265
1413 MHz
41°48'
45'
42'
Declination (1950.0)
03h15m00s
40s
Right Ascension (1950.0)

Figure 4

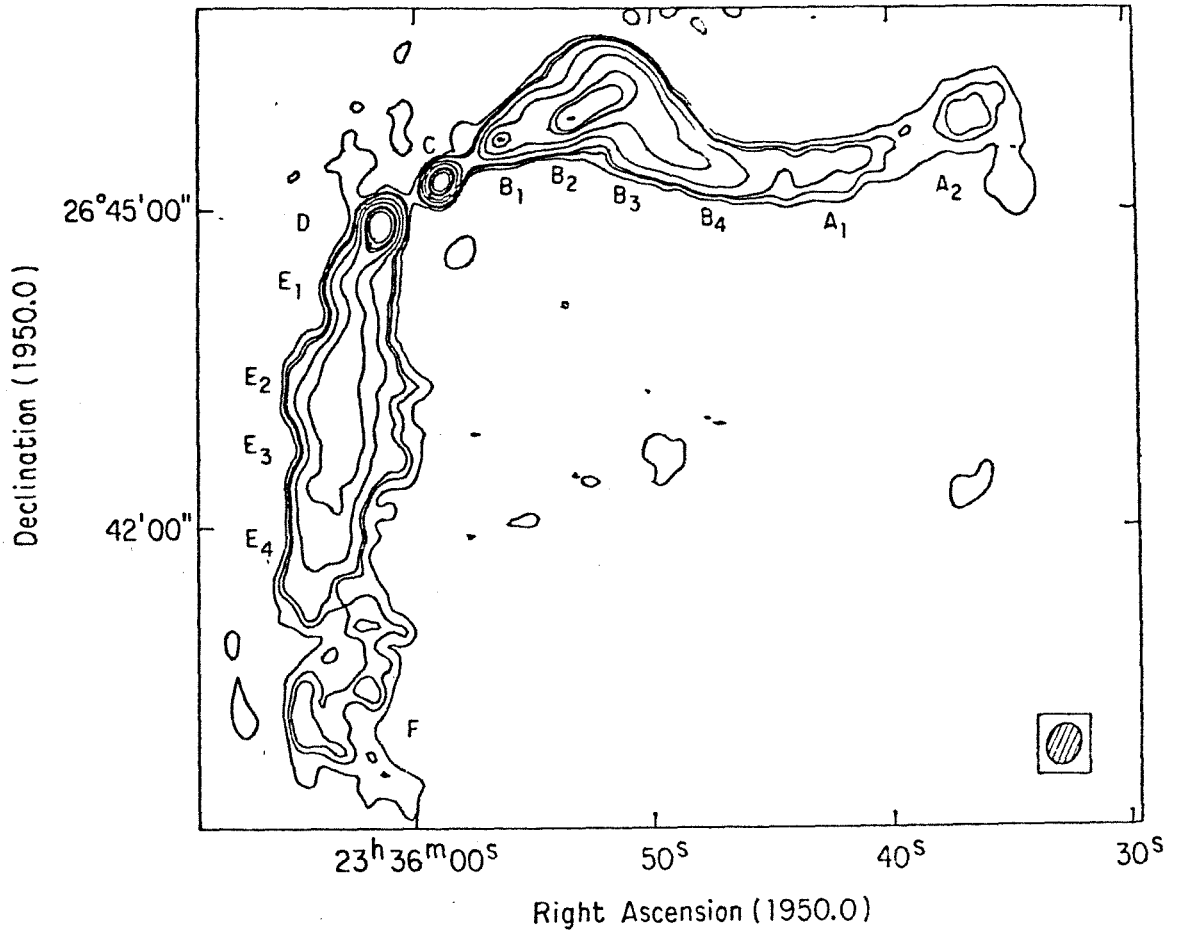
26°45'00"
42'00"
Declination (1950.0)
C
D
E1
E2
E3
E4
F
B1
B2
B3
B4
A1
A2
23h36m00s
50s
40s
30s
Right Ascension (1950.0)

Figure 5

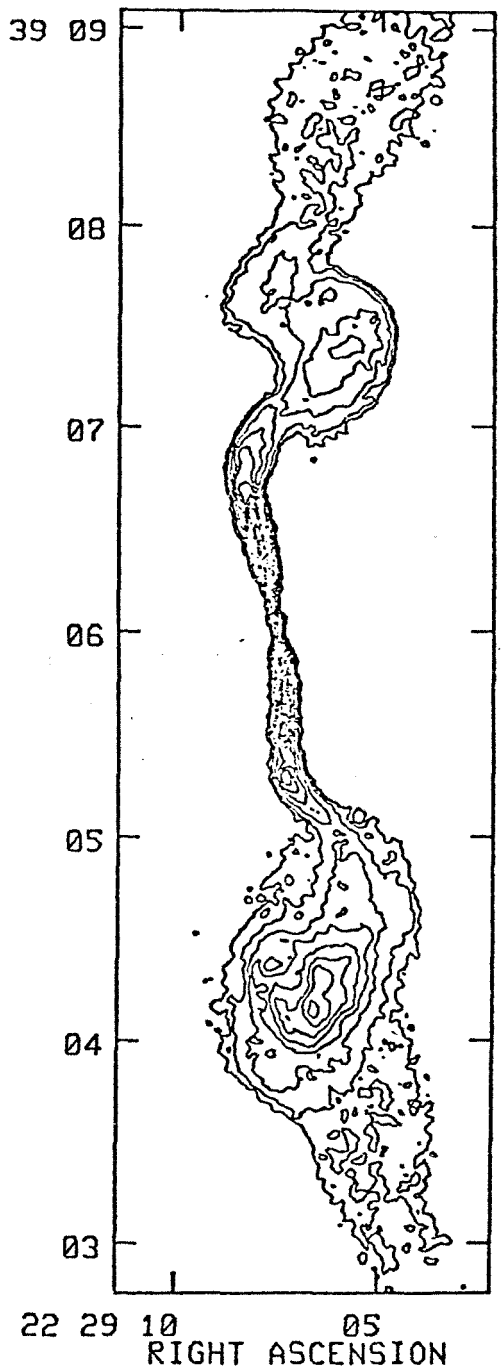

Figure 6

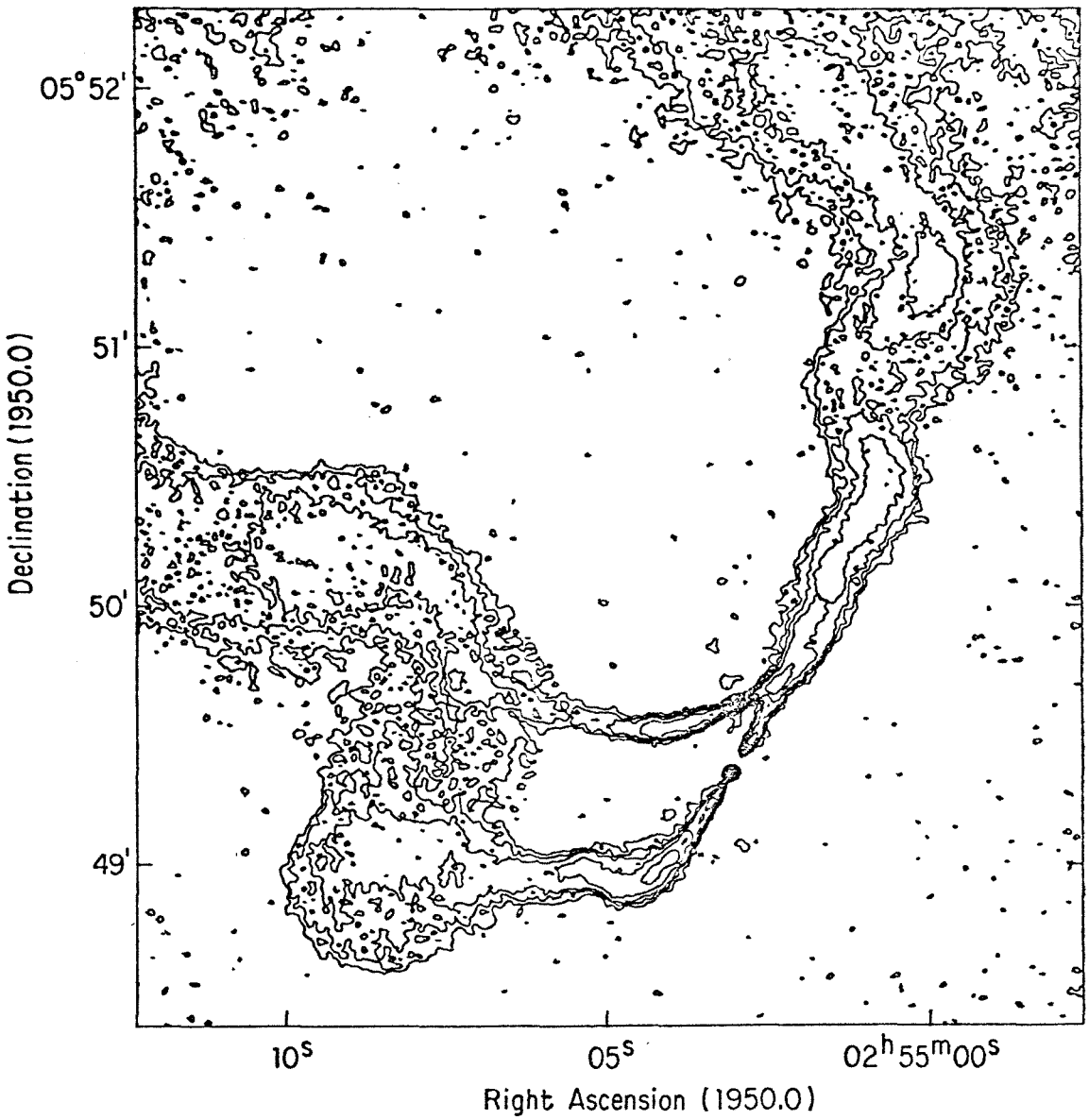
05°52'
51'
50'
49'
Declination (1950.0)
10s
05s
02h55m00s
Right Ascension (1950.0)

Figure 7

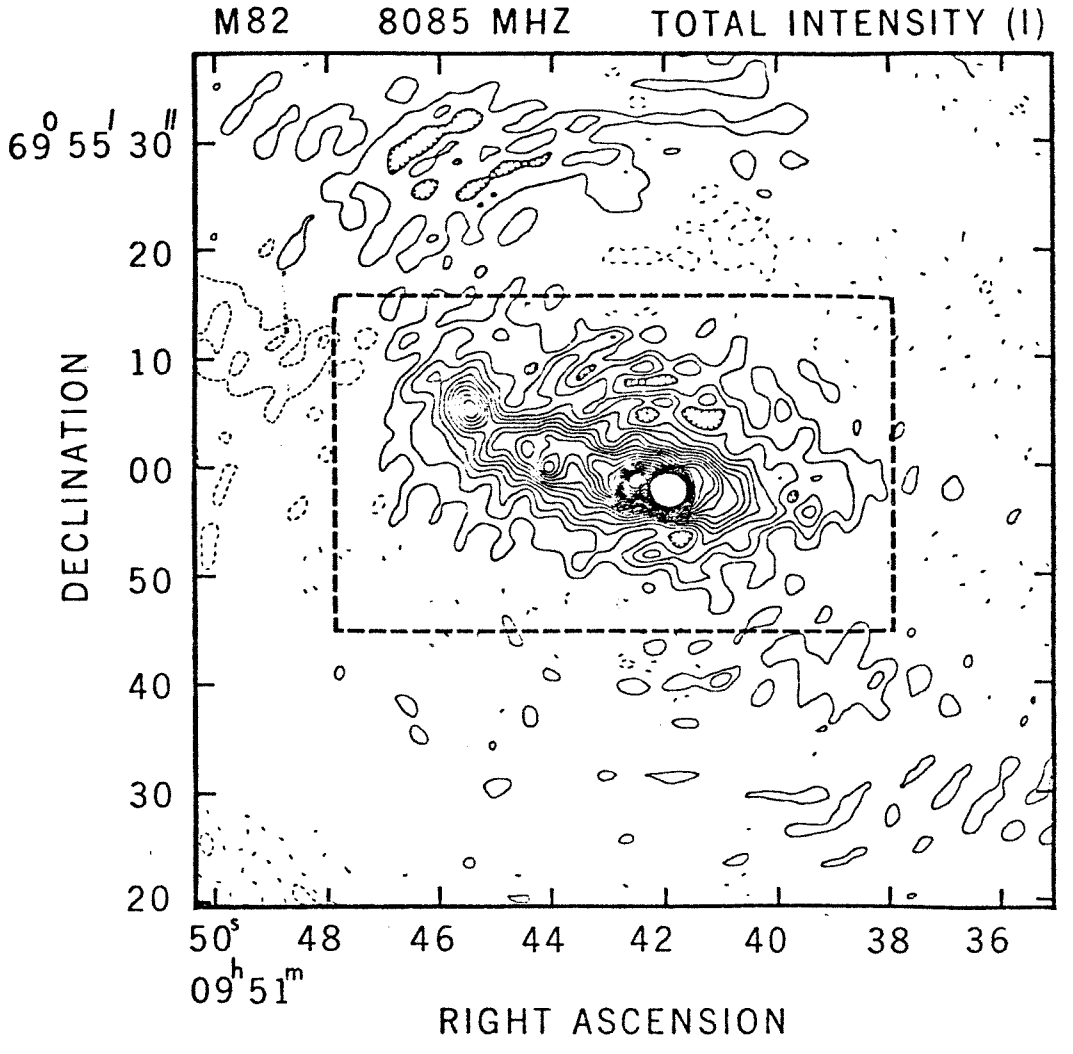
M82 8085 MHZ TOTAL INTENSITY (I)
69° 55' 30"
20
10
00
50
40
30
20
DECLINATION
50s 48 46 44 42 40 38 36
09h 51m
RIGHT ASCENSION

Figure 8

CHAPTER 2

OBSERVATIONS OF 3C371

1. Introduction

The two-dimensional imaging of low-level extended emission on milliarcsecond scales is both highly desirable and demanding. The typical VLBI map contains a compact core and a few bright knots extended along a position angle which is more or less aligned with the large-scale structure. It is customary to interpret these knots as regions of enhanced emission embedded in an underlying continuous flow field, but there is rarely evidence for continuity in the radio emission, and the maps often are, from a purely observational standpoint, equally well described by the emission of discrete packets of plasma from a well-aligned central engine. However, it is suspected that the knots are shocks in a continuous flow, which is itself unseen due to the limited dynamic range of the maps. In order to distinguish between the various models of VLBI "jets", this underlying emission must either be demonstrably absent to some reasonable brightness limit, or mapped, preferably with sufficient transverse resolution to reveal both axial and radial structure.

Such maps are not impossible to make, but they are difficult, and any attempted observations of underlying VLBI jets should be planned with care, from source selection to data reduction. The source or sources to be observed should be at relatively low redshift in order to obtain high linear resolution for a given angular resolution, i.e., redshift $z \leq 0.5$, which gives 10 parsecs per milliarcsecond for $H_0 = 75$. The source brightness must be large enough, at least one Jansky at 6 cm, to allow the detection of faint structure. Since resolution both transverse to and along the jet is required, it must be located at a high enough declination to provide uniform coverage with the present VLBI array, i.e., $50° \leq \delta \leq 80°$. Also, there should already be indications of extended structure on existing maps, especially if the underlying emission is to be mapped rather than simply detected. Any sources which would fit these requirements should already be included in some

flux-limited sample, and in fact would have been observed as part of the Pearson and Readhead flux-limited sample (Pearson and Readhead 1984). Examination of this sample revealed a number of good candidates. Of these, the best candidate for the mapping of underlying faint extended structure was 3C371, with $z = 0.05$, $\delta = 70°$, $F_{5\mathrm{GHz}} = 1.86$ Jy, and evidence for continuous emission on the survey maps.

In order to maximize dynamic range, the observation should maximize signal to noise and minimize sidelobes by using long tracks with many stations, which is also required for uniform angular resolution. They should be done using an intermediate frequency, such as 5 GHz, to obtain high resolution and allow for good a priori calibration. While coverage is important, ample time should be devoted to calibration in order to provide the best possible basis for accurate convergence in the self-calibration of the data. Previous experiments have partially met these requirements. NGC6251 had a known jet and was observed with complete coverage using a large number of stations, but the observations were made at a lower frequency (Jones *et al.* 1986). 3C120 (Walker *et al.* 1984) is nearby and has been observed with complete coverage at an intermediate frequency, but is at low declination. 3C273 (Unwin *et al.* 1985; Biretta *et al.* 1985) is also located at a low declination, which was compensated for by the addition of a station in South Africa or Brazil, but is at high redshift. Ideally, the search for underlying jets should be carried out for a number of sources, to provide a solid observational basis for theoretical modeling of the jets.

2. Previous Observations

3C371 is a nearby N galaxy ($z = 0.051$) located in a small cluster of galaxies (Sandage 1966; Miller 1975). The optical radiation can be separated into two components. The first is a small bright galaxy with $m_v = 16$, corresponding to a moderately luminous elliptical galaxy. This galaxy has the weak emission lines typical of an AGN, but the lines are much weaker than those for the typical Seyfert. The second component is a smooth nonthermal pointlike continuum source centered on the galaxy, similar to the core of a BL Lac object; this nucleus can vary by roughly one magnitude centered near $m_v = 15$ (Oke 1967; Oke 1978; Miller 1975; Worrall *et al.* 1984). Recent optical observations indicate a variable polarized optical continuum, with $m_v \approx 14.5$ and 12% polarization. Over one three-month time period, the optical and ultraviolet flux varied by 35% (Worrall *et al.* 1984; Staubert *et al.* 1986), which is typical of blazars. There was no evidence for either infrared or radio variability on a time scale of months (Worrall *et al.* 1984), although moderate radio variability is claimed over a time scale of years (Aller *et al.* 1982). The total radio flux is 1.5% polarized along position angle 38° (as compared to the VLBI position angle of 110°); VLA observations indicate that this is the sum of two polarized components (Wrobel and Lind 1986). The ratio of X-ray to radio flux indicated a Doppler beaming factor $\delta \geq 10$, where $\delta \equiv (1-\beta^2)^{\frac{1}{2}}/(1-\beta\cos\theta)$, where βc is the bulk velocity of the emitting material relative to the observer, and θ is the angle to the line of sight (Worrall *et al.* 1984). This was confirmed by detection of X-ray variability on time scales of from tens of minutes to days using EXOSAT (Staubert *et al.* 1986). The beamed continuum and structural changes in survey maps at different epochs made 3C371 a good candidate for superluminal motion (Pearson and Readhead 1984).

A number of radio interferometric observations of this source have been made at various resolution scales. VLA observations at 5 GHz indicate an arcsecond scale jet extending along position angle $-115°$, and a secondary component located 25" from the core along P.A. $-100°$ (Perley *et al.* 1980; Perley 1982; Wrobel and Lind 1986) (fig. 1). A Westerbork map at the same frequency shows similar structure, and also reveals a halo around the core and the inner component of extent 12" along P.A. 150° and 20" along P.A. 30° (van der Laan *et al.* 1984). The structure on the VLA and Westerbork maps are nearly aligned with the structure found on MERLIN maps at 408 MHz and 1666 MHz (Browne and Orr 1981; Browne *et al.* 1982) and at 5 GHz (Browne and Muxlow 1986) (figs. 8 and 9). The combined VLA and MERLIN maps show a large-scale bend, in which the jet is oriented along P.A. $-100°$ near the core, bends to a P. A. of $-120°$ over a distance of a couple arcseconds (corresponding to approximately 2 kpc for $H_0 = 75$), and then bends back to P. A. $-100°$ on the largest scales. There is no evidence for a counterjet in any of these maps, with a jet to counterjet brightness ratio $\geq 30 : 1$.

The 5 GHz VLBI maps made as part of the Pearson and Readhead survey (Pearson and Readhead 1984) show a jet of length $\sim$ 5 mas at 15% of peak surface brightness along P.A. $-97°$, and an isolated component which appears to be slightly misaligned with the jet, along P.A. $-100°$, in good agreement with the barely resolved extension observed on the MERLIN map. While there were structural variations in the VLBI maps over a period of four years, no definite relation between components could be established to see if there were systematic internal motions.

3. Observational Procedure

3C371 (1807+698) was observed from 11 UT 28 May 1985 to 11 UT 29 May 1985 at 5 GHz using the NRAO Mark II VLBI recording system . A total of 12 stations participated in this experiment, five stations from the European VLBI Network (EVN) plus a station in Metsahovi, Finland, and six stations from the U.S. VLBI Network (Table 1). 3C84 and 3C345 were each observed for one-half hour for fringe finding, and ten assorted half-hour observations of two calibrators, 0016+784 and 1739+528, were made to aid in the final calibration of the data.

The observing schedule for the VLA was modified to allow for the making of a polarization map of 3C371 using the phased array data in B array. Also, since 3C371 is slightly resolved at 5 GHz in B array over the phase calibration interval, it was necessary to observe a nearby source, 1803+784, to phase up the array periodically. We also chose to observe 1807+874 for ten minutes out of every thirty minutes in phased and normal mode in order to adjust the antenna phases and confirm the phase stability for the phased array map. Simulations of the visibility curves given the known orientation of the jet were used to select a 90-minute interval in which to observe a number of flux calibrators in normal mode, and to observe 3C286 for calibration of the antenna polarizations. This procedure allowed us to use the phased-array data to make a polarization map of 3C371 with resolution $\sim$ 1 arcsecond (Wrobel and Lind 1986). The effective duty cycle of the VLA was reduced to 60% because of these additional observations.

The actual coverage obtained for this experiment was exceptionally uniform and complete (fig. 2). The factor of two redundancy obtained by using 24-hour tracks prevented the calibration scans on the global network or the VLA from degrading the coverage to a serious extent. Coverage was somewhat reduced by the failure of NRL due to unknown causes, by equipment difficulties at Metsahovi,

and by coherence problems at Iowa. The last is a serious problem because the resolution corresponding to U.S. baselines to Iowa (roughly 5-10 mas) is likely to contain a considerable amount of structure. It is hoped that a future global fitting of the data using the present model may improve fringe detection to Iowa and allow the use of those baselines.

The data were reduced using the Caltech Block 0 correlator, and were then transferred to the NRAO AIPS package for global fringe fitting and modeling. The global fitting procedure (Schwab and Cotton 1983) was done using a point-source model. The model was passed through three iterations, using successively smaller delay and rate windows. The first window was 1500 ns by 250 mHz using an unconstrained FFT (the "one-baseline" solution) over eight-minute integration intervals, for a coarse fringe search. The remaining two windows, 250 ns by 50 mHz and 100 ns by 15 mHz, were done using three baseline constraints over 30-second integration intervals. The resulting amplitude and phase data appeared exceptionally smooth and error free, except for some occasional noise in the amplitudes on the baselines to Onsala and Jodrell Bank and unreliable phases to Iowa and Metsahovi. The data were then coherently integrated for thirty seconds and transferred to the Caltech VLBI package, where they were calibrated and edited. An initial hybrid mapping pass (Readhead and Wilkinson 1978) was used to find constant gain corrections from self-calibration. The corrected data was averaged incoherently to four minutes and was returned to the AIPS package for hybrid mapping using MX, which is a multiple-window implementation of the Clark CLEAN algorithm (Högbom 1974; Clark 1980), and self-calibration using VSCAL (Cornwell and Wilkinson 1981). Three iterations allowing only phase corrections were used to produce a phase-corrected dataset. The phase-corrected

dataset was self-calibrated allowing long-term ($\geq$ 2 hours) corrections to the amplitudes, and the resulting self-calibrated data were mapped. The new model was then used to self-calibrate the phase-corrected dataset, and the process was repeated. After a few iterations, when the model and the long-term amplitude corrections appeared to have converged, amplitude self-calibration was applied to the individual four-minute data points in the phase-corrected dataset until the model once again had converged. The final iterations of hybrid mapping applied the gain corrections to the amplitude-corrected dataset obtained from the previous hybrid mapping iteration; by this time, the model had almost converged, and very few additional corrections were necessary. The dynamic range in the final map is of order 400:1, which is only a factor of 3 or so above the estimated thermal noise level.

4. Theoretical Noise Limit

The theoretical noise temperature of an interferometer with nonidentical stations, in the limit where the power received from the source at each telescope is small compared to the other noise sources, is proportional to the r.m.s. system temperature of the array, which is given by:

$$S_{array} = \left(\frac{2}{N(N-1)} \sum_{\substack{i=1,N \\ j=i+1,N}} S_i S_j \right)^{\frac{1}{2}}$$

where S_i is the system temperature of the i_{th} antenna in Janskys (scaled to sky sensitivity) and N is the number of antennas (Crane and Napier 1986). The estimated system temperature for the full array excluding NRL, Iowa, and Metsahovi was $S_{array} = 539$ Jy, which is larger than but on the order of the arithmetic average.

The noise level for a perfect interferometer is obtained by dividing this number by the square root of the number of independent samples, which is given by the total observing time multiplied by the bandwidth and the number of baselines:

$$N_{samples} = t_{obs} \Delta\nu \frac{N(N-1)}{2}.$$

Note that each baseline, not each station, is considered an independent sample. This is because the noise is uncorrelated between stations, and therefore the random interference patterns generated by the noise for each pair of stations are independent. For this set of observations, the number of independent samples was $N_{sample} = 5.60 \times 10^{12}$, using $t_{obs} = 24$ hours, $\Delta\nu = 1.8$ MHz, and N=9. This gives an ideal noise level, for nine non-identical antennas all observing constantly for 24 hours, of $\Delta S_{array}^{(\text{ideal})} = 0.23$ mJy/beam. The noise level must be expressed in

mJy/beam because the noise level applies randomly to each independent picture element. This is a lower limit, since the inclusion of such factors as time off-source and variations in gain with elevation angle would increase the noise estimate.

This noise estimate is for an ideal interferometer. Quantization errors, errors in the fringe power estimates based on the form of the fringe fitting function, and various other corrections increase the noise level by the b factor, which for the Caltech Block 0 correlator and present software is known to be about 2.5. The final estimate for the thermal noise is therefore $\Delta S_{array} \geq 0.55$Jy/beam. The lowest believable contour is at about 2.5 mJy/beam, with the r.m.s. noise far from the core measured to be on the order of 1 mJy/beam. This is consistent with the calculated thermal noise, given that what we calculated was a lower bound, and so the true thermal limit is probably about 1 mJy, and the lowest believable surface brightness contour is 2.5 times the thermal limit. It is hoped that a second global fit may reduce the attained noise level, especially since the global fit should pull in at least one additional station (Iowa), which will increase the number of stations and reduce the sidelobes. The effect of sidelobes on the noise level was not included in this calculation, but the presence of sidelobes can add considerable nonthermal noise to the map if not removed carefully by use of the CLEAN algorithm (Högbom 1974; Clark 1980) or the maximum entropy method (Gull and Daniell 1978). Noise may also be added by nonclosing errors due to mismatched bandpasses and coherence losses, or by the failure of self-calibration to compensate for errors in the a priori calibration. In short, future careful work may lower the noise level in the map by a factor of two, but it is doubtful that the map will ever reach the thermal noise limit.

5. May 1985 VLBI Map of 3C371

5.1. General Appearance

The full resolution map of 3C371 from the May 1985 data (fig. 3; component list table 2) shows a number of interesting features. It is definitely one-sided; the apparent counterjet in Figure 3 is not visible on the tapered map (fig. 4; component list table 3), and is almost certainly due to closure phase errors on the very longest triangles (Linfield 1986). The jet to counterjet brightness ratio on the tapered map is on the order of 30:1, using the inner part of the jet, or 10:1 if the comparison is made with component CT.

The straightness of the jet is one of the more unusual features. The position angles differ by no more than 8°, and in fact all but two components line up to within 3°. The jet opening angle — defined as the angle subtended by the first contour level down from the peak of component FU as measured from the core — is on the order of 5°, which is small enough that a bend of a few degrees should be detectable. A detailed examination of the tapered and untapered maps confirms this. Both of these maps show two bends of order $30 - 40°$ in the jet, associated with components AT, BT, and CT (or CU, DU, and EU) and BT, CT, and DT. This suggests that the measured variations in the position angles are not due to large-scale misalignment or radial expansion, but are caused by semi-periodic deviations (henceforth called "wiggles") in the jet. A ridgeline drawn by eye through the peak emission regions on the two maps gives a series of wiggles in the jet, increasing in wavelength from 5 to 20 mas and in amplitude (lateral displacement) from 0.3 to 1.5 mas (measured from an assumed symmetry axis passing through the aligned components) (fig. 5). The good fit to the visibility phase attained by the data reduction procedure and the abundance of long spacings

in all directions in the (u-v) plane (Appendix) make it plausible that the *existence* of wiggles is not an artifact of the analysis, although the details of the wiggles are questionable, and the displayed ridgeline should be taken as suggestive only, *not* as a detailed model. The general appearance is that of a wiggle increasing in wavelength from 5 mas to about 20 mas, and in amplitude from a fraction of a milliarcsecond to possibly 3 mas. This would be the expected appearance of a jet undergoing helical oscillations, and would explain the brightening at the end of the jet (ET) and the apparent recollimation (FT) as a shock developing where the oscillation goes nonlinear. It would be premature to suggest a physical explanation of the wiggle without a second epoch observation of comparable sensitivity, and preferably identical coverage.

The general appearance of the source is that of a wiggling jet which decreases monotonically in surface brightness out to DT. Beyond this point, there is a gap, followed by a bright region associated with component ET, and apparent recollimation of the presumed outflow associated with component FT. The apparent drop in jet brightness at the end of the jet is an artifact of the limited field of view, which is due to the use of a four-minute integration time. A shorter integration would decrease SNR, but would allow mapping of the jet extension to see if it continues.

5.2. Comparison With 1982.9 Map

The data from the December 1982 6 cm VLBI observation of 3C371 made as part of the Pearson/Readhead flux-limited survey (Pearson and Readhead 1984) were transferred to the AIPS package and remapped using MX. The results were excellent; the r.m.s. noise level in the map was 1.5 mJy, only 50% above the r.m.s. noise level in the May 1985 map. The full resolution map of 3C371 (fig. 6; component list table 4) shows essentially the same features as the May 1985 map. In fact, the components seen in the May 1985 map are almost all evident in the December 1982 map, but with different shapes and brightnesses. This is also seen on the tapered map (fig. 7; component list table 5). The jet to counterjet ratio is at least 30:1 on both maps.

The jet is at least as straight at this epoch as at the later epoch. The position angles differ by no more than 5°; in fact, all components but DU line up to within 3°. If the outer edges of component FT, along with the outer edges of components CT and DT, are taken to define a jet opening angle, then that opening angle is on the order of 7°; a detailed examination of the tapered and untapered maps confirms this. Both maps show two bends of order 30° in the jet associated with the jet and the central component complex. This suggests that the size of the opening angle may be increased by wiggles in the jet. As in the May 1985 map, the inner jet appears to have some small wiggles, and the tapered map suggests that the misaligned components in the untapered map are actually peaks in a more or less continuous wiggling jet of wavelength on the order of 10 mas. The apparent recollimation at the end of the jet is not seen in this map.

5.3. Comparison With MERLIN Map

MERLIN was used to observe 3C371 at 5 GHZ in April 1982. The full resolution MERLIN map (Browne and Muxlow 1986)(fig. 8; component list table 6) consists of a slightly extended compact core aligned along P.A. $-101°$ and a jet which curves through 20° to a knot located along P.A. $-110°$. The tapered MERLIN map (fig. 9; component list table 7) shows this jet continuing to bend to a position angle of $-120°$. There is considerable low-level diffuse emission along this position angle, but no really well-defined jet. The jet to counterjet brightness ratio is again on the order of 30:1.

The MERLIN maps are characterized by a steadily increasing bend (excluding DT), with a total change in position angle of about 20°, in which the strong inner jet breaks up into a broad extended region of weak emission after 200 mas ($\sim$ 200 pc). There is a hint of a bend near the end of the inner jet, but this is certainly not apparent in the untapered map. The position angle of the inner jet agrees with the VLBI position angle, and the position angle of the outer jet agrees with the VLA position angle.

The most serious discrepancy is that the MERLIN map contains 15% less flux in the core than the total flux in either of the two VLBI maps. The possibilities are that the core flux of 3C371 underwent a sudden increase between April and December of 1982, which seems unlikely, or that there is an error in the absolute calibration. The VLBI maps agree to within 5% in their total flux despite being independently calibrated, which suggests that the MERLIN calibration was in error. On the other hand, given the structural changes in 3C371, there is no apparent reason why the fluxes should be the same. Since the MERLIN and 1982.9 VLBI datasets were processed almost four years ago, it is impossible to investigate this discrepancy properly. The best that can be done at this point is

to examine the May 1985 VLBI data for clues as to whether the calibration for the later observation was in error.

6. Discussion

The N galaxy 3C371 has an extended VLBI jet which appears to be the base of the arcsecond scale jet observed at the VLA. The orientation of the jet can be traced over many resolution scales, and the misalignment between the milliarcsecond jet and the arcsecond jet is explained by the bending seen in the MERLIN map. If the jet asymmetry is assumed to be due to beaming, rather than intrinsic, a weak limit may be put on the jet speed and orientation from the jet to counterjet brightness ratio limit of 30:1; this corresponds to $\beta \cos\theta \geq 0.56$, or $\Gamma \geq 1.24$ and $\theta \geq 56°$.

The VLBI jet is straight to within $\eta \sim 3°$, with most of the deviations in the position angle attributable to wiggles in the jet rather than large-scale bending, but with bend angles in the jet of order 30°. The apparent total bending angle of 3° already indicates that the VLBI jet is remarkably straight, even without any amplification of the angle due to projection effects. This is even more remarkable, considering that there are apparent local bends of order 10 times the apparent overall bending angle. Such large bends in a jet would normally be associated with instabilities, which should disrupt the flow. In fact, the exceptionally high surface brightness in the outermost VLBI component, which, in conjunction with the surrounding emission region accounts for 12% of the compact flux, may be indicative of a shock or instability in the jet. This contention is supported by the apparent recollimation of the flow behind the emission peak in the tapered map, which may be indicative of a shock followed by a recollimation. Even if this is an instability, it still may not disrupt the flow sufficiently to explain the large wiggles in the jet. Furthermore, the apparent smoothness of the tapered May 1985 map, and the large percentage of low-brightness extended flux in the jet (e.g., complex DU-EU), suggest a relatively strong underlying jetlike component.

This also supports the contention that the underlying flow is stable, since strong shocks in the jet should give the jet a more irregular appearance, especially if they were beamed (Jones *et al.* 1986).

One solution to this dilemma is to assume that the large-scale bend is relatively unprojected, and the local bends are highly projected, i.e., the large-scale bending is close to the plane containing the jet and the observer, and the local bends are perpendicular to that plane. Then, if the apparent overall bending angle is assumed to be equal to the actual overall bending angle, and the actual local bending angle is on the order of the actual overall bending angle (to maintain stability), then the angle between the line of sight and the average jet axis would be $\theta_{obs} = 5°$. The deprojected length of the 35 mas jet would then be about 400 mas, corresponding to 400 pc for $H_0 = 75$. This model is admittedly contrived, but illustrates how the angle from which a source is viewed may affect the interpretation of the source. A simpler solution is to assume that the jet is well-collimated, but is undergoing helical oscillations, possibly due to precession (Gower *et al.* 1982); however, this fails to explain the stability of the jet.

A rough estimate of relativistic motion may also be made from large-scale changes in the two VLBI maps by assuming that the brightness changes in the component complexes occur coherently across at least a fraction of each complex, where that fraction is given by the fractional change in the total flux from the complex. This is fairly conservative, as the appearance in the maps is that the entire complex changes, and not just a fraction of it. In the central component complex (BT, CT, and DT in both epochs), the flux dropped from 200 mJy to 65 mJy between the two epochs. A drop in flux of 65% in 2.5 years over a region of linear extent 10 mas corresponds to an estimated rate of change of $0.65 \times$ 10 mas/2.5 years $= 2.6$ mas/yr, or about 8c for $H_0 = 75$ $\mathrm{kms}^{-1}\mathrm{Mpc}^{-1}$. The

outer component complex (ET and FT in both epochs) increased in flux from 82 mJy to 185 mJy over a distance of about 13 mas, giving an estimated rate of change of 0.55×13 mas/2.5 years = 2.9 mas/yr, or about 9c. This is comparable to the estimate of 10c made on the basis of X-ray to radio flux (Worrall *et al.* 1984). The wiggles in the jet do not appear to be the same in both jets, but are difficult to identify and quantify in the sky-plane map of the source, and the nonidentical coverage in the two data sets makes comparisons of the visibility phases unreliable in terms of tracing such a subtle effect. The measurement of source changes of this nature requires the use of two nearly identical arrays with identical coverage processed with identical methodology, to eliminate any question as to the reality of the observed variations in visibility phase.

The understanding of the source structure and orientation requires that the changes be mapped and confirmed over several epochs. To do this reliably for a 2 Jy source requires large global experiments, especially where there are changes over many resolution scales. Confirmation of the existence and details of rapid changes in 3C371 awaits the repetition of the May 1985 experiment to allow direct comparison of the visibilities at a low level in both amplitude and phase. The final conclusion as to the structure and changes in 3C371 is that they suggest relativistic motion, but it will take considerable time and resources to confirm it.

References

Aller, M.F., Aller, H.D., and Hodge, P.E. 1982, in *IAU Symposium 97: Extragalactic Radio Sources* ed. D.S. Heeschen and C.M. Wade (Reidel: Boston), p. 335.

Biretta, J.A., Cohen, M.C., Hardebeck, H.E., Kaufmann, P., Abraham, Z., Perfetto, A.A., Scalise, E. Jr., Schaal, R.E., and Silva, P.M. 1985, *Ap. J. (Letters),* **292**, L5.

Blandford, R.D. and Königl, A. 1979, *Ap. J.,* **232**, 38.

Browne, I.W.A. and Orr, M.J.L. 1981, in *Optical Jets in Galaxies* ed. B. Battrick and J. Mort (ESA: Paris), p. 87.

Browne, I.W.A., Orr, M.J.L., Davis, R.J., Foley, A., Muxlow, T.W.B., and Thomasson, P. 1982, *M.N.R.A.S.,* **198**, 673.

Browne, I.W.A. and Muxlow, T.W.B. 1986, private communication.

Clark, B.G. 1980, *Astr. Ap.,* **89**, 377.

Cornwell, T.J. and Wilkinson, P.N. 1978, *Ap. J.,* **223**, 25.

Crane, P.C. and Napier, P.J. 1986, in *Synthesis Imaging* ed. R.A. Perley, F.R. Schwab, and A.H. Bridle (NRAO: Green Bank, West Virginia), p. 87.

Gower, A.C., Gregory, P.C., Hutchings, J.B. and Unruh, W.G. 1982, *Ap. J.,* **262**, 478.

Gull, S.F. and Daniell, G. 1978, *Nature,* **272**, 686.

Högbom, J. 1974, *Ap. J. Suppl.,* **15**, 417.

Jones, D.L., Unwin, S.C., Readhead, A.C.S., Sargent, W.L.W., Seielstad, G.A., Simon, R.A., Walker, R.C., Benson, J.M., Perley, R.A., Bridle, A.H., Pauliny-Toth, I.I.K., Romney, J., Witzel, A., Wilkinson, P.N., Bååth, L.B., Booth, R.S., Fort, D.N., Galt, J.A., Mutel, R.L., and Linfield, R.P. 1986, *Ap. J.*, **305**, 684.

Linfield, R.P. 1986, *A.J.*, **92**, 213.

Marscher, A.P. 1986, in preparation.

Marscher, A.P. and Gear, W.K. 1985, *Ap. J.*, **298**, 114.

Miller, J.S. 1975, *Ap. J. (Letters)*, **200**, L55.

Oke, J.B. 1967, *Ap. J. (Letters)*, **150**, L5.

Oke, J.B. 1978, *Ap. J. (Letters)*, **219**, L97.

Pearson, T.J. and Readhead, A.C.S. 1984, in *IAU Symposium 110: VLBI and Compact Radio Sources* ed. R. Fanti, K. Kellerman, and G. Setti (Reidel: Boston), p. 15.

Perley, R.A. 1982, *A.J.*, **87**, 859.

Perley, R.A., Fomalont, E.B., and Johnston, K.J. 1980, *A.J.*, **85**, 649.

Readhead, A.C.S. and Wilkinson, P.N. 1978, *Ap. J.*, **223**, 25.

Sandage, A. 1966, *Ap. J.*, **145**, 1.

Scheuer, P.A.G. 1986, in preparation.

Schwab, F.R. and Cotton, W.D. 1983, *A.J.*, **88**, 487.

Staubert, R., Brunner, H., Worrall, D.M. 1986, preprint.

Unwin, S.C., Cohen, M.C., Biretta, J.A, Pearson, T.J., Seielstad, G.A., Walker, R.C., Simon, R.S., and Linfield, R.P. 1985, *Ap. J.*, **289**, 109.

van der Laan, H., Zieba, S., and Noordam, J.E., in *IAU Symposium 110: VLBI and Compact Radio Sources* ed. R. Fanti, K. Kellerman, and G. Setti (Reidel: Boston), p. 9.

Walker, R.C., Benson, J.M., Seielstad, G.A., and Unwin, S.C. 1984, in *IAU Symposium 110: VLBI and Compact Radio Sources* ed. R. Fanti, K. Kellerman, and G. Setti (Reidel: Boston), p. 121.

Worrall, D.M., Puschell, J.J., Bruhweiler, F.C., Miller, H.R., Rudy, R.J., Ku, W.H.-M., Aller, M.F., Aller, H.D., Hodge, P.E., Matthews, K., Neugebauer, G., Soifer, B.T., Webb, J.R., Pica, A.J., Pollock, J.T., Smith, A.G., and Leacock, R.J. 1984, *Ap. J.*, **278**, 521.

Wrobel, J. and Lind, K.R., in preparation.

Table 1. List of Stations in 1985 Global Array

Institution	Location	Diameter
Onsala Space Obs.	Onsala, Sweden	25.6m
MPIfR(BONN)	Effelsburg, W. Germany	100m
Westerbork	Westerbork, Netherlands	14 × 25m
Metsähovi Radio Obs.	Kirkkonummi, Finland	15m
Nuffield Radio Astr. Lab.	Jodrell Bank, England	25m
Bologna	Medicina, Italy	32m
Haystack Obs.	Westford, Massachusetts	36.6m
Naval Research Lab.	Maryland Point, Maryland	25.9m
NRAO	Green Bank, W. Virginia	42.7m
North Liberty Radio Obs.	North Liberty, Iowa	18.3m
NRAO(VLA)	Socorro, New Mexico	26 × 25m
Owens Valley Radio Obs.	Big Pine, California	39.6m

The stations used for the May 1985 VLBI observations are listed in order of longitude from east to west. The present map excludes data from Metsähovi Radio Observatory (METS), North Liberty Radio Observatory (IOWA), and the Naval Research Laboratory (NRL), although data from the first two stations may be salvageable.

Table 2. Component Table for Untapered May 1985 Map

Component	P.A.(degrees)	Distance(mas)	Flux(mJy)
CJU	69	2.8	13
CCU	—	0	1126
AU	-101	2.8	—
BU	-93	4.2	—
AU-BU	—	—	134
CU	-101	5.6	35
DU	-93	9.6	5
EU	-101	11.8	9
DU-EU Complex	-99	7.4 to 24.1	65
FU	-99	26.3	58
GU	-98	30.2	11
FU-GU Complex	-99	24.1 to 34.3	185

The various components in the untapered map of 3C371 made with 9 stations from data taken in May 1985 are listed in order of increasing distance from the core. The resolution is 1 mas. The regions included in the flux calculations are shown in Figure 3.

Table 3. Component Table for Tapered May 1985 Map

Component	P.A.(degrees)	Distance(mas)	Flux(mJy)
CCT	—	0	1290
AT	-99	6.9	97
BT	-97	9.6	—
CT	-102	12.0	8
DT	-97	16.4	—
BT-DT Complex	-99	9.6 to 19.1	39
ET	-99	26.9	49
FT	-100	33.3	—
ET-FT Complex	-99	19.1 to 39.0	182

The various components in the tapered map of 3C371 made with 9 stations from data taken in May 1985 are listed in order of increasing distance from the core. The resolution is 2.5 mas. The regions included in the flux calculations are shown in Figure 4.

Table 4. Component Table for Untapered December 1982 Map

Component	P.A.(degrees)	Distance(mas)	Flux(mJy)
CCU	—	0	1205
AU	-99	1.6	—
BU	-96	3.4	—
AU-BU	-97	1.2 to 5.5	200
CU	-98	6.1	34
DU	-103	12.3	20
EU	-99	15.5	—
FU	-99	17.7	—
DU-FU Complex	-101	10.0 to 19.0	79
GU	-98	26.6	15
GU Complex	-98	21.4 to 28.6	85

The various components in the untapered map of 3C371 made with 6 stations from data taken in December 1982 as part of the Pearson and Readhead survey (Pearson and Readhead 1984) are listed in order of increasing distance from the core. The resolution is 1 mas. The regions included in the flux calculations are shown in Figure 6.

Table 5. Component Table for Tapered December 1982 Map

Component	P.A.(degrees)	Distance(mas)	Flux(mJy)
CJT	104	3.7	1
CCT(extended)	-95	0	1241
AT	-95	5.3	—
BT	-103	8.7	—
AT-BT Complex	-99	2.5 to 8.7	198
CT	-103	12.4	23
DT	-99	14.7	12
CT-DT Complex	-99	9.6 to 18.8	80
ET	-96	20.2	—
FT	-98	26.2	30
FT Complex	-99	22.2 to 31.1	77
GT	-103	36.0	3
BT-GT Complex	-99	14.7 to 39.0	180

The various components in the tapered map of 3C371 made with 6 stations from data taken in December 1982 as part of the Pearson and Readhead survey (Pearson and Readhead 1984) are listed in order of increasing distance from the core. The resolution is 2.5 mas. The regions included in the flux calculations are shown in Figure 7.

Table 6. Component Table for Untapered MERLIN Map

Component	P.A.(degrees)	Distance(mas)	Flux(mJy)
CCU	—	0	1366
AU	-101	138	—
BU	-110	267	—
CU	-110	391	22
AU-CU Complex	-110	133 to 550	46

The various components in the untapered map of 3C371 made with MERLIN from data taken in April 1982 are listed in order of increasing distance from the core. The resolution is 0.1". The regions included in the flux calculations are shown in Figure 8.

Table 7. Component Table for Tapered MERLIN Map

Component	P.A.(degrees)	Distance(mas)	Flux(mJy)
CJT	110	333	<1
CCT	—	0	1403
AT	-110	333	—
BT	-118	590	—
AT-BT Jet	-115	330 to 600	27
CT	-115	820	—
AT-CT Complex	-115	330 to 1025	58
CT	-129	1718	17
CT Complex	-120	1025 to 2300	48
DT	-118	3250	36
DT Complex	-120	2300 to 4230	81

The various components in the tapered map of 3C371 made with MERLIN from data taken in April 1982 are listed in order of increasing distance from the core. The resolution is 2.5". The regions included in the flux calculations are shown in Figure 9.

Figure Captions

Figure 1. VLA Map of 3C371 at 5 GHz

A polarization map made from the phased-array data taken at the VLA as part of the May 1985 VLBI observations is displayed (Wrobel and Lind 1986). The first window shows the region near the core, and the second shows the diffuse outer component. The contour levels are at intervals of 10% of the peak flux; the total flux in the map is 1.86 Jy.

Figure 2. Coverage for May 1985 VLBI Experiment

The theoretical maximum coverage attainable with the full 12-station array is displayed above the actual coverage attained with the nine stations used; the axes are in units of $10^6\lambda$, where $\lambda = 6$cm. The loss of U.S. baselines to Iowa causes the serious gap in coverage near $3 \times 10^7\lambda$. However, the final coverage is exceptionally uniform and complete for a VLBI experiment, and sidelobes should be relatively small.

Figure 3. Untapered May 1985 VLBI Map

The full resolution map made from the May 1985 VLBI data is shown, with reference locations marked. The beam is circular, with diameter 1 mas. The contour levels are at -0.4, 0.4, 0.8, 1.6, 3.2, 6.4, 12.8, 25.6, 51.2 percent of the peak brightness of 843 mJy/beam. The total flux in the map is about 1.6 Jy.

Figure 4. Tapered May 1985 VLBI Map

The tapered resolution map made from the May 1985 VLBI data is shown, with reference locations marked. The two-dimensional visibilities were tapered using a spherical gaussian, resulting in an effective circular beam with diameter

2.5 mas. The contour levels are at -0.4, -0.2, 0.2, 0.4, 0.8, 1.6, 3.2, 6.4, 12.8, 25.6, 51.2 percent of the peak brightness of 1094 mJy/beam. The total flux in the map is about 1.6 Jy.

Figure 5. Wiggles in the May 1985 VLBI Maps

Apparent wiggles in the structure of the tapered and untapered May 1985 maps are shown superimposed on the maps (figures 3 and 4). The fit is drawn by eye, and is not intended as a rigorous fit to the ridgeline. The wiggle, if real, could be due to either a planar wiggle in the jet or a helical wiggle (corkscrew) in the jet.

Figure 6. Untapered December 1982 VLBI Map

The full resolution map made from the December 1982 VLBI data is shown, with reference locations marked (Pearson and Readhead 1984). The beam is circular, with diameter 1 mas. The contour levels are at -0.4, 0.4, 0.8, 1.6, 3.2, 6.4, 12.8, 25.6, 51.2 percent of the peak brightness of 840 mJy/beam. The total flux in the map is about 1.6 Jy.

Figure 7. Tapered December 1982 VLBI Map

The tapered resolution map made from the December 1982 VLBI data is shown, with reference locations marked (Pearson and Readhead 1984). The two-dimensional visibilities were tapered using a spherical gaussian, resulting in an effective circular beam with diameter 2.5 mas. The contour levels are at -0.4, -0.2, 0.2, 0.4, 0.8, 1.6, 3.2, 6.4, 12.8, 25.6, 51.2 percent of the peak brightness of 1079 mJy/beam. The total flux in the map is about 1.6 Jy.

Figure 8. Untapered April 1982 MERLIN Map

The full resolution map made from the April 1982 MERLIN data is shown, with reference locations marked (Browne and Muxlow 1986). The beam is circular, with diameter 100 mas. The contour levels are at -0.4, -0.2, 0.2, 0.4, 0.8, 1.6, 3.2, 6.4, 12.8, 25.6, 51.2 percent of the peak brightness of 1300 mJy/beam. The total flux in the map is about 1.4 Jy.

Figure 9. Tapered April 1982 MERLIN Map

The tapered resolution map made from the April 1982 MERLIN data is shown, with reference locations marked (Browne and Muxlow 1986). The two-dimensional visibilities were tapered using a spherical gaussian, resulting in an effective circular beam with diameter 250 mas. The contour levels are at -0.4, -0.2, 0.2, 0.4, 0.8, 1.6, 3.2, 6.4, 12.8, 25.6, 51.2 percent of the peak brightness of 1094 mJy/beam. The total flux in the map is about 1.4 Jy.

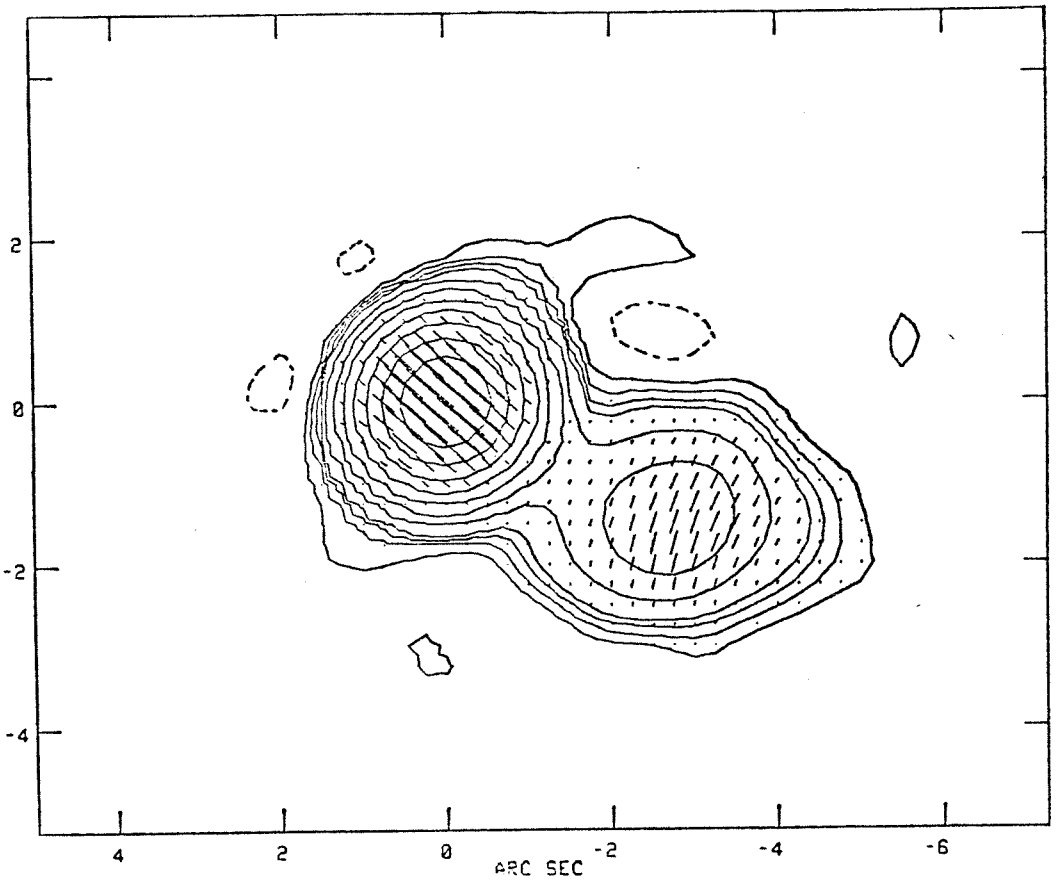

Figure 1

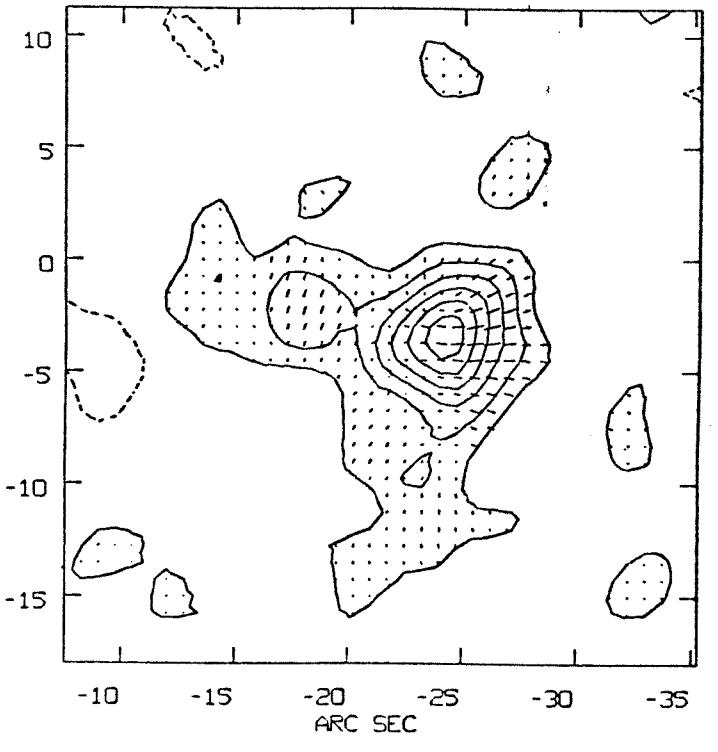

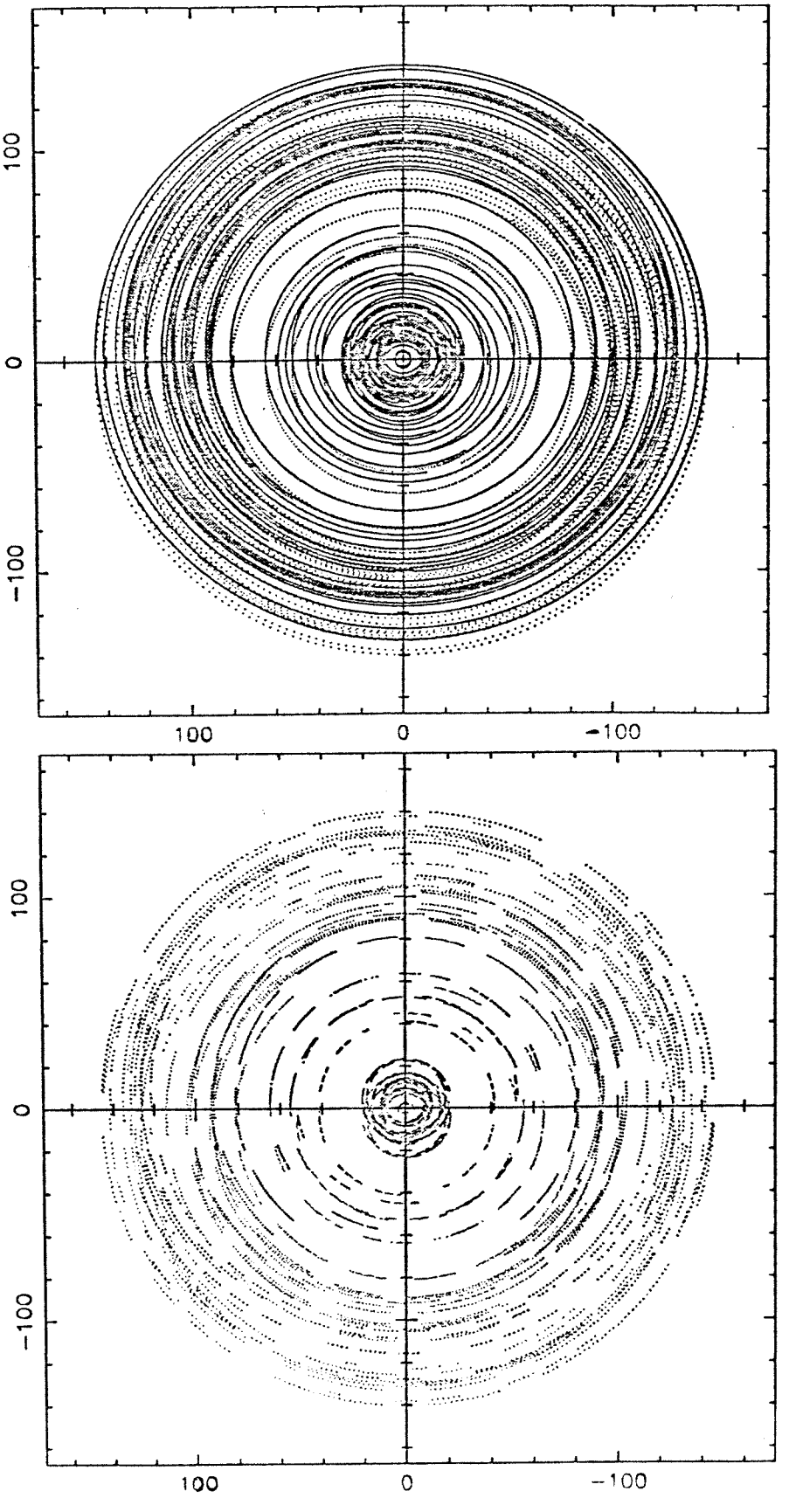

Figure 2

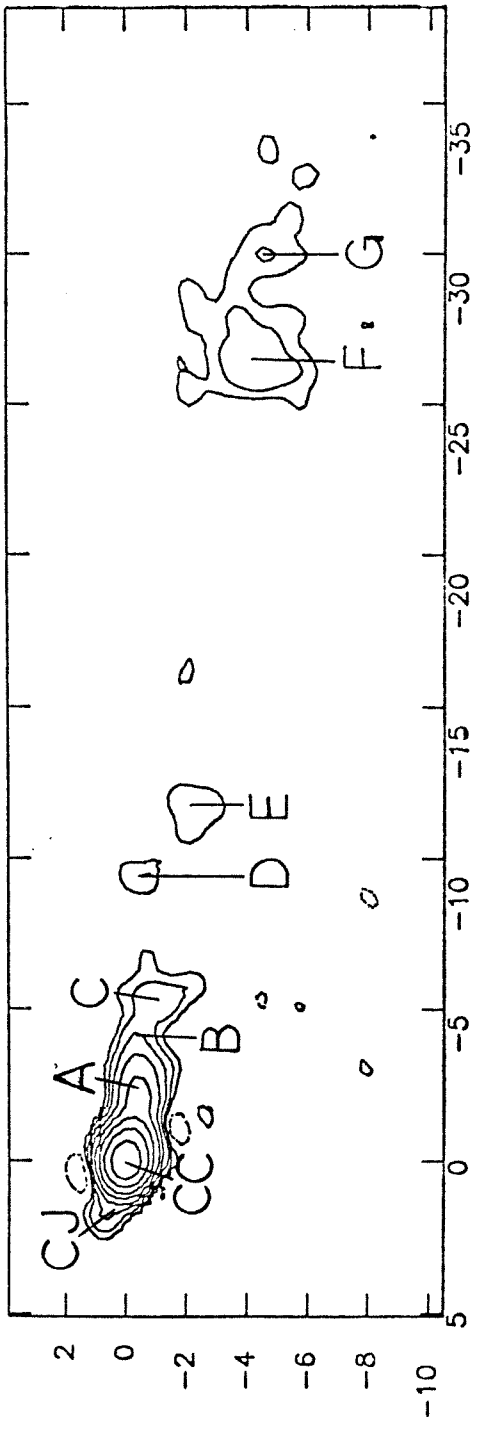

Figure 3

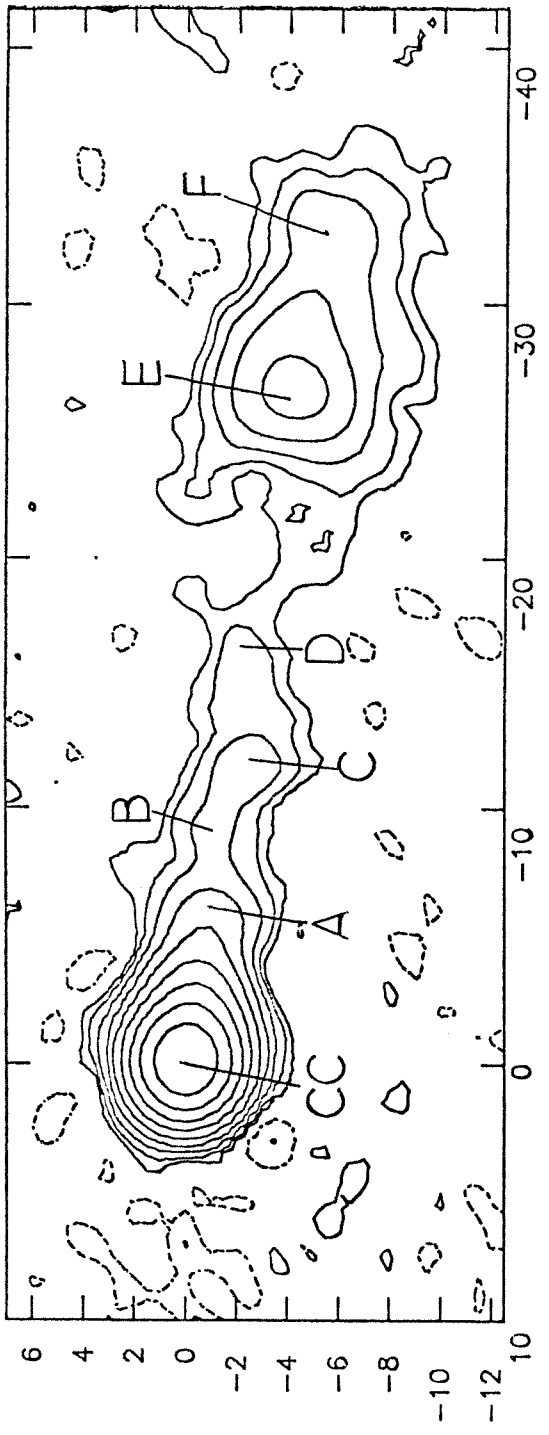

Figure 4

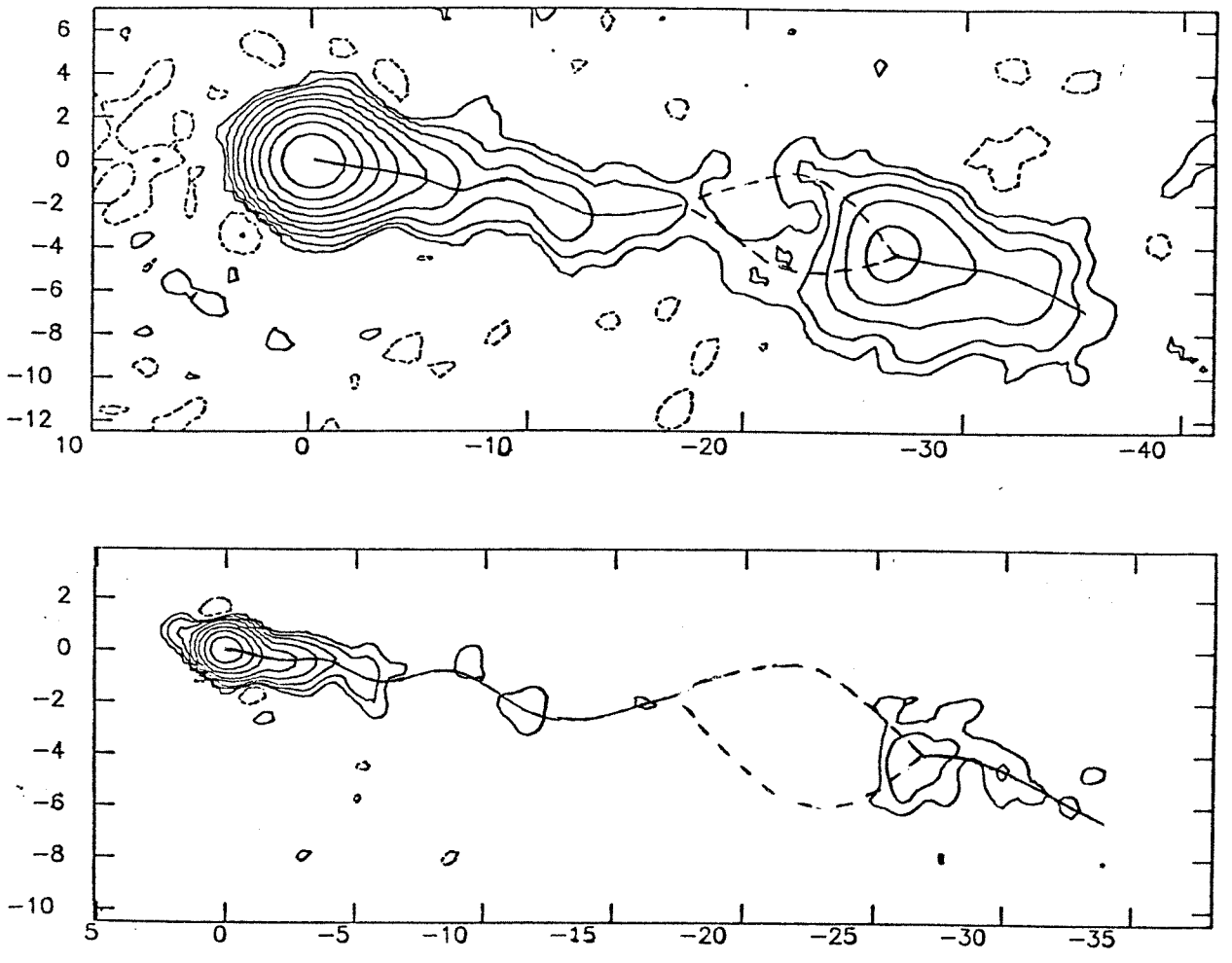

Figure 5

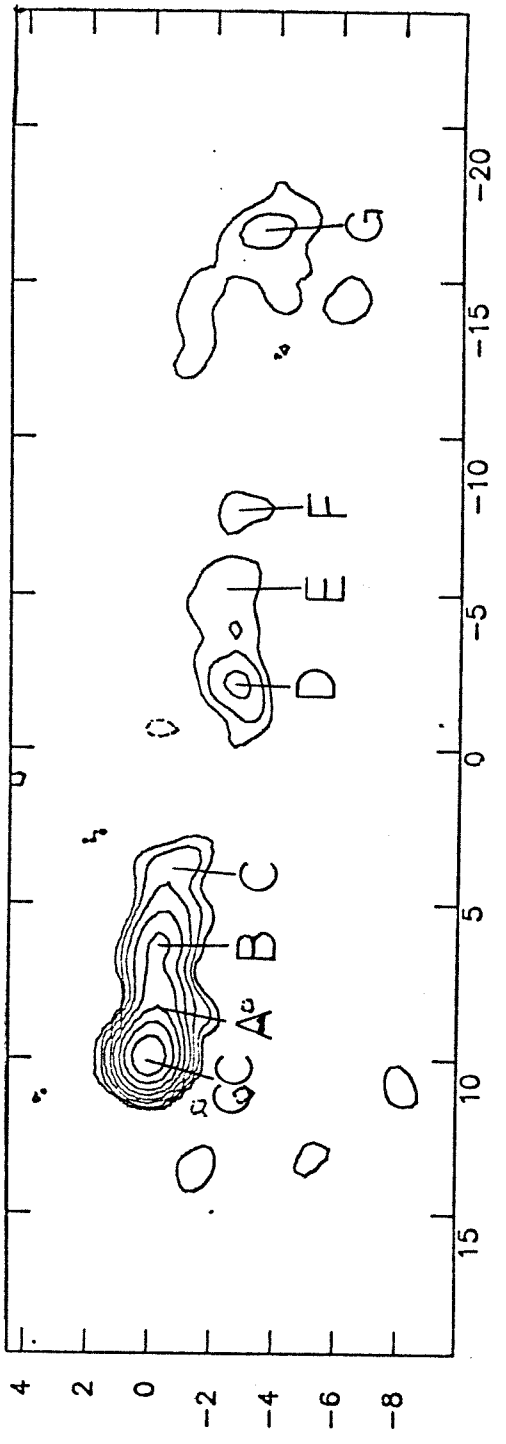

Figure 6

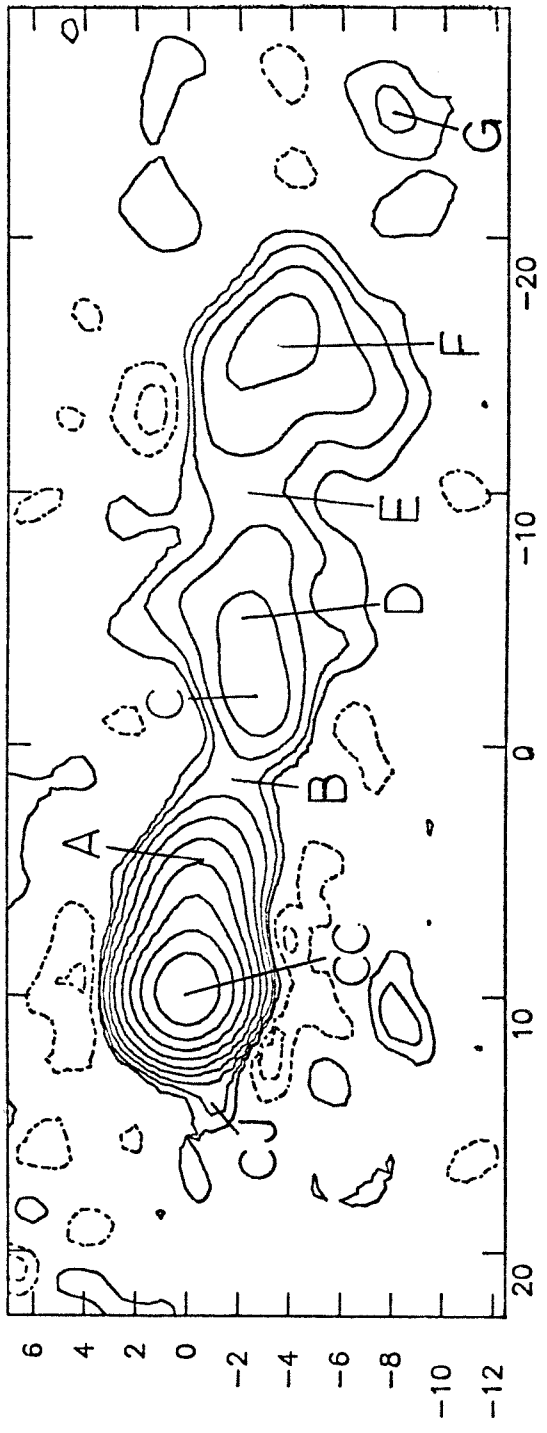

Figure 7

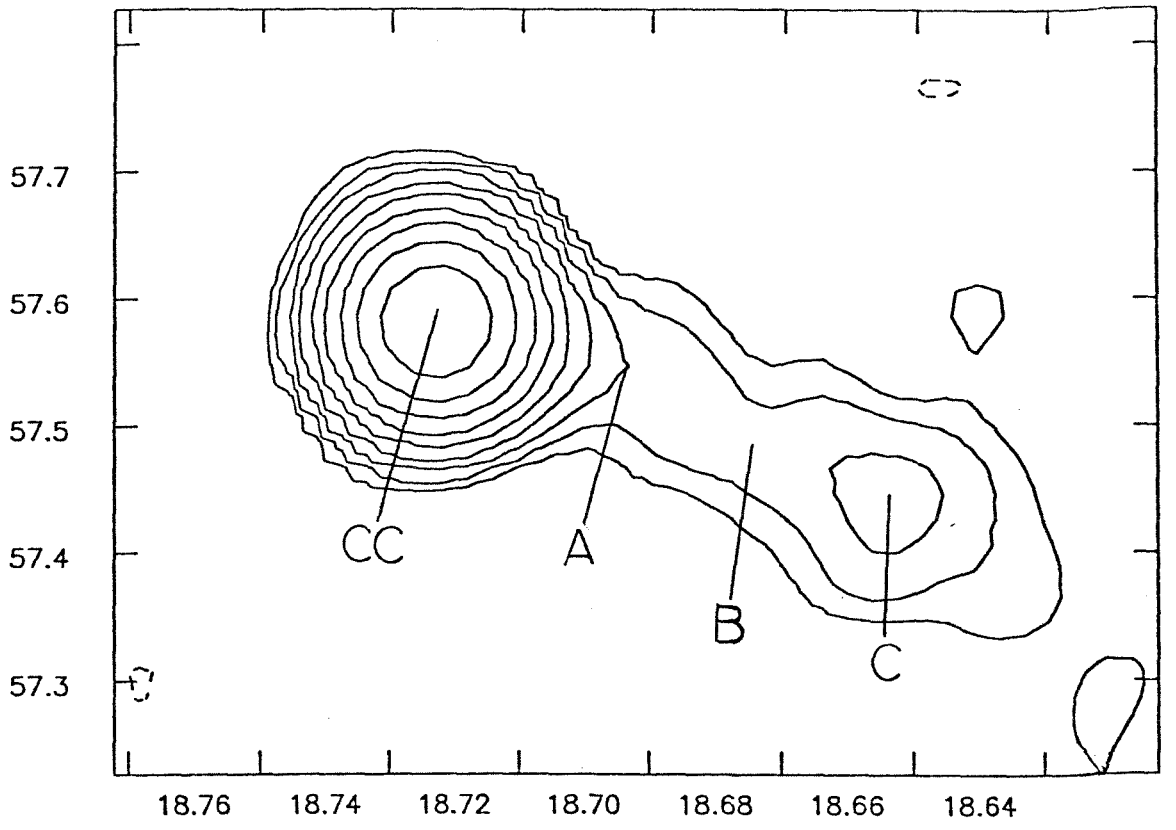

Figure 8

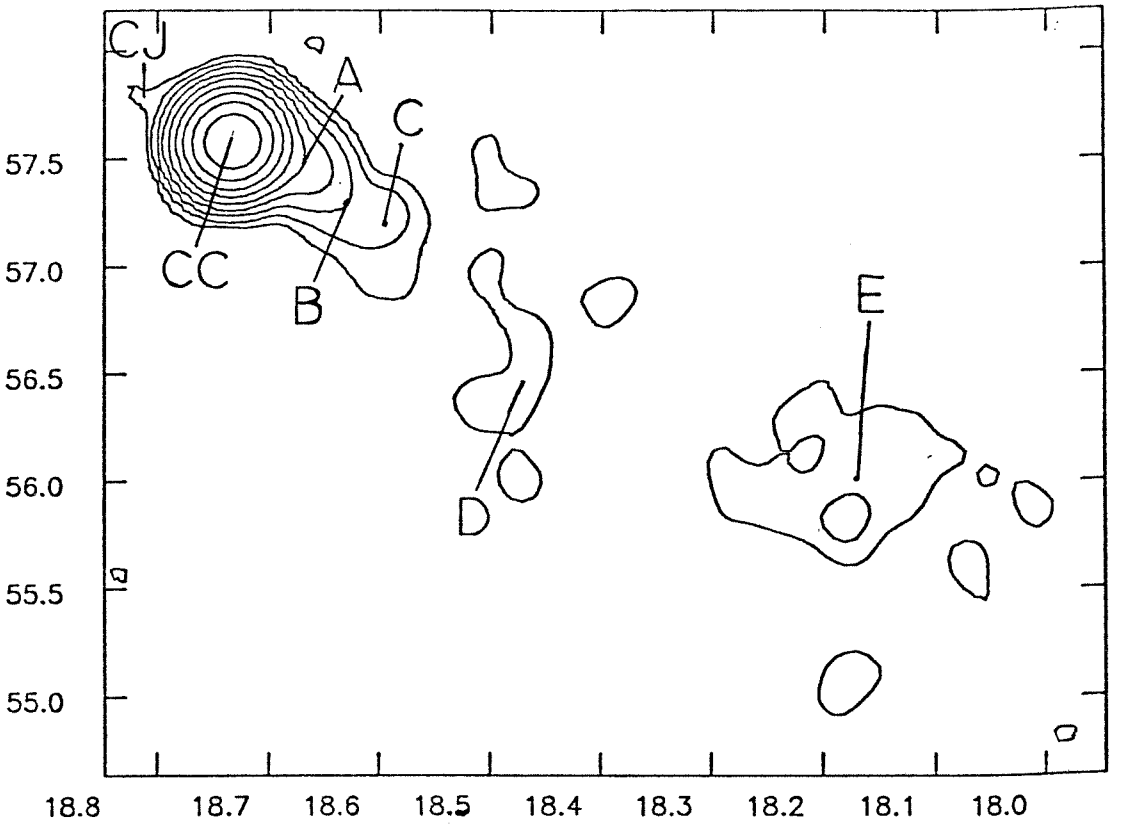
CJ
A
C
CC
B
D
E
57.5
57.0
56.5
56.0
55.5
55.0
18.8
18.7
18.6
18.5
18.4
18.3
18.2
18.1
18.0

Figure 9

Appendix. Visibilities for May 1985 Data

The visibility data are displayed in terms of the amplitude and the phase. The data are plotted as individual points, and the visibilities of the model shown in Figure 3 are plotted as lines. Error bars are not plotted because of difficulties with the software interface between the Caltech VLBI package and the NRAO AIPS packages, but a good estimate of the error may be seen in the point scatter. The fits to both the amplitude and phase are very good on all baselines, except for a few points on a few baselines where a small amount of flux appears to be missing from the model. This may be attributable to structure outside of the field of view or to errors in the global fitting caused by the use of a point source model.

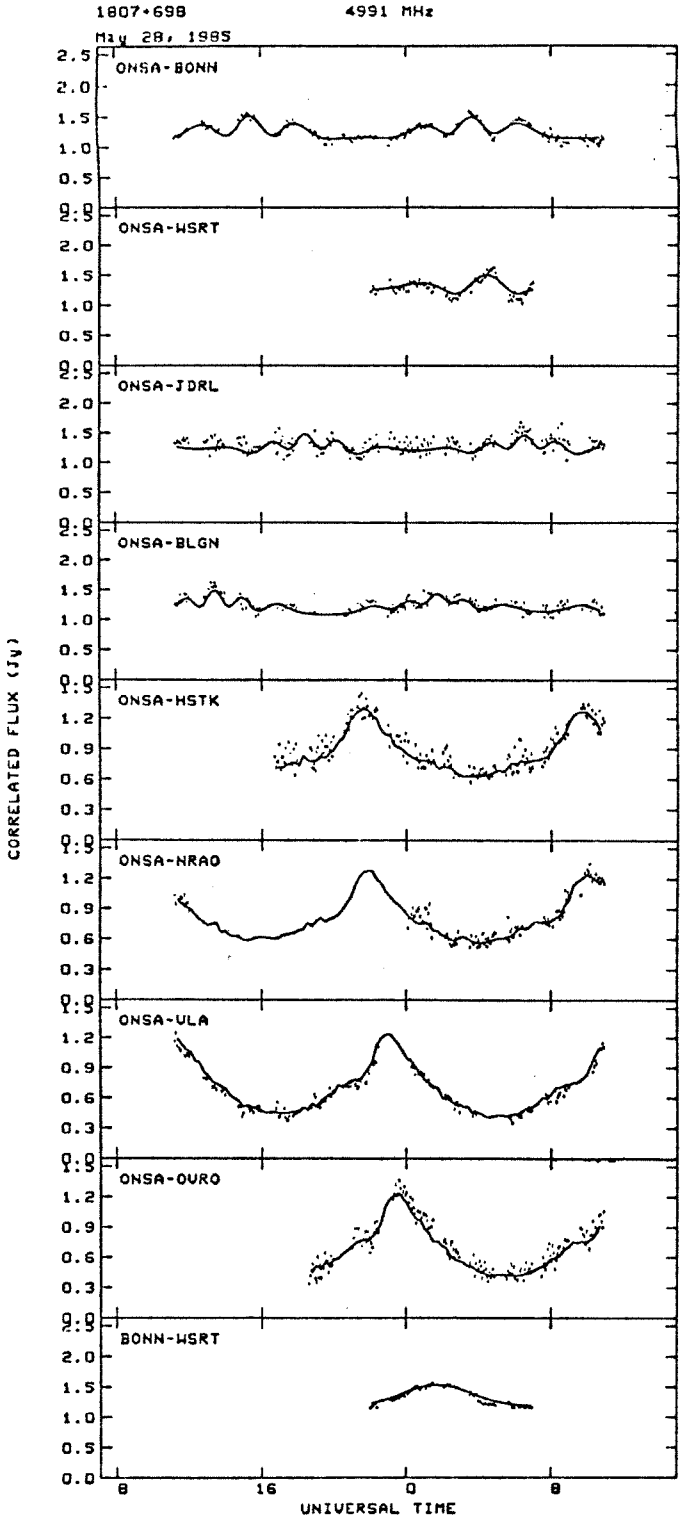
1807+698
4991 MHz
May 28, 1985
ONSA-BONN
ONSA-WSRT
ONSA-JDRL
ONSA-BLGN
ONSA-HSTK
ONSA-NRAO
ONSA-ULA
ONSA-OVRO
BONN-WSRT
CORRELATED FLUX (Jy)
UNIVERSAL TIME
8
16
0
8

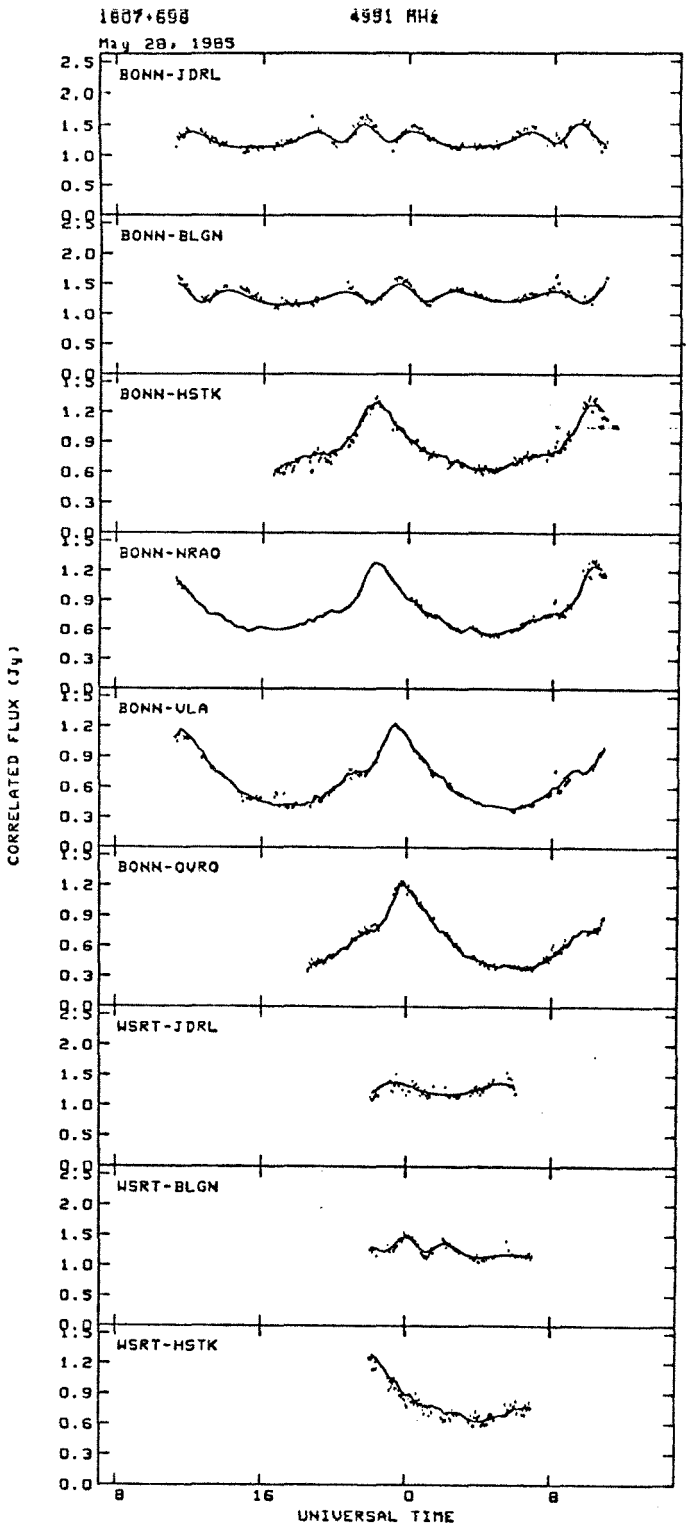
1807+698
4991 MHz
May 28, 1985
BONN-JDRL
BONN-BLGN
BONN-HSTK
BONN-NRAO
BONN-VLA
BONN-OVRO
WSRT-JDRL
WSRT-BLGN
WSRT-HSTK
CORRELATED FLUX (Jy)
UNIVERSAL TIME
8
16
0
8

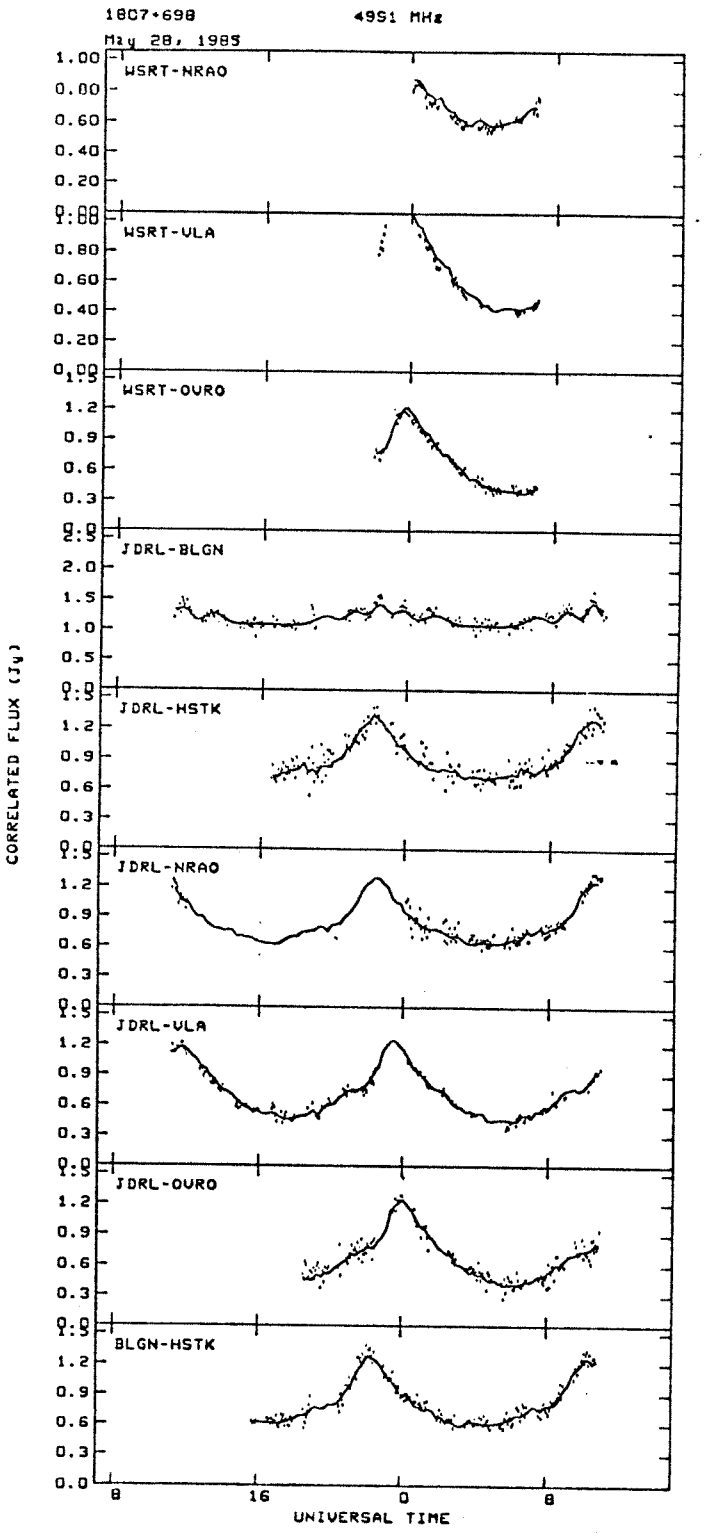
1807+698
4951 MHz
May 28, 1985
WSRT-NRAO
WSRT-VLA
WSRT-OVRO
JDRL-BLGN
JDRL-HSTK
JDRL-NRAO
JDRL-VLA
JDRL-OVRO
BLGN-HSTK
CORRELATED FLUX (Jy)
UNIVERSAL TIME
8
16
0
8

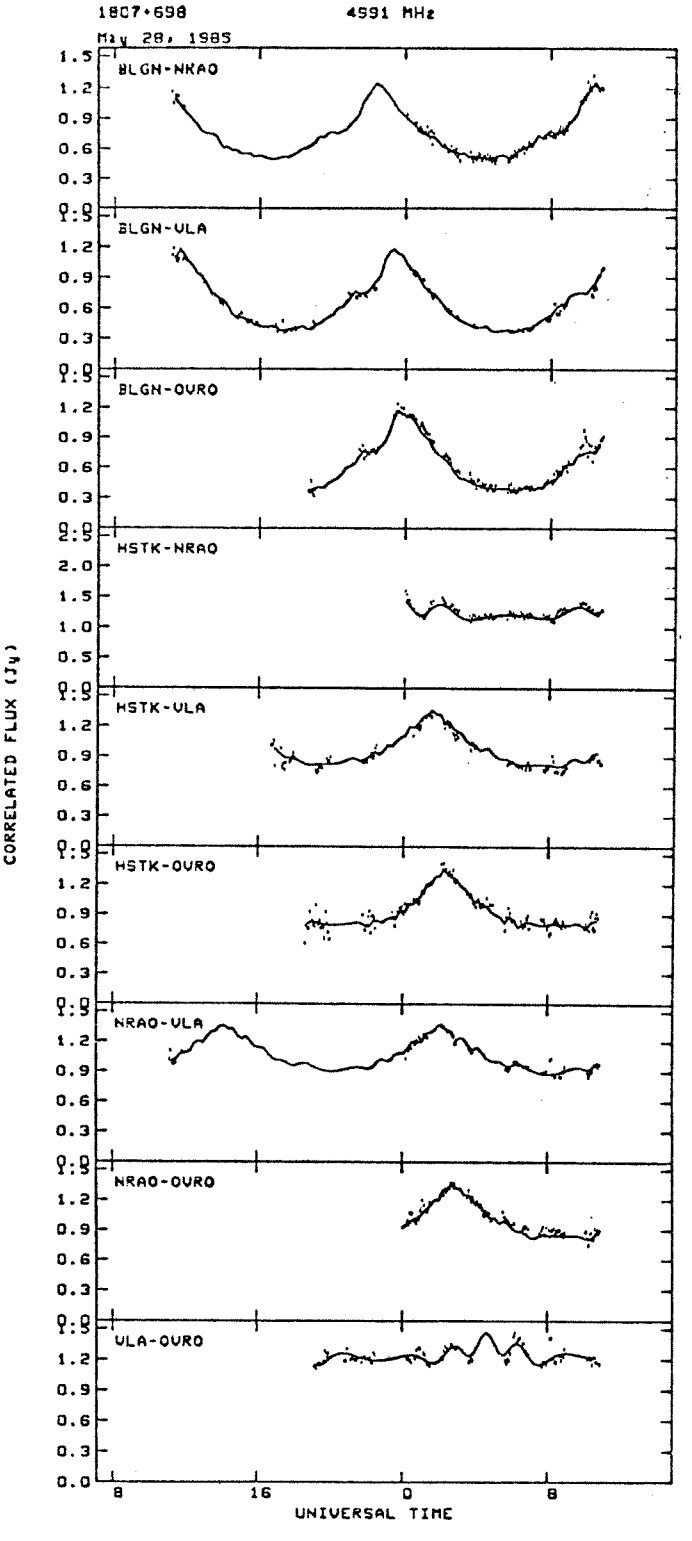
1807+698
4991 MHz
May 28, 1985
BLGN-NRAO
BLGN-VLA
BLGN-OVRO
HSTK-NRAO
HSTK-VLA
HSTK-OVRO
NRAO-VLA
NRAO-OVRO
VLA-OVRO
CORRELATED FLUX (Jy)
UNIVERSAL TIME
8
16
0
8

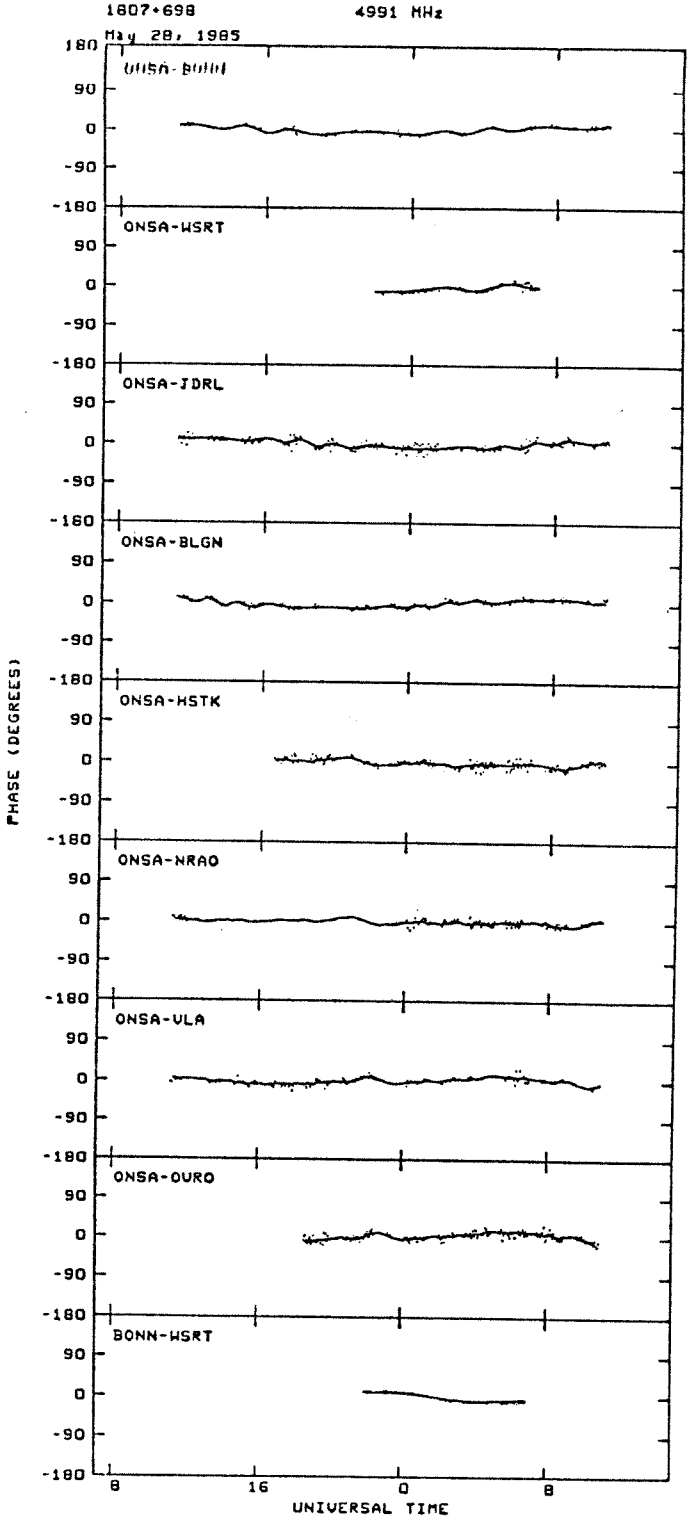
1807+698
4991 MHz
May 28, 1985
ONSA-BONN
ONSA-WSRT
ONSA-JDRL
ONSA-BLGN
ONSA-HSTK
ONSA-NRAO
ONSA-VLA
ONSA-OURO
BONN-WSRT
180
90
0
-90
-180
PHASE (DEGREES)
8
16
0
8
UNIVERSAL TIME

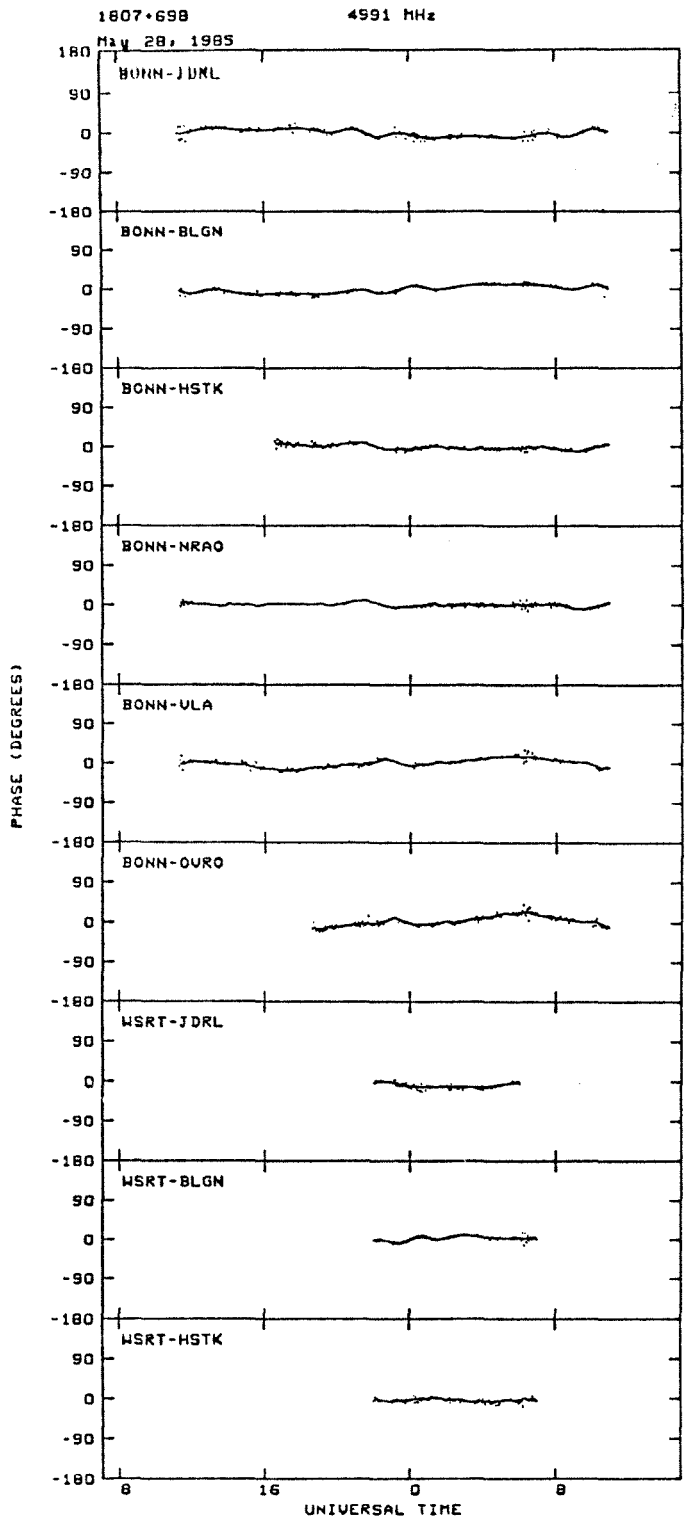
1807+698
4991 MHz
May 28, 1985
BONN-JDRL
BONN-BLGN
BONN-HSTK
BONN-NRAO
BONN-VLA
BONN-OVRO
WSRT-JDRL
WSRT-BLGN
WSRT-HSTK
180
90
0
-90
-180
PHASE (DEGREES)
8
16
0
8
UNIVERSAL TIME

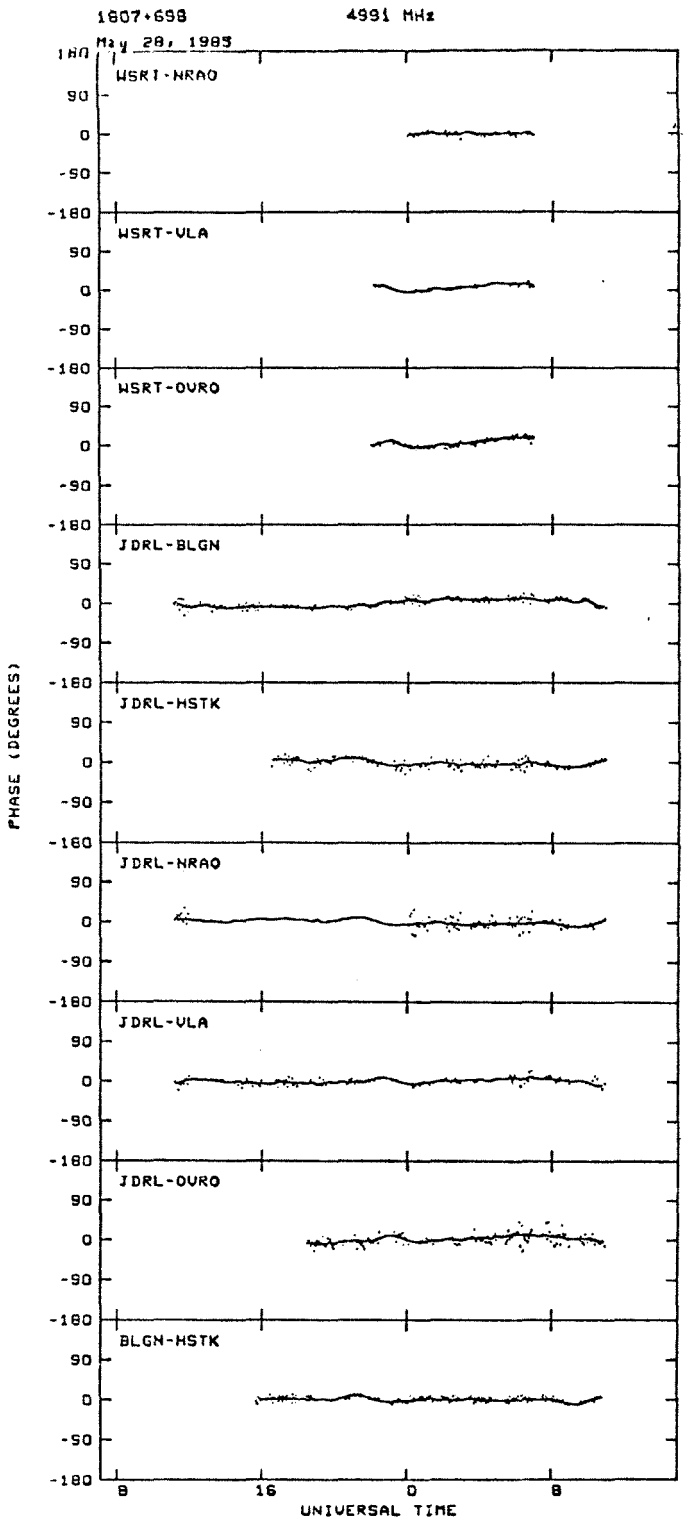
1807+698
4991 MHz
May 28, 1983
WSRT-NRAO
WSRT-VLA
WSRT-OVRO
JDRL-BLGN
JDRL-HSTK
JDRL-NRAO
JDRL-VLA
JDRL-OVRO
BLGN-HSTK
180
90
0
-90
-180
PHASE (DEGREES)
8
16
0
8
UNIVERSAL TIME

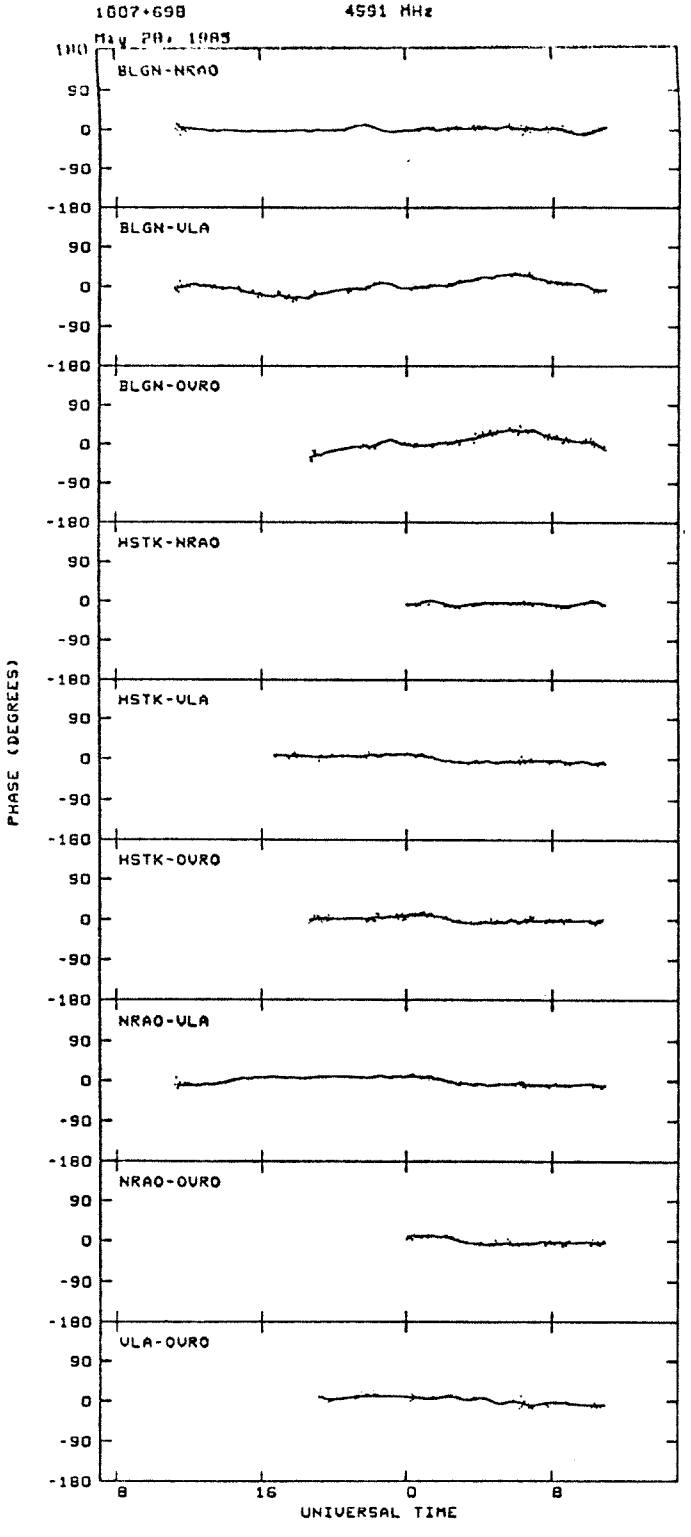
1607+698
4991 MHz
May 28, 1985
BLGN-NRAO
BLGN-VLA
BLGN-OVRO
HSTK-NRAO
HSTK-VLA
HSTK-OVRO
NRAO-VLA
NRAO-OVRO
VLA-OVRO
180
90
0
-90
-180
PHASE (DEGREES)
8
16
0
8
UNIVERSAL TIME

CHAPTER 3

SEMIDYNAMICAL MODELS OF RADIO JETS: RELATIVISTIC BEAMING AND SOURCE COUNTS

I. INTRODUCTION

Recent VLBI observations have shown that many compact extragalactic radio sources have core-jet structure. They have also confirmed the presence of apparent superluminal expansion in some of the more powerful sources. These observations, which are reviewed in the conference proceedings edited by Kellermann and Setti (1984), have been widely interpreted in terms of a simple model in which radio-emitting plasma moving with relativistic speed is collimated within a narrow beam directed towards the observer. If this is indeed the case, then our classification of a particular radio source must be strongly influenced by our orientation with respect to the beam. Furthermore, for every strong superluminal source beamed towards us, there should be several weak sources beamed away from us. These have been separately associated with the radio-quiet quasars (e.g.,Scheuer and Readhead 1979) and the extended quasars (e.g.,Orr and Browne 1982). This type of model has several immediate attractions. It introduces a partial unification of active galactic nuclei. It alleviates the so-called "inverse Compton problem" in the highest brightness radio components (e.g.,Marscher and Broderick 1982) and it can also account for low frequency variability (e.g.,Condon, Ledden, O'Dell, and Dennison 1979 and *Proceedings of the NRAO Workshop on Low Frequency Variability of Extragalactic Radio Sources*, Cotton and Spangler (ed.) 1982; but see Coe, Bowring, Hall, and Stephen 1983). Furthermore, relativistic speeds are naturally expected if the outflow derives from the vicinity of a massive black hole.

Attempts to make this theory quantitative and to confront the observations have not been particularly successful for a variety of reasons. Foremost amongst these is the realization brought about by recent high dynamic range VLBI maps that the source structures are genuinely complex. VLBI jets are

generally inhomogeneous rather than smooth and continuous. Many such jets appear to be bent and do not necessarily point towards the associated cores (e.g., Readhead, Hough, Ewing, Walker, and Romney 1983; Cohen and Unwin 1983). Fainter features have been found extending in other position angles (e.g., Simon 1983). In addition, it now appears to be the case that superluminal expansion is only common amongst the very brightest sources and to date no further confirmed cases have been found in a larger sample of fainter compact sources (Readhead and Pearson 1983).

These complications are not readily interpreted in terms of the rectilinearly moving plasmoids that feature either explicitly or implicitly in most theoretical discussions of these sources. This type of model is not just inadequate morphologically. It is also quite unrealistic from a theoretical perspective. We believe that compact radio sources comprise relativistic, supersonic outflows and that most of their energy is contained in bulk kinetic form. However, the brightest radio features are presumably created where this flow becomes dissipative, i.e. where the bulk kinetic energy is most efficiently converted into relativistic electron internal energy and magnetic field energy. This necessarily implies a change in the velocity of outflow with a consequent change in the Doppler factor which controls the brightness of the feature. If bulk Lorentz factors of $\gamma \sim 10$ are in fact common then the Lorentz boosts are so large that relatively small velocity changes suffice to span the complete dynamic range of existing observations of individual sources. The observed structure of a source is highly sensitive to this velocity field.

Shock waves constitute a particularly natural method of introducing dissipation into the flow. Shock waves are an almost universal component of other supersonic outflows in astronomy such as the solar wind, supernova remnants and winds from hot stars (e.g., McKee and Hollenbach 1980). They feature

prominently in numerical simulations of extragalactic jets (e.g., Norman, Winkler, and Smarr 1983). They are also known to accelerate relativistic electrons with high efficiency (see e.g.,the reviews by Drury 1983 and Blandford and Eichler 1984). It therefore seems quite probable that the major emitting components of compact radio sources are associated with shock waves (Blandford and McKee 1977). Wilson and Scheuer (1983) calculated the relativistic flow of a jet at a bow shock and from this derived the intensity distribution and flux of a hotspot at the end of a mildly relativistic jet in the optically thin limit. They showed that the backflow of relativistic fluid at the bowshock slightly decreased the brightness contrast $S(\theta)/S(180^\circ - \theta)$ between the hotspots formed by a jet traveling at a viewing angle θ relative to the observer and its counterjet. While they concluded that the results for bowshocks and plasmoids were very similar in the case of mildly relativistic fluid flow, there should be larger differences in observed flux in the case of extreme relativistic flow.

Observational and theoretical considerations suggest the need for more detailed dynamical models of compact radio sources. However, since present observations do not allow us to distinguish between detailed fully dynamical models, a more approximate semi-dynamical treatment is called for in order to gain a qualitative understanding of the effects of shock-related emission at relativistic speeds. We emphasize that we do not intend that the results of our model calculations be fit *directly* to VLBI observations.

In section II, we review the calculation of the appearance of a source moving at relativistic speed in which there is a stationary though not necessarily static pattern of emission. We also explain how to compute the distribution of flux density from a particular source as it is viewed with random orientation. We go on in section III to consider specific source models. These models are kinematically exact though only "semi-dynamical". This means that the velocity fields

are simplified versions of the true flows that would result from complete solution of the full dynamical equations. This seems adequate in view of our ignorance of the behavior of the volume emissivity which we specify in an ad hoc fashion. We contrast the properties of models based on relativistic shocks with simple plasmoid models. Our brief, and somewhat negative, conclusions are collected in Section IV.

A preliminary report on this work was presented in Blandford (1984).

II. APPEARANCE OF STATIONARY EMISSION PATTERNS

In this section we review the appearance according to special relativity of a steadily moving but stationary pattern of emission. This is intended to simulate the flow behind a steady shock front at which relativistic particles are presumed to be accelerated and magnetic field is believed to be amplified. In practice, the flow need not be stationary; we only require that the shock structure be constant for the light crossing time in the frame of the shock. The appearance of a relativistic shock differs from that of a uniform spherical plasmoid in three important respects. Firstly, the synchrotron-emitting plasma is advected away from the shock, so the velocity of the emitting plasma differs from the velocity of the shock relative to the observer. Secondly, astrophysical shocks are rarely even approximately planar and the post-shock flow lines will not be parallel. The radiation can then be beamed over a larger solid angle than the emission from individual fluid elements. Thirdly, as the shock structures are likely to be highly non-spherical, any optically thick flux would be quite sensitive to the viewing angle of the observer, even in the absence of Doppler boosting.

We assume that the emission region has a boundary Σ' which is at rest in some (primed) inertial frame, the "pattern" frame. The intensity $I'_{\nu'}$ crossing Σ' along some direction is determined by solving the equation of radiative transfer

along the ray.

$$I'_{\nu'}(\nu',\vec{\mathbf{n}}') = \int j'_{\nu'}(\nu',\vec{\mathbf{n}}',x')e^{-\int_0^{x'} d\xi' \kappa(\nu',\vec{\mathbf{n}}',\xi')} dx' \tag{2.1}$$

$j'_{\nu'}$ is the volume emissivity in the direction $\vec{\mathbf{n}}'$ and κ' is the corresponding absorption coefficient. x' is distance measured back along the ray from Σ'.

$j'_{\nu'}$ and κ' are measured in this pattern frame through which the fluid moves with a velocity $\vec{\beta}'(x')$. (c = 1 henceforth.) The emissivity and opacity are most conveniently computed in the rest (double-primed) frame of the fluid where we shall assume that they are isotropic. They are transformed into the pattern frame in the standard manner (e.g., Rybicki and Lightman 1979)

$$j'_{\nu'}(\nu',\vec{\mathbf{n}}') = \delta'^2 j''_{\nu''}(\nu'' = \nu'/\delta') \tag{2.2}$$

$$\kappa'(\nu',\vec{\mathbf{n}}') = \delta'^{-1}\kappa''(\nu'' = \nu'/\delta') \tag{2.3}$$

where

$$\delta' = \frac{(1-\beta'^2)^{1/2}}{1-\vec{\beta}'\cdot\vec{\mathbf{n}}'} = \frac{\nu'}{\nu''} \tag{2.4}$$

is the Doppler factor of the moving fluid in the pattern frame. If the emissivity in the fluid rest frame is a power law with spectral index $\alpha = -d\log j''_{\nu''}/d\log\nu''$, $\tau \ll 1$ then

$$j'_{\nu'}(\nu',\vec{\mathbf{n}}') = \delta'^{2+\alpha} j''_{\nu''}(\nu') \tag{2.5}$$

For the specific case of synchrotron radiation $\kappa(\nu'') \propto \nu''^{-(\alpha+5/2)}$ and so

$$\kappa'(\nu',\vec{\mathbf{n}}') = \delta'^{\alpha+3/2}\kappa''(\nu') \tag{2.6}$$

If we now observe the source from the observer (unprimed) frame through

which the pattern moves with velocity $\vec{\beta}$, then the projected shape of the surface Σ will be congruent to that of Σ' seen along the rotated direction $\vec{n}'$ in the pattern frame (Terrell 1960). A quick way to verify this is to consider two photons that propagate along parallel rays and cross a perpendicular plane (such as a photographic plate) simultaneously. If the perpendicular separation of the rays is s, then the interval between any two events involving these two photons is $\Delta t^2 - \Delta x \cdot \Delta x = -s^2$, which is Lorentz invariant. This immediately implies that the perpendicular separation of the rays is s in all frames. This is true for any pair of rays. There will then be no apparent contraction of the observed shape of a body as a result of a Lorentz transformation; the projection of the source on the sky will be a rotation in all frames. The usual Lorentz contraction is exactly compensated by the extra light travel time associated with the transformation. This is a manifestation of the conformal invariance of null geodesics in space-time. The angle of observation transforms according to:

$$\cos\theta' = \frac{\cos\theta - \beta}{1 - \vec{\beta}\cdot\vec{n}} \tag{2.7}$$

$$\sin\theta' = \frac{(1-\beta^2)^{1/2}}{1 - \vec{\beta}\cdot\vec{n}}\sin\theta \tag{2.8}$$

and the observed frequency and intensity will Lorentz transform according to a second Doppler factor δ, which relates the pattern frame to the observer frame.

$$\delta = \frac{(1-\beta^2)^{1/2}}{(1 - \vec{\beta}\cdot\vec{n})} = \frac{\nu}{\nu'} \tag{2.9}$$

$$I_\nu(\nu,\vec{n}) = \delta^3 I'_\nu(\nu' = \nu/\delta,\vec{n}') \tag{2.10}$$

Cosmological corrections can be inserted at this stage by replacing δ by $\delta/(1+z)$ etc., but we shall not do this. We calculate the observed brightness distribution of a relativistic source following this procedure. The total observed

flux density is obtained by integrating the intensity over the observed brightness of the body.

The relative importance of shape and internal fluid velocity in determining the flux can be seen by examining equation (2.1) for different optical depths. In the optically thin limit $\tau \ll 1$,

$$I_\nu = \int_0^s j_\nu \, dx, \tag{2.11}$$

and the flux $S_\nu = \int I_\nu d\Omega$, where Ω is observed solid angle. Since $d\Omega = dA' / D^2$, where D is the angular diameter distance to the source and dA' is an element of area in the pattern frame perpendicular to the direction of the transformed ray, then the flux can be rewritten

$$S_\nu(\nu) = \frac{1}{D^2}\int_{\Sigma'} \delta^3 \int_0^s j'_{\nu'}(\nu' = \nu/\delta)\, dx'\, dA' = \frac{\delta^3}{D^2}\int_{V'} j'_{\nu'}(\nu' = \nu/\delta)\, dV' \tag{2.12a}$$

or, for $j''_{\nu''}$ obeying (2.5),

$$S_\nu(\nu) = \frac{\delta^{3+\alpha}}{D^2}\int_{V'} \delta'^{2+\alpha} j''_{\nu''}(\nu)\, dV' \tag{2.12b}$$

where V' is volume. Thus, in the optically thin limit, the flux observed is independent of the shape of the emitting region, as expected.

In the optically thick limit $\tau \gg 1$, then

$$I_\nu(\nu, \vec{n}) = \delta^3 \frac{j'_{\nu'}(\nu' = \nu/\delta, \vec{n}', \tau = 0)}{\kappa'(\nu' = \nu/\delta, \vec{n}', \tau = 0)} \tag{2.13}$$

The flux is given by

$$S_\nu = \frac{\delta^3}{D^2}\int_{\Sigma'} \frac{j'_{\nu'}(\nu' = \nu/\delta)}{\kappa'} dA' \tag{2.14a}$$

or, for $j''_{\nu''}$ and κ'' obeying (2.5) and (2.6),

$$S_\nu = \frac{\delta^{3/2}}{D^2}\int_{\Sigma'} \delta'^{3/2}\frac{j''_{\nu''}(\nu)}{\kappa''(\nu)}dA' \tag{2.14b}$$

which depend only on the observed shape and the surface velocity distribution. As a general rule, optically thick models will be more sensitive to shape, and optically thin models will be more sensitive to the internal fluid velocity in the pattern frame. In practice, the optical depth varies dramatically as a function of viewing angle θ if the source moves relativistically. For a given observer frequency ν,

$$\tau = \int_0^{x'} \kappa''(\nu'' = \nu/\delta\delta')\,d\xi' \tag{2.15a}$$

or, for κ'' obeying (2.6),

$$\tau = \delta^{\alpha+5/2}\int_0^{x'} \delta'^{\alpha+3/2}\kappa''(\nu)\,d\xi' \tag{2.15b}$$

In most realistic source models, we are observing several source components with various optical depths simultaneously. Furthermore, arguments based on relativistic beaming and adiabatic expansion of synchrotron emitting components suggest that each component should reach its peak observed brightness when its optical depth is approximately unity. Results obtained by assuming that the whole source is either optically thin or optically thick can therefore be quite misleading.

III. RADIO EMISSION FROM RELATIVISTICALLY MOVING SOURCES

We have computed the radio emission to be expected from a variety of source models both analytically and, where necessary, numerically. Our

procedure is to specify the emissivity and the absorption coefficient in the fluid frame, then to transform these quantities into the pattern frame and perform the radiative transfer. We transform the emergent intensity into the observer frame to obtain the observed brightness distribution. Details of these transformations have been described in Section II. The flux S_ν is obtained by integrating the intensity over the observed solid angle. We can use this to compute a partial luminosity function P(S) for the probability of observing flux S_ν in excess of S for a given source model at a given distance oriented randomly relative to the observer.

We first analyze some simple source models involving plasmoids and uniform jets, and compute the P(S) relations, which are plotted in figure 1. We then contrast the brightness distributions and P(S) relations of these models with those obtained from radiative transfer calculations of semi-dynamical shock models.

a) Plasmoids

The simplest type of model, which has featured in most discussions of beaming, is the spherical "plasmoid" moving uniformly at an angle θ to the observer. For simplicity, we neglect the flux from components moving away from the observer. Even this model contains some subtleties which appear not to have been recognized. If the plasmoids are optically thin then, using equation (2.12), the observed flux is

$$S_\nu(\nu) = \frac{\delta^{3+\alpha}}{D^2}\int j'_\nu(\nu)\,dV \qquad (3.1)$$

with δ calculated using the plasmoid velocity; the fluid and pattern frames coincide, and we need only be concerned about the transformation to the observer frame. For individual plasmoids with constant emissivity, it takes an interval

$dt_0 = \delta^{-1} dt'$ of observer time to receive radiation emitted in an interval dt' of proper time. Assume that the plasmoids emit for a fixed interval of proper time (finite lifetime). As the observed flux decreases monotonically with increasing θ, the probability of observing a source with flux in excess of S is given by

$$dP(S) \propto \frac{dt_0}{dt'} d\mu \propto (1 - \beta\mu) d\mu \tag{3.2}$$

where $\mu = \cos\theta$.

Integrating and normalizing for θ from 0 to $\pi/2$, the probability of observing a source with total flux density exceeding a value S is

$$P(S) = \frac{(1-\beta)^2}{\beta(2-\beta)} \left[\left(\frac{S_{max}}{S} \right)^{2/(3+\alpha)} - 1 \right] \tag{3.3a}$$

$$(1-\beta)^{3+\alpha} S_{max} \leq S \leq S_{max}$$

This distribution differs from that used by Scheuer and Readhead (1979) and Orr and Browne (1982):

$$P(S) = \frac{(1-\beta)}{\beta} \left[\left(\frac{S_{max}}{S} \right)^{1/(3+\alpha)} - 1 \right] \tag{3.3b}$$

$$(1-\beta)^{3+\alpha} S_{max} \leq S \leq S_{max}$$

Both of these distributions (3.3a), (3.3b) are plotted in figure 1. The above authors implicitly assumed that the plasmoid has a constant emissivity for a fixed interval of observer time; if we see the plasmoids for a fixed interval of proper time, then we can see the brightest plasmoids for a shorter interval of observer time and thus somewhat less frequently. Although both of these models are rather unrealistic, they do demonstrate that P(S) is quite sensitive to assumptions made about source component evolution.

We can further de-accentuate plasmoids moving towards us by assuming that their emissivity decays inversely as some power of the radius. For example, suppose that the source is optically thin and $\int_{V'} j'_{\nu'}(\nu')\,dV' \propto r^{-n}$. The source will then have a flux in excess of S out to a radius r(S) given by equation (2.12b) where

$$r(S) \propto S^{-1/n}(1-\beta\mu)^{-(3+\alpha)/n} \tag{3.4}$$

The probability of observing a flux in excess of S then satisfies

$$P(S) \propto \int r(1-\beta\mu)\,d\mu \propto S^{-1/n}\int (1-\beta\mu)^{1-(3+\alpha)/n}\,d\mu \tag{3.5}$$

In this case, the shape of the P(S) curve is dictated by the exponent n and the spectral index α. Carrying out the integration, we see that $P(S) \propto S^{-2/(3+\alpha)}$ for $S > S_{max}\gamma^{-(3+\alpha)}$ and $P(S) \propto S^{-1/n}$ for $S < S_{max}\gamma^{-(3+\alpha)}$. This distribution is also shown in figure 1 for $\alpha = 0$ and $n = 2$, ignoring counterjets. Incidentally, if $n > 3+\alpha$, the brightest sources in a sample will tend to be those moving at large angles to the line of sight; in particular, for two-sided jets, we will see more bright jets moving away from us than toward us!

The above analyses all assume that the plasmoid is optically thin or optically thick for all angles θ. As noted at the end of Section II, however, since we observe the plasmoids at a fixed observer frequency ν, the optical depth $\tau \propto \delta^{\alpha+5/2}$, and hence the assumption of a single power law, i.e., extremely optically thin or optically thick, may not be reasonable in practice.

b) Multiple Plasmoids (Simple Jets)

In the above simple example, the sample for which we computed P(S) only included those plasmoids that were radiating at a given observer time; we excluded from our sample sources in which one plasmoid had faded and the next

had not yet appeared. Since the cores of core-jet sources, which appear to dominate the high-frequency flux, appear to be permanently bright, it is more reasonable to assume that we are seeing several plasmoids in the core at a given observer time. In the limit in which the plasmoids merge together to form a continuous jet, we have a stationary pattern in the observer frame, through which the synchrotron-emitting plasma is flowing. The emissivity and absorption coefficient must be transformed from the frame comoving with the plasma according to equations (2.2) and (2.3) in order to calculate the intensity

$$j_\nu(\nu,\mu) = \delta^2 j''_{\nu''}(\nu'' = \nu/\delta) \tag{3.6}$$

$$\kappa(\nu,\mu) = \delta^{-1}\kappa''(\nu'' = \nu/\delta) \tag{3.7}$$

For an optically thin source, the observed flux is

$$S_\nu(\nu) = \frac{\delta^{2+\alpha}}{D^2}\int j''_{\nu''}(\nu)\,dV \propto (1-\beta\mu)^{-(2+\alpha)} \tag{3.8}$$

Hence,

$$P(S) = (1-\mu) = \left[\frac{1-\beta}{\beta}\right]\left[\left[\frac{S_{max}}{S}\right]^{1/(2+\alpha)} - 1\right] \tag{3.9}$$

$$(1-\beta)^{2+\alpha}S_{max} \le S \le S_{max}$$

This distribution is again plotted in figure 1. Detailed jet models, in which we see down to a photosphere where $\tau \approx 1$ (e. g., Blandford and Königl 1979, Reynolds 1982ab), have somewhat similar kinematic properties to optically thin sources, in which α is interpreted as the combined flux density spectral index.

c)Propagating Pattern, or Excitation, Model

We now look at a third type of model in which a pattern --- which we select to be spherical for simplicity --- propagates with velocity $\vec{\beta}$ through a medium which is at rest in the observer frame. The scattering of strong electromagnetic waves by relativistic electrons held in place by the inertia of their associated ions provides a possible physical realization of this model (e.g., Blandford, McKee, and Rees 1977). In this case, $\delta' = \delta^{-1}$, and, if $j''_{\nu''}$ and κ'' obey (2.5) and (2.6), then equation (2.1) becomes

$$I_\nu(\nu) = \delta \int_0^{s'} j''_{\nu''}(\nu) e^{-\delta \int_0^{l'} \kappa''(\nu)\, d\xi'} dl' \tag{3.10}$$

Thus, for optically thin isotropic emission, $\tau \propto \delta$ and $I_\nu \propto \delta$ [1]. Both of these results can be derived geometrically, the optical depth by considering the Lorentz contraction of the pattern and the path length for a light ray in a moving volume element, and the intensity by considering the Lorentz contraction of the pattern and the time measured by the observer for a pattern element to move a distance dr in the fluid frame. Therefore, the optically thin flux $S_\nu \propto \delta$. If we assume that the outbursts are well separated, as in (a), then

$$P(S) = \frac{(1-\beta)^2}{\beta(2-\beta)} \left[\left(\frac{S_{\max}}{S} \right)^2 - 1 \right] \tag{3.11}$$

$$(1-\beta) S_{\max} \leq S \leq S_{\max}$$

This distribution is plotted in figure 1.

For optically thick emission from a spherical source, I_ν is independent of θ, as the depth of the "photosphere" decreases in proportion as the emissivity increases. The effects of beaming vanish in this case.

[1] In fact, if the emission arises from wave scattering, then the emission is anisotropic in the fluid frame and $I_\nu \propto \delta^{-1}$ (as in the "light echo" theory, cf. Lynden-Bell 1977).

d) Plane Perpendicular Shock Model

When we turn to more realistic models involving shock fronts, we must distinguish the pattern frame from both the fluid frame and the observer frame. Consider a plane shock wave of circular cross section moving outward through slowly moving plasma (figure 2a). The radio emissivity of the gas will increase dramatically immediately behind the shock front, where particle acceleration and magnetic field amplification should occur. However, a rarefaction wave should propagate inwards at the sound speed (assumed to be $1/\sqrt{3}$ as appropriate for a relativistic plasma) relative to the moving fluid from the perimeter of the shock front. We assume that a rapid expansion occurs where the post-shock flow encounters the rarefaction wave downstream from the shock front and the synchrotron emission of a fluid element falls drastically thereafter. We model this by assuming that emissivity is uniform within a conical volume the base of which is the shock front and the generators of which are defined by the rarefaction wave. The emissivity vanishes outside this cone.

If the post-shock flow is optically thin, then for an individual plane shock $S_\nu \propto \delta^{3+\alpha}\delta'^{2+\alpha}$, which is similar to the plasmoid model discussed in section IIIa with the fluid speed behind the plane shock in the observer frame identified with the speed of the plasmoid. Alternatively, if there is a succession of these optically thin plane shocks, then $S_\nu \propto \delta^{2+\alpha}\delta'^{2+\alpha}$. This mimics the continuous jet model discussed in section IIIb. In fact, a continuous jet moving at speed β will give the same dependence of flux on angle as a stream of plane shocks moving at speed

$$\beta_s{}^2\left[\beta + \left[\beta^2 + \frac{1}{\beta_s{}^2}\right]^{\frac{1}{2}}\right]$$

where β_s is the sound speed, which is $1/\sqrt{3}$ in the relativistic limit. Note that

the shocks will have a higher pattern speed than that deduced from the flux distribution obtained by assuming the emitter is a continuous jet.

At low enough frequency, the spectrum will become optically thick, and the intensity will only be boosted by a factor of δ^{2} on transforming from the pattern frame to the observer frame. Since the observed flux is quite sensitive to the projected area of the component in the optically thick case, and is not strongly dependent on δ, the flux may even begin to increase with increasing viewing angle θ when $\theta > \cos^{-1}\beta$, due to projection effects.

However, for intermediate frequencies, we cannot assume that the source is either optically thin or optically thick for all viewing angles. We must consider the variation of the optical depth with viewing angle. Since $\delta' \ll \delta$ for reasonably large γ, this effect can be large. For example, for $\gamma = 7$, $\tau(\theta)$ decreases by a factor of about of about 10^5, as θ increases from 0 to π. Thus, we expect the flux to decrease more rapidly with increasing viewing angle as the viewing angle becomes large and the shock becomes optically thin.

We have calculated the observed brightness distribution and the total flux numerically for various optical depths and shock speeds. In figure 3 we exhibit the relation between observed flux and viewing angle, $S_\nu(\theta)$ for $\gamma = 7$ at various frequencies corresponding to different optical depths. The results are consistent with predictions made from optically thin and optically thick models, taking into account the decrease of optical depth with increasing viewing angle.

e) Conical Shock Model

In this model, we attempt to take account of the fact that shocks in relativistic jets are likely to be non-planar, by assuming that a conical shock propagates outward along a slowly moving jet. This could be caused by a dense cloud or fast stream moving at relativistic speed up the center of the jet. We

assume for simplicity that the post-shock flow -- the emitting region -- is contained between two cones with common apices, with the edge of the inner cone parallel to the velocity vectors of the post-shock fluid (figure 2b). This assumption implies that the post-shock velocity is constant and allows us to assume that the emissivity of the post-shock fluid is also constant. The jump conditions are obtained most simply by Doppler boosting the flow of a plane perpendicular shock parallel to the shock front. The post-shock speed β' and the angle ξ between the flow direction and the symmetry axis can be expressed in terms of the preshock velocity β, the sound speed β_s, and the opening angle of the cone η (Königl 1980) by

$$\beta' = \frac{\beta_s^2}{\beta} \frac{\left[(1-\beta^2\cos^2\eta)^2 + \left(\beta/\beta_s\right)^4 \cos^2\eta \sin^2\eta\right]^{1/2}}{\sin\eta} \tag{3.12}$$

$$\tan\xi = \frac{\left[\left(\beta/\beta_s\right)^2 - 1\right]\tan^2\eta - (1-\beta^2)}{\tan\eta\left[\tan^2\eta + 1 + \left(1/\beta_s - 1\right)\beta^2\right]} \tag{3.13}$$

where $\beta_s = 1/\sqrt{3}$ in the relativistic limit.

For a given value of β, η must lie between some minimum value, $\eta = \eta_{min}$ and 90°, where η_{min} is given by

$$\sin(\eta_{min}) = \tan(\eta_{Mach}) = \frac{\beta_s(1-\beta^2)^{1/2}}{\beta(1-\beta_s{}^2)^{1/2}}. \tag{3.14}$$

Equation (3.14) implies that $\eta_{Mach} < \eta_{min}$ where η_{Mach} is the relativistic Mach angle. We expect that the shock, and consequently the emissivity, will both weaken as η approaches η_{min}, which corresponds to $\beta' = 0$ from (3.12). By selecting η, we can generate conical shocks with flux dependence on viewing angle $S_\nu(\theta)$ ranging from that for planar shocks (section IIId) to that for undisturbed excitation (section IIIc).

In figure 4 we exhibit the relation between observed flux and viewing angle, $S_\nu(\theta)$ for $\gamma = 7$ at various frequencies corresponding to different optical depths, using two values of η. The optical depth decreases with increasing viewing angle more slowly than it would in the case of a planar shock (section IIId), but more rapidly than it would in the case of an "excitation" (section IIIc). For optically thin emission, the $S_\nu(\theta)$ relation of this model lies between those of the planar shock model and the excitation model, as expected.

An alternative type of model is possible if the jet flows past some obstacle and the conical shock extends downstream. For simplicity, we have selected the preshock fluid speed to be equal to the pattern speed. In these models, the pattern and fluid velocities are parallel rather than antiparallel, and beaming is strong. The optical depth is an extremely strong function of viewing angle, and the optically thin assumption is correspondingly less realistic. However, since δ is so large, optically thin flow is very highly beamed, and the P(S) relation is very highly peaked toward small viewing angles. The optically thick flux is not as highly beamed, and is totally dominated by the optically thin flux unless the absorption coefficient is so large that no part of the pattern is optically thin. This is shown in figure 5 for a shock with large cone angle. The corresponding figure for a small opening angle is off scale, i.e. $S < 10^{-2} S_{max}$ for $\theta > 2.5^\circ$.

In figure 6 we exhibit the brightness distribution for a conical shock with $\gamma = 7$ and viewing angle $\theta = 5^\circ$ in the frame of the observer at decreasing frequencies corresponding to increasing optical depth by a factor of ten for each diagram. As expected, the brightness distribution is sharp for small optical depth (figure 6a), broadens as the optical depth exceeds unity (figure 6b), and approaches uniform brightness for large optical depth (figure 6c). The numerical calculations behave as expected, and agree with analytic calculations when it is possible to make them.

It has been assumed throughout that the speed of the jet can be neglected. In fact, since the final boost is from the frame of the shock to the frame of the observer, this assumption does not affect the beaming due to this final boost. It does, however, affect the assumed value for the preshock fluid velocity in the shock frame, which will in turn affect the details of the model. For planar shocks, this effect is small; for conical shocks, this effect could be large. The result will be to broaden the P(S) relations calculated for a given pattern speed and type of model.

IV. DISCUSSION

In figures 7 and 8, we compare the relations between flux and viewing angle $S(\theta)$ (from which can be derived P(S)) for the models described in the previous sections in the optically thin limits for pattern bulk Lorentz factors $\gamma = 2$ and $\gamma = 7$. As discussed in section II under equations 2.11 and 2.12, the observed flux will be independent of the shape of the source. However, the different velocities of the emitting plasma in the different models result in quite distinct P(S) curves. Recall that β_1 is the pattern speed and β_2 is the speed of the emitting fluid in the pattern frame. For the plasmoid, which has no shock, $\beta_2 = 0$. For the continuous jet, $\beta_2 > 0$ but $\beta_1 = 0$. For the plane shock model, $\beta_2 = \beta_s^2/\beta_1$ with the post-shock fluid velocity parallel to the preshock fluid velocity in the pattern frame, where β_s is the sound speed, which is $1/\sqrt{3}$ for an extreme relativistic fluid. For the conical shock model, $\beta_2 > \beta_s^2/\beta_1$, with the post-shock fluid velocity directed at some angle to the preshock fluid flow in the pattern frame. We can arrange the models in the order: narrow inverse conical shock (obstacle model), wide inverse conical shock, plasmoid, plane shock, continuous jet, wide conical shock (cannonball model), narrow conical shock, excitation model, where flux from earlier models decreases more quickly with increasing viewing angle (is

more highly beamed). This order is also the order of the post-shock fluid speeds, i.e.,the post-shock fluid speed is the dominant factor in determining the relation between flux and viewing angle. However, in the conical shock models, some decrease in the beaming is attributable to the fact that the post-shock fluid flow is no longer parallel to the symmetry axis but fans out.

As the optical depth approaches unity and the source becomes optically thick, structural details (such as shape) become increasingly important. This is especially true for models where the optical depth is a strong function of viewing angle, as for all the shock models, or where projected surface area is a strong function of angle, as for the conical shock.

The theoretical P(S) relations calculated above are not complete, for they assume that the observed sources consist of single shocks with intrinsic luminosity independent of distance from the source. As mentioned in Section II.a., this will be modified if we assume that the sources evolve. To illustrate this, assume a modified finite lifetime model in which source components are emitted by the central engine with a fixed time interval t_e. Let each component emit a constant fixed luminosity over a fixed time t_l as measured in the frame of the central engine. The lifetime of a component as measured by a stationary observer at viewing angle θ is $t_{obs} = t_l(1-\beta\cos\theta)$. The stationary observer then observes $N_{obs} = t_{obs}/t_e = K\delta^{-1}$ components at a fixed time in his own frame, where $K = t_l/(t_e\gamma)$. The time averaged flux is

$$S_{obs} = N_{obs}S_s = K\delta^{-1}S_s$$

where S_s is the flux from an individual source component, and the flux is averaged over a time $t_{av} \geq max(t_e, t_{obs})$. This simple example demonstrates that evolution of source components can modify P(S) relations for multiple component sources.

The above model also demonstrates that variability may also depend on source component evolution. The flux calculated above is averaged over time; the observer actually sees an integral number of components, one fewer when one dies out and one greater when one is emitted. The observed flux varies by the flux received from a single component, and the fractional flux variation is

$$f_{var} = \frac{\Delta S}{S} = \frac{S_s}{S_{obs}} = \frac{1}{N_{obs}} = \frac{\delta}{K}$$

Thus, variability depends on both the creation and evolution of source components, where effects due to evolution should tend to cause the fractional flux variation to increase with decreasing viewing angle, i.e.,the most highly beamed sources are likely to be the most variable also. This is consistent with the theory and observation of BL Lac objects (or blazars).

In summary, the details of theoretical P(S) relations are strongly model dependent; simple, physically reasonable models can be constructed which give radically different relations from the standard models and from each other. The observed P(S) relations probably do show evidence for relativistic beaming, but cannot be used to derive a value for the flow velocity because of this uncertainty in the models. The comparison of theoretical P(S) curves to data is a good general test for beaming, but will not provide detailed parameters if the detailed structure of each source is not known accurately.

V. ACKNOWLEDGEMENTS

We thank Ian Browne for useful discussion. We acknowledge support by the National Science Foundation under grant AST 82-13001 and the Alfred P. Sloan Foundation (RB).

REFERENCES

Blandford, R. D. 1984, in *I.A.U. Symposium 101, Compact Radio Sources and VLBI*, ed. K. I. Kellermann and G. Setti (Dordrecht:Reidel) p.

Blandford, R. and Eichler, D. 1984, in preparation

Blandford, R. and Königl, A. 1979, *Ap.J.*, **232**, 34

Blandford, R. D. and McKee, C. F. 1977, *M.N.R.A.S.*, **180**, 343

Blandford, R. D., McKee, C. F., and Rees, M. J. 1977, *Nature*, **267**, 211

Coe, M. J., Bowring, S. R., Hall, C. J., and Stephen, J. B. 1983, *Astrophys. Space Sci.*, **91**, 35

Cohen, M. H. and Unwin, S. C. 1983, in *I.A.U. Symposium 97, Extragalactic Radio Sources*, ed. D. S. Heeschen and C. M. Wade (Dordrecht:Reidel) p. 345

Condon, J. J., Ledden, J. E., O'Dell, S. L., and Dennison, B. 1979, *A.J.*, **84**, 1

Cotton, W. D. and Spangler, S. R. (editors) 1982, *Proceedings of the NRAO Workshop on Low Frequency Variability of Extragalactic Radio Sources* (Green Bank, WV:NRAO)

Drury, L. 1982, *Space Sci. Rev.*, **36**, 57

Kellermann, K. I. and Setti, G. (editors) 1984, *I. A. U. Symposium 110, Compact Radio Sources and VLBI* (Dordrecht:Reidel)

Königl, A. 1980, *Phys. Fluids*, **23**, 1083

Lynden-Bell, D. 1977, *Nature*, **270**, 396

Marscher, A. P. and Broderick, J. J. 1982, *Ap.J.(Letters)*, **247**, L49

McKee, C. F. and Hollenbach, D. J. 1980, *Ann. Rev. Astr. Ap.*, **18**, ed. G. Burbidge, D. Layzer, and J. G. Phillips (Palo Alto, CA:Annual Reviews, Inc.) p. 219

Norman, M. L., Winkler, K.-H. A., and Smarr, L. 1983, in *Astrophysical Jets; Proceedings of the International Workshop Held in Torino, Italy 1982 Oct 7-9* ed. A. Ferrari and A. G. Pacholczyk (Dordrecht:Reidel) p. 227

Orr, M. J. L. and Browne, I. W. A. 1982, *M.N.R.A.S.*, **200**, 1067

Readhead, A. C. S., Hough, D. H., Ewing, M. S., Walker, R. C., and Romney, J. D. 1983, *Ap.J.*, **265**, 107

Readhead, A. C. S. and Pearson, T. J. 1983, in *I. A. U. Symposium 97, Extragalactic Radio Sources*, ed. D. S. Heeschen and C. M. Wade (Dordrecht:Reidel) p. 279

Reynolds, S. P. 1982, *Ap.J.*, **256**, 13

Reynolds, S. P. 1982, *Ap.J.*, **256**, 37

Rybicki, G. and Lightman, A. 1979, *Radiative Processes in Astrophysics* (New York:Wiley) p. 145

Scheuer, P. A. G. and Readhead, A. C. S. 1979, *Nature*, **277**, 182

Simon, R. S. 1983, thesis, California Institute of Technology.

Terrell, J. 1960, *Phys. Rev.*, **116**, 1041

Wilson, M. J. and Scheuer, P. A. G. 1983, *M.N.R.A.S.*, **205**, 449

FIGURE CAPTIONS

Figure 1. P(S) for Standard Models

The theoretical P(S) curves are plotted as log P versus log S for a bulk Lorentz factor $\gamma = 7$ for:

A: Plasmoid model with finite source component lifetime,

B: Plasmoid model with constant intrinsic source component flux,

C: Plasmoid model with radial decay specified by $\alpha = 0$ and $n = 2$,

D: Continuous jet model, and

E: Excitation of a stationary medium in the optically thin limit.

Note that source evolution and optical depth significantly affect the theoretical P(S) relations.

Figure 2. Shock Models

The geometries for the shock models are shown. In both models, β_1 is the preshock fluid speed in the shock frame, β_2 is the post-shock fluid speed in the shock frame, and η is the cone opening angle, where $\tan\eta = \rho / l$. Small dashed lines are flow lines of the fluid.

A: The plane shock model has cone angle η fixed by the sound speed and the preshock fluid speed.

B: The conical shock models may have a range of cone opening angles η. The inner cone angle ξ is fixed by the outer cone angle η according to the oblique shock jump conditions. The long dashed lines indicate the symmetry axis and the boundary of the inner cone.

Details of these models are discussed in Section III of the text.

Figure 3. Flux Distribution for Plane Shock Model

The distribution of flux with total solid angle is interpreted as log P(S) versus log S at several different frequencies, corresponding to different mean optical depths:

A: $\nu = 10$, $\bar{\tau} \approx 0.01$

B: $\nu = 3$, $\bar{\tau} \approx 0.1$

C: $\nu = 1$, $\bar{\tau} \approx 1$

D: $\nu = 0.3$, $\bar{\tau} \approx 10$

where $\bar{\tau}$ is roughly the mean optical depth at a viewing angle of $\theta = \cos^{-1}\beta$.

The flux was obtained by numerically integrating over the calculated intensity distributions. Smooth curves were then drawn through the calculated points. The optically thin flux is determined by the post-shock fluid velocity. The optically thick flux is strongly influenced by the shape of the pattern.

The relations between observed flux and angle are interpreted as P(S) relations. This is strictly true for models A, B, and C in which the flux decreases monotonically with increasing viewing angle. If monotonicity does not hold, as in model D, it is necessary to correct the plotted relation by calculating the total solid angle subtended with the model oriented such that the observed flux is greater than S. This integration over solid angle transforms the dip plotted in the figure into a monotonic curve.

Figure 4. Flux Distribution for Conical Shock Models

The distribution of flux with angle is interpreted as log P(S) versus log S for two values of cone opening angle η at several frequencies, corresponding to several mean optical depths:

A: $\nu = 10$, $\bar{\tau} \approx 0.01$

B: $\nu = 3$, $\bar{\tau} \approx 0.1$

C: $\nu = 1$, $\bar{\tau} \approx 1$

D: $\nu = 0.3$, $\bar{\tau} \approx 10$

where $\bar{\tau}$ is roughly the mean optical depth at a viewing angle of $\theta = \cos^{-1}\beta$. The wide conical shock (a) has cone opening angle $\eta = 30°$, corresponding to $\tan\eta = \beta_s / \beta_p$, where β_s is the sound speed and β_p is the pattern speed. Thus, η is equal to the nonrelativistic Mach angle. The narrow conical shock (b) has cone opening angle $\eta = 10°$, which was chosen to be somewhat larger than the minimum cone opening angle $\eta_{min} = 6°$.

The flux was obtained by integrating over the observed intensity distributions. Smooth curves were then drawn through the calculated points. The optically thin flux is determined by the post-shock fluid velocity. The optically thick flux is determined primarily by the shape of the pattern.

The relations between observed flux and angle are interpreted as P(S) relations. This is strictly true for models A, B, and C in which the flux decreases monotonically with increasing viewing angle. If monotonicity does not hold, as in model D, it is necessary to correct the plotted relation by calculating the total solid angle subtended with the model oriented such that the observed flux is greater than S. This integration over solid angle transforms the dip plotted in the figure into a monotonic curve.

Figure 5. Flux Distribution for Inverse Conical Shock Model

The distribution of flux with angle is interpreted as log P(S) versus log S at several different frequencies corresponding to different optical depths:

A: $\nu = 10$, $\bar{\tau} \approx 0.01$

B: $\nu = 3$, $\bar{\tau} \approx 0.1$

C: $\nu = 1$, $\bar{\tau} \approx 1$

where $\bar{\tau}$ is roughly the mean optical depth at a viewing angle of $\theta = \cos^{-1}\beta$. The cone opening angle $\eta = 30°$ as in figure 5a.

The flux was obtained by integrating over the observed intensity distributions. Smooth curves were then drawn through the calculated points. The optically thin flux is determined by the post-shock fluid velocity. The optically thick flux is determined primarily by the shape of the pattern. Since the fluid velocity is roughly parallel to the pattern velocity, the flux is highly beamed.

Figure 6. Sample Intensity Distributions

Sample intensity distributions are shown for a conical shock with cone opening angle $\eta = 30°$, viewing angle $\theta = 5°$, and pattern Lorentz factor $\gamma = 7$ for:

A: $\nu = 3$, $\bar{\tau} \approx 0.1$

B: $\nu = 1$, $\bar{\tau} \approx 1$

C: $\nu = 0.3$, $\bar{\tau} \approx 10$

where $\bar{\tau}$ is roughly the mean optical depth at a viewing angle of $\theta = \cos^{-1}\beta$. The contour levels for A and B are multiples of 10% of the peak intensity. The contour levels for C are 90%, 95%, 96%, 97%, 98%, and 99% of the peak intensity. The scale for C is stretched to better display its slight departure

from uniform brightness.

These distributions were calculated by numerical solution of the equations of radiative transfer along lines of sight. These distributions are consistent with those expected in the optically thin and optically thick limits.

Figure 7. Flux Distributions for Pattern Lorentz Factor $\gamma = 7$

The flux distribution with angle for pattern Lorentz factor $\gamma = 7$ in the optically thin limit is plotted as log P(S) versus los S for the models calculated:

A: Planar shock model for $\log(S/S_{max})$ large; inverse planar shock model for $\log(S/S_{max})$ small (upper limit for inverse conical shock models),

B: Wide conical shock model for $\log(S/S_{max})$ large; inverse wide conical shock model for $\log(S/S_{max})$ small. The cone opening angle $\eta = 30°$ in both cases,

C: Narrow conical shock model (inverse narrow conical shock model cannot be displayed on this scale). The cone opening angle $\eta = 10°$,

D: Excitation of a stationary medium,

E: Continuous jet model, and

F: Plasmoid model with constant intrinsic source component flux.

In the limit η goes to η_{min}, the flux distribution for the conical shock model approaches that for the excitation model. In the limit η goes to 90 degrees, the flux distribution for the conical shock approaches that for the plane shock.

Figure 8. Flux Distributions for Pattern Lorentz Factor $\gamma = 2$

The flux distribution with angle for pattern Lorentz factor $\gamma = 2$ in the optically thin limit is plotted as log Ω versus los S for the models calculated.

A: Planar shock model for $\log(S/S_{max})$ large; inverse planar shock model for $\log(S/S_{max})$ small (upper limit for inverse conical shock models).

B: Wide conical shock model for $\log(S/S_{max})$ large; inverse wide conical shock model for $\log(S/S_{max})$ small. The cone opening angle $\eta = 34°$ for both models.

C: Narrow conical shock model for $\log(S/S_{max})$ large; inverse narrow conical shock model for $\log(S/S_{max})$ small. The cone opening angle $\eta = 27°$ for both models, where the minimum cone opening angle is $\eta_{min} = 24°$.

D: Excitation of a stationary medium.

E: Continuous jet model, and

F: Plasmoid model with constant intrinsic source component flux.

While the range of possible fluxes is much smaller than for $\gamma = 7$, beaming is clearly still important.

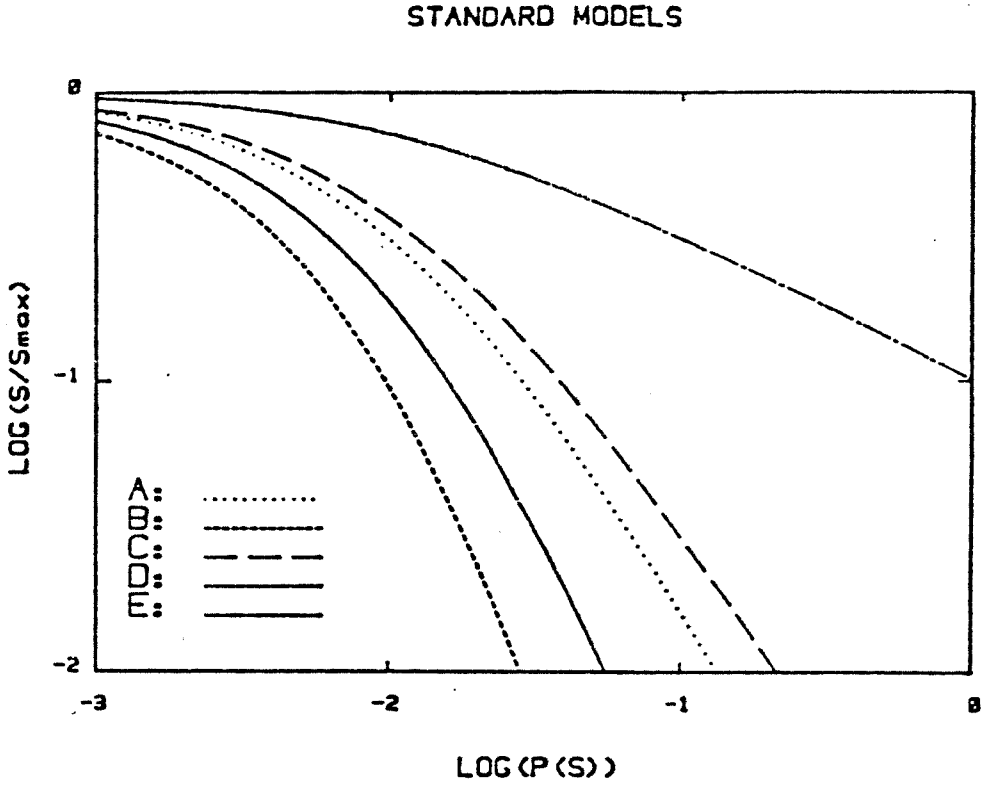

FIGURE 1

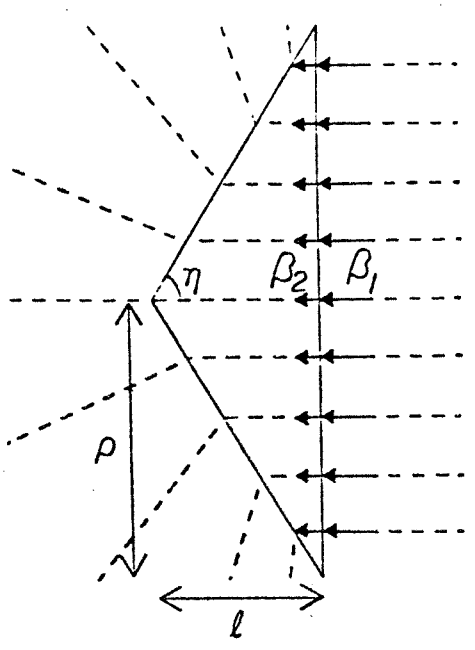

FIGURE 2A

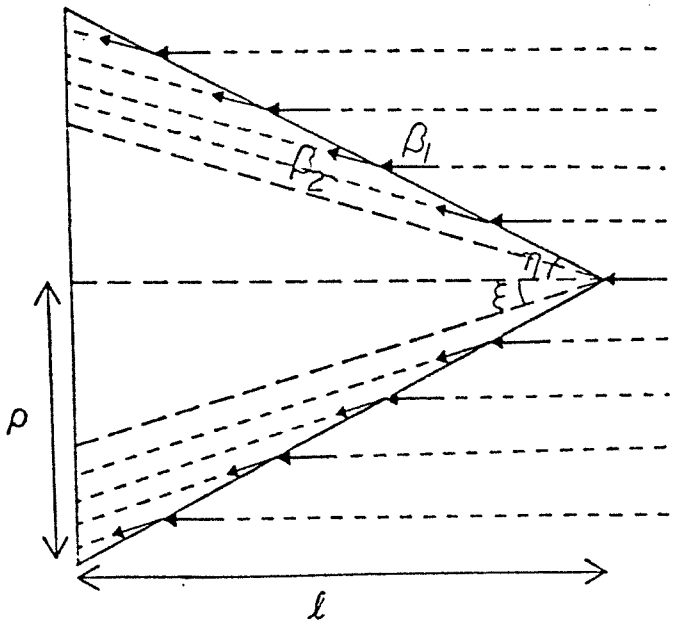

FIGURE 2B

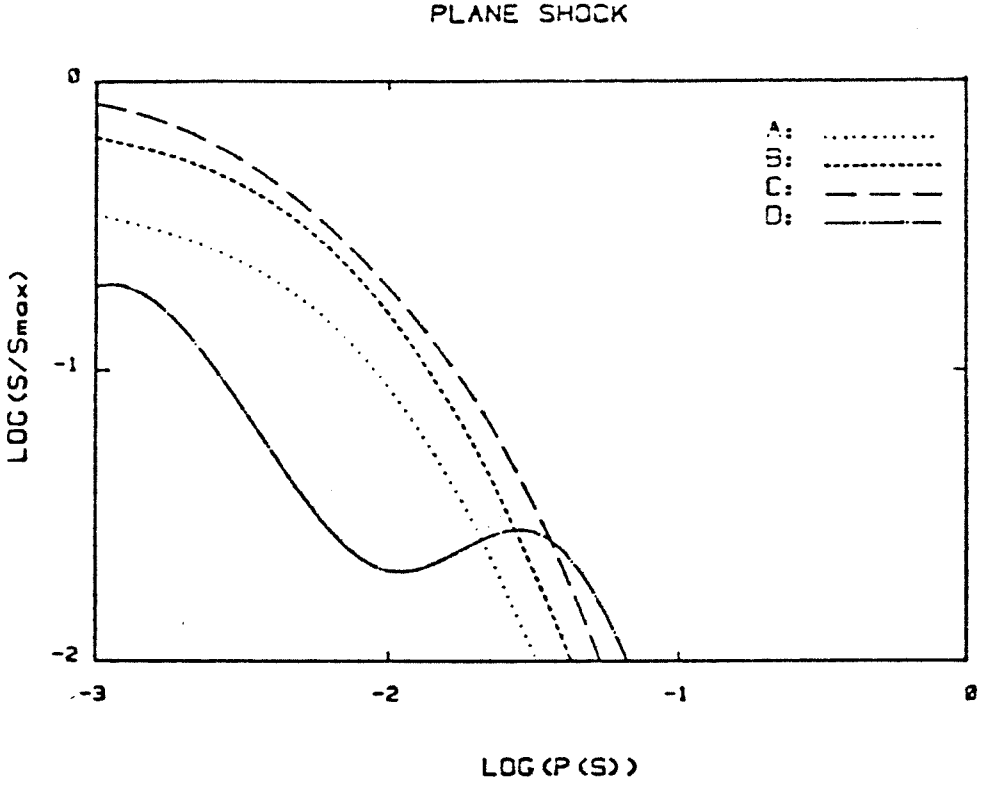

FIGURE 3

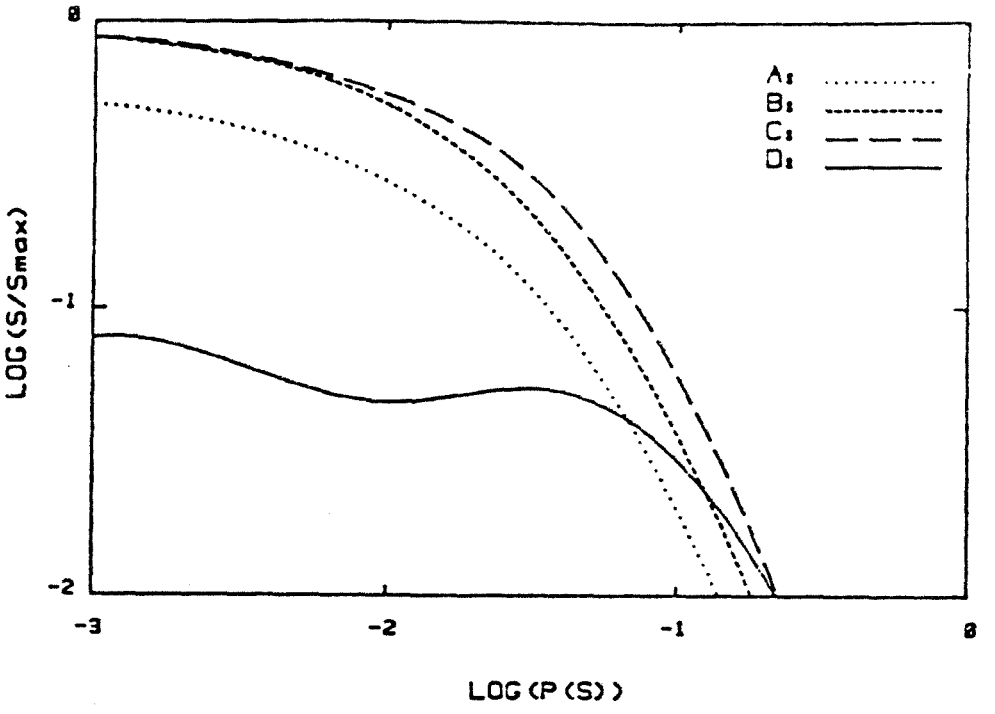

FIGURE 4A

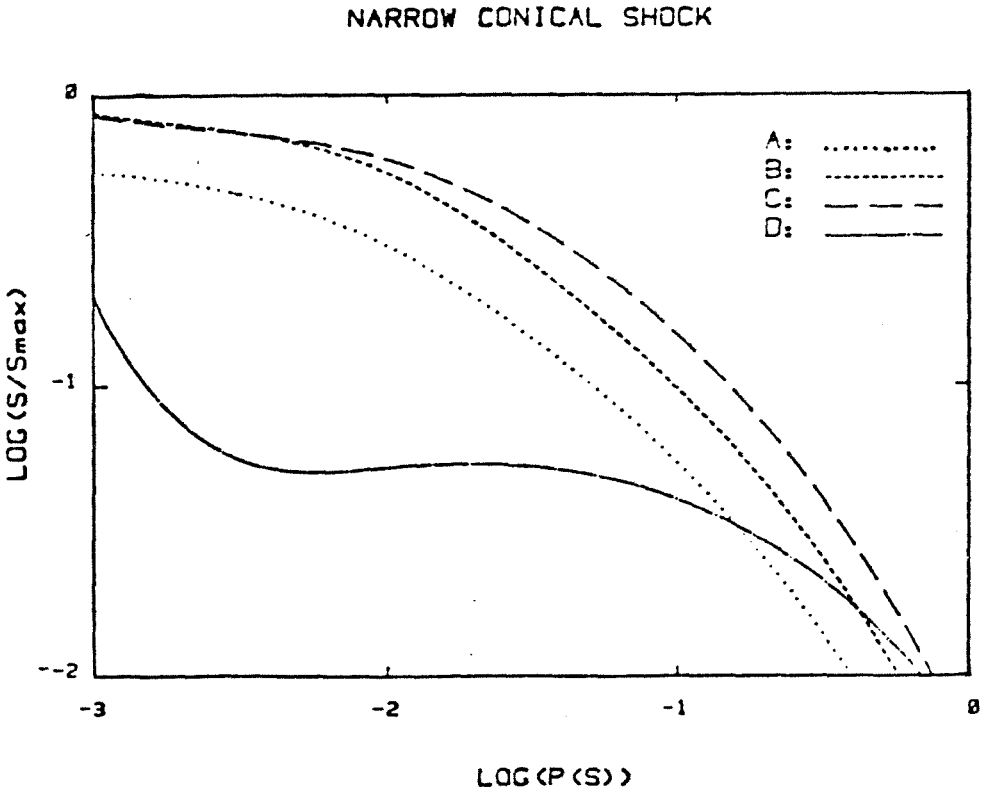

FIGURE 4B

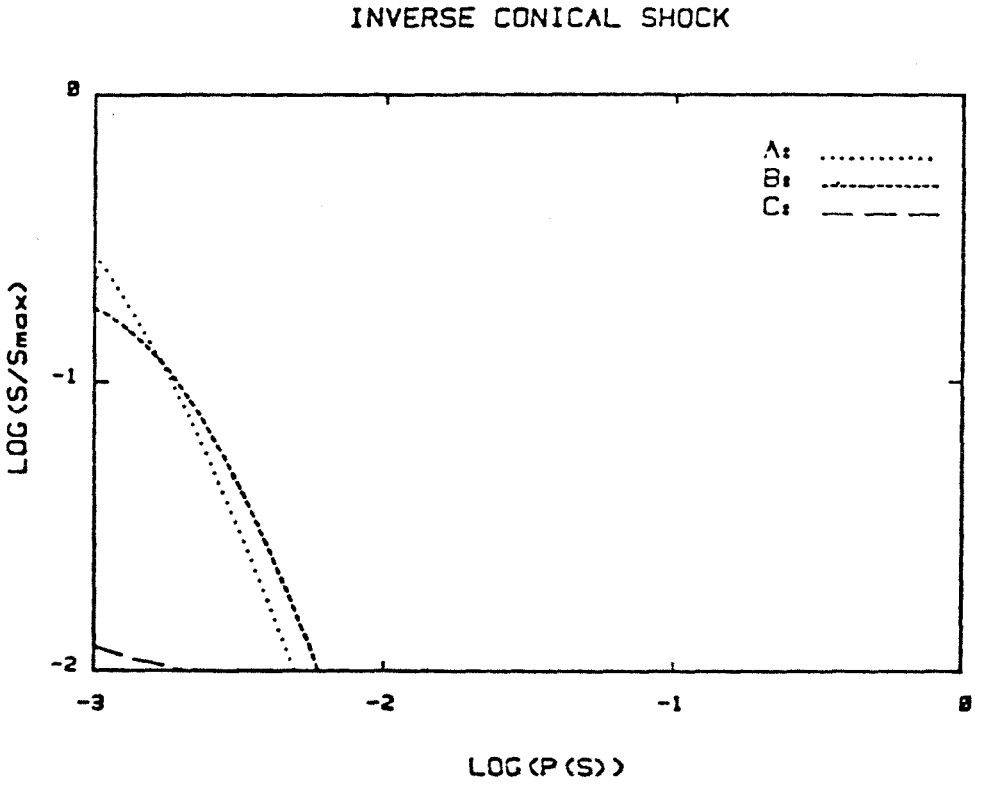

FIGURE 5

MODEL A

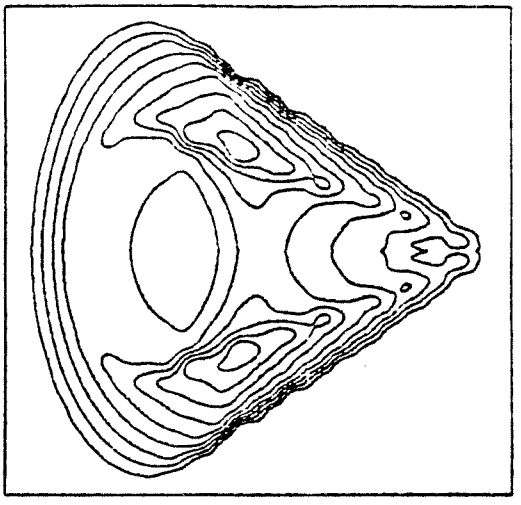

MODEL B

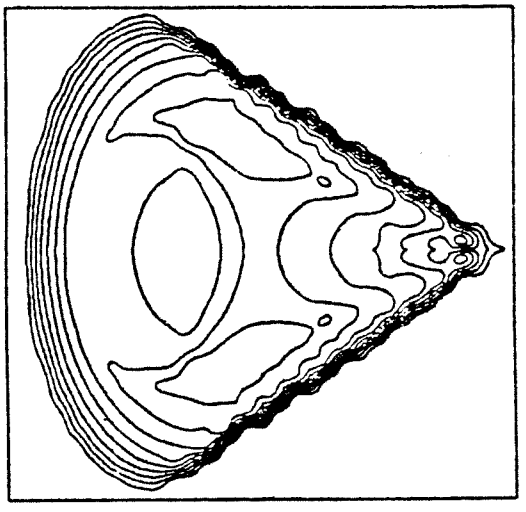

MODEL C

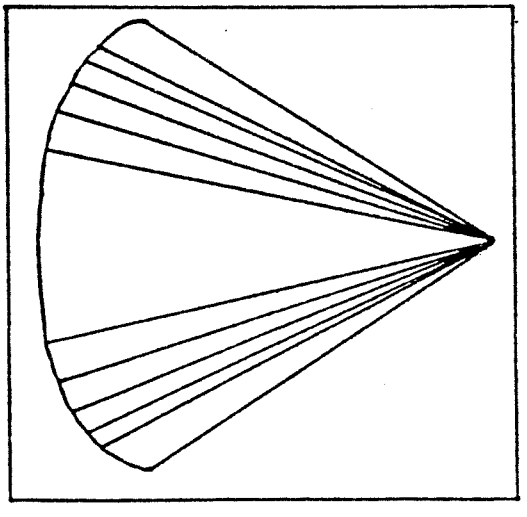

FIGURE 6

THIN MODELS. GAMMA = 7

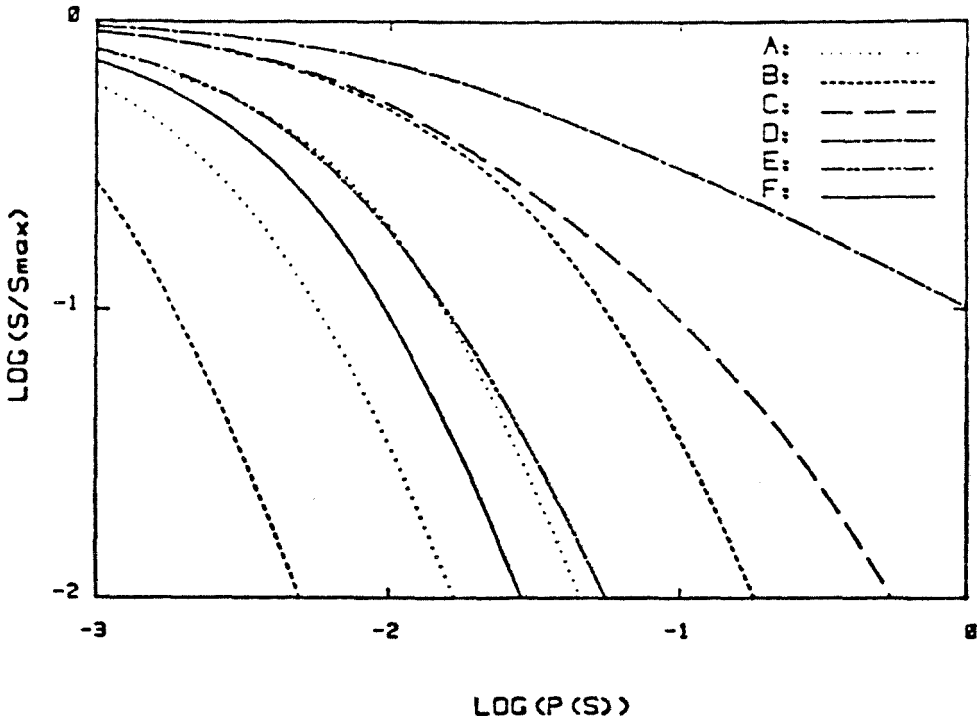

FIGURE 7

THIN MODELS. GAMMA = 2

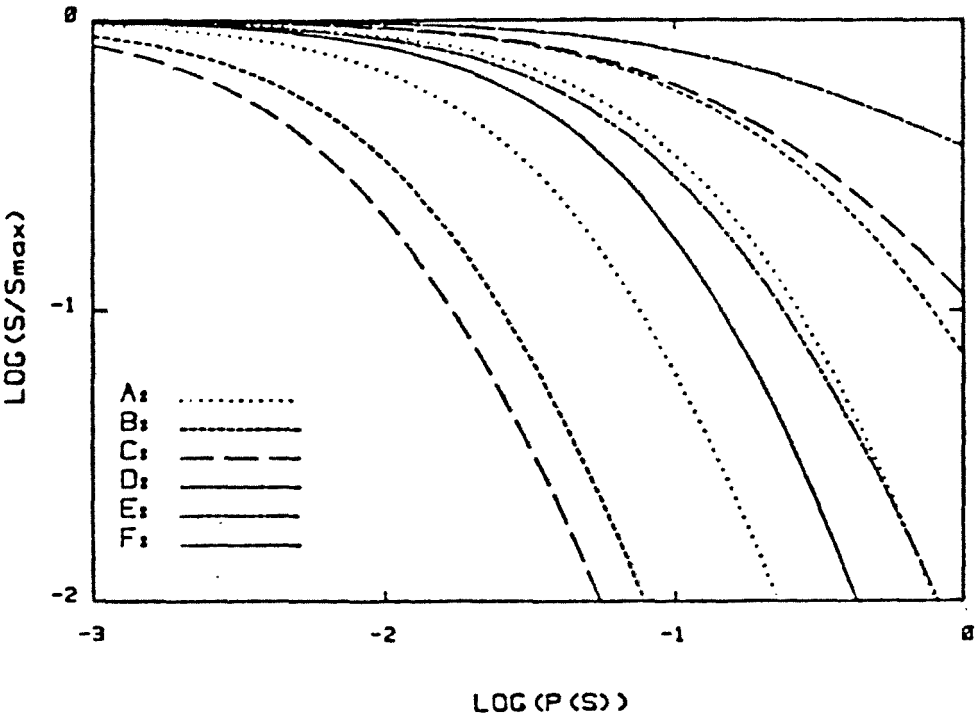

FIGURE 8

CHAPTER 4

NUMERICAL SIMULATIONS OF MAGNETIZED JETS I. CODE DEVELOPMENT

1. Introduction

Numerical modeling is in many ways an observational technique, in which the sources are extremely well defined, and are distributed, not in physical space, but in parameter space. The instrument by which "numerical observations" are made is the code, which is primarily designed in software rather than hardware, but otherwise is designed just like any other instrument. To carry the analogy further, the graphics package associated with the code may display a variety of quantities, just as one can attach any number of receivers, imagers, spectrographs, or photometers on the various types of telescopes. Then, if the code is an instrument, it is important for the "numerical observing" community — both those who design and run the codes (observers) and those who interpret them in terms of basic physical processes (theorists) — to be familiar with the design and calibration of their numerical instruments. This chapter has two purposes. The first is to introduce terms and concepts pertinent to simulation codes which may not be familiar to those who interpret the results of these codes. The second is to describe the development of a particular code, which was designed to simulate two-dimensional axisymmetric magnetized jets propagating into a uniform ambient medium.

There are a number of aspects in numerical modeling which deal with the technical details of the code. These terms require some definition and discussion, for they are essential for understanding this code and its limitations.

Most numerical hydrodynamic and MHD codes use a *conservative* formulation of the difference equations. Changes in the values of quantities within a cell are treated as fluxes at the cell boundaries, so that the flux of a physically conserved quantity (such as mass or energy) out of one cell is also the flux into an adjacent cell. This guarantees that quantities which are physically conserved are conserved numerically as well. It is not always desirable to update conserved quantities;

for example, difficulties arise in estimating the pressure from the total energy, momentum, and mass density, and it may be desirable to update internal energy (nonconservative) rather than total energy (conservative) if the precise value of the pressure is of great dynamical importance (e.g., if radiative losses dominate). In general, it is best to maintain a conservative formalism as much as possible, since it allows the imposition of physical conservation conditions on the numerical solutions.

Steady and unsteady flows may be solved either *explicitly* or *implicitly*. An explicit formulation does a direct numerical time integration of the time-dependent equations, for each updated quantity at each point in the grid. The timestep used in the numerical integration, Δt, is determined over the entire grid by the shortest characteristic time scale in the grid. An implicit formulation uses the steady-state or time-dependent equations to construct a matrix equation with the equations to be solved on one side, and a correction matrix on the other; the matrix equation is then solved iteratively until the corrections converge to zero. In short, implicit techniques treat time as another parameter, whereas explicit techniques treat it as the integration variable. If all that is desired is a steady-state solution, or if there are two or more highly discrepant time scales in the problem (for example, in stellar evolution, the nuclear time scales are much shorter than the hydrodynamic time scales), then an implicit treatment is best. In particular, in the case of stellar evolution, an explicit formulation would be limited to using a timestep less than the characteristic time scale for nuclear processes, whereas an implicit formulation could solve for a steady-state nuclear solution given the slowly varying hydrodynamic solution, which could then be iterated to converge to the hydrodynamic solution, and would use a timestep which would be short relative to the hydrodynamic time scales but could be long relative to the nuclear

time scales. In general, an explicit code can be used to solve most any problem, but an explicit code may be much faster if there is only one characteristic time scale in the problem since it need not invert matrices. Most hydrodynamic and magnetohydrodynamic jet codes (including this code) solve the flow equations explicitly for this reason.

A code is *of order* N in space if the terms remaining in the Taylor expansion after the numerical equations have been generated are of order $O(\Delta r^N, \Delta z^N)$, and in time if the temporal remainders are $O(\Delta t^N)$. A second-order code requires that a linear interpolation be used to estimate the values of quantities located away from cell centers, where the values of the quantities are defined. The errors in this case will decrease as the square of the grid spacing, i.e., if Δr were halved, the errors should drop to one-fourth of their original value. This is a valuable principle to use in debugging a code; if the error does not fall off fast enough, there has probably been some error in implementation.

Algorithms which use *operator splitting* separate the two-dimensional solution for the flow equations into two independent one-dimensional solutions, i.e., the radial integration is done separately from the axial integration. This separation makes it easier to code and debug, because two one-dimensional algorithms are used rather than one complex two-dimensional algorithm. Bias is reduced by alternating the order in which the radial and axial updates are carried out.

A *predictor-corrector* algorithm calculates time derivatives by updating the model for a portion of the desired time step, re-calculating the fluxes and forces given their interim values, and then either updating the original values for a full time step using the corrected values or calculating correction terms based on the interim values. In effect, the use of these interim values provides a linear interpolation of the time derivative, which is used to raise the time accuracy to second

order. There are ways to achieve second-order accuracy without recalculating the time derivative, but tests using this code indicated that, in this case, they were no faster and, in some cases, not as stable.

Monotonicity is the requirement that extrema and gradients retain their character under advection (van Leer 1974; van Leer 1977; van Leer 1979). In particular, if the value of f_i lies between f_{i-1} and f_{i+1}, then it is required to do so after advection unless f_{i+1} is an extremum. In practice, what is enforced is that the gradient chosen within a cell gives a value at the edge of the cell which is between the cell center value and the center value of the neighboring cell if at all possible; if not possible, our code sets the gradient to zero. This greatly improves the stability of the solution and reduces diffusion but clips or flattens extrema; sharp peaks or troughs tend to be replaced with flatter distributions.

The value of the gradient is used to determine the flux in cooperation with *upwind differencing*, which simply states that the values used in calculating advection are estimated from values located upwind of the quantity being calculated. In short, it assumes that quantities are transported along with the flow. Centered differencing, which uses values centered on the quantity being calculated, is usually used to estimate the force, or non-transport, terms, which are not carried along with the flow but are due to the local state of the fluid. By contrast, downwind differencing, which estimates the advective terms using quantities located downwind of the flow, feeds any errors in the advection back into the calculation and is generally extremely unstable.

The *Courant number* is defined by $N_C \equiv |v + \sqrt{c_s^2 + c_A^2}|\Delta t/\Delta x$, where v is velocity, c_s is the sound speed, c_A is the Alfven speed, Δx is the grid spacing, and Δt is the timestep. The Courant number is interpreted as the number of grid zones over which a signal may propagate; for $C_N \leq 1$, no physical wave may travel any

farther than one grid zone Δx in time Δt; for $N_C > 1$, there may be solutions to the analytic equations which allow signals to propagate more than one grid zone. Since cells may only interact with nearest neighbors for explicit algorithms, the domain of dependence for the analytic equations will be greater than the domain of dependence for the numerical equations if $N_C > 1$. In this case, the numerical solution will cease to approximate the analytic solution, and will typically become unstable. The resulting requirement, that $N_C \leq 1$, is known as the Courant-Friedrichs-Lewy, or CFL, condition (Courant *et al.* 1967). In practice, loss of accuracy begins to occur for $N_C < 1$, with the critical value of N_C dependent on the algorithm, but it is usually not much less than one. This code may be run with $N_C \sim 0.4$ without extreme loss of accuracy, but has generally been run at $N_C = 0.2$ to ensure high accuracy.

A *staggered grid* refers to the method of locating quantities on the numerical grid, in which different quantities are updated at different points in the grid (fig. 1). This often improves the stability of flux estimates at cell boundaries, and in particular may reduce biasing and errors resulting from the interpolation of zone-centered quantities to the cell boundaries. In the case of non-Cartesian coordinate systems, it may also be desirable to move the positions of the calculated quantities away from the centers of the cells, which is simple to account for in the numerical equations. Our algorithm was implemented with a staggered grid and a unstaggered grid; the staggered grid was superior in stability of solution and in modeling flows near steep gradients.

Adaptive gridding and *interface tracking* are two techniques designed to maintain discontinuities and improve the accuracy of transport terms. Adaptive gridding varies the positions of the cell centers and boundaries according to the structure of the flow in order to better track shocks and interfaces, better resolve regions

with steep gradients, and deal with flows which are not aligned with on of the principal dimensions. It is complicated to code, requires considerable computing time to adapt the grid for complex flows, and eliminates the use of operator splitting. Interface tracking is a simpler and somewhat more specialized method which does permit the use of operator splitting. The position of a two-fluid interface is calculated within each cell, and that interface is treated as a massless impermeable boundary in the difference equations. This technique is essential when studying poorly resolved flows, but increasing the resolution of the grid almost always gives better improvement. For these reasons, these features have not been implemented in our code.

Artificial viscosity is a term, similar to physical viscosity, which is added to the numerical equations to diffuse the updated quantities. This is often necessary to model shocks and other unresolved structures, in order to spread them out over a couple of grid zones. Otherwise, severe instabilities and oscillations can develop at these structures, which may lead to spurious features which in turn dominate the flow. Our code includes artificial viscosity as an option, but it has not been needed. The viscosity implicit in our algorithm, which is introduced by gridding and the limited accuracy of the linear approximation, combined with updating total rather than internal energy, is sufficient to stabilize the flow without the explicit use of artificial viscosity.

Considerations related to these concepts and techniques enter into every stage of code development, from the formulation of the analytic equations from which the numerical difference equations are derived, to the treatment of boundaries. The specific design of the code depends on the details of the physical system which it is meant to model, and usually involves tradeoffs based on the above

considerations. For example, there are situations in which a particular nonconservative formulation of the difference equations will give superior results over a conservative formulation, or where an improper implementation of monotonicity will seriously reduce the accuracy of the code. The most important consideration in the development of any code is how well it models the physical system of interest, followed by whether the calculation may be carried out with the available resources.

2. The Physical Equations

The magnetohydrodynamic equations are solved in fully conservative form. Axisymmetry, zero viscosity, and infinite conductivity are assumed. The equations are written in cylindrical coordinates, as is appropriate for axisymmetric jets; the extension to a Cartesian, or slab, geometry is straightforward and is not considered here.

All dynamical quantities are considered as functions of radius r, axial distance z, and time t; they are constant with respect to angular position ϕ. The scalar quantities used are density ρ, gas pressure p_g, and total energy $e = u_k + u_g + u_m$, the sum of kinetic, internal gas, and magnetic energies. The vector variables are momentum $\vec{S} = (S_r, S_\phi, S_z)$, velocity $\vec{v} = (v_r, v_\phi, v_z)$, magnetic field $\vec{B} = (B_r, B_\phi, B_z)$, magnetic vector potential $\vec{A} = (A_r, A_\phi, A_z)$, and current density $\vec{J} = (J_r, J_\phi, J_z)$.

The basic magnetohydrodynamic equations in operator form are:
The hydrodynamic equations:

$$\frac{\partial \rho}{\partial t} + \nabla \cdot (\rho \vec{v}) = 0 \tag{2.1}$$

$$\frac{\partial \vec{S}}{\partial t} + (\vec{v} \cdot \nabla)\vec{S} + \vec{S}\nabla \cdot \vec{v} = -\nabla p_g + \frac{1}{c}\vec{J} \times \vec{B} \tag{2.2}$$

$$\frac{\partial u}{\partial t} + \nabla \cdot [(u + p)\vec{v}] = \vec{J} \cdot \vec{E}, \qquad \text{where} \tag{2.3}$$

$$u \equiv \frac{1}{2}\rho v^2 + \frac{p_g}{\gamma - 1}$$

The MHD approximation of Maxwell's equations:

$$\nabla \cdot \vec{E} = 0 \tag{2.4}$$

$$\nabla \cdot \vec{B} = 0 \tag{2.5}$$

$$\nabla \times \vec{E} = -\frac{1}{c}\frac{\partial \vec{B}}{\partial t} \tag{2.6}$$

$$\nabla \times \vec{B} = \frac{4\pi}{c}\vec{J} \tag{2.7}$$

The constituitive equation:

$$\vec{J} = \sigma\left(\vec{E} + \frac{\vec{v}}{c} \times \vec{B}\right) \qquad (\sigma = 0), \qquad \text{which implies}$$

$$\vec{E} = -\frac{\vec{v}}{c} \times \vec{B} \tag{2.8}$$

Since perfect conductivity has been assumed, the electric field and current can be eliminated from these equations, giving the standard equations for nonrelativistic MHD :

$$\frac{\partial \rho}{\partial t} + \nabla \cdot (\rho \vec{v}) = 0 \tag{2.9}$$

$$\frac{\partial \vec{S}}{\partial t} + (\vec{v} \cdot \nabla)\vec{S} + \vec{S}\nabla \cdot \vec{v} = -\nabla p_g - \nabla\left(\frac{B^2}{8\pi}\right) + \frac{1.}{4\pi}(\vec{B} \cdot \nabla)\vec{B} \tag{2.10}$$

$$\frac{\partial e}{\partial t} + \nabla \cdot \left[\left(e + p + \frac{B^2}{8\pi}\right)\vec{v}\right] = \nabla \cdot \left[\frac{1}{4\pi}(\vec{v} \cdot \vec{B})\vec{B}\right], \qquad \text{where} \tag{2.11}$$

$$e \equiv \frac{1}{2}\rho v^2 + \frac{p_g}{\gamma - 1} + \frac{B^2}{8\pi}$$

$$\frac{\partial \vec{B}}{\partial t} + \vec{B}\nabla \cdot \vec{v} + \vec{v}\nabla \cdot \vec{B} = (\vec{B} \cdot \nabla)\vec{v} \tag{2.12}$$

$$\frac{\partial \vec{A}}{\partial t} + \vec{v} \times (\nabla \times \vec{A}) = 0 \tag{2.13}$$

The code is two-dimensional and axisymmetric, so all gradients in the angular direction $\frac{\partial}{\partial \phi} \equiv 0$, and the equations can be written in coordinate notation as:

$$\frac{\partial \rho}{\partial t} = -\frac{1}{r}\frac{\partial}{\partial r}(r\rho v_r) - \frac{\partial}{\partial z}(\rho v_z) \tag{2.14}$$

$$\begin{aligned}\frac{\partial e}{\partial t} = &-\frac{1}{r}\frac{\partial}{\partial r}\left[r\left(e + p_g + \frac{B^2}{8\pi}\right)v_r\right] - \frac{\partial}{\partial z}\left[(e + p_g + \frac{B^2}{8\pi})v_z\right] \\ &+ \frac{1}{4\pi r}\frac{\partial}{\partial r}\left[r\left(v_r B_r + v_\phi B_\phi + v_z B_z\right)B_r\right] \\ &+ \frac{1}{4\pi}\frac{\partial}{\partial z}\left[\left(v_r B_r + v_\phi B_\phi + v_z B_z\right)B_z\right]\end{aligned} \tag{2.15}$$

$$\frac{\partial B_\phi}{\partial t} = -\frac{\partial}{\partial r}(v_r B_\phi) - \frac{\partial}{\partial z}(B_\phi v_z) + \frac{\partial}{\partial r}(v_\phi B_r) + \frac{\partial}{\partial z}(B_z v_\phi) \tag{2.16}$$

$$\frac{\partial S_r}{\partial t} = -\frac{1}{r}\frac{\partial}{\partial r}(rS_r v_r) - \frac{\partial}{\partial z}(S_r v_z) - \frac{\partial p_g}{\partial r} - \frac{\partial}{\partial r}\left(\frac{B_\phi^2}{8\pi}\right) - \frac{\partial}{\partial r}\left(\frac{B_z^2}{8\pi}\right) \tag{2.17}$$

$$- \frac{B_\phi^2}{4\pi r} + \frac{B_z}{4\pi}\frac{\partial B_r}{\partial z} + \frac{v_\phi S_r}{r}, \qquad \text{where}$$

$$- \frac{\partial p_g}{\partial r} \text{ is due to gas pressure;}$$

$$- \frac{\partial}{\partial r}\left(\frac{B_r^2}{8\pi}\right) - \left(\frac{\partial}{\partial r}\frac{B_\phi^2}{8\pi}\right) - \left(\frac{\partial}{\partial r}\frac{B_z^2}{8\pi}\right) \text{ is due to magnetic pressure;}$$

$$\left(\frac{\partial}{\partial r}\frac{B_r^2}{8\pi}\right) - \frac{B_\phi^2}{4\pi r} + \frac{B_z}{4\pi}\frac{\partial B_r}{\partial z} \text{ is due to magnetic tension; and}$$

$$\frac{v_\phi S_\phi}{r} \text{ is the centripetal acceleration.}$$

$$\frac{\partial S_\phi}{\partial t} = -\frac{1}{r}\frac{\partial}{\partial r}(rS_\phi v_r) - \frac{\partial}{\partial z}(S_\phi v_z) + \frac{1}{4\pi r}\frac{\partial}{\partial r}(rB_\phi B_r) + \frac{B_\phi B_r}{4\pi r} \tag{2.18}$$

$$+ \frac{1}{4\pi}\frac{\partial}{\partial z}(B_\phi B_z) - \frac{v_\phi S_r}{r}, \qquad \text{where}$$

$$\frac{1}{4\pi r}\frac{\partial}{\partial r}(rB_\phi B_r) + \frac{B_\phi B_r}{4\pi r} + \frac{1}{4\pi}\frac{\partial}{\partial z}(B_\phi B_z) \text{ is due to field twisting; and}$$

$$- \frac{v_\phi S_r}{r} \text{ is the Coriolis acceleration.}$$

$$\frac{\partial S_z}{\partial t} = -\frac{1}{r}\frac{\partial}{\partial r}(rS_z v_r) + \frac{\partial}{\partial z}(S_z v_z) - \frac{\partial p_g}{\partial z} - \frac{\partial}{\partial z}\left(\frac{B_r^2}{8\pi}\right) - \frac{\partial}{\partial z}\left(\frac{B_\phi^2}{8\pi}\right) \tag{2.19}$$

$$+ \frac{B_r}{4\pi}\frac{\partial B_z}{\partial r}, \qquad \text{where}$$

$$- \frac{\partial p_g}{\partial z} \text{ is due to gas pressure;}$$

$$- \frac{\partial}{\partial z}\left(\frac{B_r^2}{8\pi}\right) - \frac{\partial}{\partial z}\left(\frac{B_\phi^2}{8\pi}\right) - \frac{\partial}{\partial z}\left(\frac{B_z^2}{8\pi}\right) \text{ is due to magnetic pressure; and}$$

$$+ \frac{\partial}{\partial z}\left(\frac{B_z^2}{8\pi}\right) + \frac{B_r}{4\pi}\frac{\partial B_z}{\partial r} \text{ is due to magnetic tension.}$$

$$\frac{\partial A_\phi}{\partial t} = -\frac{\partial}{\partial r}(rA_\phi v_r) - \frac{\partial}{\partial z}(A_\phi v_z) + A_\phi\left(\frac{1}{r}\frac{\partial}{\partial r}(rv_r) + \frac{\partial v_z}{\partial z}\right), \qquad \text{where} \tag{2.20}$$

$$B_r \equiv -\frac{\partial A_\phi}{\partial z} \text{ is the radial magnetic field; and} \tag{2.21}$$

$$B_z \equiv \frac{1}{r}\frac{\partial}{\partial r}(rA_\phi) \text{ is the axial magnetic field.} \tag{2.22}$$

If radial and axial magnetic fields are neglected, i.e., the only magnetic field contribution is the toroidal field, then no torque is exerted on the jet (v_ϕ = constant). In this case, $v_\phi = 0$, $S_\phi = 0$, $A_\phi = 0$, $B_r = 0$, and $B_z = 0$. The remainder of this chapter shall neglect these terms, and will discuss the development of a magnetohydrodynamic code which includes toroidal field only.

3. The Difference Equations

The differential forms of the equations of perfect MHD are solved approximately by dividing the physical region of interest into a uniform grid and integrating the differential equations over each grid zone. The resulting integrated difference equations are then integrated over a finite time integral to obtain self-consistent difference equations appropriate for numerical solution.

The method used is second-order in both time and space. A second-order algorithm was chosen because of the need for accuracy and need for efficiency. A first-order code, in which all gradients are ignored, will fail to model regions with strong gradients properly; in particular, it will do a poor job of modeling shocks. On the other hand, a third-order code requires considerably more computation time per node per timestep than the equivalent second-order code. Thus, a second-order algorithm was chosen to give sufficient accuracy using minimal computation time. It was implemented using operator splitting to ensure the independence of the radial and axial integrations. The temporal evolution was made second-order through the use of a simple predictor-corrector scheme.

To understand the details of the integration, in particular, of the Lagrangian or advective terms, consider the time evolution of the density $\rho(r,z,t)$ in cylindrical coordinates. Let i denote the i^{th} radial cell, j the j^{th} axial cell, and k the k^{th} time interval, where Δt in particular is allowed to vary with each iteration so as to satisfy the CFL condition. The basic equation, integrated over time t and spatial variables r and z, is:

$$\int_{t_k}^{t_{k+1}}\int_{z_j}^{z_{j+1}}\int_{r_i}^{r_{i+1}} r\frac{\partial \rho}{\partial t}drdzdt = \tag{3.1}$$

$$-\int_{t_k}^{t_{k+1}}\int_{z_j}^{z_{j+1}}\int_{r_i}^{r_{i+1}} r\left[\frac{1}{r}\frac{\partial}{\partial r}(rv_r\rho)+\frac{\partial}{\partial z}(v_z\rho)\right]drdzdt$$

Doing the exact integrals:

$$\int_{z_j}^{z_{j+1}} \int_{r_i}^{r_{i+1}} r(\rho^{k+1} - \rho^k) dr dz = \tag{3.2}$$
$$- \int_{t_k}^{t_{k+1}} \int_{z_j}^{z_{j+1}} (r_{i+1} v_{ri+1} \rho_{i+1} - r_i v_{ri} \rho_i) dz dt$$
$$- \int_{t_k}^{t_{k+1}} \int_{r_i}^{r_{i+1}} r(v_{zj+1} \rho_{j+1} - v_{zj} \rho_j) dr dt$$

The remaining spatial integrations are simply volume-weighted means of the product of the velocity and the density. These are equal to the products of the means of the quantities to second order, i.e.,

$$\int_{z_i}^{z_{i+1}} \rho v_z dz / \Delta z = \left(\int_{z_i}^{z_{i+1}} \rho dz / \Delta z \right) \left(\int_{z_i}^{z_{i+1}} v_z dz / \Delta z \right) + O(\Delta\rho \Delta v_z).$$

In other words, the use of operator splitting is permitted if second-order accuracy is desired.

The two-dimensional equation for advection may now be expressed as two one-dimensional equations:

$$\rho^{k+1}_{i+1/2,j+1/2} = \rho^{k}_{i+1/2,j+1/2} \qquad \text{(radial)} \tag{3.3}$$
$$- \frac{1}{r_{i+1/2}} \left(r_{i+1} \bar{v}_{ri+1,j+1/2} \bar{\rho}_{i+1,j+1/2} - r_i \bar{v}_{ri,j+1/2} \bar{\rho}_{i,j+1/2} \right) \frac{\Delta t}{\Delta r}$$
$$+ O(\Delta r^2) + O(\Delta z^2)$$

$$\rho^{k+1}_{i+1/2,j+1/2} = \rho^{k}_{i+1/2,j+1/2} \qquad \text{(axial)} \tag{3.4}$$
$$- \left(\bar{v}_{zi+1/2,j+1} \bar{\rho}_{i+1/2,j+1} - \bar{v}_{zi+1/2,j} \bar{\rho}_{i+1/2,j} \right) \frac{\Delta t}{\Delta z}$$
$$+ O(\Delta r^2) + O(\Delta z^2)$$

where the barred quantities are determined at $t_{k+1/2}$ during the predictor step in the time integration, and the values of various quantities at intermediate positions $r_{i+1/2}$, etc., are determined by either averaging or some type of interpolation. The

formal calculation of flux terms at the cell boundaries and the use of mass density, momentum density, and total energy density insures enforcement of the physical conservation laws; such a formulation is referred to as conservative.

In order to improve the accuracy of the interpolation, and hopefully improve the stability of the model, a staggered grid was used. The following conserved quantities are centered near $(r_{i+1/2}, z_{j+1/2})$, where $x_{i+1/2} = (i+1/2)\Delta x$: density ρ, total energy density e, and magnetic field strength B. The derived quantities located at these points are: gas pressure p_g, sound speed c_s, and Alfven speed c_A. These quantities are referred to as scalar quantities, and the points in the grid where they are defined are called scalar nodes. Similarly, vector nodes are located near (r_i, z_j), where $x_i = i\Delta x$. Conserved vector quantities are radial momentum S_r and axial momentum S_z; the corresponding derived quantities are radial velocity v_r and axial velocity v_z. Tests of the algorithm using a one-dimensional Cartesian code indicated that shocks were sharper and had less overshoot when a staggered grid was used, and that rarefaction waves and contact discontinuities were more or less unchanged.

The interpolation used for a Cartesian grid is simply

$$\rho(z) \simeq \rho_{j+1/2} + \Delta\rho_{j+1/2}\frac{(z - z_{j+1/2})}{\Delta z} \tag{3.5}$$

However, if the interpolation for a radial grid in cylindrical coordinates is

$$\rho(r) \simeq \rho_{i+1/2} + \Delta\rho_{i+1/2}\frac{(r - r_{i+1/2})}{\Delta r} \tag{3.6}$$

then

$$\int_{r_i}^{r_{i+1/2}} r\left[\rho_{i+1/2} + \Delta\rho_{i+1/2}\frac{(r - r_{i+1/2})}{\Delta r}\right] dr = r_{i+1/2}\Delta r\rho_{i+1/2} + \frac{1}{12}\Delta r^2\Delta\rho_{i+1/2} \tag{3.7}$$

which is of second order if and only if $\Delta\rho/\rho \leq \Delta r/r$, and likewise for all other quantities.

3.1. Behavior Near the Axis

The symmetry axis requires special attention because of the large relative size of the gradients. Near $r = 0$, while $\Delta\rho \ll \rho$, note that $\Delta r \sim r$ and also $\Delta v_r \sim v_r$. Theoretically, no order of accuracy should be sufficient to model radial behavior of the flow near $r = 0$. In practice, reasonable results are obtained when radial terms of order Δx^2 are included, which implies ρ constant, p_g constant, and $v_r \propto r$. There are several ways to satisfy this condition near $r = 0$:

(1) Avoid the origin $r = 0$ by extrapolating the solution onto the origin, and only update the model for $r > r_0$, where $r_0 > \Delta r$. In fact, this is necessary to some extent for the radial momentum S_r to avoid a particular instability. However, such an interpolation in general fails to model oblique shocks near $r = 0$, and use of it should be minimized.

(2) Use the quantities rQ rather than Q for the interpolation. The linear estimate would then be $r\rho(r) \simeq r_{i+1/2}\rho_{i+1/2} + \Delta(r\rho)_{i+1/2}\frac{(r-r_{i+1/2})}{\Delta r}$. This effectively reduces the order of accuracy near the origin (i.e., for $v_r \propto r$, then $rv_r \propto r^2$, which cannot be fit properly by a linear distribution), and while this formally solves the integral, it fails to solve the problem.

(3) Use an offset linear distribution for the estimated quantity, with the offset determined so that ρ takes its volume-weighted mean value at the point offset from the cell center (fig. 1). The linear estimate is $\rho(r) \simeq \rho_{i+1/2} +$

$\Delta\rho_{i+1/2}\frac{(r-r_{i+1/2}+\sigma_{i+1/2}\Delta r)}{\Delta r}$. This retains the full accuracy of the linear approximation of the quantity itself, while eliminating the error at the origin. To calculate σ for both scalar and vector quantities, simply substitute the offset distribution for the centered distribution in equation 3.7 and select σ to eliminate the gradient term. This process gives:

$$\sigma_{i+1/2} = \frac{1}{12}\frac{\Delta r}{r_i + 1/2} \tag{3.8}$$

$$\sigma_i = \frac{1}{12}\frac{\Delta r}{r_i}, \qquad \text{for } i > 0 \tag{3.9}$$

$$\sigma_0 = \frac{1}{3} \tag{3.10}$$

In summary, the Lagrangian or advective terms are updated using equations (3.3) and (3.4), where quantities are estimated radially by:

$$Q(r) = \bar{Q}_{i+1/2} + \bar{\Delta}^{(r)}_{i+1/2}\frac{r - r_{i+1/2} - \sigma_{i+1/2}\Delta r}{\Delta r} \qquad \text{(scalar)(3.11)}$$

$$Q(r) = \bar{Q}_i + \bar{\Delta}^{(r)}_i\frac{r - r_i - \sigma_i\Delta r}{\Delta r} \qquad \text{(vector)(3.12)}$$

3.2. Force Terms

The force terms are of several different types, each of which must be properly integrated in terms of the appropriate linear distribution. The derivations will be done in terms of the radial interpolation; similar results are found for the axial case by taking the limit $\sigma \to 0$. The integrations will be written in terms of vector cells; application to the scalar cells is trivial.

In terms of notation, let A_i be the value of A at the zone center (not the offset position), and let $\bar{A}_i$ be the mean value, which is offset from the center for the

radial case. These values are related by $A_i = \bar{A}_i - \sigma_i \Delta A_i$. Define $x \equiv \frac{r-r_i}{\Delta r}$ for convenience.

There are four possible integration terms involving only one quantity. The integral over r times the quantity itself is, by definition, the mean value times the volume element:

$$\int_{r_{i-1/2}}^{r_{i+1/2}} rAdr = r_i \bar{A}_i \Delta r \tag{3.13}$$

In contrast, the integral over the quantity is simply the value of the quantity at the grid center times the grid spacing:

$$\int_{r_{i-1/2}}^{r_{i+1/2}} Adr = A_i \Delta r \tag{3.14}$$

Due to the use of a linear interpolation, the direct and volume weighted integrals of the gradient are similar:

$$\int_{r_{i-1/2}}^{r_{i+1/2}} r\frac{\partial A}{\partial r} dr = r_i (A_{i+1/2} - A_{i-1/2}) \tag{3.15}$$

$$\int_{r_{i-1/2}}^{r_{i+1/2}} \frac{\partial A}{\partial r} dr = A_{i+1/2} - A_{i-1/2} \tag{3.16}$$

There are a number of possible integration terms involving two quantities. These require somewhat more care to calculate than for the single quantity, because of the products of the offset and the gradients with the mean values of the quantities.

The integral for fluxlike terms is exact:

$$\int_{r_{i-1/2}}^{r_{i+1/2}} \frac{\partial}{\partial r}(rAB) dr = r_{i+1/2} A_{i+1/2} B_{i+1/2} - r_{i-1/2} A_{i-1/2} B_{i-1/2} \tag{3.17}.$$

If the radius r is taken out of the differentiation, then the results are the same to second order, but there is a correction to second order which can become

significant near $r = 0$:

$$\int_{r_{i-1/2}}^{r_{i+1/2}} r\frac{\partial}{\partial r}(AB)dr$$

$$\simeq \int_{1/2}^{1/2}(r_i + x\Delta r)\frac{\partial}{\partial x}\left\{[\bar{A}_i + (x-\sigma_i)\bar{\Delta}A_i][\bar{B}_i + (x-\sigma_i)\bar{\Delta}B_i]\right\}dx$$

$$= r_i(\bar{A}_i\bar{\Delta}B_i - \bar{B}_i\bar{\Delta}A_i)$$

$$= r_i(A_i\bar{\Delta}B_i - \sigma_i\bar{\Delta}A_i\bar{\Delta}B_i + B_i\bar{\Delta}A_i - \sigma_i\bar{\Delta}A_i\bar{\Delta}B_i)$$

$$= r_i(A_{i+1/2}B_{i+1/2} - A_{i-1/2}B_{i-1/2} - 2\sigma_i\bar{\Delta}A_i\bar{\Delta}B_i), \tag{3.18}$$

where the approximations

$$\bar{\Delta}A_i \simeq A_{i+1/2} - A_{i-1/2};$$

$$A_i \simeq \frac{A_{i-1/2} + A_{i+1/2}}{2}$$

are applied to simplify the mixed product terms.

The magnetic tension terms in particular take the form:

$$\int_{r_{i-1/2}}^{r_{1+1/2}} ABdr \simeq \int_{-1/2}^{1/2}[\bar{A}_i + (x-\sigma_i)\bar{\Delta}A_i][\bar{B}_i + (x-\sigma_i)\bar{\Delta}B_i)dx\Delta x$$

$$= A_iB_i + \frac{1}{12}\bar{\Delta}A_i\bar{\Delta}B_i; \tag{3.19}$$

the gradient term is in general significant only near the origin and only for those quantities which tend to zero for $r \to 0$, since it is of second order.

The form of the terms which describe the effects of field twisting is included here for completeness; it does not occur when $B_z = B_r = v_\phi = 0$:

$$\int_{r_{i-1/2}}^{r_{i+1/2}} rA\frac{\partial B}{\partial r}dr \simeq \int_{-1/2}^{1/2}(r_i + \Delta r)[\bar{A}_i + (x-\sigma_i)\bar{\Delta}A_i]\bar{\Delta}B_i dx$$

$$= r_i\bar{A}_i\bar{\Delta}B_i \tag{3.20}$$

All of the above terms are accurate to at least second order, and are stable in the body of the grid. The difference equations themselves are constructed by substituting the appropriate quantities into the appropriate integrals and substituting into equations (2.14) to (2.22).

4. Implementation

The code in its present form utilizes the difference equations derived above, which are solved on a staggered grid in cylindrical coordinates assuming axisymmetry. The quantities ρ, e, and B_ϕ are updated at scalar nodes; the momenta are calculated at vector nodes. Angular momentum and poloidal magnetic field are set to zero at present. The remaining questions to be dealt with at this stage are the stability of the algorithm, especially along the axis $r = 0$, and what to use for the gradient. Several test problems for both Cartesian and cylindrical coordinates were used to investigate possible difficulties with the algorithm and to determine which form of the gradient would give the best results. The accuracy of the code was considerably improved, especially for more complex models with shocks (*cf.*, Sod 1978), by the use of a monotone gradient (*cf.*, van Leer 1974; van Leer 1977, van Leer 1979), although the precise implementation of monotonicity used was not critical.

Monotonicity refers to the order of the magnitudes of the values of a quantity at adjacent points in the computational grid, e.g., $Q_{i-1} < Q_i < Q_{i+1}$ is monotone increasing in Q. A monotone gradient is one which preserves this order for pure advection, such that, if $Q(x - \Delta x, t) < Q(x, t) < Q(x + \Delta x, t)$, then $Q(x - \Delta x + v\Delta t, t + \Delta t) < Q(x + v\Delta t, t + \Delta t) < Q(x + \Delta x + v\Delta t, t + \Delta t)$ for a constant speed v. The consequence is, that the advection remains stable even for very steep gradients, since no cell is excessively evacuated to the point where it can set up numerical oscillations on the scale of a grid spacing. This is implemented by selecting a gradient such that the values of the quantity extrapolated to the cell boundaries are between the value at the cell center and the values at the adjacent cell centers except at an extremum; that is, $Q_{i-1} < Q_i - \frac{1}{2}\bar{\Delta}Q_i < Q_{i+1}$ for a monotone increasing distribution. Clearly, this avoids the evacuation of a

cell, even for steep gradients, for Courant number less than 1. Several monotone gradients were tested; of these, the monotone gradient suggested by van Albada (van Albada *et al.* 1982), which allows for a non-zero gradient near extrema, and a simple monotone gradient suggested by van Leer (van Leer, 1977), which sets the gradient to zero near extrema, provided the best model results. We selected the van Leer version because of its use in similar codes, and because we were somewhat more familiar with it, although the tests suggested that the van Albada version preserved traveling localized extrema better.

The gradient used was:

$$\bar{\Delta}^{(r)}Q_i = \begin{cases} 2\dfrac{\left(\frac{\bar{Q}_{i+1}-\bar{Q}_i}{\bar{r}_{i+1}-\bar{r}_i}\right)\left(\frac{\bar{Q}_i-\bar{Q}_{i-1}}{\bar{r}_i-\bar{r}_{i-1}}\right)}{\left(\frac{\bar{Q}_{i+1}-\bar{Q}_i}{\bar{r}_{i+1}-\bar{r}_i}\right)+\left(\frac{\bar{Q}_i-\bar{Q}_{i-1}}{\bar{r}_i-\bar{r}_{i-1}}\right)}, & \text{if } (\bar{Q}_{i+1}-\bar{Q}_i)(\bar{Q}_i-\bar{Q}_{i-1})>0; \\ 0, & \text{otherwise.} \end{cases} \tag{4.1}$$

where $\bar{r}_i \equiv r_i + \sigma_i \Delta r$ is the location of the mean value of the quantity in the cell (for a Cartesian grid, $\sigma_i = 0$, and so $\bar{r}_i = r_i$ is the cell center). This generalization of the van Leer gradient was used to account for the uneven spacing of the quantities, under the conditions that a linear distribution should maintain a constant gradient with the gradient equal to the actual slope, and that monotonicity should be maintained. The only serious problem with this gradient is that it "clips" extrema. Clipping refers to the leveling off of advected localized ($\sim \Delta x$) maxima or minima, such that a sharp peak in the distribution will broaden out into a plateau as the distribution is transported even with a uniform velocity. Formally, the code reduces to first-order accuracy in the neighborhood of an extremum due to the vanishing of the gradient, producing considerable implicit numerical viscosity which causes diffusion of the quantity being advected. Because the effect is to increase the numerical viscosity at the extremum, this does not cause numerical instabilities at extrema.

The approximation of the distributions of the quantities with piecewise linear distributions can cause numerical instabilities to arise at the $r = 0$ boundary. This is caused because of the symmetry conditions which must be imposed along the axis for cylindrical symmetry. Those quantities which are antisymmetric about the $r = 0$ axis — radial and toroidal components of vectors and pseudovectors — are well approximated by a linear distribution near the axis. Unfortunately, the Taylor expansion for the symmetric quantities consists only of a constant and even powers of $r/\Delta r$ near the axis. In the body of the grid, this is identified with the clipping of extrema, and leads to diffusion but not instability. On the axis, however, this causes a systematic overestimate of the pressure for the total energy formulation of the difference equations. Since the error is systematic and fixed in position, it can build up even though the code is not formally unstable for outflow. A similar problem arises in the estimation of the magnetic force terms nears the axis; like p_g, p_m is quadratic near the origin, and, although it is possible in this case to impose the condition $p_m(r = 0) = 0$, the error in the magnitude of the force term arises from the assumption that the distribution is linear rather than quadratic when integrating the force terms.

Radial inflow near the origin is unstable because of the use of a staggered grid. If the grid is staggered with the boundary of the innermost vector cell inside the boundary of the innermost scalar cell, this can excite a inflow instability for radial flow outwards. To see this, consider that the pressure is derived from the total energy by $p_g = (\gamma-1)(e-\frac{1}{2}S^2/\rho)$, and the radial velocity is derived from the radial momentum by $v_r = S_r/\rho$. If S_r is negative and is perturbed so as to increase in magnitude, then the increase in S^2 will cause the gas pressure p_g to decrease, which makes the radial momentum force term more negative. If this occurs at $r = 0$, where p_g is already underestimated and there is no flux at the inner boundary,

then there is nothing to counteract this increasingly negative pressure gradient except for inflow from the upper zone boundary. Because the outer boundary of the innermost vector cell is inside the outer boundary of the innermost scalar cell, then the advection of negative radial momentum inwards will exceed the advection of total energy inwards, causing the pressure to decrease even more and accelerate the flow inwards. The initial buildup of negative momentum required to reach the threshold for this instability can be caused by an inward moving nonlinear wave; the clipping of the pressure extremum near the axis reduces the pressure gradient which would reverse such a wave before it could build up the radial momentum to the instability threshold. The solution is twofold: the radial gas and magnetic pressure gradients along the axis must be calculated using quadratic distributions rather than piecewise linear distributions, and the innermost vector cell should extend from $r = 0$ to $r = \frac{3}{2}\Delta r$, using a higher order interpolation to find S_r and S_z for the calculation of the pressure near $r = \frac{1}{2}\Delta r$. The change in cell boundary guarantees that the innermost scalar cell boundary is inside the innermost vector cell boundary, so that the pressure can build up more quickly than negative radial momentum and oppose the inflow instability. The higher order approximations for the pressures are required to model the first non-constant terms in the pressures, from which the lowest order force terms are derived. The change in cell boundary has an additional minor advantage; if the innermost vector zone center is designated $r_1 = \Delta r$ and the interpolation to $r = \frac{1}{2}\Delta r$ is designated r_0, then $\sigma_1 = 0$ and σ_0 is arbitrary. This can be used to minimize the size of formal correction terms arising from the use of cylindrical coordinates.

The equation for the innermost vector cells is calculated by a straightforward integration of the equations of motion, using the interval in $x \equiv r/\Delta r$ from 0 to

$\frac{3}{2}$:

$$\begin{aligned}\int_0^{\frac{3}{2}} x\Delta r(\bar{S}^*_{r1} - \bar{S}_{r1})dx\frac{\Delta r}{\Delta t} = &- r_{\frac{3}{2}}v_{r\frac{3}{2}}S_{r\frac{3}{2}} \qquad \text{(advection)} \\ &- \int_0^{\frac{3}{2}} x\frac{\partial p_g}{\partial x}dx\Delta r \qquad \text{(gas pressure)} \\ &- \int_0^{\frac{3}{2}} x\frac{\partial}{\partial x}\frac{B_\phi^2}{8\pi}dx\Delta r \qquad \text{(magnetic pressure)} \\ &- \int_0^{\frac{3}{2}} \frac{B_\phi^2}{4\pi}dx\Delta r \qquad \text{(magnetic tension)}\end{aligned} \tag{4.2}$$

Let $S_r(x) = \bar{S}_{r1} + (x - \sigma_1)\Delta^r\bar{S}_{r1} + O(\Delta r^3)(\sigma_1 = 0)$. This fit is good to second order because the radial momentum is antisymmetric about the symmetry axis, and therefore only odd powers are allowed in the Taylor expansion about $r = 0$. The integration simply gives the mean value for the radial momentum density times a volume adjustment of $\frac{8}{9}$, which gives:

$$\begin{aligned}\bar{S}^*_{r1} = S_{r1} &- \frac{8}{9}r_{\frac{3}{2}}v_{r\frac{3}{2}}S_{r\frac{3}{2}}\frac{\Delta t}{\Delta r^2} \\ &- \frac{8}{9}\left[\int_0^{\frac{3}{2}} x\frac{\partial p_g}{\partial x}dx\Delta t + \int_0^{\frac{3}{2}} x\frac{\partial}{\partial x}\left(\frac{B_\phi^2}{8\pi}\right)dx\Delta t + \int_0^{\frac{3}{2}} \frac{B_\phi^2}{4\pi}dx\Delta t\right]\end{aligned} \tag{4.3}$$

The integration over the gas pressure is centered at the origin, and assumes that the gas pressure varies quadratically: $p_g(x) = p_{g0} + \bar{\Delta}^2 p_g x^2 + O(\Delta x^4)$. Since p_g is symmetric about the axis, there are no odd powers in the Taylor expansion, and so this estimate is good to third order. The quadratic is fit to the points $p_g(\frac{1}{2})$ and $p_g(\frac{3}{2})$, and the pressure equation integrated over this fit. The result is:

$$\frac{8}{9}\int_0^{\frac{3}{2}} x\frac{\partial p_g}{\partial x}dx = p_{g\frac{3}{2}} - p_{g\frac{1}{2}}. \tag{4.4}$$

The magnetic pressure and tension are both symmetric and go to zero at $r = 0$; this requires the use of the quartic fit $B_\phi^2(x) = \bar{\Delta}^2(B_\phi^2)x^2 + \bar{\Delta}^4(B_\phi^2)x^4 + O(\Delta x^6)$

because the Taylor expansion about the axis contains only odd terms, with two points at which the magnetic field is known. The fit is made to $B^2_\phi(\frac{1}{2})$ and $B^2_\phi(\frac{3}{2})$ and the magnetic equations are integrated using this fit. The result is:

$$\frac{8}{9}\int_0^{\frac{3}{2}}\left[x\frac{\partial}{\partial x}\left(\frac{B^2_\phi}{8\pi}\right)+\frac{B^2_\phi}{4\pi}\right]dx=\frac{1}{45}\left[\frac{81B^2_{\phi\frac{1}{2}}}{8\pi}+\frac{71B^2_{\phi\frac{3}{2}}}{8\pi}\right]. \tag{4.5}$$

The equation for updating S_{z1} is obtained from the equation for S_{z1} by setting the force terms to zero. The momentum equations in the innermost vector cell are therefore:

$$\bar{S}^*_{r1}=\bar{S}_{r1}-\frac{8}{9}r_{\frac{3}{2}}v_{r\frac{3}{2}}S_{r\frac{3}{2}}\frac{\Delta t}{\Delta r^2}-(p_{\frac{3}{2}}-p_{\frac{1}{2}})\frac{\Delta t}{\Delta r} \qquad \text{(radial)(4.6)}$$
$$-\frac{1}{45}\left(\frac{81B^2_{\frac{1}{2}}}{8\pi}+\frac{71B^2_{\frac{3}{2}}}{8\pi}\right)\frac{\Delta t}{\Delta r}$$

$$\bar{S}^*_{z1}=\bar{S}_{z1}-\frac{8}{9}r_{\frac{3}{2}}v_{r\frac{3}{2}}S_{z\frac{3}{2}}\frac{\Delta t}{\Delta r^2} \qquad \text{(axial)(4.7)}$$

There are three different ways to calculate $\bar{S}_{r0}$, which is located at $\bar{r}_0 = \sigma_0\Delta r = \frac{1}{2}\Delta r$:

(1) $\bar{S}_{r0}\simeq\frac{1}{2}\bar{S}_{r1}$.

This is a strictly linear approximation for S_r, where S_r is antisymmetric across the symmetry axis. Use of this linear approximation tends to allow the formation of anomalous pressure extrema near the axis, but without exciting the inflow instability.

(2) $S_r\simeq\Delta^{(1)}S_rx+\Delta^{(3)}S_rx^3$

A cubic fit to S_r is made using $\bar{S}_{r1}$ and $\bar{S}_{r\frac{3}{2}}$; $\bar{S}_{r0}$ is then extrapolated from this fit. This is not consistent with the assumption of a piecewise linear distribution, but does provide a good estimate of the gas pressure and has given good results

for a variety of models.

(3) Same as (2)

The distribution again is fit to $\bar{S}_{r\frac{3}{2}}$, but the volume-weighted mean of the distribution is fit to $\bar{S}_r1$, i.e., $\int_0^{\frac{3}{2}} x(\Delta^{(1)}S_r x + \Delta^{(3)}S_r x^3)dx = \bar{S}_{r1}$. The two cubic fits to S_r differ: for option two, the fit gives $\bar{S}_{r0} = \frac{4}{5}S_{r1} - \frac{1}{5}S_{r\frac{3}{2}}$, and for option three, it gives $\bar{S}_{r0} = \frac{10}{9}S_{r1} - \frac{11}{27}S_{r\frac{3}{2}}$.

Option three weights $S_{r\frac{3}{2}}$ more relative to S_{r1} than does option two, and so may be more sensitive to changes outside the innermost cell; for example, it may respond to incoming nonlinear waves before they have actually reached the axis to a greater extent than would option two. On the other hand, option three is more self-consistent. Option two was chosen with no very strong prejudice; both options do a good job of estimating the momentum near the origin, as evidenced by the calculated pressure. Neither seem to cause any anomalous transport.

The value for S_{z0} could be obtained either by a linear interpolation across the axis — which implies $S_{z0} = S_{z1}$ because it is symmetric across the origin — or by a quadratic interpolation across the axis. It was found necessary to avoid the quadratic interpolation, and to interpolate the axial velocity rather than calculate it from the density and the interpolated momentum, because of density undershoots on the axis near strong oblique shocks. The use of a quadratic approximation for the axial momentum caused a numerical instability, which evacuated the matter density from the innermost cells, to develop at a late time in the flow; it is not clear precisely what caused it, but the use of the linear approximation eliminated most of its effects. However, a residual density undershoot of 20% near the axis increased the on-axis velocity by 25%. This reduced the average timestep by 25%, which increased the computational time for a given running time – and the

expense of running the code — by 33%. An additional extrapolation, of the axial velocity, was then used, since the velocities one cell away from the axis were not affected. This improved the economics of running the code, and further reduced the density undershoot along the axis.

The problem of dealing with short-wavelength nonlinear incoming waves near the axis was handled in the same manner as in the rest of the grid: by the imposition of monotonicity. Without the explicit imposition of monotonicity, the momentum estimates, and hence the pressure, along the symmetry axis would be subject to large, short wavelength ($\sim$ one grid spacing) oscillations for strong incoming pressure/momentum waves. The monotonicity constraint is clearly satisfied for S_{z0} by $S_{z0} = S_{z1}$. However, the cubic fit is not inherently monotone, and so the actual value of $\bar{S}_{r0}$ is determined from $\bar{S}_{r0}^{fit}$ by:

$$\bar{S}_{r0}^{fit} = \frac{4}{5}S_{r1} - \frac{1}{5}S_{r\frac{3}{2}} \tag{4.8}$$

$$\bar{S}_{r0} = \begin{cases} 0, & \text{if } \mathrm{sign}(\bar{S}_{r0}^{fit}) \neq \mathrm{sign}(\bar{S}_{r1}); \\ \bar{S}_{r0}^{fit}, & \text{if } \mathrm{sign}(\bar{S}_{r0}^{fit}) = \mathrm{sign}(\bar{S}_{r1}) \text{ and } |\bar{S}_{r0}^{fit}| \leq |\bar{S}_{r1}|; \text{ and} \\ \bar{S}_{r1}, & \text{otherwise.} \end{cases} \tag{4.9}$$

and the value of $\bar{S}_{z0}$ by:

$$\bar{S}_{z0} = S_{z1} \tag{4.10}$$

where $\bar{r}_0 = \sigma_0 \Delta r$ is the point at which they are calculated.

This implementation of the basic algorithm successfully modeled all one and two-dimensional test problems at all points in the grid, including the origin. It introduced no anomalous axial or radial transport for unperturbed flow, and exhibited no signs of instability for large or small perturbations in the radial momentum density. A remaining difficulty is that there is a pressure undershoot at strong, unresolved shocks where there is a large gradient in the momentum parallel to the

shock. This error is inherent to the use of a total energy formulation for the difference equations. Since the undershoot only occurs near strong shocks or where the momentum gradients are large, the pressure in these regions is of little dynamical importance. Inasmuch as the pressure deficit does not appear to be advected away from these regions, this should not be a serious limitation when radiative losses are insignificant. If radiative losses were to be implemented, however, the lack of radiation from the undershoot could be significant.

5. Artificial Viscosity

All codes contain some sort of diffusion. Implicit viscosity, or numerical diffusion, is inherent in the algorithm used, and results in finite widths for shocks and the damping of numerical instabilities. If this is not sufficient to damp these instabilities, serious errors can develop in the vicinity of strong compressions, which may then propagate throughout the grid. Errors at strong compressions, such as shocks, can be reduced by distributing the compression over several additional grid zones. The simplest way to do this is by use of explicit artificial viscosity.

There exist several methods for adding artificial viscosity to stabilize numerical calculations. We use the method suggested by Lapidus (Lapidus 1967; von Neumann and Richtmyer 1950), in which the diffusion is calculated as an additional flux term. For a quantity Q_i, the viscosity term in the radial direction is given by:

$$\begin{aligned} D^{(r)}[Q_i] &= -\frac{\Delta t}{r_i \Delta r}\left(q^{(r)}_{i+\frac{1}{2}} - q^{(r)}_{i-\frac{1}{2}}\right) \\ q^{(r)}_{i+\frac{1}{2}} &= -\nu r_{i+\frac{1}{2}} \Delta f_{i+\frac{1}{2}} |\Delta v_{ri+\frac{1}{2}}| \end{aligned} \tag{5.1}$$

and the viscosity term in the axial direction is given by:

$$\begin{aligned} D^{(z)}[Q_j] &= -\frac{\Delta t}{\Delta z}\left(q^{(z)}_{j+\frac{1}{2}} - q^{(z)}_{j-\frac{1}{2}}\right) \\ q^{(z)}_{j+\frac{1}{2}} &= -\nu \Delta f_{j+\frac{1}{2}} |\Delta v_{zj+\frac{1}{2}}| \end{aligned} \tag{5.2}$$

where ν is the coefficient of artificial viscosity (typically chosen $\sim$ 1) and the artificial viscosity terms are simply added to the flux terms for the quantity Q.

This method of evaluating the artificial viscosity is conservative, in that it ensures global conservation of all updated quantities, and is significant near large velocity gradients. Because the total energy is updated in this code, the shock jump conditions are solved explicitly for all quantities. The resulting lack of shock

oscillations has so far allowed this code to model all flows attempted with no artificial viscosity added. When tests were run with and without artificial viscosity, the improvement in flow stability downstream from shocks was more than offset by the loss of resolution at the shock itself, and it was decided to run without artificial viscosity until it was clearly needed.

6. Boundary Conditions and Initialization

Numerical difference equations, like differential equations, require the specification of boundary conditions and initial conditions. All evolution of the model is done by solution of the difference equations relative to the constraints imposed at the boundaries. In this sense, there is no such thing as a "wrong" boundary condition (unless it is nonphysical); any physically realizable boundary condition allows the solution of a physically valid model. The question is, whether the boundary conditions chosen are appropriate for the intended calculation, and whether they are properly implemented. Boundary conditions which are improperly implemented usually set up a nonphysical situation which causes oscillations or instabilities which are quite obvious, and will incidentally mask much of the physically real behavior in the model. A physically real but inappropriate boundary condition will give a reasonable looking result, but may not solve the problem of interest. Errors in the selection of physically appropriate initial and boundary conditions may not be obvious, but will strongly effect the interpretation and physical implications of the model; errors in the implementation should be apparent at the time the model is initialized or soon after the beginning of model evolution.

Our program, FLOW, allows the solution of a number of test problems using a variety of boundary conditions, as well as a jet injected into an ambient medium and a smooth jet extending through the entire grid surrounded by an ambient medium. Each initial model is determined by parameters set by the user at the time of initialization, with the boundary conditions set independently at each edge. All initialization and boundary setting are done in independent subroutines for ease of debugging and modification.

There are eight separate subroutines for setting boundary conditions:

(1) Conditions along $r = 0$

(2) Conditions along $r = r_{max}$

(3) Conditions along $z = 0$

(4) Conditions along $z = z_{max}$

(5) Conditions at the corner $r = 0$, $z = 0$

(6) Conditions at the corner $r = r_{max}$, $z = 0$

(7) Conditions at the corner $r = 0$, $z = z_{max}$

(8) Conditions at the corner $r = r_{max}$, $z = z_{max}$

where the boundary setting at the corners was separated from the boundary setting at the edges to aid in adapting the code to a concurrent processor. It also allows more versatility in determining how the intersection of two different types of boundaries should behave.

6.1. Initial Conditions

The initial conditions fall into two categories: test problems and jets.

Test problems are used for debugging, code verification, and calibration. Both one and two-dimensional tests are used, with and without magnetic fields. They are intended to test every term in the difference equations as independently as possible, so that errors can be quickly isolated.

(1) Constant Advection

All quantities are initialized to be constant, so that the model is of a uniform flow of a uniform medium. This is a very elementary test of advection. Note that, since $\lim_{r \to 0} v_r = 0$, this model can only be used to test axial flow.

(2) Constant Pressure Gradient

All quantities are set constant except for the pressure, which increases linearly with axial position. Since the velocity gradient is zero, this can only be used to test the axial gas pressure force.

(3) Constant Velocity Gradient

All quantities are set constant except for the velocity, which is proportional to position in the grid. This model can be used to test either radial or axial advection, and the two-dimensional version can be used to test spherical flow. Since pressure is set constant, this is a pure test of advection. Magnetic pressure gradients can be added to test the magnetic force terms.

(4) Self-Similar MHD with gradients

Both pressure and density are allowed to vary in this model, and so there is a gas pressure force. Once advection has been tested, this can be used to test the gas pressure force terms.

(5) Shock Tubes

Shock tube profiles, and in particular the shock tube problem used by Sod (Sod 1978), test the ability of the code to model shocks, rarefactions, and contact discontinuities. It does not isolate any terms, but is useful for finding errors at shocks and contact discontinuities.

(6) Jets

Jets are used both for testing and for calculations. There are two types of jet models. One model is a jet extending the length of the grid axially, allowing only radial variations in the jet quantities. This can be used to examine the evolution of instability modes (Hardee 1984; Payne and Cohn 1985). The other model is a jet which is injected into an ambient medium at $z = 0$, and is useful for comparing code calculations with experiment (Norman *et al.* 1982a; Ladenburg *et al.* 1949). A wide variety of parameters can be used to control the values and profiles of dynamically important quantities describing the jets. The magnetic boundary conditions allow injection into unmagnetized and magnetized external media, in

which the return current can be distributed within the jet or concentrated on the boundary.

6.2. Boundary Conditions

The boundary conditions are set independently for each boundary to allow the maximum versatility in setting up models. There are three different classes of boundary: the symmetry axis, at $r = 0$; the base of the grid, at $z = 0$; and the outer edges of the grid, at $r = r_{max}$ and $z = z_{max}$.

(1) Inner Radial Boundary ($r = 0$)

All scalars and axial components of vectors and pseudovectors are symmetric ($Q(-r) = Q(r)$) and all radial or toroidal components of vectors and pseudovectors are antisymmetric ($Q(-r) = -Q(r)$) at $r = 0$, where antisymmetry and symmetry are determined in the Cartesian sense by reflecting the quantities through the origin across a plane passing through the origin. In this way, radial and toroidal components of vectors and pseudovectors are required to take the value zero along the symmetry axis and reverse direction in a Cartesian sense upon reflection through the origin, and all quantities are required to have the same magnitude at a given distance from the origin. This is not so much of a boundary condition as a geometric constraint; in terms of the theory of partial differential equations, the symmetric boundary conditions impose a Neumann condition by requiring that the derivative be zero on the symmetry axis, whereas the antisymmetric boundary conditions impose a Dirichlet condition by requiring that the value of the quantity be zero at the symmetry axis.

(2) Edge Boundaries (Common to $z = 0$, $z = z_{max}$, and $r = r_{max}$)

There are a number of boundary conditions at the edges of the grid which are common to all three edges. They are:

(A) One-point extrapolation. The values of all quantities are assumed to be constant across the boundary, i.e., all derivatives are zero.

(B) Two-point extrapolation. The values of all quantities are assumed to be linear across the boundary, i.e., all second derivatives are zero.

(C) Three-point extrapolation. The values of all quantities are assumed to be quadratic across the boundary, i.e., all third derivatives are zero.

(D) Advective outflow. The values of all quantities except the velocity component perpendicular to the boundary are assumed to be constant across the boundary, i.e., all derivatives are zero. The velocity component perpendicular to the boundary is equal to the velocity component one zone inside the grid if it causes flow out of the grid, but is set to zero if it would cause flow into the grid. Thus, no material is allowed to flow into the grid through the boundaries (Wilson and Falle 1985) (fig. 2).

(3) Axial Boundaries (Common to $z = 0$ and $z = z_{max}$)

The only boundary condition which is common only to the axial boundaries is the periodic boundary condition, in which it is assumed that the flow is periodic, with the "wavelength" equal to the length of the grid. For consistency, periodic conditions must be specified at both $z = 0$ and $z = z_{max}$.

(4) Inner Axial Boundary ($z = 0$)

There are two boundary conditions which are unique to the inner axial boundary: reflection and injection.

(A) Reflection. All scalars and radial or toroidal components of vectors and pseudovectors are symmetric ($Q(-z) = Q(z)$), and all axial components of vectors and pseudovectors are antisymmetric ($Q(-z) = -Q(z)$) at $z = 0$. This would model the behavior of a flow in which there was a plane of symmetry, such as a blast wave.

(B) Injection. Quantities inside of the injection region ($r \leq r_{jet}$) are set according to the jet parameters; quantities outside the jet are set equal to the value of the quantity at the edge of the grid, with the axial velocity limited to outflow only. The jets used assume uniform density and momentum density. The pressure is uniform for unmagnetized jets, but varies for magnetized jets so that the net force at any point within the jet is zero. Two different magnetic profiles are allowed. In the first case, the magnetic field inside the jet increases linearly out to the jet radius, at which point it either vanishes or falls off as $1/r$; the return current is allowed to flow outside of the jet. In the second case, the magnetic profile causes the current to flow inside the jet itself; in essence, the return current is restricted to inside the jet. The pressure profile also varies between models. One of the models in the case of the linear magnetic field and the only model for the case which sets up a volume return current within the jet balance the forces within the jet and at the boundary of the jet, so that there are no net forces anywhere. One of the disadvantages of this for the linear gradient is that it restricts the initial gas pressure at the center of the jet to twice the pressure of the ambient medium. The two other pressure profiles allow an arbitrarily large central gas pressure in the jet; one balances forces within the jet, and the other puts in a zero gradient for the pressure, resulting in a net inward force.

(5) Outer Boundaries (Common to $r = r_{max}$ and $z = z_{max}$)

The only boundary condition which is common only to the outer boundaries is the damping boundary condition. The values of all quantities except the velocity component perpendicular to the boundary are assumed to be constant across the boundary, i.e., all derivatives are zero. The velocity component perpendicular to the boundary is set according to the sound speed so as to damp out any incoming waves, $v_z(z_{max}) = c_s^2/|v_z(z_{max} - \Delta z)|$ (Wilson and Falle, 1985). The advective

conditions were found to be more effective at reducing wave reflection back into the grid, so this condition is rarely used.

Ideally, there would be no need for any outer boundary conditions; one would simply expand the grid until the calculation was finished. This is impossibly expensive in terms of CPU usage and processor memory required, so boundary conditions are needed which allow waves to pass out of the grid with minimal reflection without injecting any additional mass, energy, or momentum into the grid. Even weak reflections can be serious, especially in cylindrical symmetry; the energy density u_{edge} of a wave reflected from $r = r_{max}$ with width δr_{max} will increase to $u_{jet} = u_{edge}(r_{max}/r_{jet})(\delta r_{max}/\delta r_{jet})$ at the surface of the jet. Even if the wave does not steepen, the energy density will still increase inversely with radius; even if this does not increase the energy density to that inside the jet, it may still be sufficient to excite or damp out disturbances. An early attempt to model an overpressured, overdense jet was thwarted in just this way, by a reflected wave disrupting cocoon formation and subsequent development of a triple shock.

6.3. Implementation of Boundary Conditions

The boundary conditions were implemented with the goals of simplicity, consistency, monotonicity, and stability. These goals are all tied together, e.g., a monotonic boundary is more likely to be stable. However, they all must be kept in mind if the boundary condition is to be easily understood and accurately implemented.

Simplicity is one of the most basic goals for any aspect of computing. A simple algorithm is generally faster, easier to implement, easier to debug, and more reliable overall than a complicated algorithm. Simple boundary conditions are physically desirable because they are easier to understand and hence interpret

than more complicated conditions. Very simple input jets lead to very complicated flows; if the input jet is kept simple, it is apparent that the complex structure in the jet is due to the basic dynamics of jets, rather than something unusual in the jet itself. In short, simple input models are easier to implement, easier to understand, easier to justify, and easier to generalize from than are more complicated input models.

Consistency is also important, although it is not always clear how to be consistent. Algorithmic consistency is fairly easy to attain; for example, a boundary condition in which material is injected into a cell which is limited to outflow only will cause a very obvious pileup of material in that cell, and it will be clear that there is a problem and how to solve it. Physical consistency is more difficult. It is often impossible to make everything consistent at the same time, so it is important to determine what is really basic to the flow. Our method has been to select a physical model and integrate the conserved quantities over each grid zone to determine how much of each conserved quantity to put into each cell, and then to select the derived quantities (*e.g.*, velocity) to give the correct flux at the cell boundaries. In short, our input jets have the correct amount of material within each cell, and inject the correct amount of flux into the grid.

Monotonicity will almost always result if the model is simple and physically consistent, but if there are large discontinuities on a staggered grid, problems can arise. Large spikes and dips in or near the boundaries should be eliminated at all costs, because they often lead to instabilities which disrupt the flow. Even if they are not unstable, they are almost always advected downstream where they then distort the rest of the flow. Earlier versions of the injection boundary conditions had to be adjusted to impose monotonicity in the velocity and pressure; setting the derived quantities so as to make fluxes physically consistent solved this problem.

Stability generally follows if the model is kept simple, consistent, and monotonic, and a problem with stability (e.g., pressure going to zero, density undershooting at the edge of the jet) usually indicates a problem in some other area as well. Stability problems tend to occur near large discontinuities, and are best solved by carefully considering exactly what should be physically occurring in such a region and setting up the boundary conditions to do it. Sometimes, however, there is a trade-off. For example, at the $z = 0$ boundary, the axial velocity outside the jet region was originally calculated using the velocity one zone in, as for the outer boundaries, to reduce any reflections. This caused a severe instability at the edge of the jet, which was solved by calculating the velocity from the nearest neighbors and imposing outflow boundary conditions. The edge of the jet nozzle is by far the hardest place to make boundary conditions work; once they work there, it is almost certain that they will work everywhere else.

7. Program Structure: The User Interface

The program which runs the numerical MHD evolution code, operates I/O for saving and restarting models, and provides a reasonably user-friendly interface is called FLOW. It was designed to be highly transportable, but optimized in particular for vector machines (such as the Cray family). The subset of FORTRAN/77 in which it was written is commonly available on the Ridge, VAX, Sun, and Cray families of computers, with all machine-dependence isolated into functions and subroutines kept in special libraries for each machine. All globally used variables are kept in COMMON, with array sizes and parameter lists defined in such a way that any changes in the parameter list or the maximum grid size require modifications in at most two well-defined locations. The non-implementation of INCLUDE statements and the use of dropfiles by CFT under the CTSS operating system is remedied by the use of a stream-editor command procedure acting on the standard source code. On all machines used so far, FLOW either operates exactly the same way as on the "standard" machine (Ridge) or prints out a concise message explaining why it does not behave the same as the "baseline".

The driver and the input and output packages are all menu-driven with on-line help, which gives the names of the tasks and their functions. The driver contains tasks which initialize a given model, evolve a given model in time, extend or contract the grid (also done automatically in the evolution task), execute system commands, and exit from the program. Errors in use of the routines, or attempts to use tasks which are not supported on that particular computer, are indicated by error messages.

The input package allows the input, output, and modification of lists of parameters which describe the model being run and the operating environment of

the program (such as the plotting window, output file names, etc.). The parameters can be listed individually, as groups, or all together. The input package also allows the input of previously run models which have been stored on disk, either for plotting or for continuing the calculation.

The output package allows the results of a calculation to be stored on disk in either formatted or unformatted form; such storage is also done periodically within the time evolution task. The output option also allows various quantities derived from the results of the calculations to be printed out, or displayed as graphs, contour plots, surface relief plots, greyscale plots, vector plots, or flow/field line plots.

A great time of effort has been devoted to making this program user-friendly, versatile, and convenient. This is especially true of the plotting package. Apart from cosmetics, there is a very good reason to make plotting fast, convenient, and informative: in practice, the bottleneck in time is the user, not the computer. Good graphics saves user time by providing useful information in a clear, quickly understandable format. This is especially crucial for debugging; several serious errors discovered in this code were first noticed in one of the plots before being seen in the numbers. The surface relief plots proved to be particularly useful at making various errors and features apparent, as were plots of derived quantities such as the velocity divergence and the current density. It is worth the effort to develop a good driver and a complete, convenient graphics package; it saves a lot of time and confusion, and helps the user to avoid potentially disastrous errors.

8. Machine Dependence and Transportability

Transportability — the ability to move a program from one machine to another without making major or difficult changes to the code — is essential to program development unless it is absolutely certain that the program will only be run on one machine, and the use of nontransportable code will result in a substantial saving of CPU time. If a code is being developed on one machine for use on another, it is extremely important, for purposes of debugging and verification, that the differences between the codes on the two machines be minimized; errors in implementing machine-dependent code can easily appear to be due to an error in the algorithm. The use of identical code on different machines can also be used to isolate troublesome features in the operating system, compiler, or load libraries which would otherwise be attributed to a coding error.

The key to transportability is finding a common language subset for all of the machines the code will be running on. A useful approach is to write in some standardized language, such as ANSI standard FORTRAN 77, and choose some one machine to hold the "official" copy of this machine-independent code. The code can then be transported to all of the machines to be tested, and a list of required changes made for each machine. As many of these changes as possible should then be implemented in the official copy, which can then be run on all the machines, excepting changes required due to inconsistencies between the machine implementation of the language and the standard. This method guarantees common source code, and thus common algorithms and common results given well-designed compilers.

There will always be some machine-dependent code; for example, each computer will require different start-up routines and will have different plotting libraries. These can generally be isolated into subroutines and stored on each

computer. Since these subroutines almost always involve setting up the control environment for the program or plot libraries, they do not affect the calculational algorithm itself if they are isolated properly. Some required functions may be specific to individual machines, such as the Cray Conditional Vector Merge functions; these can be mimicked by user-defined functions when necessary, which are then kept on the individual machines. The final type of machine-dependent code is also the most troublesome, which is nonimplementation of standard features, or their implementation in a nonstandard way. The Cray FORTRAN compiler CFT under the operating system CTSS provides two excellent examples of this type of machine dependence: common text cannot be inserted via INCLUDE statements but by "cliches", and the STOP command must be replaced by CALL EXIT if any of the more useful debug and program continuation options are to be used. These can be treated by writing an editor command procedure which replaces all such occurrences with the required equivalent. If done properly, the process can be made sufficiently automatic and consistent so as to avoid the possibility of changing the algorithm between machines. As a general rule, to make code transportable, minimize and isolate machine-dependent code, and where the code must be changed between machines, automate the editing process.

One machine-dependent aspect which should never be minimized is vectorization. Vectorization means that the machine processes a vector or parts of a vector concurrently, provided that the vector is processed in an inner DO loop which does not contain any non-vectorizable commands. Calculations in the inner DO loop are not repeated so much as done simultaneously over the range of the DO loop. The program FLOW increased in speed by a factor of ten to fifteen as a result of vectorization, and the slowdown due to the use of a vectorizable algorithm is generally negligible on a scalar machine. In fact, almost any modularized or

structured code can be translated directly into a vectorized form, and structured coding practice is advisable apart from vectorization. Structured programming, in which the algorithm is implemented as smaller independent modules, increases ease of understanding and modifying the code for both the original programmer and future programmers. This also improves verification of the code, since the code can be debugged in simple isolated subsections and errors can be more easily isolated in a particular subsection. Any large code should be written in a structured way, and any code which is to be run on a vector machine should then be vectorized.

The vectorization of code is described in the NCAR CFT manual (McArthur 1984); here are examples of (a) unstructured code, (b) structured code, and (c) vectorized code. In these examples, the array elements V(IR,IZ) are set equal to Q(IR,IZ)/R(IR,IZ) if Q(IR,IZ) is greater than zero, and are set equal to F(IR,IZ) otherwise.

(a) UNSTRUCTURED

```
      DO 1030 IR = 1, 10
        DO 1020 IZ = 1, 10
          IRT = IR
          IZT = IZ
          IF ( Q(IR,IZ) .LE. 0.)  GO TO 40
   10     CONTINUE
          V(IR,IZ) = Q(IR,IZ)/R(IR,IZ)
 1020   CONTINUE
 1030 CONTINUE
      GO TO 50
   40 V(IRT,IZT) = F(IRT,IZT)
```

```
      GO TO 10
   50 CONTINUE
```

The jump out of the DO loop is clumsy and confusing, could easily be overlooked, and may transfer control almost anywhere should an error be made in typing or assigning statement numbers.

(a) STRUCTURED

```
      DO 1030 IR = 1, 10
        DO 1020 IZ = 1, 10
          IF ( Q(IR,IZ) .LE. 0.)  THEN
            V(IR,IZ) = F(IR,IZ)
          ELSE
            V(IR,IZ) = Q(IR,IZ)/R(IR,IZ)
          END IF
 1020   CONTINUE
 1030 CONTINUE
```

The task here is clearly isolated, and the logic of the algorithm is clear. An error would be easily isolated and fixed, and any modifications could be easily and confidently implemented.

(c) VECTORIZED

```
      DO 1030 IR = 1, 10
        DO 1020 IZ = 1, 10
          V(IR,IZ) = CVMGP(Q(IR,IZ)/R(IR,IZ), F(IR,IZ), Q(IR,IZ))
 1020   CONTINUE
 1030 CONTINUE
```

The CVMGP function does exactly the same thing as the BLOCK IF statement, but manipulates vectors rather than individual array elements. Note that it the

algorithm did not change between the structured and vectorized examples; in fact, our practice was to use the vectorized version and write a user-defined CVMGP function for use on non-vector machines. A code which is already properly structured can almost always be vectorized by changing BLOCK IF statements to one or more conditional vector merge functions with no change in the algorithm. The difficult part of vectorization is making certain that the code is properly structured; after that, the details of translating scalar functions into vectorized functions is tedious but straightforward.

9. Discussion and Future Development

FLOW is a user-friendly, menu driven program based on a 2-D axisymmetric upwind differenced monotone MHD code to study the evolution of hydrodynamic and magnetohydrodynamic jets. A modified predictor-corrector algorithm is used to achieve second-order accuracy in time, and a monotone upwind differencing scheme (van Leer 1974; van Leer 1977; van Leer 1979) assuming an offset linear extrapolation within cells to achieve second-order accuracy in space. The primary quantities (which are updated) are matter density, radial and axial momenta, total energy density, and toroidal magnetic field strength. Quantities within cells are allowed to mix freely (no interface tracking), and explicit artificial viscosity is implemented using the method of Lapidus (Lapidus 1967; von Neumann and Richtmyer 1950), although it has so far proven unnecessary to use it. A variety of test problems and jet profiles can be selected, as well as boundary conditions at each the grid edge.

9.1. Comparison with Previous Codes

Four major codes used to model astrophysical jets are those of

(1) Williams and Gull (Williams and Gull 1984; Williams and Gull 1985),

(2) Wilson and Falle (Wilson and Falle 1985),

(3) Norman (Norman *et al.* 1982a; Norman *et al.* 1982b; Norman *et al.* 1984; Clarke *et al.* 1986), and

(4) Woodward (Colella and Woodward 1984),

and the theoretical work of van Leer (van Leer 1974; van Leer 1977; van Leer 1979) upon which at least two of these codes are based. All of the codes except for Woodward's Piecewise Parabolic Method, or PPM (4) are second-order in space and time; PPM is third order. None of them use a predictor-corrector method for

second-order accuracy in time, but instead use a single pass which is second order in the local Courant number. None of them utilized an offset linear approximation to deal with the volume element in a cylindrical coordinate system. All of these codes evolve the internal energy rather than the total energy.

The predictor-corrector method in FLOW uses a double time pass to calculate second-order accurate time derivatives, whereas the other programs use a single pass which is second order in the local Courant number (advection velocity) (van Leer 1977). Early trials with the FLOW algorithm found that either method gave good results, even in the presence of steep gradients, but that the double time pass was slightly faster and could give somewhat more stable results in some situations.

The offset linear distribution near the symmetry axis was used so that the metric terms could be accounted for in the interpolation without using the metric times the quantity in the linear interpolation. This gives excellent results near the origin, even for long-term radial outflows, but does not make very much difference more than a few grid zones from the axis (results differ by less than a percent for $r > 5\Delta r$ or so). The need for an offset linear distribution can be avoided by using very many resolution elements across the jet (2), working in three dimensions on a Cartesian grid (1), or avoiding evolution near the axis by interpolating all quantities into the center. Errors due to improper treatment of the symmetry axis are considerable only near the axis and where there is rapid or persistent radial flow, but if the axial flow is either stagnated or fairly constant with radius, they can build up and distort the flow field, and so cannot be neglected.

The use of total rather than internal energy guarantees the accurate modeling of shocks with no explicit artificial viscosity. However, the pressure must be determined by subtracting the kinetic from the total energy, and if the flow is strongly momentum dominated at that point, the pressure is likely to be underestimated in

the vicinity of large gradients. In practice, serious pressure undershoots have only appeared upwind of strong shocks, and so have had no dynamical significance. In the case of radiation dominated flows, the undershoot in pressure would result in an underestimation of the radiation from that region, which could affect the dynamics. On the other hand, the use of internal energy generally requires that some artificial viscosity be introduced to reduce shock oscillations, which also has some dynamical effect. This particular feature has both advantages and disadvantages, and it is not clear which quantity results in the most accuracy and stability.

Each code has its merits and its problems. The FLIC code (1) and the multigridded FLIC code (2) are based on the oldest algorithm (Gentry *et al.* 1966). They are diffusive, which makes it necessary to use a relatively fine grid to deal with turbulence and instabilities, but the algorithm is well understood and relatively fast. Even when run on a coarse grid, it is more than adequate to determine global properties and delineate large structures where large scale turbulence does not dominate, it is extremely reliable in terms of interpreting the structure in the calculation, can be quickly coded, debugged, and verified, and reasonable models can be run on a normal mainframe. It is an excellent exploratory code, and is particularly useful for testing out simple hypotheses regarding global properties of supersonic jets, and is accessible to investigators at all levels of computing experience. The multigridding algorithm makes the code more complicated and hence less accessible, but makes it possible to do finely gridded calculations in a reasonable time and thereby calculate more detailed flow structure.

The hydrodynamic and magnetohydrodynamic codes of Norman and his collaborators (3) are very similar to FLOW in accuracy, although they do not use a predictor-corrector algorithm, an offset linear distribution, or total energy updating. The advection in this code is based on conservation of matter and of the

specific density of other properties. This method, called specific advection, considers the matter density flux as the primary advective quantity, and calculates the remaining fluxes by multiplying the matter density flux by the specific density in the cell of origin. This method deals particularly well with isentropic flows, and calculations demonstrate that it is also effective at handling shocks. In the case of strong shocks, where the shock gradient is much larger than any surrounding gradients, the consistent advective flux should reduce to the standard conservative advective flux. In fact, consistent advection should only run into difficulties if there are large gradients within cells, in which case the preceding argument regarding shocks should apply, and the gradient will simply be resolved into two cells. Since all codes have some level of this "shock smearing" due to implicit viscosity — which also reduces oscillations near large gradients — this is not a serious problem. It appears that consistent advection is capable of handling momentum-dominated flows, and should be particularly useful for calculating radiative flows, in which the specific internal energy is dynamically dominant.

A unique feature of the above code among astrophysical jet codes is the use of interface tracking. Interface tracking minimizes the diffusion of contact discontinuities by estimating their positions within cells and treating advective and force terms as if the interface were an impermeable membrane. The technical advantage is, that it can model and track small isolated regions of entrained material without diffusing them into the surrounding flow, and can trace out small structure along the edge of the jet where Kelvin-Helmholtz instabilities develop. Practically, it is easy to trace the jet and ambient material, since they are treated as different quantities. The technical advantage is greatest, however, when the jet is poorly resolved; while interface tracking clearly improves structural resolution for poorly resolved jets, doubling the resolution has at least as great an effect (Norman and

Winkler 1985). Where the grid spacing is insufficient to resolve flow structure, interface tracking improves the calculation; where resolution is sufficient, this is questionable. Also, if jets undergo turbulent mixing on the scale of the grid spacing, it would be inappropriate to suppress this mixing through the use of interface tracking, and since the diffusive length scales in astrophysical jets are unknown, the use of interface tracking is not required scientifically. However, in the case of a relativistic flow, which is characterized by large gradients, interface tracking may be essential to maintain gradients at slip surfaces even on a fine grid.

Another feature of this code which minimizes diffusion and improves stability is monotonicity (van Leer 1974; van Leer 1977; van Leer 1979), which is also used in FLOW and PPM (4). By minimizing spatial oscillations due to overestimating advective fluxes, diffusion and oscillations at shocks, the working surface, and along the interface between the jet and cocoon were considerably reduced (Norman and Winkler 1985). However, while monotonicity reduces oscillations and diffusion across gradients, it reduces the order of accuracy of advection from second to first order at localized peaks and troughs in the distribution, and tends to diffuse these inherently non-monotonic features by clipping extrema in the distributions. Usually such features are noise, and it is desirable to eliminate them, but when these features are real, the code treats them as if they were noise. Given that distinguishing between extrema due to numerical noise and extrema due to "real" features would probably be computationally expensive, the diffusion of localized extrema is an acceptable price to pay for increased stability in the rest of the flow.

The most accurate — and complex — code of this collection is PPM (4). It is third-order accurate in space, with a Riemann solver to estimate advection in Cartesian coordinates, and sharpens contact discontinuities by tracing fluid flow back along characteristics and compensating for numerical diffusion at interfaces.

The calculations give flows with sharp, well-defined gradients and interfaces, with accurate modeling of large-scale vorticity and turbulence. The primary disadvantage is its complexity. The coding of a PPM code requires considerable expertise and time, and reduces its speed. However, the reduction in speed per cycle is mitigated by the increased accuracy, which allows the use of larger timesteps. If the time and expertise are available, this is the best code available for the modeling of astrophysical flows. The upgrade from unmagnetized flow to magnetized flow with toroidal field only should cause only minor modifications to the characteristic tracing, essentially the substitution of the magnetosonic velocity for the sound speed. The addition of poloidal field makes the wave speed anisotropic and greatly complicates the tracing of characteristics; the development of a PPM code for the fully magnetic jet would be very difficult, but not impossible, and should give very impressive results.

The codes presently used for the modeling of astrophysical jets vary in complexity, speed, and accuracy, with the more accurate code typically the more complex to code and the slowest to run. FLOW lies midpoint in this collection; it is more complex than FLIC (1), but considerably simpler than PPM (4), and lies somewhere near multigridded FLIC (2) and Norman's code (3). Each of these codes has its advantages, which define its best realm of application; FLOW is designed to provide reasonably accurate models of magnetized flows for the minimum investment of programming and CPU time.

9.2. Future Work

FLOW presently solves the time-explicit 2-D axisymmetric equations of perfect MHD with toroidal field only in a self-consistent, conservative manner. It can produce a wide variety of graphical output for the display and analysis of results.

It has demonstrates the ability to handle shocks with Mach numbers of order 10-100 with no difficulties other than a pressure undershoot at the base of the shock. Since the code appears to work for these cases, it is desirable to modify the basic algorithm to improve the code and apply it to new problems.

One area of interest is the display of results. Individual models reveal a number of interesting features, but it is often difficult to determine how they evolve. Two possibilities are, first, the use of false color to make it easier to perceive flow characteristics, and then the making of movies using the false color plots to show how the features in the flow evolve. This would be especially useful to do with the density, pressure, and magnetic field, since these are the most dynamically important scalar quantities. This would require the availability of large amounts of data storage space (preferably disk rather than tape), highly automated output routines, and a great deal of effort. However, it would aid in the physical understanding of the jet, and while it may be tedious, there is no real technical difficulty beyond the availability of computer resources.

The most important scientific upgrade is the addition of poloidal fields and angular momentum. This will take at least two steps to develop. First, the results of FLOW to date suggest that reorganization of the grid would improve stability near the axis and reduce diffusion due to averaging, as well as improve implementation of the boundary conditions. Since the addition of poloidal fields requires the updating of the vector potential and the subsequent determination of the radial and axial field from its derivatives, it would be wise to reorganize the grid so as to locate these derivatives, and the velocities, as close as possible to the appropriate grid boundaries. The details of this reorganization have already been determined, and it remains only to implement it for a flow with toroidal field only. Once this is shown to be working properly, then the additional fields and

momentum may be added. While the equations have already been worked out for the full MHD equations, the implementation and debugging are anticipated to take several months. In addition to ordered fields, it may be desirable to include tangled magnetic field (for which the equations have *not* been worked out), which would introduce a varying anisotropic pressure response to compression, rarefaction, and shearing.

Two quantities which have been neglected to this point are physical viscosity and finite conductivity. The addition of physical viscosity could be done immediately, as artificial viscosity is already implemented and the terms are very similar. The difficulty would lie in selecting a reasonable value for the coefficient of viscosity; the best guess anyone could make is that the viscosity is probably dominated by turbulence, with the details of this microturbulence totally unknown. A similar problem exists for finite conductivity; there is no difficulty in including a diffusion term proportional to $\nabla^2\vec{B}$ in the equations, but considerable difficulty in selecting an appropriate conductivity. This would also decouple the current from the magnetic field, and allow the generation of electric potentials and spatial charge densities from the Hall effect. This could eventually lead to a full plasma treatment of the flow, which would be required for solar wind modeling, and may eventually be desirable for modeling very hot magnetized winds from accretion disks. However, this is a drastic upgrade, and it is doubtful that any of these terms besides turbulent viscosity are dynamically significant in supersonic extragalactic radio jets.

Modeling bipolar outflows and the generation of jets from accretion disks would require including gravitational forces in some way. There are two possibilities. If the mass of the jet material is insignificant compared to the mass of the central object or disk, then the gravitational field can be closely approximated by a fixed

potential, and all that is required is that a gravitational force be assigned to each position in the grid at the beginning of the program. This addition should be trivial. On the other hand, if the dynamical material has significant self-gravity, then the alternatives are to either calculate the gravitational force on each cell using two-body interactions with every other grid cell, or calculate the gravitational potential by solving the Laplacian $\nabla^2\phi_g = 4\pi G\rho$ and taking the gradient. The latter is considerably faster and quite adequate so long as the gravitational field does not change too quickly, which it should not do if the pressure and magnetic terms dominate the dynamics. It is doubtful that self-gravitation will ever be significant in the models of interest, and the addition of a fixed potential term to the code is trivial.

The modeling of outflows from stars and disks may also require the use of different grid boundaries, which would require setting boundary conditions inside the present grid boundary. This would involve rewriting the boundary condition subroutines, and perhaps some adaptation of the integration routines. If the radius of the star is greater than one grid zone, boundary conditions on a hemispherical surface at the base of the grid, or on a spherical surface embedded somewhere along the axis, will have to be set. Likewise, if the disk is not infinitely thin, it may be necessary to set boundary conditions on a cylindrical surface. This would require considerable reorganization of the code. If the boundary surfaces vary considerably, then a number of versions of the boundary condition and integration routines may need to be developed, one for each type of grid. Each version would require considerable verification and testing. The reorganization of boundary conditions would be a moderately difficult task, and would be done after the upgrades to full MHD including all field and momentum terms.

Another possible addition to the code would be radiative terms, both for emission and absorption. If the material is assumed to be optically thin, then all that is required is to calculate the emission and absorption coefficients in each grid zone and determine the change in momentum and energy due to emission and absorption of radiation. The effects of a radiation from a central object or disk would be easy to calculate as well. Difficulties would arise if the optical depth began to approach unity, as absorption of self-radiation could then become dynamically significant within the jet, and the radiation field would be a function of the structure of the jet. Some consideration may also need to be given to light travel time along the jet, adding another characteristic velocity to the problem. Finally, any difficulties with the pressure must be solved, since emission and absorption are typically dependent on the pressure, especially in the case of synchrotron radiation. This may require that the internal energy be updated rather than the total energy.

The modeling of relativistic jets, or the modeling of jets near black holes, would require the addition of special and general relativity (Wilson 1972) This upgrade would almost certainly require the inclusion of radiation and electric field terms as well as metric terms and Lorentz factors. The Lorentz factors in particular would make the equations highly nonlinear in the mildly relativistic limit, and so it may be better to work first in the highly relativistic limit and then allow velocities and Lorentz factors to depart from unity simultaneously. The steepness of gradients may require that a more complex algorithm such as PPM (4) be used. In any case, the addition of special or general relativity introduces major modifications to the MHD equations. As desirable as this upgrade may be for the modeling of VLBI jets, the development of a relativistic MHD jet code is better viewed as a totally separate project rather than an upgrade of an existing nonrelativistic code.

The final scientific upgrade could be to implement FLOW in three dimensions. This could be done in either Cartesian or cylindrical coordinates; doing the calculations in terms of Cartesian coordinates is easier and provides for uniform resolution of a bending jet. Implementing the equations would not be difficult, apart from ensuring that the divergence of the magnetic field should remain zero; the limitation is in computing time. For example, a three-dimensional calculation on a 50 by 50 by 100 grid requires the same resources as a two-dimensional calculation on a 250 by 1000 grid; the Cray X-MP at the San Diego Supercomputer Center can handle at most a 150 by 600 calculation. With presently available computers, a three-dimensional calculation must be either coarsely gridded or very localized.

One technical possibility, which would alleviate the size problem, would be to adapt the code to a concurrent processor. The decomposition of the problem onto a grid of processors is elementary, and the architecture of the present code is designed to minimize the difficulties in adapting to a concurrent architecture. The primary difficulties are obtaining time on concurrent processors, as they are currently still under development, and calling the proper internal communications protocols.

A number of upgrades are both possible and desirable. First, the grid should be reorganized and the remaining magnetic field and momentum terms added, along with color capability. The next upgrade will probably include gravity, followed by some level of radiative energy and momentum transfer. The next improvements are unclear. If concurrent processors are generally available, some attempt at running three-dimensional models will be made. Otherwise, the choices are to add finite conductivity and viscosity or relativity. Relativity is difficult to add to the code; one may as well approach it as a totally new problem. On the other hand, conductivity and viscosity effects are of considerably less interest due to the

almost total uncertainty in the values of the coefficients. Even without relativity, the two-dimensional code should be able to calculate a large range of jet models, as well as the generation of jets from winds originating from a disk.

References

Clarke, D.A., Norman, M.L., and Burns, J.O. 1986, preprint.

Colella, P. and Woodward, P.R. 1984, *J. Appl. Phys.*, **54**, 174.

Courant, R. and Friedrichs, K.O. 1967, *Supersonic Flow and Shock Waves* (New York: Springer-Verlag).

Courant, R., Friedrichs, K.O., and Lewy, H. 1967, *IBM Journal*, **11**, 215.

Gentry, R.A., Martin, R.E., and Daly, B.J. 1966, *J. Comp. Phys.*, **1**, 87.

Hardee, P. 1984, in *Physics of Energy Transport in Extragalactic Radio Sources* ed. A.H. Bridle and J.A. Eilek (NRAO: Green Bank, West Virginia), p. 144.

Hawley. J. 1984, Ph.D. thesis, University of Illinois.

Ladenburg, R., van Voorhis, C.C., and Winckler, J. 1949, *Phys. Rev.*, **76**, 662.

Lapidus, A. 1967, *J. Comp. Phys.*, **2**, 154.

McArthur, G.R. (ed.) 1984, *The Cray-1 Computers: A Guide to Supercomputing at NCAR (NCAR/TN-226+IA)* (NCAR: Boulder, Colorado).

Norman, M.L., Smarr, L., Winkler, K.-H.A., and Smith, M.D. 1982a, *Astr. Ap.*, **113**, 285.

Norman, M.L., Winkler, K.-H.A., and Smarr, L. 1982b, in *Astrophysical Jets* ed. A. Ferrari and A.G. Pacholczyk (Reidel: Boston), p. 227.

Norman, M.L. and Winkler, K.-H.A. 1985, *Los Alamos Science*, **12**, 38.

Norman, M.L., Winkler, K.-H.A., and Smarr, L. 1984, in *Physics of Energy Transport in Extragalactic Radio Sources* ed. A.H. Bridle and J.A. Eilek (NRAO: Green Bank, West Virginia), p. 150.

Payne, D.G. and Cohn, H. 1985, *Ap. J.*, **291**, 655.

Sod, G. 1978, *J. Comp. Phys.*, **27**, 1.

van Albada, G.D., van Leer, B., Roberts, W.W. 1982, *Astr. Ap.*, **108**, 76.

van Leer, B. 1974, *J. Comp. Phys.*, **14**, 361.

van Leer, B. 1977, *J. Comp. Phys.*, **23**, 276.

van Leer, B. 1979, *J. Comp. Phys.*, **32**, 101.

von Neumann, J. and Richtmyer, R.D. 1950, *J. Appl. Phys.*, **21**, 232.

Wardle, J.F.C. and Potash, R.I. 1982, in *IAU Symposium 97: Extragalactic Radio Sources* ed. D.S. Heeschen and C.M. Wade (Reidel: Boston), p. 131.

Williams, A.G. and Gull, S.F. 1984, *Nature*, **310**, 33.

Williams, A.G. and Gull, S.F. 1985, *Nature*, **313**, 34.

Wilson, J.A. 1972, *Ap. J.*, **173**, 431.

Wilson, M.J. and Falle, S.A.E.G. 1985, *M.N.R.A.S.*, **216**, 971.

Figure Captions

Figure 1. The Computational Grid.

The computational grid is displayed, with the locations at which each major quantity is stored indicated. The vector cells (associated with the quantities S_r, S_z, v_r, and v_z) are located at integral multiples of Δr and Δz. The scalar cells (associated with the quantities ρ, e, B_ϕ, p_g, and p_m) are offset from the vector cells by $\frac{1}{2}\Delta r$ and $\frac{1}{2}\Delta z$. Note that the quantities are not centered in the cells, but are offset radially from the cell center.

Figure 2. Advective Boundary Condition.

This illustrates the outflow-only, or advective, boundary condition. The velocity perpendicular to the edge of the grid is restricted to be greater than of equal to zero, and is extrapolated from one zone in from the edge. No restrictions are placed on the velocity parallel to the edge of the grid.

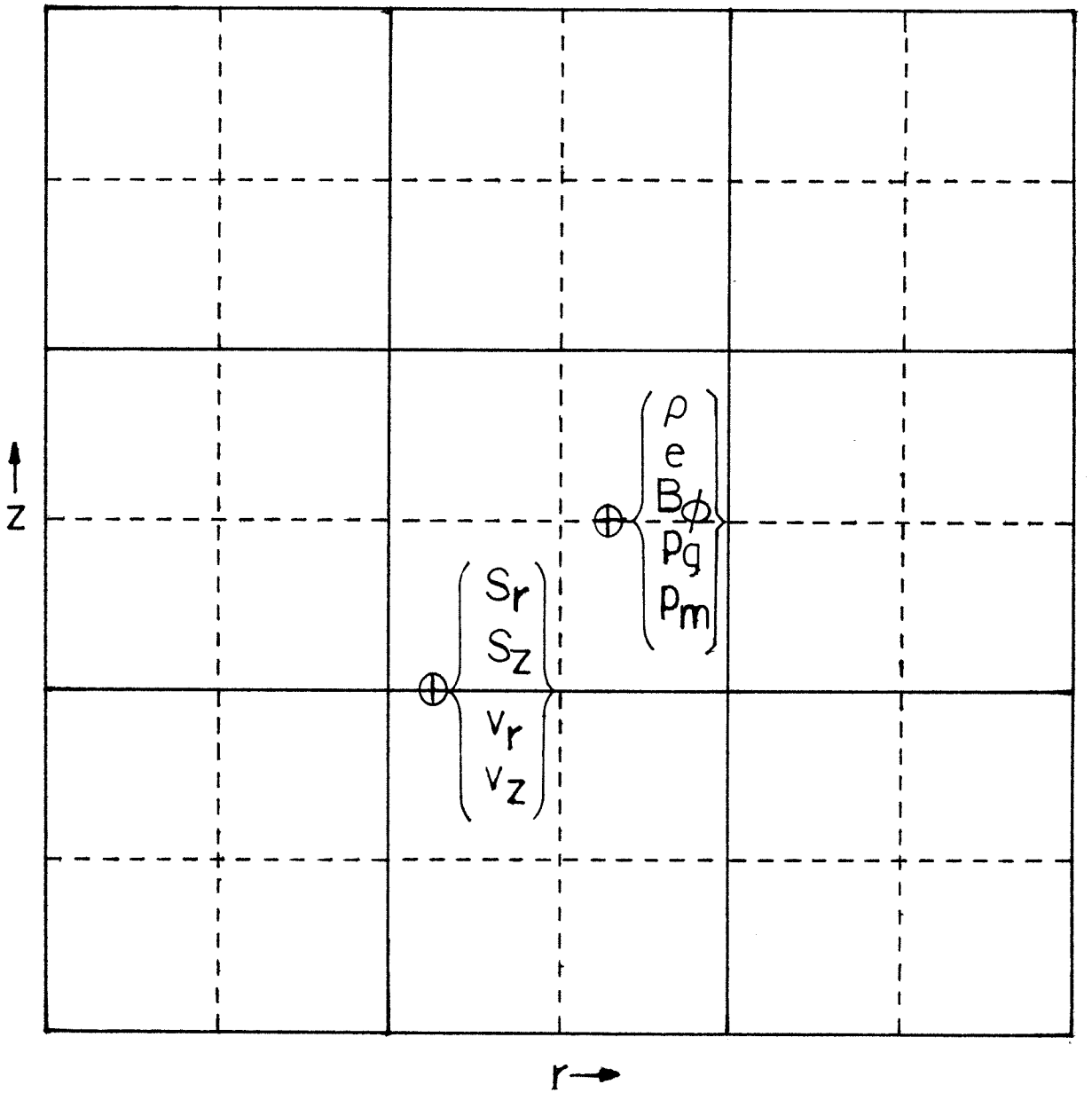

Figure 1

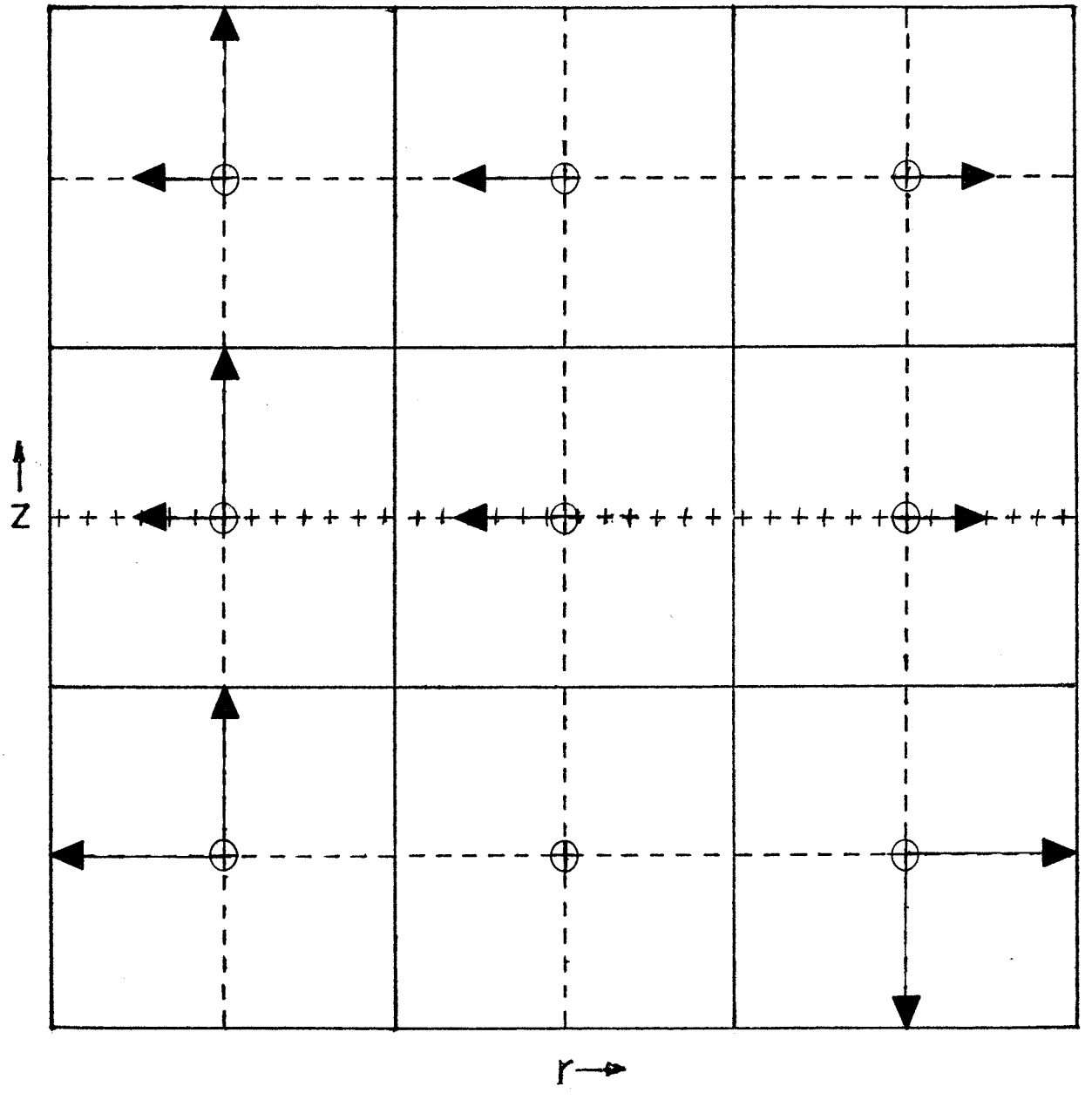

Figure 2

CHAPTER 5

NUMERICAL SIMULATIONS OF MAGNETIZED JETS II. TEST PROBLEMS AND CODE CALIBRATION

1. Introduction

Debugging and calibration are essential to the development of any code. They are particularly crucial where the results of the code are complicated and therefore errors are not immediately obvious. This is particularly true of jet codes. The calculation of the time evolution of an MHD jet with toroidal field requires the simultaneous solution of five coupled nonlinear partial differential equations, with a total of nineteen terms in the difference equations composed of various combinations of five quantities (ρ, e, B_ϕ, S_r, S_z). An error in any of these terms will eventually propagate into all of the quantities, which can result in a very confusing error with no obvious source or, worse, an apparently correct but actually totally erroneous solution. The only way to eliminate these errors — and no code is without errors of some sort initially — is to utilize simple test problems. These simple problems are also useful in examining such features as the diffusion (or "clipping") of extrema due to the use of a monotone gradient or numerical overshoots at shocks. Even though these features are not due to coding errors, they are still inaccuracies in the code calculations relative to the actual physical solution, and must be understood for the results of the code to be properly interpreted. A code is the same as any other scientific instrument; it must be tested and calibrated before it can be used with any confidence.

Many published supersonic hydrodynamic code tests refer to the Sod shock tube problem (Sod 1978), which involves solving for the propagation of a weak shock in a one dimensional Cartesian grid. In several ways, this is a good test problem. The solution is known analytically. There is a gradient in every quantity, making it possible to examine the advective terms for possible errors. Since the shock is weak, the pressure terms are dynamically significant, making it possible to test the force terms. The Sod shock problem tests every nonmagnetic term

in the difference equations, and that is both its great advantage and its great disadvantage. It demonstrates the overall behavior of the code and indicates problems resulting from interactions between several terms, but fails to isolate the terms and thus fails to indicate the sources of errors. A better strategy is to have an ensemble of tests, each of which isolates a small subset of terms for testing, with a set of perturbations to these test problems to seek possible instabilities. A further subset of tests should include more complex analytic and semi-analytic test problems, which are used to excite more subtle errors and indicate problems which were not considered during the selection of the simple test problems. The simple problems will generally find all of the simple errors that were anticipated but not avoided; the more complex problems will find the more subtle errors which were not anticipated or which resulted from interactions between terms. Since some terms involve both momenta, and because problems can arise at slip surfaces (i.e., coding errors involving indices of arrays), both one and two-dimensional test problems are required for the testing of a two-dimensional code, despite the use of operator splitting to separate the two-dimensional integration into two one-dimensional integrations.

Our code, FLOW, required especially careful testing because it was not based on any obvious ancestor. It was designed and coded from scratch using concepts and methods from several sources, including some original features. Since neither the coding nor the algorithm had been tested previously, a great deal of care was devoted to debugging and verification of the algorithm itself and several variations as well, to detect errors and determine the importance of various features. This involved the generation of a moderate number of simple test problems, as well as gleaning a number of more complicated test problems from the literature. These tests were applied after every major revision in the code; as a result, it is possible to

claim very high reliability and stability for this code, and to estimate the numerical errors on the basis of test results. While many of these tests may be generally known to the numerical community, they are nowhere discussed in terms of a global strategy for code verification, and it is the intent of this chapter to discuss this issue. This is not meant to imply that these tests are any better than any others, nor that any particular code besides ours is necessarily unreliable, but the strategy we used proved to be effective, and may prove useful in the development of other codes. As a practical remark on the need for program verification, new errors were found after every major change in the code and most minor changes, and it is not unlikely that this case is the rule rather than the exception.

The basic principle used in this method is that every term should be tested in as much isolation as possible, and that similar terms should be treated in as similar a way as possible. Parallelism in coding aids in debugging and calibration because errors can then be detected and removed from an entire class of terms simultaneously; for example, if all advective terms are done in parallel, errors in the advective flux for density, radial and axial momentum, and total energy are detected and removed simultaneously, reducing the effective number of tests required from four to one. Isolation helps in identifying errors by restricting the possible sources of error. It is not necessary to remove all terms but those being tested in order to isolate errors, either. It is sufficient to test a small number of terms, and then, once those are confirmed to be correct, add other terms, so that the test problem involves a collection of terms previously verified as correct with a small number of terms to be tested. Terms can be eliminated either by commenting out lines or by selecting test problems which do not involve certain terms. In this way, code reliability is built in a modular or structured way, just as the code itself may be written in a structured or modular way.

2. Basic Equations

The basic equations are written in terms of the density, radial and axial velocity, pressure, and toroidal magnetic field as:

$$\frac{\partial \rho}{\partial t} = -\frac{1}{r}\frac{\partial}{\partial r}(r v_r \rho) - \frac{\partial}{\partial z}(v_z \rho) \tag{2.1}$$

$$\frac{\partial v_r}{\partial t} = -v_r \frac{\partial v_r}{\partial r} - v_z \frac{\partial v_r}{\partial z} - \frac{1}{\rho}\frac{\partial p}{\partial r} - \frac{\partial}{\partial r}\left(\frac{B_\phi^2}{8\pi}\right) - \frac{B_\phi^2}{4\pi r} \tag{2.2}$$

$$\frac{\partial v_z}{\partial t} = -v_r \frac{\partial v_z}{\partial r} - v_z \frac{\partial v_z}{\partial z} - \frac{1}{\rho}\frac{\partial p}{\partial z} - \frac{\partial}{\partial z}\left(\frac{B_\phi^2}{8\pi}\right) \tag{2.3}$$

$$\frac{\partial}{\partial t}\left(\frac{p}{\rho^\gamma}\right) = -v_r \frac{\partial}{\partial r}\left(\frac{p}{\rho^\gamma}\right) - v_z \frac{\partial}{\partial z}\left(\frac{p}{\rho^\gamma}\right) \tag{2.4}$$

$$\frac{\partial B_\phi}{\partial t} = -v_r \frac{\partial B_\phi}{\partial r} - v_z \frac{\partial B_\phi}{\partial z} \tag{2.5}$$

Alternatively, density can be removed from equation (2.4), which can then be written:

$$\frac{\partial p}{\partial t} = -v_r \frac{\partial p}{\partial r} - v_z \frac{\partial p}{\partial z} - \gamma p\left(\frac{1}{r}\frac{\partial}{\partial r}(r v_r) + \frac{\partial v_z}{\partial z}\right) \tag{2.6}$$

These equations are written in terms of density, radial and axial velocity, gas pressure, and toroidal magnetic field, although the numerical algorithm tested will typically solve for density, radial and axial momentum, internal or total energy density, and toroidal magnetic field. The pressure is solved for explicitly because a number of test problems are isentropic, which means that $p \propto \rho^\gamma$, and because the gas pressure force depends only on the pressure gradient; the solutions for the pressure tend to be fairly simple. The velocity solutions also tend to be fairly simple; in fact, for the similarity solutions, the velocities are some linear function of r and z. No matter what quantities are calculated numerically, it is trivial to compare them with analytic solutions.

3. Self-similar Models

Self-similar models are the most useful type for testing the terms in flow models. The forms of the solutions are the products of time-independent profiles and time-dependent scale factors; changes in the time-independent profile of any quantity clearly indicates an error independent of time calibration. The solutions are usually simple enough that major errors are quickly visible, and more subtle errors usually show up after a number of iterations. Also, the value of a quantity at a given point is easy to relate to a time, so that it is simple to determine whether the time in the numerical calculation and the time in the analytic calculation really agree. The only disadvantage is, that the set of such solutions is restricted, and so it is not always possible to generate a solution which will test a given term in a really independent way.

The first terms which should be tested are the advection terms, simply because every test problem involves nonzero velocities at some point, which involves advection. Advection terms are tested by setting the magnetic field to zero and the pressure to some constant. This generally requires that the density be set to some constant also, or that the evolution of pressure and the momenta be commented out so that the advection of a waveform at a constant velocity can be examined. Even if there are no density gradients, the use of parallelism in the advective terms will test the advection of a gradient if there is a gradient in the momentum, and the time evolution of the density will indicate errors in the density advection in any case.

3.1. Constant Advection

The most basic test is to set radial velocity to zero and the density, pressure, and axial velocity to constants, with some form of free-flow boundary condition.

The evolution of this model should be constant in time; if there are changes, then either there are errors which fail to conserve some quantity with respect to advection (if the error appears over the entire grid), or there is an error in the boundary conditions (if it appears only at the edge of the grid). Since the values of all quantities are constant, this model can also be used to confirm that derived quantities are consistent with evolved quantities (i.e., that axial velocity is indeed equal to axial momentum divided by density).

3.2. Constant Velocity Gradient

In cylindrical coordinates, the radial velocity must go to zero near the origin, and so the advection of a radial velocity with an axial dependence is not tested. Likewise, the axial velocity must be independent of r in order to obtain a similarity solution, and so the advection of an axial velocity with a radial dependence cannot be tested. If the advection equations are kept parallel, however, the axial advection of the radial velocity (or momentum) will indicate whether radial gradients behave properly under axial advection, and vice versa using the radial advection of the axial velocity (or momentum).

The constant velocity gradient assumes constant density and pressure, and constant radial gradient for the radial velocity and constant axial gradient for the axial velocity (and zero magnetic field). The boundary conditions are symmetric at $r = 0$ and $z = 0$, and free-flow at the outer edges of the grid. The solution is:

$$\rho = \frac{\rho_0}{(1+at)^2(1+bt)} \tag{3.1}$$

$$v_r = \frac{ar}{1+at} \tag{3.2}$$

$$v_z = \frac{bz}{1+bt} \tag{3.3}$$

$$p = \frac{p_0}{(1+at)^{2\gamma}(1+bt)^{\gamma}} \tag{3.4}$$

$$B_\phi = 0 \tag{3.5}$$

For $a = 0$, the flow is simply a one-dimensional self-similar flow in a Cartesian coordinate system. For $b = 0$, the flow is simply a one-dimensional self-similar flow in a cylindrical coordinate system. For $a = b$, the flow is a self-similar spherical outflow. For arbitrary a and b, the flow is a self-similar ellipsoidal outflow. The one-dimensional tests allow independent tests of radial and axial advection, whereas the ellipsoidal and spherical tests allow testing of advection in both directions. In particular, the spherical test problem can be used to confirm that the times for radial and axial advection are actually on the same scale, i.e., that a radial velocity of unity and an axial velocity of unity really refer to the same magnitude of velocity. If the time or velocity scales disagree, the spherical outflow will be distorted into an elliptical outflow.

The toroidal field is zero in this case for the same reason that the pressure is constant; the toroidal field must go to zero on the axis, so the only way to introduce nonzero magnetic field is to introduce a magnetic field gradient and hence a force. Since this test is to include advection only, the magnetic field must therefore be excluded.

3.3. Constant Pressure Gradient

The constant pressure gradient test in cylindrical coordinates is a purely one-dimensional solution, because the velocity in the direction of the pressure gradient is constant in space but changes with time, and so $v_r = 0$ at $r = 0$ would be violated for radial pressure gradients.

The solution for this case is:

$$\rho = \rho_0 \tag{3.6}$$

$$v_r = 0 \tag{3.7}$$

$$v_z = v_{z0} - \frac{a}{\rho_0} t \tag{3.8}$$

$$p = p_0 \left(1 + \frac{a v_{z0}}{p_0} t - \frac{a^2}{2 \rho_0 p_0} t^2 \right) + az \tag{3.9}$$

$$B_\phi = 0 \tag{3.10}$$

Given that advection has already been tested, this problem is designed to test the gas pressure force in the axial direction. Of course, if the coordinate system used is two-dimensional Cartesian, then this solution can be used in either direction, or generalized to act as a one-dimensional problem at an arbitrary angle to the axes.

3.4. Restricted Magnetohydrodynamic Self-Similar Solution

The restricted MHD self-similar solution (derived by David Payne) is a one-dimensional cylindrical outflow with zero density and pressure gradients. It allows a magnetic field gradient, however, and so this test is used to verify the magnetic force terms, given that advection and gas pressure have already been tested. The solution is somewhat more complicated than for the previous test problems:

$$\rho = \rho_0 \exp\left(-\frac{1}{2}(m_0^2 - m^2) \right) \tag{3.11}$$

$$v_r = v_{r0} \frac{r}{r_0} \frac{m}{m_0} \exp\left(-\frac{1}{4}(m_0^2 - m^2) \right) \tag{3.12}$$

$$v_z = v_{z0} \tag{3.13}$$

$$p = p_0 \exp\left(-\frac{\gamma}{2}(m_0^2 - m^2) \right) \tag{3.14}$$

$$B_\phi = B_{\phi 0} \frac{r}{r_0} \exp\left(-\frac{1}{2}(m_0^2 - m^2) \right), \qquad \text{where} \tag{3.15}$$

$$t(m) = \frac{\sqrt{\pi}}{2} \frac{r_0}{a_0} \exp\left(\frac{m_0^2}{4} \right) \left[\operatorname{erf}\left(\frac{m_0}{2} \right) - \operatorname{erf}\left(\frac{m}{2} \right) \right], \qquad \text{for} \tag{3.16}$$

$$t < t_c = \frac{\sqrt{\pi}}{2}\frac{r_0}{a_0}\exp\left(\frac{m_0^2}{4}\right)\mathrm{erf}\left(\frac{m_0}{2}\right), \qquad \text{where} \tag{3.17}$$

$$a_0^2 = \frac{B_{\phi 0}^2}{4\pi\rho_0}, \qquad \text{and} \tag{3.18}$$

$$m_0^2 = \frac{v_{r0}^2}{a_0^2} \tag{3.19}$$

Note that the all quantities, including time, are written as functions of the Alfvenic Mach number m, which is independent of position in the flow. The values at a given time must be found by inverting the equation for time to find m, and then substituting that value of m into the remaining equations. Also, note that there is a critical value of the time, t_c, at which the Alfvenic Mach number goes to zero; at this point, the flow begins to contract. The test problem is stopped at this point because of the instability of inflow boundary conditions with evolution occurring outside as well as inside the grid.

3.5. *Generalized Magnetohydrodynamic Self-Similar Solution*

This similarity solution (Achterberg *et al.* 1983) is also rather complicated, but includes a number of additional terms which finally allow the testing of most, if not all, terms in the numerical difference equations. This solution includes angular momentum and axial and radial magnetic fields for the sake of generality, but these can be set to zero for the toroidal field case.

The solutions are:

$$\rho = \rho_0\left(\frac{R_0}{R}\right)^2 g(\xi) \tag{3.20}$$

$$v_r = v_{r0}V(R/R_0)\xi \tag{3.21}$$

$$v_\phi = v_{\phi 0}\left(\frac{R_0}{R}\right)\xi \tag{3.22}$$

$$v_z = v_{z0} \tag{3.23}$$

$$p = p_0 \left(\frac{R_0}{R}\right)^{2\gamma} k(\xi) \tag{3.24}$$

$$B_r = 0 \tag{3.25}$$

$$B_\phi = B_{\phi 0} \left(\frac{R_0}{R}\right) m(\xi) \tag{3.26}$$

$$B_z = B_{z0} \left(\frac{R_0}{R}\right)^2 b(\xi), \qquad \text{where} \tag{3.27}$$

$$\xi \equiv \frac{r}{R(t)} \tag{3.28}$$

The function $V(R/R_0)$ is related to the time t via:

$$V^2(R/R_0) = 1 + C_1 \frac{S_0}{\gamma(\gamma-1)} \left[1 - \left(\frac{R}{R_0}\right)^{-2(\gamma-1)}\right] \tag{3.29}$$

$$+ (C_3 H_0^2 + v_{\phi 0}^2) \left[1 - \left(\frac{R}{R_0}\right)^{-2}\right] - 2C_2 A_0^2 \ln(R/R_0) \qquad \text{and}$$

$$t = \frac{R_0}{v_{r0}} \int_1^{R/R_0} \frac{dR}{R_0 V(R/R_0)}, \qquad \text{where} \tag{3.30}$$

$$S_0 \equiv \frac{\gamma p_0}{\rho_0} \qquad \text{is the sound speed,} \tag{3.31}$$

$$H_0 \equiv \frac{B_{z0}^2}{4\pi\rho_0} \qquad \text{is the Alfven speed for the axial magnetic field, and} \tag{3.32}$$

$$A_0 \equiv \frac{B_{\phi 0}^2}{4\pi\rho_0} \qquad \text{is the Alfven speed for the toroidal magnetic field.} \tag{3.33}$$

The constants C_1, C_2, and C_3 determine the self-similar distributions of various quantities by:

$$k = 1 - C_1 \int_0^\xi x g(x) dx \tag{3.34}$$

$$\xi^2 m^2 = 2C_2 \int_0^\xi x^3 g(x) dx \tag{3.35}$$

$$b^2 = 1 - 2C - 3 \int_0^\xi x g(x) dx \tag{3.36}$$

Given the above constants, it is possible to solve for the time by numerical integration. Terms can be isolated by a careful choice of the constants. The only

problem is that there are no axial gradients in this problem, and the solutions for a number of quantities (such as the radial magnetic field) are highly restricted. However, this is the most complete self-similar solution which we have been able to derive.

3.6. Additional Self-Similar Solutions

There are a number of other self-similar solutions which would be desirable. Any solution which included an axial magnetic field gradient would be particularly useful. Another useful solution is a spherical polar magnetic flow. Such a solution is already available, but may only be solved outside of a cone centered on the symmetry axis. It has not been implemented because of the difficulties involved in implementing these boundary conditions.

4. The Shock Tube

The Sod shock tube is the standard test problem in the literature (Sod 1978). This problem is a Riemann shock tube, which is an infinitely long one-dimensional tube of unmagnetized gas with a contact discontinuity at some point $z = z_{c0}$. At time $t = 0$, the hypothetical wall between these two regions is removed, and the flow is allowed to evolve. The solution to this problem involves five distinct fluid states, separated by four lines in the (z,t) plane diverging from the point (z_{c0},0)(fig. 1). Region I is the undisturbed hot, dense gas, specified by Sod as $\rho_{\rm I} = 1$, $p_{\rm I} = 1$, $v_{\rm I} = 0$, and $\gamma = 1.4$. Region 5 is the undisturbed cool, rarefied gas, specified by Sod as $\rho_{\rm V} = 0.125$, $p_{\rm V} = 0.1$, $v_{\rm I} = 0$, and $\gamma = 1.4$. Region II is the rarefaction region, in which the hot, dense gas is expanding; it is separated from region I by the head of a rarefaction wave (A). Region III contains the already rarefied hot, dense gas; it is separated from region II by the tail of a rarefaction wave (B). A contact discontinuity (C) separates the gas in region 3, which was originally part of the undisturbed hot, dense gas, from the gas in region IV, which is gas which was originally cool and rarefied, but which has passed through the weak shock (D) which is propagating into the undisturbed cool, dense gas in region V. A complete derivation of the Riemann shock tube solution may be found in Courant and Friedrichs(Courant and Friedrichs 1976); short derivations can be found in the computational (Sod 1978) and astrophysical (Hawley 1984) literature. This solution is done for Cartesian coordinates only; however, the strength of the shock, the qualitative behavior of the contact discontinuity, and the speed of advance of the rarefaction must still be consistent with local values of the various quantities. Since the cylindrical metric approaches a Cartesian metric far from the axis, these can be used as limited tests involving radial shocks. Another variation is to run

the Sod shock in a periodic axial grid to examine the magnitude of oscillations at the collision of two shocks.

The Sod shock tube demonstrates the ability of a code to calculate the behavior of nonlinear waves, but has two serious limitations in terms of debugging MHD codes. First, it is purely hydrodynamical; there is no way to test the magnetic field. Second, it fails to isolate any particular terms, and hence any errors detected by calculating a shock tube cannot be easily isolated into any specific terms in the difference equations.

5. The Underexpanded Jet

This test problem involves the modeling of an underexpanded experimental jet which is injected into a large chamber filled with air at approximately room temperature; the jet material is dense ($\rho_{\rm jet} = 3.26\rho_{\rm atm}$), overpressured ($p_{g\rm jet} = 2.75p_{g\rm atm}$), and transonic ($M = 1$) (Ladenburg *et al.* 1949). This specific test problem was chosen for two reasons. First, it was used as a demonstration problem for a previous code (Norman *et al.* 1982a), and so it is a comparison with experimental results and with another, well-understood code. Second, the transonic regime is the most difficult regime to model accurately, since advective and pressure terms have roughly equal weight. In supersonic jets, advection (i.e., momentum transport) clearly dominates over pressure forces, and so the pressure terms are negligible in the direction of the jet flow. In subsonic flows, the pressure terms dominate, and so the pressure has ample opportunity to compensate for errors in advection. When the terms are comparable, subsonic and supersonic phenomena in both the axial and radial direction must be modeled correctly for the calculation to appear similar to the experimental results. Thus, this is a quite stringent test.

A particularly useful feature of the flow is the triple shock configuration at the edge of the Mach disk (fig. 6). The triple shock provides an excellent test of the ability of the code to handle shocks; it has a strong perpendicular shock, a strong oblique shock of considerable length, and a short weak oblique shock, all of which intersect at a single point. One of the major tests of the code was the ability to reproduce the triple shock accurately.

Like the Sod shock tube, this test problem tests all of the hydrodynamic terms simultaneously; hence, it demonstrates the accuracy of the entire code, but fails to isolate terms and so is not useful for debugging. Unlike the Sod shock, it

is a two-dimensional problem, and so tests the radial integration terms as well. Even though it is nonanalytic, the flow is simple, and contains various well-defined features which can be easily compared with the results of numerical calculations. Unfortunately, this model does not test the magnetic field terms in any way; it is doubtful that a highly magnetized jet could develop into a magnetically determined steady-state configuration without wall reflections strongly influencing the final jet configuration, and the modeling of those edge effects would be a serious problem in itself. An experimental MHD jet used for similar purposes would likely be so strongly affected by boundary conditions that it would be of at most limited usefulness.

6. Comparison With Tests

The tests were run on both a Cray and a VAX-equivalent computer to ensure that we had compensated for all system dependencies, and then the test problems were run so as to isolate errors in all terms independently. First, the constant solution was run to search for gross errors in advection, followed by the one-dimensional constant velocity gradient solutions (Equations 3.1-5) to search for more subtle errors. The two-dimensional constant velocity gradient solution (Equation 3.1-5) was then used to confirm that the one-dimensional integrations were independent and that the time calibration was the same for each direction. The pressure in the axial direction was then tested with the constant velocity gradient problem (Equations 3.6-10). The radial magnetic field terms were tested with the restricted MHD similarity solution (Equations 3.11-19), and a version of the generalized MHD similarity solution (Equations 3.20-36) was used to test the radial pressure terms. No tests involving the axial advection of the magnetic field were carried out, but these terms could be coded in parallel to the axial advection of the density, and so are considered highly reliable. Unfortunately, no tests with an axial magnetic pressure gradient were found; thus, these terms are relatively untested, although they were carefully coded in analogy with the radial magnetic pressure temrs and so are reasonably reliable. After the self-similar solutions were reproduced to our satisfaction, the shock tube and transonic underexpanded jet problems were run to test overall code performance.

Each self-similar solution was run twice, with the resolution doubled in the second run. Since errors should go as Δx^2 for a second-order code, the errors in the two cases were compared to confirm that errors had indeed been reduced by roughly the correct order by the doubling of the grid resolution. In general, this proved to be so, although errors arising from boundary conditions, especially near

the symmetry axis and the outer boundary, prevented the errors from reducing at the rate expected. The errors for the two-dimensional advection were also compared to the individual results for the one-dimensional advection; theoretically, since the errors were typically a fraction of a percent, then the percent errors should essentially add at a given point if the integrations in the two dimensions are truly independent. This proved to be so, except for some additional error near the corners of the grid due to boundary effects.

The results of one of the self-similar tests, the restricted MHD test with a magnetic gradient, are discussed in detail, followed by the results of the tests of the shock tube and transonic jet models.

6.1. Self-Similar Tests

The percentage errors for the restricted MHD self-similar solution (Equations 3.11-3.19) are used to demonstrate the results of code testing (Tables 1-6). Only the worst errors, which occur near the edge of the grid, are shown. Over the remainder of the grid, the errors are considerably, and reduce to a quarter of their original value when the grid spacing is halved, as expected. Near the boundary, the errors decrease when the grid spacing is halved, but not to a quarter of the errors on the coarse grid, as in the body of the grid. There are a number of reasons for this. First, errors near the edges may be caused by boundary effects; in this case, the linear extrapolation at the outer boundary works well for the momentum, but is seriously in error for the total energy, which is a quadratic quantity. The coupling in the equations tends to spread out errors among the various terms, and so these errors propagate, not only across the grid, but also across terms. Since boundary condition errors can propagate as weak shocks, they cannot necessarily

be tracked by following the advection; note that errors propagate inwards from the outer boundary even though the flow is outward.

The most important observations for the results of the testing are, that in the body of the grid, the errors decrease as the square of the grid spacing. This was demonstrated by the use of an extremely coarse grid, far coarser than would be used for research purposes; the coarseness was deliberate, so that the errors seen would clearly have been caused by algorithmic rather than machine precision. Even near the edge of the grid, errors are typically a fraction of a percent, and are of order a thousandth of a percent in the inner parts of the grid. The percent errors do not show any serious increase with time except near the boundary, where such errors were expected. The other self-similar solutions all show similar behavior. All solutions give improvements close to the predicted 4:1 in the body of the grid when the resolution is doubled. The errors in the two-dimensional cases are consistent with the radial and axial errors being uncoupled.

6.2. Shock Tube Test

The shock tube results demonstrate that the code handles shocks quite well (figs. 2-5)(Sod 1978). The results are shown at time 25 on a 100 zone wide grid. The undershoots and overshoots at the shock front, contact discontinuity, and rarefaction fronts are small in all quantities; in particular, there is no velocity overshoot at the shock front, although there is one at the base of the rarefaction fan, which is associated with a density and pressure undershoot. The jump conditions are all solved to a fraction of a percent, and diffusion is limited to two zones for the shock and about five zones for the contact discontinuity. The pressure remains constant across the contact discontinuity, as required. The general

result confirms the ability of the code to handle hydrodynamic compression and rarefaction waves without explicit artificial viscosity.

The shock tube was also used to test various forms of the advective (outflow only) boundary conditions, in which fluid motion into the grid is suppressed. Shocks of various strengths were allowed to evolve until they passed through the edge of the grid. After they had passed, the results were compared with shocks which had been evolved on a larger grid, to determine the strength of reflected waves. In general, it was found that weak shocks were more strongly reflected by the boundary than were strong shocks, and that the reflection was very sensitive to the formulation of the boundary condition. The best implementation of the boundary condition was also tested by running a coarse jet off the edge of the grid and measuring the strength of the reflected bowshock. These results indicated that, in the worse case, the reflection was of order a couple of percent, and propagated at no more than one fifth of the local speed of advance of the shock. Even in the case of weak shocks, the reflected wave appeared to damp out within ten zones of the boundary.

6.3. Underexpanded Jet Test

The experimental results for the underexpanded jet are displayed next to the results of a previous code and the results for our code (figs. 6-8)(Norman *et al.* 1982a; Ladenburg *et al.* 1949). Both codes successfully reproduce the initial expansion and the Mach disk – triple shock configuration. The only disagreement is in the details of the upwind oblique shock; our code reproduces it as extremely straight with a terminal vortex, in excellent agreement with the experimental results, whereas these features are not so pronounced in the previous code results. The ability of the code to reproduce a straight oblique shock in a cylindrical

geometry verifies the ability of the code to handle the metric terms which arise in this geometry. Furthermore, the agreement between the experimentally observed shock angles and the calculated shock angles indicate that the code models oblique shocks accurately; thus, shocks in both Cartesian and cylindrical geometries are accurately modeled, and there appears to be little diffusion or distortion when the shocks are not parallel to the zone boundaries.

7. Discussion

A procedure has been developed for the testing and calibration of MHD codes. It is based on parallelism in coding — effectively reducing the number of terms requiring testing by using parallel algorithms and code wherever possible — and successive verification, i.e., testing terms one at a time, starting with the advective terms. The ensemble of test problems which are utilized in this procedure range from the simplest possible self-similar flows to complex two-dimensional jet simulations. Quite simply, the radial and axial integrations are tested independently, adding terms only after previous terms have been thoroughly verified. At various points, two dimensional test problems are used to verify that the terms in the two integrations remain independent, i.e., that the flux vector splitting has been properly implemented. Once every term has been tested, more complicated tests, such as the Sod shock tube and the transonic underexpanded jet, may be run to confirm that no unanticipated subtle errors have crept into the code. At any point, if terms are written in parallel, such as the advection of density and total energy, they can be tested simultaneously. Only after the code has performed satisfactorily for all tests is it released for research purposes.

References

Achterberg, A., Blandford, R.D., and Goldreich, P. 1983, *Nature,* **304**, 607.

Courant, R. and Friedrichs, K.O. 1967, *Supersonic Flow and Shock Waves* (New York: Springer-Verlag).

Hawley. J. 1984, Ph.D. thesis, University of Illinois.

Ladenburg, R., van Voorhis, C.C., and Winckler, J. 1949, *Phys. Rev.,* **76**, 662.

Norman, M.L., Smarr, L., Winkler, K.-H.A., and Smith, M.D. 1982a, *Astr. Ap.,* **113**, 285.

Sod, G. 1978, *J. Comp. Phys.,* **27**, 1.

van Albada, G.D., van Leer, B., Roberts, W.W. 1982, *Astr. Ap.,* **108**, 76.

Table 1. Percent Errors for Restricted MHD Test

10×10 grid at t=1.0

Radius	ρ	e	B_ϕ	S_r
0	+0.09	+0.10	+0.12	-1.50
1	-0.01	-0.02	-0.01	-1.35
2	-0.03	-0.05	-0.02	-0.48
9	-0.04	-0.02	-0.04	-0.19
10	-0.31	-0.19	-0.34	-0.44

The percent errors are displayed for the restricted magnetohydrodynamic similarity solution described in section 3.4. The calculation is done on a 10×10 grid with $\Delta r = \Delta z = 1$; the results are shown at time $t = 1$. Near the symmetry axis, the errors in the scalar quantities, ρ, e, and B_ϕ, drop by a factor ~ 10 away from the axis, whereas the error in the vector quantity S_r only drops as factor of 3, at node 2 rather than node 1. Similar behavior is seen at the outer edge of the grid. Throughout most of the grid, the error is under 0.1%; since this problem was done on a deliberately very coarse grid, this is consistent with the expected errors.

Table 2. Percent Errors for Restricted MHD Test

10×10 grid at t=9.0

Radius	ρ	e	B_ϕ	S_r
0	+0.21	+0.21	+0.42	+0.34
1	+0.15	+0.17	+0.16	+0.27
2	+0.10	+0.14	+0.11	+0.22
9	+2.83	+2.79	+2.89	-0.38
10	+4.39	+3.92	+4.61	-0.49

The percent errors are displayed for the restricted magnetohydrodynamic similarity solution described in section 3.4. The calculation is done on a 10×10 grid with $\Delta r = \Delta z = 1$; the results are shown at time $t = 9$. The percent errors in the scalar quantities, ρ, e, and B_ϕ, have increased over the grid, especially near the outer boundary, and do not drop as noticeably with distance from the symmetry axis. The vector quantity, S_r, has improved in percent accuracy near the symmetry axis, and the percent errors near the outer boundary have undergone only a minor increase. This suggests that the boundary conditions are a dominant source of error, and that the errors become redistributed with time between the various quantities. Note also that, because the values of the quantities decrease with time, an increase in the percent error does not imply an increase in the absolute error.

Table 3. Percent Errors for Restricted MHD Test

20×10 grid at t=1.0

Radius	ρ	e	B_ϕ	S_r
0	+0.06	+0.08	+0.07	-0.14
1	+0.01	+0.02	+0.01	-0.21
2	-0.001	-0.004	-0.0004	-0.25
9	-0.11	-0.01	-0.12	-0.14
10	-0.24	-0.08	-0.25	-0.08

The percent errors are displayed for the restricted magnetohydrodynamic similarity solution described in section 3.4. The calculation is done on a 20×10 grid with $\Delta r = 0.5$ and $\Delta z = 1$; the results are shown at time $t = 1$. Near the symmetry axis, the errors in the scalar quantities, ρ, e, and B_ϕ, drop by a factor ~ 5 away from the axis, whereas the error in the vector quantity S_r remains more or less constant across the grid. Similar behavior is seen at the outer edge of the grid. Throughout almost all of the grid, the error is under 0.1%, with clear improvement over the coarser grid.

Table 4. Percent Errors for Restricted MHD Test

20×10 grid at t=9.0

Radius	ρ	e	B_ϕ	S_r
0	+0.07	+0.08	+0.12	+0.08
1	+0.06	+0.07	+0.06	+0.06
2	+0.05	+0.07	+0.05	+0.05
9	+1.18	+1.13	+1.20	-0.14
10	+1.68	+1.55	+1.72	-0.18

The percent errors are displayed for the restricted magnetohydrodynamic similarity solution described in section 3.4. The calculation is done on a 20×10 grid with $\Delta r = 0.5$ and $\Delta z = 1$; the results are shown at time $t = 9$. Near the symmetry axis, the errors in all of the quantities, ρ, e, and B_ϕ, barely drop away from the axis. Throughout almost all of the grid, the error is under 0.1%, with clear improvement over the coarser grid. It is interesting to note that the improvements using the finer grid at $t = 9$ are comparable to the improvements using the finer grid at $t = 0$ near the axis; this suggests that the boundary conditions are the major source of error, at least near the edge of the grid.

Table 5. Percent Errors for Restricted MHD Test

Ratio of Errors, Fine/Coarse Grid, at $t = 1$

Radius	ρ	e	B_ϕ	S_r
0	+0.667	+0.800	+0.583	+0.093
1	-1.000	-1.000	-1.000	+0.156
2	+0.033	+0.080	+0.020	+0.520
9	+0.275	+0.500	+3.000	+0.736
10	+0.774	+0.421	+0.735	+0.182

The ratios of the percent errors are displayed for the restricted magnetohydrodynamic similarity solution described in section 3.4. The results are shown at time $t = 9$. Theoretically, the ratios of the errors should be of order 0.25; in practice, the ratios of the percent errors vary widely, but in general demonstrate a definite improvement in accuracy by refining the grid. The most obvious exception, B_ϕ at node 9, may be due to boundary conditions.

Table 6. Percent Errors for Restricted MHD Test

Ratio of Errors, Fine/Coarse Grid, at $t = 9$

Radius	ρ	e	B_ϕ	S_r
0	+0.333	+0.381	+0.286	+0.235
1	-0.400	+0.412	-0.375	+0.222
2	+0.500	+0.500	+0.455	+0.227
9	+0.417	+0.405	+0.415	+0.368
10	+0.383	+0.395	+0.373	+0.367

The ratios of the percent errors are displayed for the restricted magnetohydrodynamic similarity solution described in section 3.4. The results are shown at time $t = 9$. Theoretically, the ratios of the errors should be of order 0.25; in practice, the ratios of the percent errors vary widely, but in general demonstrate a definite improvement in accuracy by refining the grid. Note that S_r near the axis has an error ratio near that predicted.

Figure Captions

Figure 1. Space-time Diagram for Shock Tube

The space-time diagram for a one-dimensional shock tube is shown. The various waves and contact surfaces radiate from the point$(z_c, 0)$ without intersecting, providing a clean test of the ability of the code to model various nonlinear waves. The different regions and the manner in which they are separated are described in the text.

Figure 2. Shock Tube — Density

The density for a 100 zone shock tube is shown at $t = 25$. The shock is two zones wide, the contact discontinuity is five zones wide, and there is an undershoot at the base of the rarefaction wave on the order of a percent.

Figure 3. Shock Tube — Sound Speed

The sound speed — which is essentially the square root of the specific internal energy – for a 100 zone shock tube is shown at $t = 25$. The shock is two zones wide and the contact discontinuity is five zones wide. There is an overshoot at the shock and at the contact discontinuity, and an undershoot at the base of the rarefaction wave, all of which are under a percent.

Figure 4. Shock Tube — Pressure

The pressure for a 100 zone shock tube is shown at $t = 25$. The shock is two zones wide, and the contact discontinuity cannot be seen, as desired. The undershoot at the base of the rarefaction wave is again on the order of a percent.

Figure 5. Shock Tube — Velocity

The velocity for a 100 zone shock tube is shown at $t = 25$. The shock is two zones wide, and the contact discontinuity cannot be seen, as desired. There is an overshoot at the base of the rarefaction wave, on the order of a few percent. Note that there is not overshoot at the shock.

Figure 6. Experimental Measurements for the Underexpanded Jet

The experimental results for the jet described in the text are shown in composite for various values of the pressure in the gas reservoir (Ladenburg *et al.* 1949; Norman *et al.* 1982a). Note that the downstream oblique shock is always straight, although the Mach disk itself bows out as the pressure is increased. For the model run, the expected width of the Mach disk is $\frac{1}{3}$ jet radii.

Figure 7. Results of Simulation — Previous Code

The density contours and velocity vectors for the numerical solution obtained by Norman and collaborators is shown (Norman *et al.* 1982a). The fit to the experimental results is good, except possibly for the curvature of the downstream oblique shock and the width of the Mach disk (which is $\frac{1}{5}$- $\frac{1}{4}$ jet radii). However, it is not clear that the model shown corresponds to the same time as the experimental results, and so it is not certain that there are any real discrepancies.

Figure 8. Results of Simulation — Present Code

The density contours and velocity vectors for the numerical solution obtained by our code are shown side by side. The fit to the experimental results is good, except possibly for the width of the Mach disk (which is $\frac{3}{4}$ jet radii). However, it is not clear that the model shown corresponds to the same time as the experimental results, and so it is not certain that there are any noticeable discrepancies.

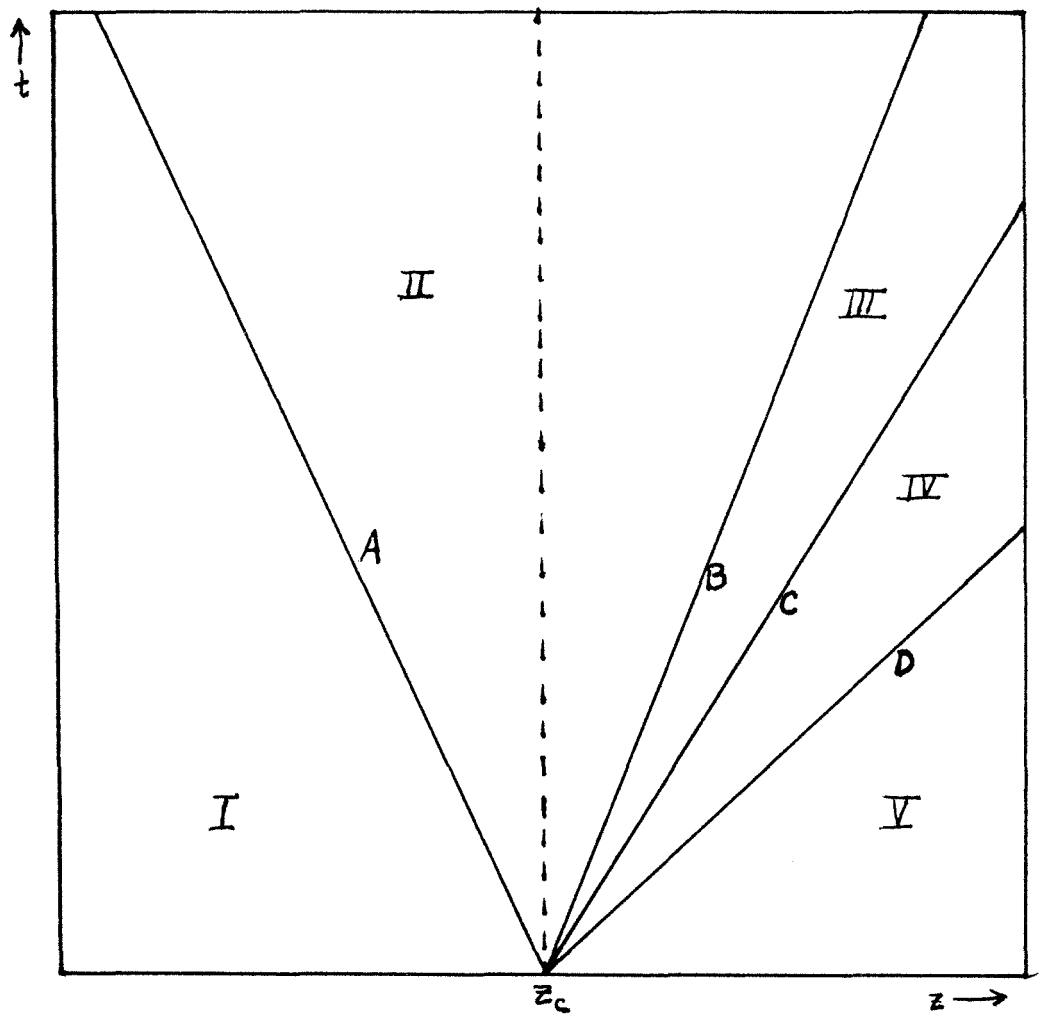

Figure 1

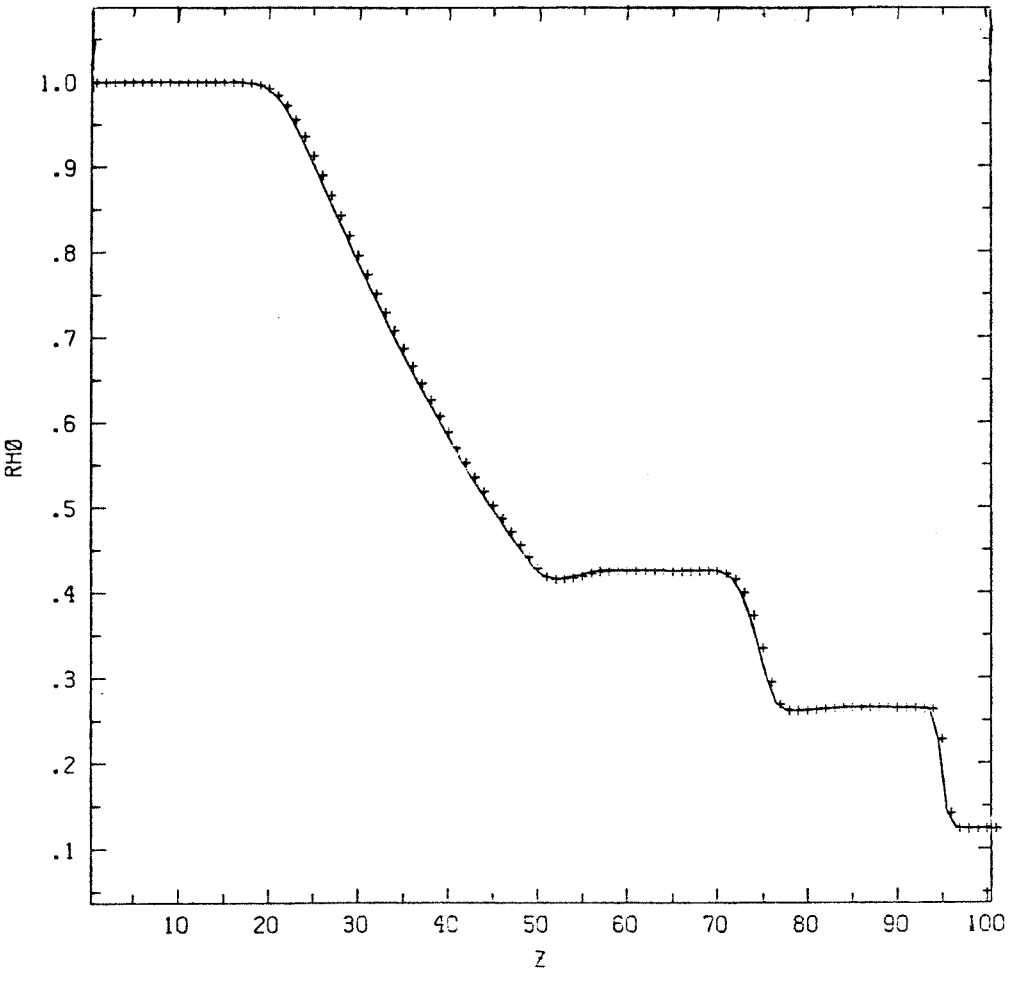

Figure 2

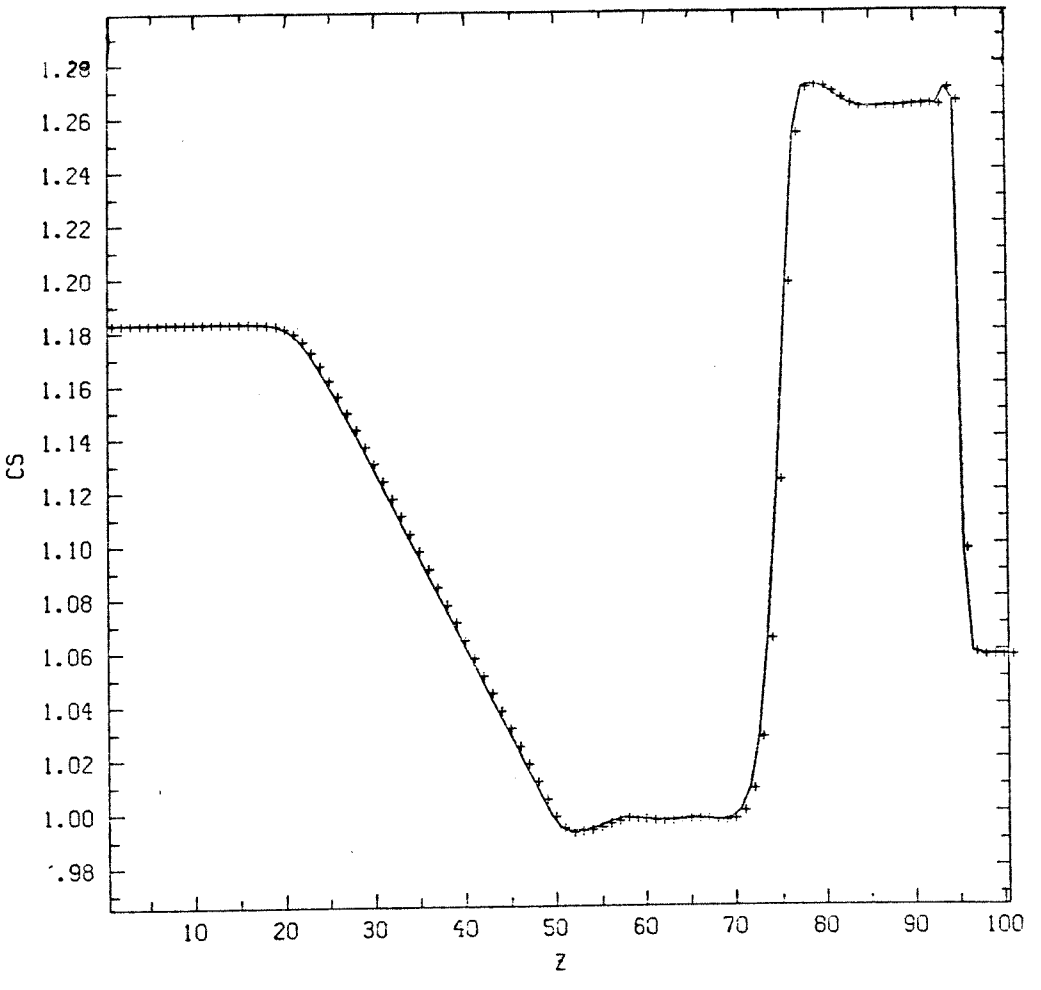
1.28
1.26
1.24
1.22
1.20
1.18
1.16
1.14
1.12
1.10
1.08
1.06
1.04
1.02
1.00
.98
CS
10
20
30
40
50
60
70
80
90
100
Z

Figure 3

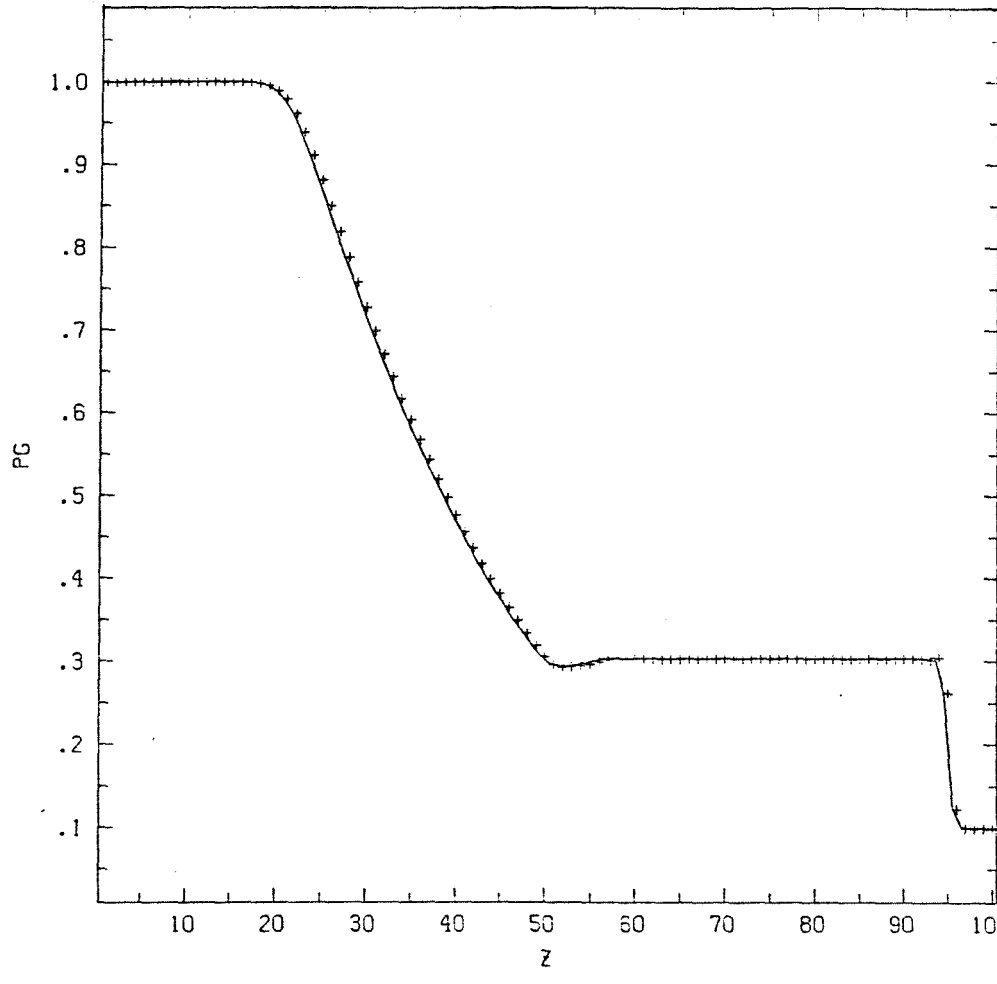

Figure 4

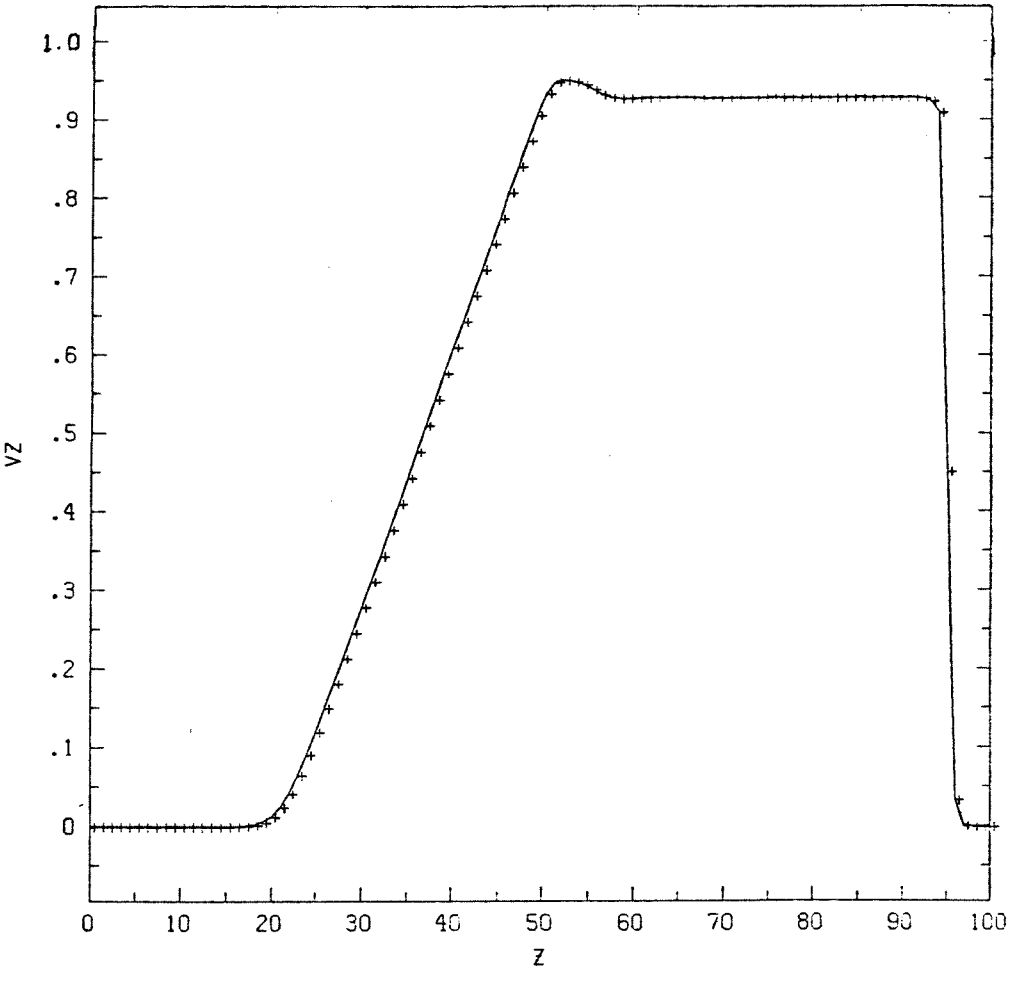

Figure 5

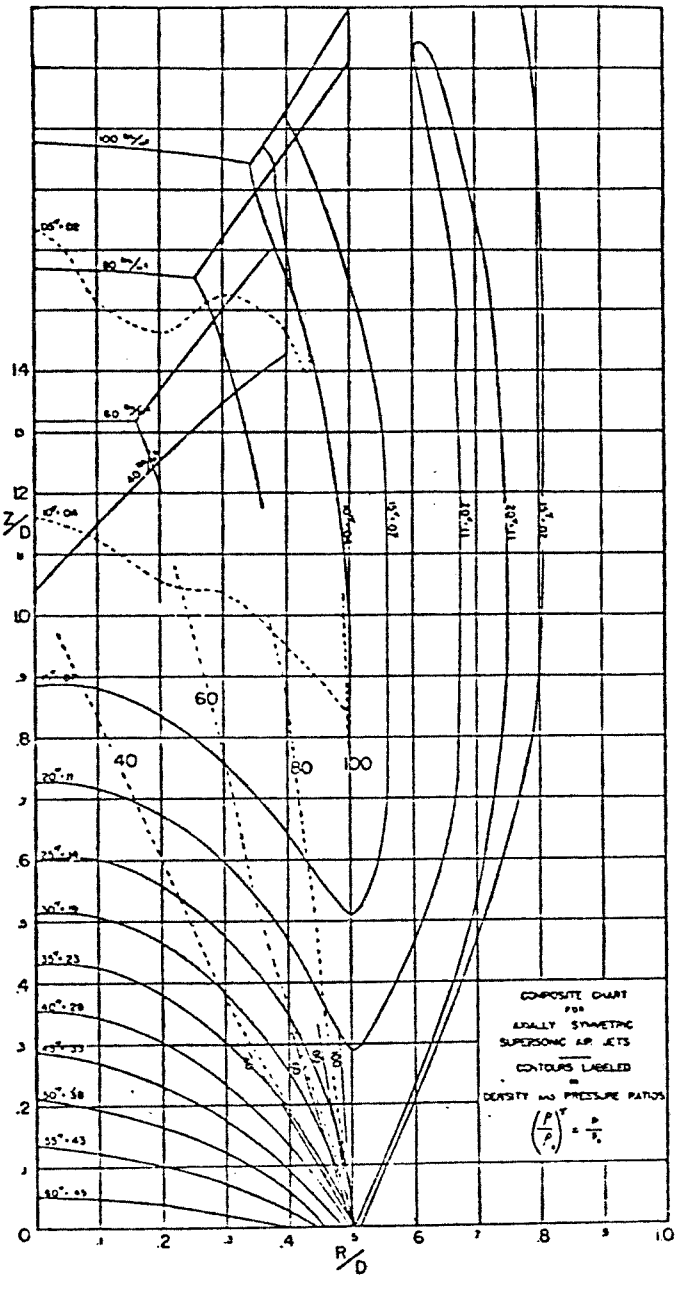
Z/D
R/D
0
.1
.2
.3
.4
.5
.6
.7
.8
.9
1.0
12
14
40
60
80
100
COMPOSITE CHART
FOR
AXIALLY SYMMETRIC
SUPERSONIC AIR JETS
CONTOURS LABELED
IN
DENSITY AND PRESSURE RATIOS

Figure 6

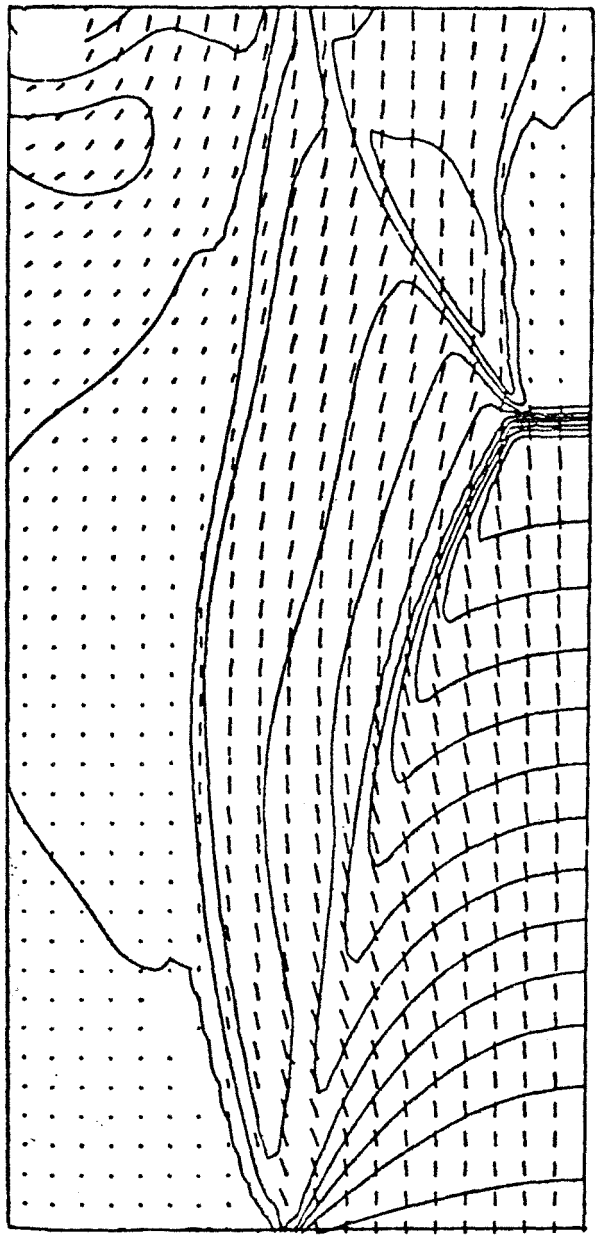

Figure 7

DENSITY VELOCITY

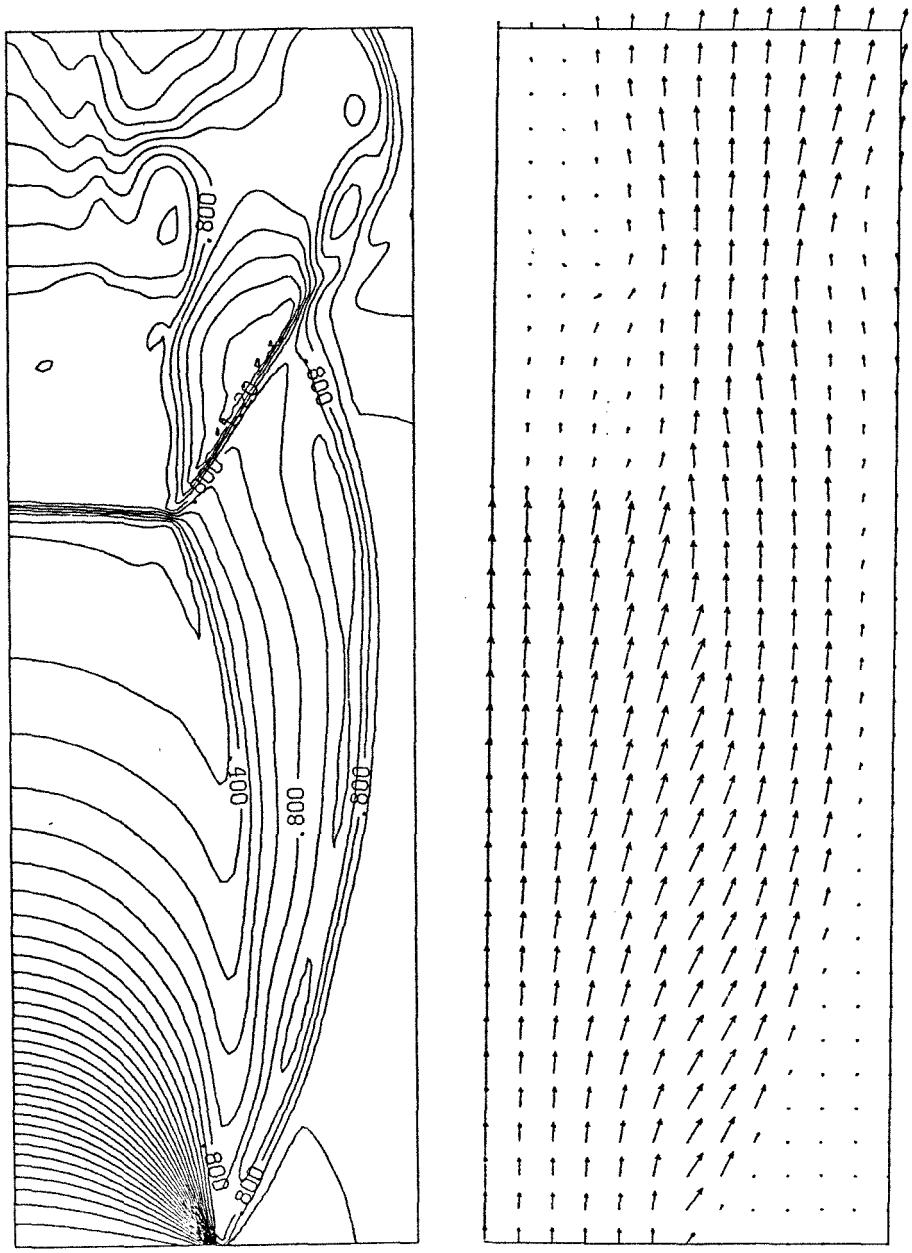

Figure 8

CHAPTER 6

NUMERICAL SIMULATIONS OF MAGNETIZED JETS III. RESULTS AND INTERPRETATION

1. Introduction

Recent observations of extragalactic radio sources obtained from the VLA, Westerbork, MERLIN, and VLBI networks reveal jetlike structure on many scales. These structures appear to be stable and well-collimated over a length of many jet radii. Many features of jets can be modeled by purely hydrodynamical simulations of jets (Norman *et al.* 1982a; Norman *et al.* 1982b; Norman and Smarr 1984; Williams and Gull 1984; Williams and Gull 1985; Wilson and Falle 1985; Arnold and Arnett 1986). However, in some observed jets, the minimum internal pressure appears to exceed the maximum external gas pressure as deduced from X-ray observations (*e.g.*, 4C32.69)(Wardle and Potash 1982). Although purely hydrodynamic jets can be locally overpressured with respect to the ambient medium by internal shocks, extensive high-pressure regions in jets probably require toroidal magnetic fields.

However, fluid jets and magnetically confined plasmas are separately known to be unstable to linear perturbations, and present indications are that this is just as true of the combination (Payne and Cohn 1985). The dominant, short wavelength, linear instabilities of high Mach number MHD jets are high-order reflection pinch (m=0) and kink (m=1) modes. However, these may not be globally disruptive to the jet. If they saturate at a finite level, then they may be responsible for the quasi-periodic knots and bends seen in sources like M87. A nonlinear numerical treatment is required to determine this.

Numerical simulations of magnetized jets were carried out for the case of toroidal field only, using a two-dimensional axisymmetric MHD code (FLOW) developed jointly at Caltech and the Jet Propulsion Laboratory, which was run on the Cray XM-P at the San Diego Supercomputer Center. The goals were to study the role of magnetic fields in maintaining jet stability over a length of many jet

radii and to investigate potential signatures of jet structure. Such jet characteristics could provide information about physical conditions in the flow, including the Mach number, the matter density ratio, and relative magnetic and gas pressures. This investigation is being carried out using a time-explicit MHD code in which matter, energy, momentum, and toroidal magnetic field are injected into an unmagnetized ambient medium, and the magnetic jet which developed was examined. The goal is to determine the ability of a magnetic field to confine a jet over a distance of many (i.e. $\sim$ 40) jet radii, the relative importance of the pinch and kink modes, the relative importance of the reflection and fundamental modes, the development of knots and their relative spacing, and the scaling of knot spacing with Mach number. The results presented in this thesis are the first results from this investigation, and the analysis is not yet completed. In our simulations, we emphasize the transition case, in which the ratio of gas pressure to magnetic pressure $\beta \sim 1$. This complements the previously referenced work done on purely hydrodynamic jets ($\beta \sim \infty$), and the recent work done by Norman and collaborators on highly magnetized (*e.g.*, $\beta = 0.2$) jets (Clarke *et al.* 1986), which came to our attention after we had done most of our work. The addition of toroidal and, eventually, poloidal field increases the size of the parameter space of possible jets, especially considering the weak observational constraints on the true nature of the magnetic field in jets.

The present simulations, which include only the toroidal component of the magnetic field, and which also inject a jet from a nozzle into a uniform medium, were done as the first step in a more extensive project to model the development and evolution of magnetically generated jets on rotating accretion disks. Although the pinch effect in the toroidal field is by itself an important determinant of jet behavior, it must be remembered that the evidence of radio polarization studies

suggests that there are considerable amounts of poloidal field and tangled field in these jets, and they must be accounted for in a complete theory of radio jets. Our approach has been to progress slowly from gas jets to combined disk-jet models with full treatment of ordered fields, angular momentum, tangled fields, and radiative energy losses; the results presented here are "perturbations" to hydrodynamic models. It is far easier and safer to study simple systems and, as these are understood, use them to progress to an understanding of more and more complex systems. Likewise, it is far easier and safer to build a complex code from a simpler code by adding additional terms than to attempt to write and debug it from scratch. Much insight may be gained from these simplified numerical models, but it must always be remembered that poloidal and tangled magnetic fields do exist and that it is unlikely that extragalactic jets are initiated by being injected from a perfectly straight, rigid nozzle into a perfectly uniform medium. The present code may be considered as examining the behavior of a magnetized jet with a highly dominant toroidal field component at far distances from the accretion disk. The knowledge gleaned from these simulations is useful for understanding the relative importance of the toroidal magnetic field in confinement of jets and knots of greatly enhanced pressure residing in the jets, and as a basis for development of more complex algorithms to deal with additional force terms and the initial development of the jet.

2. Hydrodynamic Jets

The basic structure of hydrodynamic jets has been discussed extensively in the literature (Norman *et al.* 1982a; Norman *et al.* 1982b; Norman *et al.* 1984; Williams and Gull 1984; Williams and Gull 1985; Wilson and Falle 1985; Arnold and Arnett 1986; Zabusky 1984). We have performed hydrodynamic simulations, for testing purposes, along with magnetic simulations, and to discuss some points which have not been emphasized in earlier discussions.

The hydrodynamic jet models of Norman and collaborators simulate the injection of a nonrelativistic fluid of adiabatic index $\gamma = 5/3$ into a quiescent ambient medium of identical adiabatic index at supersonic velocities, imposing axisymmetry. These models cover the range of parameter space bounded by transonic to strongly supersonic flow ($1.5 \leq \mathrm{M_j} \leq 12$) and a very diffuse to rather dense medium ($0.01 \leq \rho_j/\rho_e \leq 10$). These computations are performed on a Cray, and are very demanding even for supercomputers; it is therefore difficult to investigate the full three-dimensional character of a real jet in any detail, since such calculations must generally be done using a very coarse grid. However, attempts at three-dimensional modeling by Williams and Gull (1985) and Arnold and Arnett (1986) are encouraging, and suggest that the two-dimensional approximation should correspond fairly well to actual three-dimensional results. Another serious consideration is the assumption of nonrelativistic flow; it is unclear whether this is an appropriate assumption, or how well these results would correspond to the behavior of a relativistic jet (Wilson and Scheuer 1983; Wiita 1978). One-sided powerful jets are generally believed to be mildly relativistic.

The parameter space traditionally used for hydrodynamic jet simulations is restricted to two dimensions — *density ratio*, $\eta \equiv \rho_j/\rho_e$, and *internal jet Mach number*, $M_j \equiv v_j/c_{sj}$ — by assuming that the *opening angle* $\theta = 0$ and that the

pressure contrast $K = 1$. This corresponds to a relaxed collimated jet in pressure equilibrium with the surrounding medium. The parameter space can be divided into three major regions (fig. 1) (Norman *et al.* 1982a). Heavy, slow jets move more or less ballistically. The jet structure is dominated by the ordinary mode Kelvin-Helmholtz instability, because the perturbations generated by interaction with the surrounding medium are relatively weak and slow, and the jet progresses along slowly until pinched off by the growth of internal modes. Faster and lighter jets are dominated by the reflection mode Kelvin-Helmholtz instability, in which more or less direct interaction with the surrounding medium excites shock patterns across the jet; this mode is less disruptive than the ordinary mode Kelvin-Helmholtz instability. The third region, which is in fact that which is believed to be the most applicable to powerful extragalactic jets, is the case of light supersonic jets with $M_j \geq 5$ and $\rho_j \leq 0.1\rho_e$; we display two examples, with $M_j = 5$ (fig. 2) and $M_j = 16.6$ (fig. 3), which correspond respectively to the Mach number and velocity in our early magnetic simulations. These jets build up a sheath or cocoon of shocked jet material, and so the jet itself interacts with the ambient medium only through an intermediary consisting of shocked jet material. This paper will be confined to a discussion of the cocoon dominated jets.

Numerical simulations of cocoon-dominated jets reveal five major regions (fig. 4); the *jet*, the *plug*, and the *cocoon* contain injected material, and the *shocked ambient medium* and the *quiescent ambient medium* contain material from the ambient medium. The jet is separated from the plug, or "beamcap", which is a relatively stagnant region containing shocked jet material, by the *terminal Mach disk*, typically a triple shock based on a strong planar shock extending over a considerable part of the central region of the jet, from which weaker oblique shocks branch forward and backwards across the jet and possibly into the cocoon. The

plug is separated from the shocked ambient medium by the *contact discontinuity.* Material from the outer part of the jet, which does not pass through the terminal Mach disk itself, flows outside of a conical slip surface in the *slipstream*, where it is diverted into the cocoon by passing through the *annular shock*, which is located near the outer edges of the contact discontinuity. The speed of advance of the jet is determined by the combined push of the strongly shocked material in the plug and the terminal annular shock against the resistance provided by the *bowshock.* The effective surface area of the jet over which ram pressure forces retard the advance of the jet is roughly measured by the area within the annular shock radius, R_w, which is given approximately (ignoring terms in M^{-2} describing the post-shock spreading of the flowlines) by

$$(\rho_j(v_j - v_s)^2 + p_j)R_j^2 \simeq (\rho_e v_s^2 + p_e)R_w^2 \tag{2.1}$$

where R_j is the radius of the injected jet, ρ_j and ρ_e are the density of the jet and the density of the ambient medium, v_j and v_s are the speed of the jet and the speed of advance of the bowshock, and p_j and p_e are the pressures in the jet and the ambient medium, which can be neglected for high Mach number flow. The speed of advance is then given by

$$\begin{aligned} v_s &\simeq \left[\left(\frac{\rho_e}{\rho_j}\right)^{\frac{1}{2}} \frac{R_w}{R_j} + 1\right]^{-1} v_j \\ &\sim \left(\frac{\rho_j}{\rho_e}\right)^{\frac{1}{2}} \frac{R_j}{R_w} v_j \end{aligned} \tag{2.2}$$

which implies that the radius of the annular shock — which is the effective radius over which momentum is transferred from the jet to the ambient medium — strongly influences the speed of advance of the jet. The length of the plug is also determined by the relative strength of the annular shock; if the annular shock is

strong, then it will advance more rapidly relative to the terminal Mach disk, and the plug will tend to increase in length.

The bowshock progresses into the ambient medium, but it is the shocked ambient material which directly retards the advance of the jet and confines the cocoon material. The cocoon confines and pinches the jet material, and so the structure of the jet is influenced by flow patterns in the cocoon. Disturbances in the jet propagate indirectly back into the jet as resultant disturbances in the cocoon.

The detailed evolution of a given volume of gas may be traced from its injection into the jet to its final coming to rest in the cocoon. The material usually travels with small deceleration by weak shocks until it reaches the terminal Mach disk. At this point, the histories diverge. Material near the axis passes through the terminal Mach disk and fills the plug. The generator of the plug is a conical slip surface along which flows the remaining gas, which has been weakly shocked by oblique shocks associated with the terminal Mach disk. This material is deflected back into the cocoon by a annular shock surrounding the contact discontinuity. Meanwhile, the material in the plug flows back into the cocoon. The inflation of the cocoon is accompanied by the convergence and divergence of streamlines within the cocoon, which regenerates supersonic flow in accordance with Bernoulli's principle and mass conservation. Thus, secondary shocks form in the cocoon, which would serve as natural sites for particle reacceleration in the case of a synchrotron-emitting radio lobe. The vorticity generated by the secondary shocks and the oblique terminal shocks is shed as vortex rings centered on the jet, creating large-scale regions of poloidal flow along the jet which may then excite the weak jet shocks observed in the simulations. Vorticity of both senses is shed by this process, with most of the vorticity generated near the front of the jet. Vortices are shed into the body of the cocoon quasi-periodically, in a way which is apparently related to

the strength of the terminal shock and the subsequent kinetic power transmitted to the annular shock; this causes the size of the plug to fluctuate in a correlated manner. The vortices themselves remain relatively fixed after they are shed, i.e., there is little net momentum transport in the cocoon. Thus, the cocoon can be characterized as a large region of shocked jet material containing large-scale vortices which may interact with the unshocked jet material to excite internal jet structure.

If the cocoon is stagnant, it is in rough pressure equilibrium with the post-bowshock ambient material. The cocoon plus the shocked ambient medium inflate to some radius R_{ce}. This radius can be estimated by considering the transport of energy into the cocoon. The energy flux along the jet is $L \sim \frac{\pi}{2}\rho_j v_j^3 R_j^2$, where the gas pressure is small relative to the kinetic energy and can be neglected. The energy flux into the cocoon and shocked ambient medium, minus the outward flux of energy originally resident in the region, is roughly equal to the increase in enthalpy, $\pi\gamma\bar{p}_{ce}/(\gamma-1)(R_{ce}^2 - R_j^2)v_s$, where $\bar{p}_{ce}$ and R_{ce} refer to the pressure and radius of the cocoon and shocked ambient medium taken together. If the cocoon is stagnant, then $\bar{p}_{ce} \sim \bar{p}_c$. The outward flux of energy originally resident in the region is simply $\pi p_e/(\gamma-1)R_{ce}^2 v_s$. Therefore,

$$\begin{aligned} R_{ce} &= R_j \left(\frac{(\gamma-1)\rho_j v_j^2}{2\gamma\bar{p}_c + 2p_e} \frac{v_j}{v_s} + 1 \right)^{\frac{1}{2}} \\ &= R_j \left(\frac{[\gamma(\gamma-1)M_j^2]p_j}{2(\gamma\bar{p}_c + p_e)} \frac{v_j}{v_s} + 1 \right)^{\frac{1}{2}} \end{aligned} \tag{2.3}$$

For $v_s = 2$, $M_j = 5$, $p_j = p_e$, and $\bar{p}_c = 2p_e$ (which is what we measure in our simulations), then $R_{ce} \sim 7.5R_j$, in rather poor agreement with the simulations. This discrepancy suggests that one of the basic assumptions in this derivation is

in error, namely, the cocoon is not stagnant but is dynamically active, and hence a considerable fraction of the energy is in local kinetic motion (vorticity).

The bowshock (if strong) advances through the quiescent ambient medium at a velocity of $v_s \simeq v_j(\rho_j/\rho_e)^{\frac{1}{2}}(R_j/R_w)$ (eq. 2.2). If the jet is initially in pressure equilibrium with the ambient medium, then $p_j = p_e$ and $c_{se}/c_{sj} = \sqrt{\rho_j/\rho_e}$. The Mach number of a strong bowshock can then be simply related to the Mach number of the injected jet material by

$$\begin{aligned} M_s &= \frac{v_s}{c_{se}} \\ &= \frac{v_j}{c_{sj}}\frac{R_j}{R_w} \\ &= M_j\frac{R_j}{R_w} \end{aligned} \tag{2.4}$$

The Mach number of the bowshock is therefore proportional to the Mach number of the injected jet, with the coefficient given by the ratio of the radii of the jet and the contact discontinuity. Conversely, the effective radius of the contact discontinuity can be defined by $R_w^{(\mathrm{eff})} \equiv (M_j/M_s)R_j$. In our simulations, this corresponds roughly to the radius of the annular shock, which confirms that the contact discontinuity is confined to this region, and that the advance of the bowshock is due to the combined push of the plug and the annular shock. For a weak bowshock, the actual value of R_w will be somewhat smaller than the estimated value.

After the transients die out, the bowshock generally turns out to be weak, with $M_s \sim 1.5$. The usual model for the advance of the bowshock matches the front of the jet directly to the bowshock (fig. 5), so that the full strength of the jet is applied over the area of the jet. In this case, $R_j = R_w$, and so $M_s = M_j$. However, if the bowshock remains strong, then the entire jet must also be strongly shocked at the terminal Mach disk, releasing almost all of the kinetic energy of the jet as internal energy. The post-shock pressure in the jet material, $\sim \rho_j v_j^2$, is

greater than the pressure in the cocoon (which is comparable to the pressure in the unshocked jet) of order $O(M_j^2) \gg 1$. The jet gas would have to decompress substantially upon flowing into the cocoon. At the same time, the cocoon gas near the working surface must have the same pressure as the shocked ambient medium, which is $\sim \rho_e v_s^2 \sin^2 \psi$, where ψ is the angle between the shock normal and the symmetry axis. This varies by only a factor of order 2, and so a strong radial pressure gradient cannot be supported. However, the sound speed in the cocoon is larger than the speed of advance of the bowshock, and so any large gradients may be reduced by subsonic flows; if this is used to define a scale height for gradients, $\lambda \equiv (c_s^2/v_s^2)L_{jet}$, then the scale height is longer than the jet, and large-scale gradients cannot be supported. There are two solutions. One is to spread out the contact surface between the jet and the bowshock, i.e., let $R_w > R_j$. Then, the post-shock pressure of the jet material is $\sim 2p_e$, allowing the shocked material to flow into the cocoon transonically and maintain pressure equilibrium with the jet. The other possibility is, that the post-shock jet material should not turn back into the cocoon, but should continue ahead of the jet, pushing the bowshock ahead of the terminal Mach disk shock (fig. 6). Simulations indicate that the former behavior invariably occurs in purely hydrodynamic jets (fig. 4). The jet is blunted by the deflection of the outer part of the jet at the oblique shocks flanking the Mach disk, causing the jet fluid to diverge while maintaining its supersonic speed. To prevent the cross-sectional area of the jet from increasing too much (since a diverging flow would counteract the blunting of the jet by accelerating the flow), the central regions of the jet are not diverted outward, but form the dense plug of strongly shocked jet fluid. In fact, the diverted region of the jet could be interpreted as locally blunting the jet, and the central region of the jet could be interpreted as pushing a region of shocked gas ahead of it rather than backflowing

into the cocoon; that is, both behaviors suggested may be seen in different parts of the jet, and the question really is, what fraction of the jet backflows into the cocoon, and what fraction stagnates in front of the jet? For a given jet, this appears to vary, as seen by the different rates of advance of the bowshock and the terminal Mach disk (fig. 7).

The bowshock itself curves considerably, especially outside the radius of the contact discontinuity, and the ambient material which passes through the bowshock at large radii is shocked obliquely. For a strong bowshock, the material passing through the bowshock at an normal angle greater than $\tan^{-1}(1/2) = 27°$ will still be locally supersonic; for a weaker bowshock, this angle decreases. This material usually undergoes subsequent shocking, forming standoff shocks upstream of the plug or cocoon (fig. 8).

3. Magnetohydrodynamic Jets

Magnetohydrodynamic jets differ from hydrodynamic jets in the addition of two force terms, the magnetic pressure and the magnetic tension. The magnetic pressure behaves like an isotropic pressure in which $p_m \propto \rho^2 r^2$, and is analogous to the gas pressure. The magnetic tension is a qualitatively different force term, insofar as it acts even in the absence of magnetic gradients, is directed only in the radial direction, and is always directed inwards toward the axis. The magnetic gradient and magnetic tension forces may both influence the flow, even if the magnetic pressure itself is much smaller than the gas pressure; if the gas pressure gradients are small, then the magnetic tension will dominate in the absence of gradients, and the gradient and tension forces will together dominate the flow dynamics if the magnetic gradients are larger than the gas pressure gradients, whatever the value of the gas pressure.

3.1. Magnetic Confinement and Focusing

As discussed in the introduction, the observational evidence implies that a number of extragalactic jets cannot be confined by the thermal pressure of the surrounding ambient medium. This confinement could be provided by magnetic fields (*e.g.*, Blandford 1976; Benford 1978; Chan and Henriksen 1980; Achterberg *et al.* 1983). To understand how magnetic fields may confine a jet, consider a highly magnetized jet ($\beta \ll 1$) which carries a net current I. It will be surrounded by a magnetic field $B_\phi = 2I/cr$. Let the return current flow at some distance from the axis, $R_{ret} \gg R_j$. The magnetic stress at the jet boundary is directed inward, and is equal to $I^2/2\pi c^2 R_j^2$, whereas the magnetic stress at the radius of the return current is directed outward, and is less than the stress at the jet boundary by a factor of $(R_j/R_{ret})^2$. If the return current were to flow along the outer boundary

of the jet cocoon, and the cocoon were to extend out to 10 jet radii — a large but not unreasonable value — then the ratio of the stresses is of order 100. Clearly, this is a drastic oversimplification, but serves to illustrate the possible importance of magnetic confinement.

Magnetic confinement will not occur if the magnetic pressure is too weak. However, if the jet propagates with a nonzero opening angle (such as might happen in the case of an extragalactic radio jet propagating in the outer part of the ISM), the adiabatic expansion of a jet which contains a significant quantity of toroidal field will eventually cause the pressure due to toroidal magnetic field to dominate over the pressure due to the poloidal magnetic field and the gas pressure. This can be seen from conservation of magnetic flux. In a cylindrical cross-section of the jet, the scaling for a given expansion of the jet is $B_{\phi 0} \propto \rho R_j$, where $\rho \propto R_j^{-2}\Delta z^{-1}$, and $B_{z0} \propto R_j^{-2}$. Therefore, $p_{m\phi 0} \propto R_j^{-2}\Delta z^{-1}$ and $p_{mz0} \propto R_j^{-4}$. Since $p_g \propto \rho^\gamma$, then $p_g \propto R_j^{-2\gamma}\Delta z^{-\gamma}$. The toroidal magnetic pressure will always be amplified over the gas pressure by an adiabatic expansion, and will be amplified over the axial magnetic pressure if the radial fractional expansion rate is greater than half of the axial expansion rate, i.e., $(dR_j/R_j) > \frac{1}{2}(d\Delta z/\Delta z)$. Thus, the tendency will be for the toroidal magnetic pressure to be amplified relative to the poloidal magnetic pressure and the gas pressure by an expansion, and the dominant component of the large-scale magnetic field should therefore be the toroidal.

The toroidal field in the jet will be advected either into the plug beyond the terminal shock or into the cocoon; since the terminal shock is located near the axis, where the toroidal field is necessarily weak by symmetry, then the major portion of the magnetic flux associated with the toroidal field should be advected into the cocoon. If the jet is light enough to have a significant cocoon, then the magnetic flux supplied to the cocoon may serve to focus the jet. For illustration, consider

a jet containing a toroidal magnetic field of strength $B_{\phi j}$ at its outer radius R_j, and a cocoon containing a toroidal magnetic field of strength $B_{\phi c}$ near its inner radius (also R_j), with an outer radius (where the return current flows) of R_{ret} If the cocoon pressure is negligible, then pressure balance at the jet boundary would impose $B_{\phi c} \sim \sqrt{1+\beta_j} B_{\phi j}$, where $\beta \equiv p_g/p_m$. If the current in the jet is uniform, then $B_{\phi j} \propto r$, and the flux per unit length in the jet is $\pi B_{\phi j} R_j$. If the current in the cocoon flows along the outer boundary, then $B_{\phi c} \propto 1/r$, and the flux per unit length in the cocoon is $2\pi B_{\phi c} R_j \ln(R_{ret}/R_j)$. The jet flows at speed v_j, and the cocoon extends axially at speed v_s behind the bowshock, so equating the magnetic flux transport along the jet with the flux transport into the cocoon gives

$$\pi B_{\phi j} R_j v_j \simeq 2\pi B_{\phi c} R_j \ln(R_{ret}/R_j) v_s \tag{3.1}$$

For the models and observed sources, $\ln(R_{ret}/R_{jet}) \leq 3$, $\beta_j \leq 1$, and $v_s \simeq 2$; if this is expressed in terms of the Mach numbers of the bowshock and the jet, assuming that the jet and the ambient medium are initially in pressure equilibrium of some sort, then

$$M_s \sim M_j \left(\frac{\rho_e}{(1+\beta_j)\rho_j} \right)^{\frac{1}{2}} \left(2\ln(R_{ret}/R_j) \right)^{-1} \tag{3.2}$$

within a factor of order one, depending on how strongly the magnetosonic speed in the jet is determined by the magnetic field. If the return current is distributed throughout the cocoon by turbulent diffusion, this result is slightly modified, but still remains roughly true for large R_c/R_j.

If $M_j = 5$ and $\rho_j = 0.1\rho_e$, then the above estimate suggests that the return current must flow at a radius on the order of $100R_j$ if the magnetic field in the cocoon alone is to confine the jet; otherwise, the cocoon cannot hold the magnetic flux which is flowing into it, for a nominal value of M_s near unity. These large cocoons are not observed in simulations. If the jet is not strongly magnetized,

then the magnetic field does not confine the jet, and the above derivation does not apply. Likewise, if the ambient medium is initially magnetized, then the return current may be removed arbitrarily far from the jet without expanding the cocoon, and the above derivation also does not apply. However, if the jet is sufficiently magnetized that the magnetic stresses dominate over the gas pressure, and the ambient medium is unmagnetized, then a large proportion of the magnetic flux must be stored outside of the cocoon, or the effective radius of the jet must be reduced by pinching.

The pinching or overconfinement of the jet may be applied uniformly or locally. If the magnetic stress were to be applied uniformly over the entire jet, the jet would simply compress, reducing the value of β within the jet. However, large-scale vortical motions in the cocoon, if not suppressed by the magnetic stresses, would transport the field along with the flow field, and would advect the magnetic field along the boundaries between vortices. This would cause the field to be transported radially inward to the jet boundary when the flow field is directed inwards, causing localized pinches. However, even if the pinch excites a strong shock, effectively terminating the flow, the jet may continue on as a result of magnetic focussing (Achterberg *et al.* 1983).

A similar effect occurs if the magnetized material accumulates in the plug rather than in the cocoon. The post-shock flow may still be focussed by the resident field, and so an extensive region of shocked magnetized material may be pushed forward ahead of the flow. This has been observed in a magnetically dominated (*e.g.*, $\beta = 0.2$) jet simulation. Note that this is an alternative to the development of an annular shock, as discussed in Section 2; in fact, the highly magnetized jet can be interpreted as a jet with a small cocoon and a large plug.

Magnetic effects will exert more influence on the flow for light ($\rho_j/\rho_e \leq 0.1$) supersonic ($M_j \gg 1$) jets. Dense magnetized jets are dominated by inertia rather than pressure, and the presence of a magnetic field should have little influence on the dynamics in the jet unless the field is very large; for $\rho_j/\rho_e \geq 1$, the jet propagates ballistically through the surrounding medium. Astrophysical jets appear to be light and supersonic, and so this study will be restricted to such jets.

3.2. Magnetic Profiles

The purpose of this study is to examine the effects of magnetic pinching on the development of the jet when the magnetic pressure is comparable to the gas pressure, i.e., in the transition between magnetic and gas dominated flows. The injected profiles of the models are constant for the density and axial velocity, and vary with radius for the magnetic field and gas pressure in such a way as to impose stress balance within the jet and at the jet boundary. The flow is assumed to be adiabatic except at shock fronts, with an adiabatic index of $\gamma = 5/3$ in both the jet and the ambient medium.

There are two general restrictions placed on the possible radial profiles for toroidal magnetic field. One is that the toroidal field must be antisymmetric in the Cartesian sense near the axis, i.e. the field forms closed loops centered on the symmetry axis. It must therefore go to zero on the axis. The requirement of a finite current density along the axis imposes the additional condition that $B_\phi \propto rf(r)$, where $f(r)$ is nonincreasing as $r \rightarrow 0$. Finally, the requirement of a finite total current imposes the condition that $B_\phi \propto g(r)/r$, where $g(r)$ is nonincreasing as $r \rightarrow \infty$. In short, the magnetic field must increase at least linearly near the symmetry axis, and must fall off as $1/r$ far from the symmetry axis.

The magnetic and gas pressure profiles were chosen by selecting a magnetic profile and then calculating the proper gas pressure profile to impose stress balance. Both linear and parabolic magnetic profiles were chosen, in order to test the sensitivity of the results to the location of the return current.

The linear distributions for magnetic field and pressure were:

$$B_\phi(r) = B_{\phi 0}\frac{r}{R_j}, \qquad \text{for } (0 \le r \le R_j) \tag{3.3}$$
$$= 0 \qquad \text{otherwise}$$
$$p(r) = p_e + \frac{B_{\phi 0}^2}{8\pi}\left[1 - 2\left(\frac{r}{R_j}\right)^2\right], \qquad \text{for } (0 \le r \le R_j) \tag{3.4}$$
$$= p_e \qquad \text{otherwise}$$

where the model run used $B_{\phi 0}^2/8\pi = 0.5p_e$, i.e. the magnetic pressure equaled the gas pressure on the jet boundary. The magnetosonic speed was given by

$$\begin{aligned} c_m &= \left(\frac{\gamma p_g}{\rho_j} + \frac{B_\phi^2}{4\pi\rho_j}\right)^{\frac{1}{2}} \\ &= \left[\frac{\gamma p_e}{\rho_j} + \frac{\gamma B_{\phi 0}^2}{8\pi\rho_j} - (\gamma - 1)\frac{B_{\phi 0}^2}{4\pi\rho_j}\left(\frac{r}{R_j}\right)^2\right]^{\frac{1}{2}} \end{aligned} \tag{3.5}$$

The model was run for $\gamma = 5/3$, with $\beta_j = 1$ at R_j, and so $B_{\phi 0}^2 = 4\pi p_e$. In this case, the magnetosonic speed dropped monotonically by 24% between the symmetry axis and the edge of the jet. The velocity was selected so that the Mach number at the jet axis $M_j = 5$, and a density ratio $\rho_j/\rho_e = 0.1$ was chosen to ensure that the resulting model would be cocoon-dominated. One of the implications of this profile is that the return current flows outside the jet; initially, it forms a surface current flowing along the outside of the jet, but the development of a magnetized cocoon moves some of the return current away from the jet, which helps to induce magnetic confinement.

The parabolic distributions for magnetic field and pressure were:

$$B_\phi(r) = B_{\phi 0}\frac{r}{R_j}\left(1-\frac{r}{R_j}\right), \qquad \text{for } (0 \le r \le R_j) \tag{3.6}$$
$$= 0 \qquad \text{otherwise}$$
$$p(r) = p_e + \frac{B_{\phi 0}^2}{8\pi}\left[\frac{1}{6} - 2\left(\frac{r}{R_j}\right)^2\right. \tag{3.7}$$
$$\left. + \frac{10}{3}\left(\frac{r}{R_j}\right)^3 - \frac{3}{2}\left(\frac{r}{R_j}\right)^4\right], \qquad \text{for } (0 \le r \le R_j)$$
$$= p_e \qquad \text{otherwise}$$

where the specific model used $p_m = p_g$ at $r = \frac{1}{2}R_j$, i.e., $B_{\phi 0}^2/8\pi = 96p_e/7$. The magnetosonic speed was given by

$$c_m = \left(\frac{\gamma p_g}{\rho_j} + \frac{B^2}{4\pi\rho_j}\right)^{\frac{1}{2}}$$
$$= \left[\frac{\gamma p_e}{\rho_j} + \frac{B_0^2}{8\pi\rho_j}\left(\frac{\gamma}{6} + 2(1-\gamma)\left(\frac{r}{R_j}\right)^2\right.\right. \tag{3.8}$$
$$\left.\left. + \left(\frac{10\gamma}{3} - 4\right)\left(\frac{r}{R_j}\right)^3 + \left(2 - \frac{3\gamma}{2}\right)\left(\frac{r}{R_j}\right)^4\right)\right]^{\frac{1}{2}}$$

which varied considerably over the jet, with a maximum at the symmetry axis and a minimum at the jet boundary. As before, a Mach number on axis of $M_j = 5$ and a density contrast of $\rho_j/\rho_e = 0.1$ were used to ensure that the model would be cocoon-dominated. One of the implications of these profiles is that all of the return current flows within the outer third of the jet. As the jet develops, and magnetic flux builds up in the cocoon, closed current loops form in the cocoon, which should cause similar behavior to the case in which the cocoon carries a net current. This was indeed observed in the simulation which was run; the buildup of flux in the cocoon allowed currents to flow outside of the jet.

A serious questions arises in terms of the magnetic field in the ambient medium; a sufficiently strong external magnetic field may, in conjunction with the internal

field of the jet, be sufficient to confine the jet independent of any external gas pressure. The most natural assumption is that the external field contains no large-scale ordered field, and that the confinement is by magnetic field which has been advected into the cocoon. However, one model with a moderate linear magnetic field in the jet, matched at the boundary by a magnetic field which falls off as $1/r$, has been run. The flow proved to be well-confined, with large overpressures on the axis, and was well-collimated. This again illustrates the possibilities for jet confinement when even part of the return current is moved to radii much larger than the jet radius.

3.3. Diagnostic Methods and Graphics

The purpose of carrying out these detailed calculations was to understand the physical processes occurring in jets on both a qualitative and semi-quantitative level. To this end, it has proven essential to display the proper quantities, such as entropy and velocity, as well as the primary quantities. Indeed, this is one of the advantages of numerical simulations; the value of every physically significant quantity in the calculation may be made available for analysis, whereas for experimental (and even more so, observational) jets, there is only a limited amount of information available. Further plans include the generation of movies.

The display summary which has been found most useful has been the superposition of shocks, contact discontinuities, and slip lines (represented as various types of line drawings) on a vector representation of the velocity field (fig. 9). Shocks are most conveniently located on plots of negative velocity divergence, and their character (strong/weak, gas/magnetic) can be determined by examination of plots of entropy, gas pressure, and magnetic pressure. Contact discontinuities can be followed very clearly through the use of plots of the magnetic field strength

and density, even in the case of a magnetized external medium. In regions where the field is weak, such as the front edge of the plug, vector representations of the current density have proven helpful as well. The close correspondence between the density and magnetic field plots testifies to the low numerical diffusive in the magnetic advection. The slip surfaces can generally be identified by examination of the velocity vectors, and are associated with discontinuous velocity changes perpendicular to the direction of the local flow field.

Another useful diagnostic of the flow is the vorticity. According to Kelvin's Theorem, vorticity will be advected along the fluid in the same manner as the magnetic field lines in the absence of poloidal field. Sources of vorticity may be associated with oblique shocks and with slip lines. At the same time, vector and streamline representations of the velocity and current fields serve to display the vorticity, and in particular current reversals along vortex boundaries are generally a good indication of magnetic pinching.

4. Propagation of a Moderately Magnetized Jet

The jet model with $M_j = 5$, $\rho_j/\rho_e = 0.1$, and a linear magnetic profile with the ratio of gas pressure to magnetic pressure $\beta = 1$ at the boundary of the jet has been run to time $t = 160\Delta r/\sqrt{p_e/\rho_e}$ on a grid which expands with the jet, to a maximum extent of 150×560. The injected jet is 15 zones wide, and so the final length of the jet (including bowshock) is $37R_j$.

The main features in the magnetized model are similar to the main features in the hydrodynamic models (figs. 10-13) The core of the jet terminates in a Mach disk, while the outer parts of the jet pass through two oblique shocks radiating from the Mach disk and terminate at an annular shock. The shocked jet is separated from the shocked ambient material by a contact discontinuity, which is separated from the unshocked ambient material by the bowshock. The rate of advance of the bowshock, contact discontinuity, and Mach disk are shown in Figure 14. The outer bowshock moves at a steadily decreasing speed, consistent with there being some mild level dissipation in the jet itself, mostly due to weak shocks. At early times, little dissipation or expansion of the jet has occurred, and so $R_j = R_w$. Equating the momentum flux in the jet and the bowshock (eq. 2.2) gives $v_s \simeq 6\sqrt{p_e/\rho_e}$, or $M_s = 4.7$, in good agreement with the observed speed of about $7\sqrt{p_e/\rho_e}$. By the end of the simulation, at time $t = 160\Delta r/\sqrt{p_e/\rho_e}$, the jet is advancing at only $2\sqrt{p_e/\rho_e}$, which corresponds to a Mach number of $M_s = 1.5$, and so the bowshock is only mildly supersonic. Since the thrust in the jet remains constant, the jet must transfer its momentum to the bowshock over a contact discontinuity of radius 3 R_j. The flow pattern verifies this; in fact, the annular shock is located at this radius, which supports the contention that the annular shock defines the effective area of the contact discontinuity. Comparison with the gas case indicates that even a weakly magnetized jet advances more quickly than an unmagnetized jet.

This is a consequence of the confinement of the slipstream, so that the momentum transfer is kept within a smaller radius. If the jet is so highly magnetized that the shocked jet material accumulates in front, then much of the advance of the jet is due to the accumulation of material upstream of the terminal Mach disk; the terminal Mach disk itself does not appear to advance much farther than in the weakly magnetized jet.

The contact discontinuity follows the bowshock with a separation of roughly $2-4R_j$ (fig. 14). The flow of the shocked external medium between the bowshock and the contact discontinuity is correspondingly simple, although weak shocks are present, especially away from the axis where the bowshock is oblique and the post-shock flow is still supersonic relative to the bowshock (fig. 8). This is also seen in unmagnetized jets, as would be expected, since the gas involved is unmagnetized in both cases. However, the terminal shock advances in a very irregular manner, occasionally even retreating back along the jet. It follows behind the bowshock at distances ranging from $2R_j$ to $12R_j$ (fig. 14). When the following distance is large, there is an extended column of strongly shocked jet fluid, bounded by slip lines which bound the flow of the weakly shocked outer jet material to the annular shock (fig. 15). The large extent of the plug is peculiar to magnetized jets, and seems to be a consequence of magnetic confinement.

The fluid in the plug no longer derives solely from jet material which has passed through the terminal shock, but is augmented by material from the outer jet which has passed through the annular shock (fig. 16). This material is diverted into the plug by the magnetic pressure gradient; even though the gas pressure is larger than the magnetic pressure at this point, the gas pressure gradient is much smaller than the magnetic pressure gradient. The interaction between the plug and the flow out to the annular shock is what influences the relative position of the

terminal shock. When the plug reaches a certain length, partially due to backflow from the annular shock, then the flow out to the annular shock becomes unstable. When this flow breaks up, the material in the plug quickly combines with the material in the bounding flows and empties back into the cocoon, accompanied by the shedding of a large ring vortex which rotates in the opposite sense to the vortices which accompany the steady diversion of jet material into the cocoon at the annular shock.

The backflow from the annular shock into the plug appears to be distinctive of magnetized jets. Because the behavior of the flow at the annular shock differs between magnetized and unmagnetized models, one might naively expect that the toroidal field should dominate at the annular shock, and there is a good argument for this. Consider the expansion of a ring of magnetized jet material, which has been deflected by the weak oblique shocks outwards toward the annular shock. Since the shocks are weak, the flow is approximately adiabatic, and so $p_g \propto \rho^\gamma$. However, conservation of mass and conservation of magnetic flux give $B_\phi \propto \rho r$. Therefore, the ratio of gas pressure to magnetic pressure will vary as $\beta \equiv 8\pi p_g / B_\phi^2 \propto \rho^{\gamma-2} r^{-2}$; for $\gamma = 5/3$, $\beta \propto \rho^{-\frac{1}{3}} r^{-2}$. Now, assume that the ring has radial thickness Δr; conservation of mass dictates that $\rho r \Delta r =$ constant, and so $\beta \propto r^{-\frac{5}{3}} \Delta r^{\frac{1}{3}}$. In the case of the annular shocks observed in the simulations, the radius increases by a factor of 2-4 whereas the width of the outer flow region Δr remains more or less constant. Given a ratio of gas pressure to magnetic pressure of β_j in the outer part of the jet, then at the annular shock, $\beta \sim (0.1 - 0.3)\beta_j$ is expected.

The results of the simulation indicate that this model is oversimplified. The immediate pre-shock material at the annular shock has $\beta = 2$, and the mean value of β in the outer two-thirds of the jet is about 3-4, which still gives an

estimate of $\beta \simeq 1$ at the annular shock. Note, however, that the entropy of the pre-shock material is two to three times larger than the entropy of the jet material. Examination of the slipstream (figs. 17-19) reveals that the flow converges as it is diverted outwards toward the annular shocks, with the compression clearly visible in the magnetic field; in fact, that particular point appears to be the intersection of two weak shocks, one of which radiates from the terminal Mach disk, and the other which originates at the edge of the jet and turns the flow parallel to the neighboring vortex. These two shocks, although individually weak, when taken together can provide sufficient net dissipation to increase β to the observed value.

4.1. Cocoon Dynamics and Pinching

The strongest pinches in the jet, as determined by both gas pressure and magnetic field, occur in conjunction with the edges of vortices in the cocoon (fig. 20). A simple model (Section 3.1) has already been discussed to demonstrate how the cocoon may influence the large-scale magnetic confinement in the magnetically dominated case. Pinching may be viewed as localized enhanced confinement, and so it is not unreasonable to expect that the cocoon structure should influence the strength and location of pinches. This requires that the cocoon be considered, not as a passively filling balloon of spent gas, but as a dynamically active and influential region (Zabusky 1984), a view which is borne out by the simulations and has observational ramifications.

The general structure of the cocoon is complex, with large vortices of considerable strength distributed along its length. The sense of the vortices alternate, and streams with considerable velocity flow through the cocoon between the vortices. Shocks are also seen in the cocoon (fig. 21). It is not at first apparent why these

secondary shocks should be able to form, since the material is moving subsonically as it passes into the cocoon. However, material in the cocoon may expand adiabatically to the point where it becomes locally supersonic. Surprisingly, these shocks do not appear to be strongly associated with the vortex flow. In particular, the shocks do not appear to be associated with de Laval nozzles formed at vortex boundaries, as one might expect.

The sense of the current in the vortices does not alternate like the velocity, but always rotates clockwise, causing a net current to flow along the outer edge of the cocoon. This outer current may be a key factor in the overall confinement of the jet. Furthermore, the currents at the edges of the vortices oppose each other, yet do not appear to cancel; this corresponds to magnetic field extrema at the edges of the vortices. Since the velocities at the edges of vortices are in the same sense, there is a net radial inflow of material in the same location as the magnetic field extrema, so that magnetic field and momentum are advected into the edge of the jet. In the moderately magnetized case, the magnetic stress contribution is small, and the pinching is in response to the momentum transport at the boundaries of the vortices. A relatively strong oblique shock is formed across the jet at the pinch (fig. 20). Note also that this behavior is not limited to the cocoon; shocks may also form within the plug, which may at times show considerable dynamical activity (fig. 22).

4.2. Pressure Contrasts

One of the primary arguments for magnetic fields in extragalactic radio sources is that there are large brightness contrasts observed in radio jets, which implies that there are localized high pressure regions in jets, which cannot be confined by the surrounding medium. Of course, these could be transient features, in which

case they need not be confined, but then the question remains as to how they form in the first place. If all of the jet could be dissipated at one standing shock, then the post-shock pressure would be $p_{gknot} \leq 2\rho_j v_j^2/(\gamma+1) \simeq 2\gamma M_j^2 p_{j0}/(\gamma+1)$, where $p_{j0} = \frac{3}{2}p_e$ for $\beta_j = 1$ to enforce stress balance. For $M_j = 5$ and $\gamma = 5/3$, $p_{gknot} \leq 47p_e$. The maximum pressure contrasts observed in the hydrodynamic models was of the order of 15:1, which is consistent with the observation that less than a third of the jet material in the hydrodynamic simulations passes through the terminal shock; the key to obtaining large pressure contrasts is to concentrate the dissipation.

The magnetic field increases the actual pressure ratio by confining the flow, so that more may be dissipated in a given localized region. This may occur directly or indirectly. For the $\beta = 1$ jet, the pressure enhancement is caused by a combination of the two, but appears to be primarily an indirect result of the dynamics in the cocoon and the annular shock.

Knots may develop either along the jet at pinches, which are associated with radial inflow along vortex boundaries in the cocoon, or at the head of the jet (fig. 13). Both types of knots are clearly transient. The knots which occur at pinches appear to be stronger, with overpressures ranging from 12:1 to 38:1. The knots at the plug are generally weaker, ranging from 12:1 to 20:1. One reason for this is that they are located downstream from the pinches, and so the initial dissipation occurs before the jet material reaches the plug. At the same time, the regions of high overpressure appear when the plug is expanding, i.e., when the terminal Mach disk has ceased to advance (fig. 23). The question is, whether the terminal Mach disk has ceased to advance because the shocks in the jet dissipate energy and momentum, or whether the shocks occur in the jet because the stationary terminal Mach disk increases the column loading on the jet, or whether the shocks occur

in the jet as a result of cocoon activity, which is associated with vortex shedding at the annular shock. All three could be coupled, as well. The process by which the behavior of the terminal Mach disk and the knots in the body of the jet are related is not clear, although it does appear that there is some connection.

The knots which form at pinches tend to be "X"-type shocks rather than Mach disk triple shocks, i.e., the pressure enhancement occurs at the terminus of two relatively strong oblique shocks. They may be isolated, or may be associated with a string of shocks extending downstream from the pinch. They are clearly stationary with the vortex, and may last from 5 to 15 time units. The knots at the plug tend to be radially extended, and are generally rounded at the downstream edge. There is often a secondary shock located upstream, associated with the backflow into the plug from the annular shock. The plug knot in this simulation lasted for 60 time units before being superseded by a new plug knot.

The life cycle of the typical plug knot has three stages. In the formation stage (fig. 24), the plug is unextended, and the annular shock is located close to the axis. The contact discontinuity is pushed up against the bowshock by the highly collimated flow into the annular shock. The terminal Mach disk is a curved surface with no attendant oblique shocks. This stage lasts from 10 to 15 time units. During this time, the vortices in the cocoon excite relatively strong shocks in the jet.

During the growth stage (fig. 20), the plug grows in length, and the annular shock moves radially outward and axially forward relative to the terminal Mach disk. The terminal Mach disk develops attendant oblique shocks, which begin to bend the slipstream outward. At the end of this stage, the plug is close to its maximum length. There is some backflow into the plug during this stage. The

development stage lasts for about 25 time units, and shocks of moderate strength form at pinches along the jet.

The breakup stage (fig. 25) begins with as backflow into the plug develops into a reverse vortex. As the reverse vortex grows, the slipstream lengthens, the terminal Mach disk shrinks, and the annular shock moves radially outward. The weak terminal Mach disk advances forward as the annular shock breaks up and the forward and reverse vortices are shed into the cocoon (fig. 26). As the vortex shedding is completed, shocks develop in the cocoon (fig. 10). This stage lasts about 25 time units, and a large number of weak shocks form along the entire length of the jet. At the end of the breakup stage, a new terminal Mach disk begins to develop, i.e., the formation stage begins again.

Four things are clear from an analysis of the contour plots. Firstly, the moderately magnetized model is better collimated than the equivalent hydrodynamic model, as evidenced by its speed of advance. Secondly, the process of plug growth and vortex shedding is more pronounced in magnetized jets than in the unmagnetized jets. Thirdly, the cocoon actively excites knots (local pressure maxima) in both the magnetized and unmagnetized models; the maximum overpressures were obtained at the knots along the jet, which were excited by the net flow of radial momentum at the vortex boundaries, not by the magnetic field. Fourthly, the behavior of the plug and the speed of advance are controlled by radius of the annular shock, as is the vortex shedding (which is the ultimate cause of the pinching of the jet). Even though the magnetic pressure is considerably less than the gas pressure throughout the entire grid, the magnetic field dominates the radial dynamics of the annular shock, simply because there is no significant radial gradient in the gas pressure at the annular shock, whereas there is a pronounced radial gradient in the magnetic pressure. The important point here is that the dynamics of the jets

is determined, not only by the sizes of quantities, but also how they are applied. A large gas pressure has less effect than a weak magnetic pressure if the gradient in the gas pressure is zero.

The question of confinement in the overall sense — that is, the confinement of the body of the jet — also depends on the relative strength of the magnetic field. As in the formation of localized overpressured regions, the confinement may either be direct, in magnetically dominated jets, or indirect, as in relatively unmagnetized jets. For reference, shocks within an unmagnetized jet, which are excited at the jet boundary by the cocoon, can raise the mean pressure in the jet and cocoon to perhaps twice the ambient pressure. The internal shocking in a weakly magnetized jet can roughly double this to 3-5 times the pressure in the ambient medium, with a mean pressure in the cocoon of roughly three times the pressure in the ambient medium.

5. Other Magnetic Models

The $\beta = 1$ jet is the most complete simulation which we have run, but two other models, which were described in Section 3.2, have been run for limited times. The two models are, a magnetized jet with a parabolic magnetic profile advancing into an unmagnetized medium, and a magnetized jet with a linear magnetic profile advancing into a magnetized medium. Both jets were injected with $M_j = 5$ and $\rho_j/\rho_e = 0.1$.

The parabolic profile jet was run to a time of 66, at which point it had attained a length of 310, about 15% longer than the $\beta = 1$ jet discussed in Section 4. The density, magnetic field, gas pressure, and velocity vectors are shown in Figure 27. The cocoon is only one jet radius wide, although the bowshock has spread considerably back along the body of the jet. The knot has an overpressure of 30:1, comparable to the overpressures observed in the $\beta = 1$ jet. Perhaps the most remarkable characteristic of this jet is the recollimation of the flow after being deflected outward by the knot. Examination of the gas pressure and magnetic field plots reveals that the flow is recollimated directly by the magnetic pressure gradient, as the is no gas pressure gradient where the flow turns back. Also note that, while the jet recollimates, the post-recollimation velocity is reduces to roughly half of its original values. This is discussed in Achterberg *et al.* (1983), in which it is shown that, after a primary magnetic pinch, subsequent confinements can occur in the flow, although considerable dissipation has occurred.

The linear profile jet in the magnetized medium was run to time 62, by which time it had attained a length of 380, roughly 25% longer than the $\beta = 1$ jet at the same time. The density, magnetic field, gas pressure, and velocity vectors are shown in Figure 28. The cocoon is one jet radius wide over most of its length, except near the head of the jet. The maximum overpressure in this model is 27:1,

again comparable to the overpressures in the $\beta = 1$ jet, but an earlier model had an overpressure of 60:1; both of these overpressures were associated with pinches where the cocoon gas impacted the axis. An examination of the region near the head of the jet shows the annular shock, backflow, the terminal Mach disk, and essentially all of the other features seen in the $\beta = 1$ jet, only more compact.

Comparison with the moderately magnetized $\beta = 1$ jet reveals a number of similarities. First, the collimation of the jet momentum is improved over the unmagnetized models, as seen in the speed of advance. There is significant dynamical activity associated with the beam cap. Finally, there is exceptionally strong pinching on the axis. All of these things appear to result from the large magnetic gradient associated with the annular shock, despite the fact that the magnetic pressure is weaker than the gas pressure over most, if not all, of the grid. In particular, it should be noted that the pinches on the axes are not magnetically confined, but are caused by vortices which are themselves created at the annular shock. Thus, a feature need not itself be magnetically dominated in order to be caused by a magnetic effect.

Another common characteristic of the magnetized models was the large extent of the plug. In fact, for both the parabolic profile jet and the jet in the magnetized medium, the cocoons were strongly suppressed, and there was evidence that much of the material continued forward rather than being swept back into the cocoon. For a highly magnetized jet ($\beta_j = 0.2$) (Clarke *et al.* 1986), the plug (referred to by Norman and collaborators as the "nose cone") may extend half the length of the jet, on the order of $30 - 40R_j$. Another difference between the highly magnetized jet of Norman and collaborators and the jet models we ran was that the cocoon was almost absent in the $\beta = 0.2$ simulations. In this case, the magnetic fields confine the gas to such an extent that vortex shedding into the cocoon is strongly

suppressed, and most of the gas which would normally be shed into the cocoon remains in the plug, which is referred to as the "nose cone". This stagnant region is dynamically active in much the same way as the cocoon is dynamically active for weaker magnetic fields, but clearly cannot pinch the jet itself. However, the jet is confined directly by the magnetic field rather than through interactions with the cocoon, and so has better overall confinement than the models with weaker magnetic field. It should be noted, however, that the highly magnetized jet is injected out of radial equilibrium, and it is likely that some of the radial dynamics should be attributed to stresses in the initial radial profile of the jet rather than interactions with the cocoon or the ambient medium.

6. Discussion

Simulations of jets with no magnetic field ($\beta = \infty$), moderate magnetic field ($\beta = 1$), and strong magnetic field ($\beta = 0.2$) reveal a number of similarities. All of them end in a terminal Mach disk, which is capped by a plug of subsonic gas. All jets are capable of producing general and localized internal jet pressures greater than that of the ambient medium. The confinement was generally caused by reflecting shocks excited by the cocoon. A cocoon is generally present, although most of the material which would normally end up in the cocoon is transferred to the plug for strongly magnetized jets. Finally, in all cases, a bowshock advances in front of the jet material, where the jet momentum is transferred from the jet to the bowshock by the plug and an annular shock, which is supported by a slipstream consisting of relatively unshocked material from the outer part of the jet. At the same time, there are a number of qualitative differences between magnetized and unmagnetized jets.

The magnetized jets advance more quickly than the unmagnetized jets. Even for a weakly magnetized jet, the additional radial force provided by the magnetic tension is sufficient to direct the axial momentum in a more focussed manner. Since the dynamics is dominated by the axial momentum, the primary pressure gradients are also axial, and it is clear that a surprisingly small radial force can have a considerable effect on the flow if sufficiently pervasive. The magnetic tension and pressure gradient forces had an unexpectedly large influence on the jet dynamics, considering their low values relative to the gas pressure, especially those effects which in some way originate at the annular shock. The plug was considerably enhanced by the presence of magnetic fields; in many ways, the plug may be viewed as a part of the cocoon which happens to sit in front of the jet, rather than off to the side.

The local overpressures obtained in knots in magnetized jets may approach the ram pressure of the unshocked jet, even if the jet is only moderately magnetized. This is a consequence of the excitement of vorticity in the cocoon by the annular shock, where the relatively large magnetic pressure gradient appears to influence the strength of the vortices. Overpressures in even the $\beta = 1$ jet were two to three times those observed in unmagnetized jets, for both localized knots and integrated pressure over the entire jet. Confinement of the jet itself appears to take place by oblique shocks generated where the cocoon pinches the jet, except for the case of a strongly magnetized jet, in which case the magnetic field may confine the jet directly.

One reason that even weak magnetic fields may have a considerable effect on the general flow is the dynamical influence of the cocoon. Typical flow velocities in the cocoon, while becoming locally supersonic at times, are considerably reduced from the flow velocities in the jet itself. Similarly, the pressure gradients are considerably reduced from what would be typical near the terminal Mach disk or the annular shock. The cocoon is seen to be an active and influential part of the jet, in which local reacceleration, shocking, and the pinching of the jet at the edges of vortices have a significant effect on the entire flow field.

All of this applies to axisymmetric jets. Simulations of three-dimensional jets by Williams and Gull (1985) and Arnold and Arnett (1986) appear to be similar to the two-dimensional simulations. The jet modeled by Williams and Gull is injected at a slowly varying angle to the mean injection axis, i.e., it wiggles around inside the cocoon, and intersects with the bowshock at locations offset from the center of the cocoon. The net effect is, as with the annular shock, to transfer the momentum to the ambient medium over a larger effective area than the jet radius. The jet simulation by Arnold and Arnett is injected axisymmetically, but

develops toroidal modes as it advances. However, the overall appearance of the simulation is roughly axisymmetric. In general, most of the structure observed in the two-dimensional simulations appears in some form in the three-dimensional simulations. However, the three-dimensional codes can be used to model features such as the nonaxisymmetric structures in the hotspots of Cygnus A.

One possibility for three-dimensional jets is bifurcation, i.e., that the jet should break up into a collection of individual jets directed off-axis at different angles. The presence of a sufficiently strong toroidal magnetic field should suppress this, since in perfect MHD flux loops cannot be broken. Thus, one possible consequence of the presence of significant amounts of toroidal magnetic field is that the jet is stabilized against bifurcation, improving both stability and collimation.

Since the cocoon contains both shocks and shear surfaces, there must be considerable dissipation within the cocoon. In some radio-emitting jets, the cocoon may emit as well as the jet. There are a number of sources (*cf.*, 3C219 and 3C341, Bridle 1984a) (fig. 29) which have twin jets surrounded by cocoons, which may be examples of dissipation in the cocoons of mildly supersonic sources. For FRII sources, there is clearly some dissipation in the lobes, as seen by in the bright filamentary structure in Cygnus A (Dreher *et al.* 1984) and the filamentary and ring structures in Hercules A (Dreher and Feigelson 1984). The ring structures are reminiscent of various shocks formed in the ambient medium by the passage of the jet, and it is possible that some of the emission could come from weakly magnetized shocked ISM. Alternatively, the jets in some of the FRI sources could be the plugs of supersonic magnetized jets, and the rapid part of the jet would itself correspond to the short, one-sided jet region seen in many FRI sources.

Much of the physics involved in the evolution of magnetized jets remains unclear, just as a number of processes in unmagnetized jets were not properly ap-

preciated until simulations of magnetized jets became available for comparison. However, it appears that the basic processes occurring in both magnetized and unmagnetized jets are becoming moderately well understood. Future work will involve the filling in of the magnetized jet parameter plane. In particular, since no direct magnetic effects — in which magnetic stresses clearly dominated over nonmagnetic stresses — were observed in the $\beta = 1$ jet, a $\beta = 0.4$ jet will be run to generate a model with a dynamically important magnetic cocoon. We also plan to look at the cases where $\rho_j \sim \rho_e$ to study their magnetic modes. Basically, there is a large region of parameter space to model, very little of which has been covered as yet. Further interpretation of the physics of magnetized jets will require a larger sample of simulations, to elucidate the relative importance of various parameters in determining the structure of the jet and the surrounding cocoon.

References

Achterberg, A., Blandford, R.D., and Goldreich, P. 1983, *Nature,* **304**, 607.

Arnold, C.N. and Arnett, W.D. 1986, *Ap. J. (Letters),* **305**, L57.

Benford, G. 1978, *M.N.R.A.S.,* **183**, 29.

Blandford, R.D. 1976, *M.N.R.A.S.,* **176**, 465.

Bridle, A.H. 1984a, in *Physics of Energy Transport in Extragalactic Radio Sources* ed. A.H. Bridle and J.A. Eilek (NRAO: Green Bank, West Virginia), p. 1.

Chan, K.L. and Henriksen, R.N. 1980, *Ap. J.,* **241**, 534.

Clarke, D.A., Norman, M.L., and Burns, J.O. 1986, preprint.

Dreher, J.W. and Feigelson, E.F. 1984, *Nature,* **308**, 43.

Dreher, J., Perley, R., and Cowan, J. 1984, in *Physics of Energy Transport in Extragalactic Radio Sources* ed. A.H. Bridle and J.A. Eilek (NRAO: Green Bank, West Virginia), p. 57.

Norman, M.L., Smarr, L., Winkler, K.-H.A., and Smith, M.D. 1982a, *Astr. Ap.,* **113**, 285.

Norman, M.L., Winkler, K.-H.A., and Smarr, L. 1982b, in *Astrophysical Jets* ed. A. Ferrari and A.G. Pacholczyk (Reidel: Boston), p. 227.

Norman, M.L., Winkler, K.-H.A., and Smarr, L. 1984a, in *Physics of Energy Transport in Extragalactic Radio Sources* ed. A.H. Bridle and J.A. Eilek (NRAO: Green Bank, West Virginia), p. 150.

Norman, M.L., Smarr, L., and Winkler, K.-H.A. 1984b, in *Numerical Astrophysics* ed. J.M. Centrella, J.M. LeBlanc, R.L. Bowers, and J.A. Wheeler (Jones and Bartlett: Boston), p. 88.

Wardle, J.F.C. and Potash, R.I. 1982, in *IAU Symposium 97: Extragalactic Radio Sources* ed. D.S. Heeschen and C.M. Wade (Reidel: Boston), p. 131.

Wiita, P.J. 1978, *Ap. J.*, **221**, 436.

Williams, A.G. and Gull, S.F. 1984, *Nature,* **310**, 33.

Williams, A.G. and Gull, S.F. 1985, *Nature,* **313**, 34.

Wilson, M.J. and Falle, S.A.E.G. 1985, *M.N.R.A.S.,* **216**, 971.

Wilson, M.J. and Scheuer, P.A.G. 1983, *M.N.R.A.S.,* **205**, 449.

Zabusky, N.J. 1984, *Physics Today,* **37**, 36.

Figure Captions

Figure 1. Parameter Space for Hydrodynamic Jets

This shows the various stability regimes for unmagnetized jets, in terms of the Mach number M and the density contrast $\eta = \rho_j/\rho_e$.

Figure 2. Mach 5 Hydrodynamic Jet

The Mach 5 hydrodynamic jet model is shown at a time of t=250.

Figure 3. Mach 16 Hydrodynamic Jet

The Mach 16 hydrodynamic jet is shown at time t=38.

Figure 4. General Structure of Jets

The general structure of a jet is shown. The five regions are (A) the jet, (B) the plug, (C) the cocoon, (D) the shocked ambient gas, and (E) the quiescent ambient gas.

Figure 5. Simplified Model of Jets

A commonly used model for jets has the jet impinge directly on the bowshock. As discussed in the text, this model is inconsistent with the relaxation of the cocoon.

Figure 6. Simple Alternative Models

Two simple alternatives to the model in figure 5 are shown. Model "A" spreads out over a large area before striking the bow shock, thereby reducing the required

gradients, whereas in model "B," the shocked jet material fills the plug rather than the cocoon.

Figure 7. Advance of the Bowshock

The axial positions of the bowshock, contact discontinuity, and terminal Mach disk are shown as a function of time for the two unmagnetized model, where "A" is the Mach 5 jet and "B" is the Mach 16.6 jet. The bowshock travels smoothly, followed closely by the contact discontinuity, but the terminal Mach disk follows the bowshock over a wide range of distances.

Figure 8. Secondary Shocks

If the bowshock becomes weak, as is expected, shocks may develop in the shocked ambient medium. The shock here is seen to stand off from the cocoon.

Figure 9. Velocity/Surface Plot

Shocks, contact discontinuities, and slip surfaces are displayed against the velocity vectors to provide a holistic view of the jet behavior.

Figure 10. Velocity/Surface Plot for Model at Time 130

Shocks, contact discontinuities, and slip surfaces are displayed against the velocity vectors for the $\beta = 1$ model at time t=130.

Figure 11. Density Plot for Model at Time 130

The density contours are displayed for the $\beta = 1$ model at time t=130.

Figure 12. Magnetic Field Plot for Model at Time 130

The magnetic field contours are displayed for the $\beta = 1$ model at time t=130.

Figure 13. Pressure Plot for Model at Time 130

The pressure contours are displayed for the $\beta = 1$ model at time t=130. Note the knot at the plug, which is further confined by the secondary shock downstream from the terminal Mach disk, and the relatively strong shock in the jet which formed where the jet was pinched.

Figure 14. Advance of the Bowshock for $\beta = 1$ Model

The axial positions of the bowshock, contact discontinuity, and terminal Mach disk are shown as a function of time for the $\beta = 1$ magnetized model. The bowshock travels smoothly, followed closely by the contact discontinuity, but the terminal Mach disk follows the bowshock over a wide range of distances.

Figure 15. Extended Plug

The plug ranges in size with time, in a way which appears to correlate with the behavior of the jet near the slipstream. This shows the pressure contours for an extended plug. Note that there is considerable structure in the plug.

Figure 16. Backflow into the Plug

Backflow into the plug, which is associated with the annular shock, is shown for the $\beta = 1$ model. This backflow appears to be characteristic of magnetized jets.

Figure 17. Flow of the Slipstream

Velocity vectors for material flowing along the slipstream toward the annular shock are displayed. Note that the flow appears to converge.

Figure 18. Magnetic Field Near the Slipstream

The magnetic field in the region surrounding the slipstream is shown. Note the magnetic field maximum in the slipstream. This may be indicative of compression, *e.g.*, shocks.

Figure 19. Velocity Divergence Near the Slipstream

The velocity divergence in the region surrounding the slipstream is shown. Note that two weak shocks cross in the path of the slipstream.

Figure 20. Velocity/Surface Plot Showing Pinch (t=100)

This plot shows a pinch where the cocoon flows into the boundary of the jet, and causes a localized pinch. Note that magnetic fields are not directly responsible for the pinching.

Figure 21. Shocks in the Cocoon

This plot of velocity divergence shows a number of shocks in the cocoon, revealing the dynamical nature of this region.

Figure 22. Shocks in the Plug

This plot of velocity divergence shows a number of shocks in the plug, associated with the backflow from the annular shock.

Figure 23. Correlation Between Maximum Pressure and Position of Mach Disk

The maximum pressure in the jet is plotted against the distance between the terminal Mach disk and the bowshock. Note that the pressures tend to be highest when the plug is short, and lowest when the plug is long. This suggests that the pinches are associated with the shedding of vortices when the slipstream breaks up.

Figure 24. Plug Formation — Time 80

The plug is beginning to form again at time 80.

Figure 25. Plug Dissipation — Time 110

The plug is beginning to break up at time 110.

Figure 26. Vortex Shedding — Time 120

The forward and reverse vortices are beginning to be shed into the cocoon.

Figure 27. Parabolic Model

The results for the magnetized jet with a parabolic magnetic field profile are shown at time 66.

Figure 28. Magnetized Medium Model

The results for the magnetized jet propagating in a magnetized medium are shown at time 62.

Figure 29. Radio Sources 3C219 and 3C341

Shown are radio maps of 3C219 and 3C341, both of which appear to have radio-emitting cocoons (Bridle 1984a).

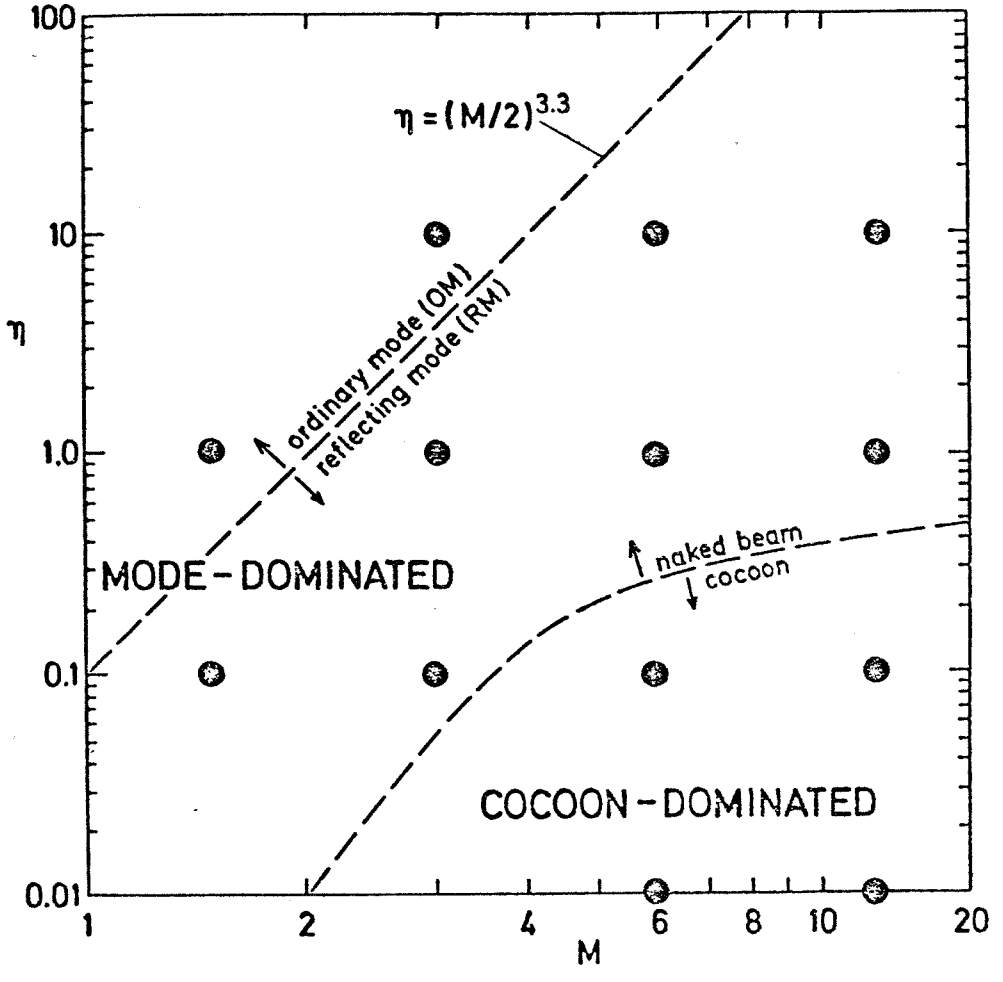
100
10
1.0
0.1
0.01
η
η = (M/2)^3.3
ordinary mode (OM)
reflecting mode (RM)
MODE-DOMINATED
naked beam
cocoon
COCOON-DOMINATED
1
2
4
6
8
10
20
M

Figure 1

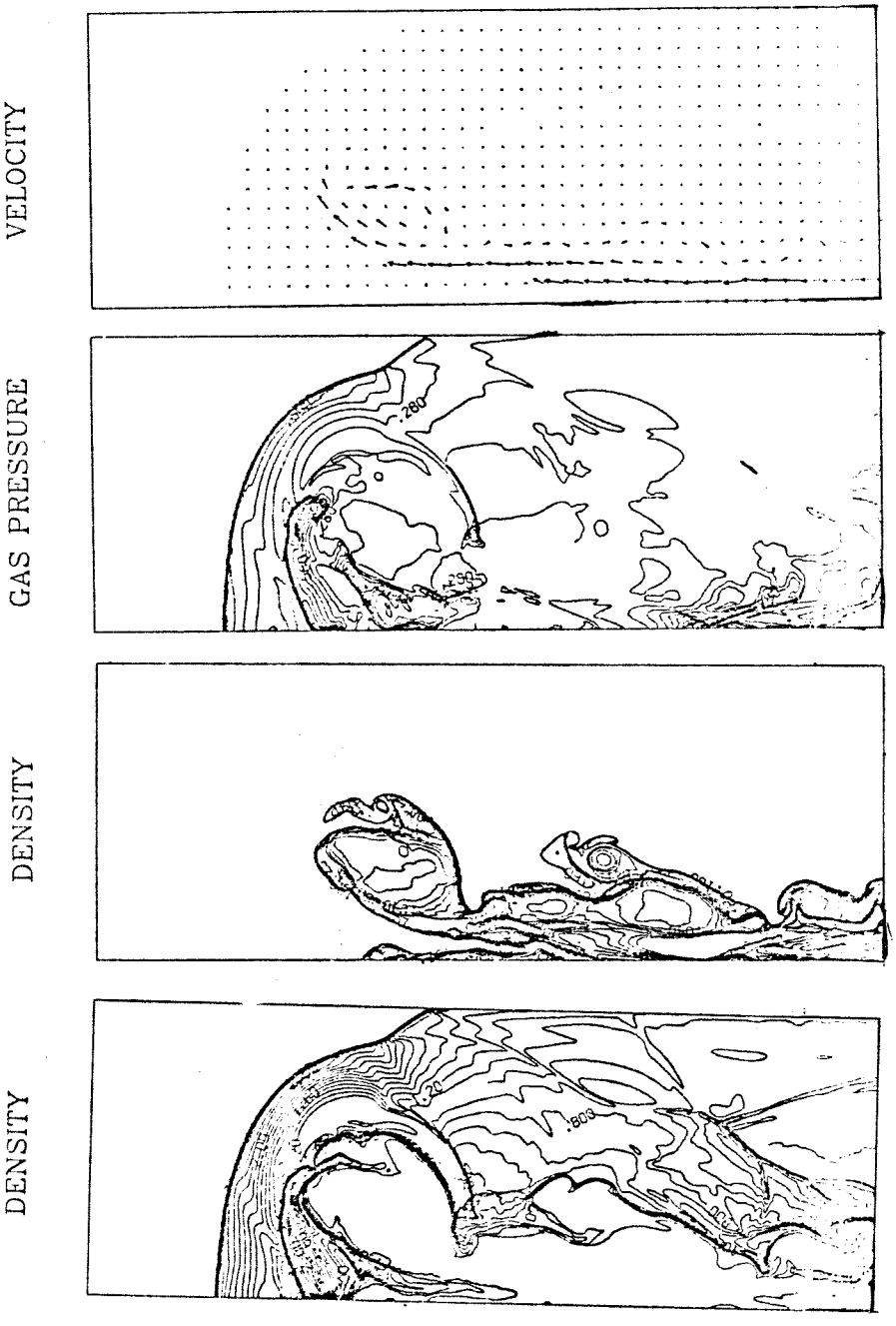

Figure 2

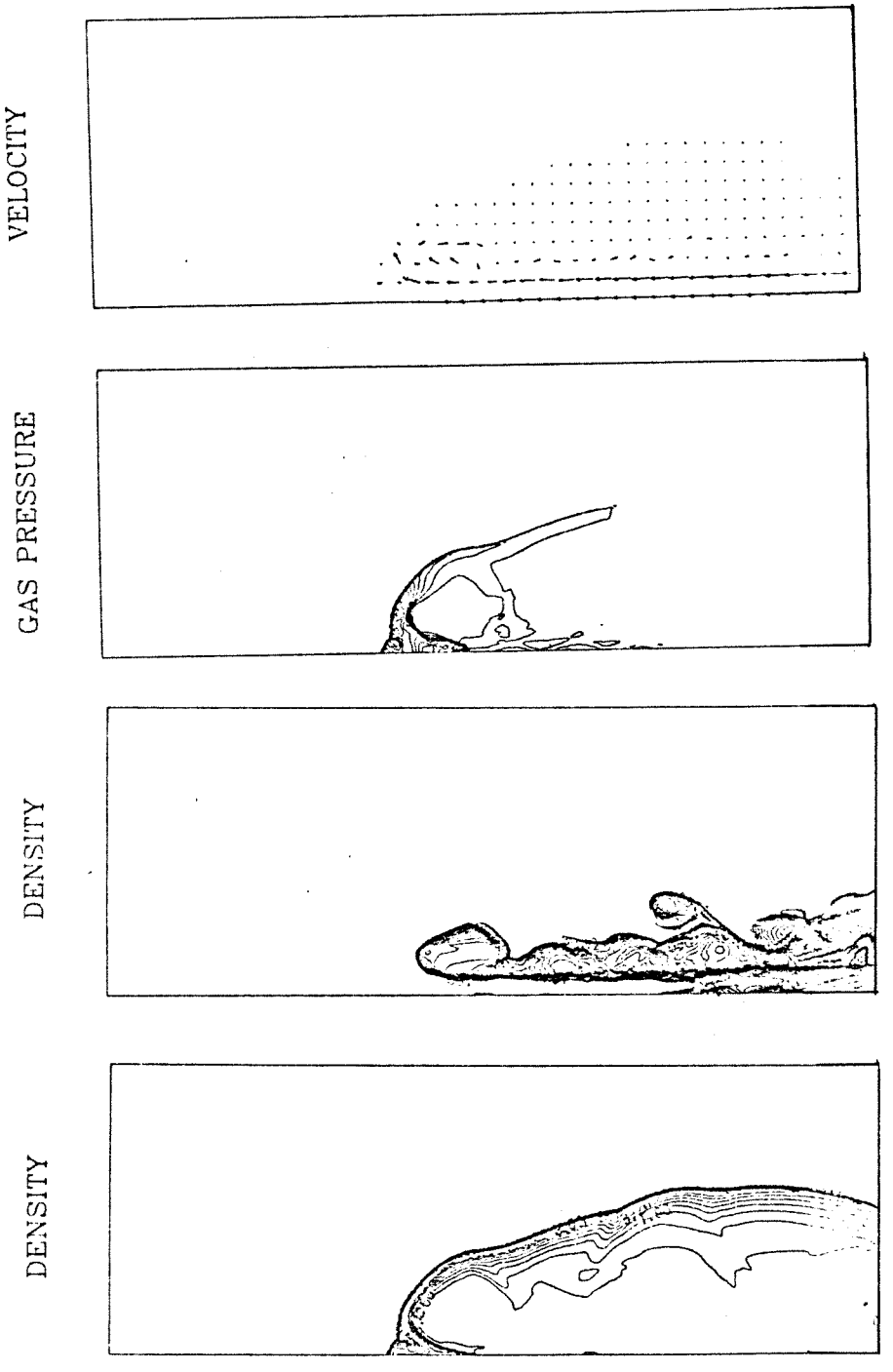

Figure 3

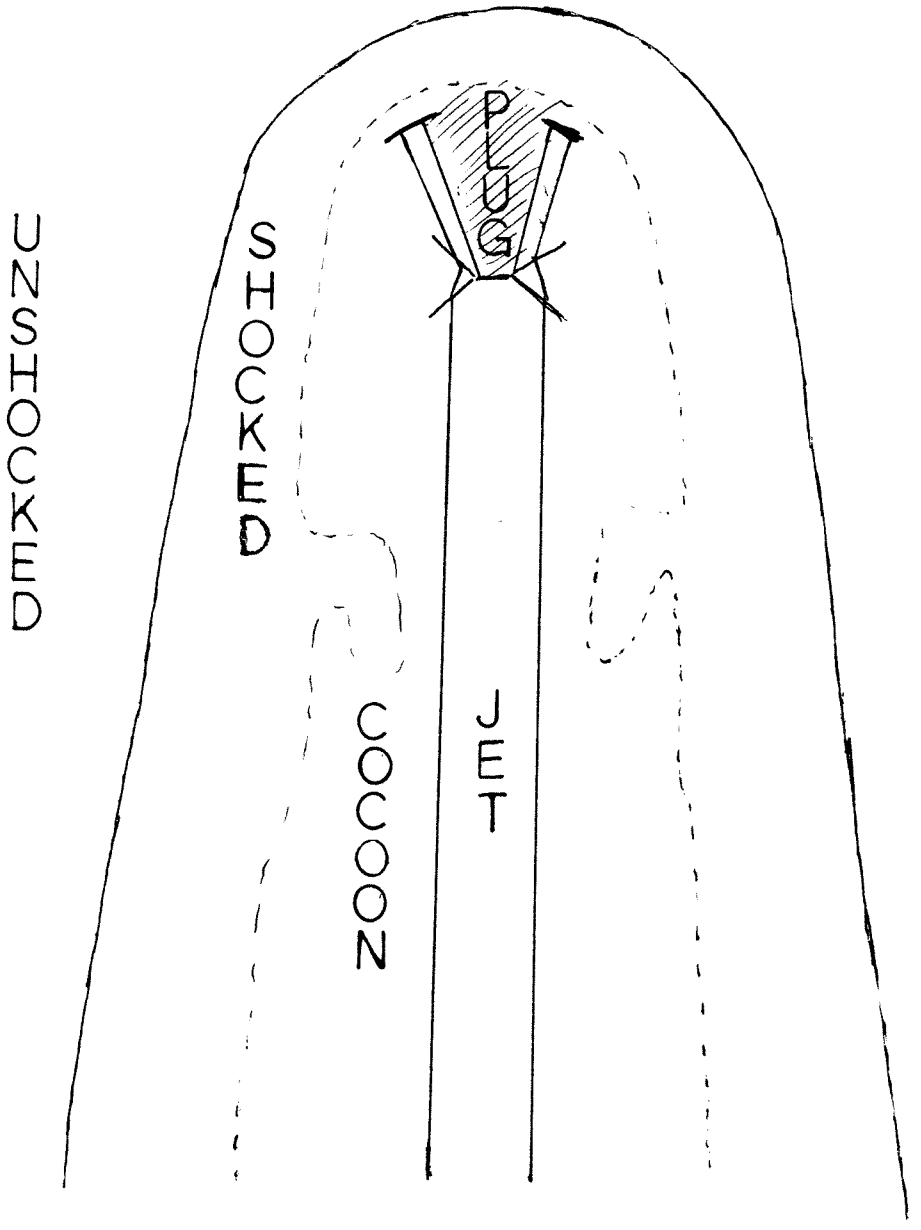

Figure 4

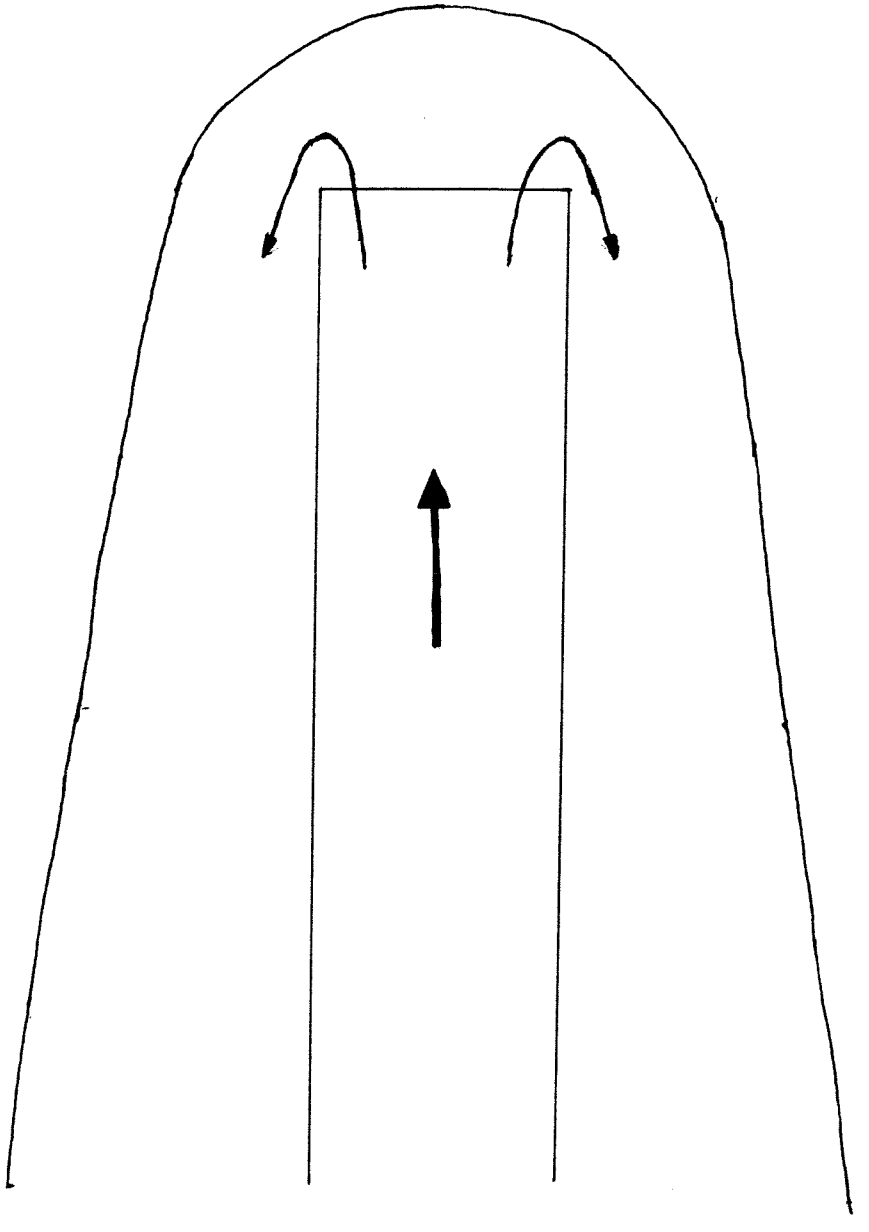

Figure 5

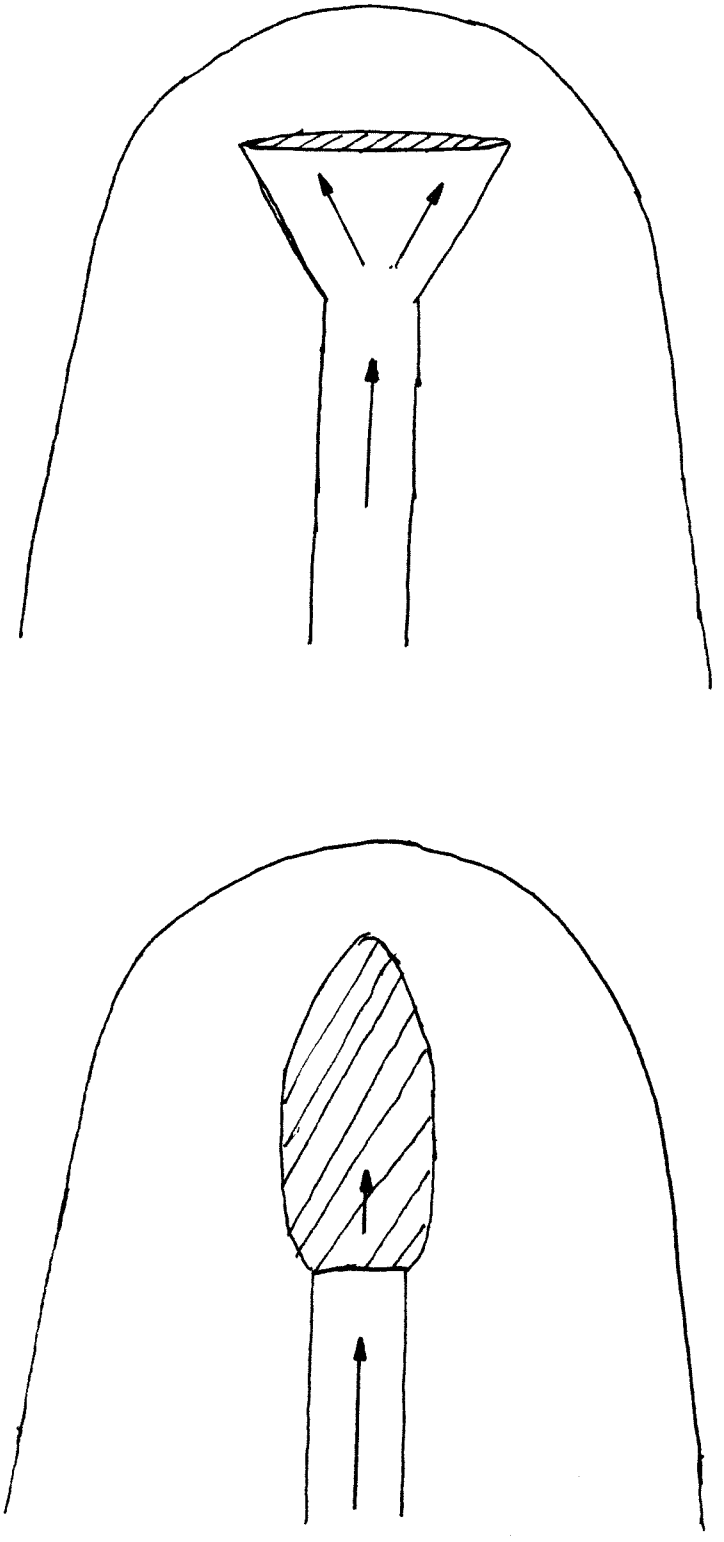

Figure 6

AXIAL POSITION VERSUS TIME

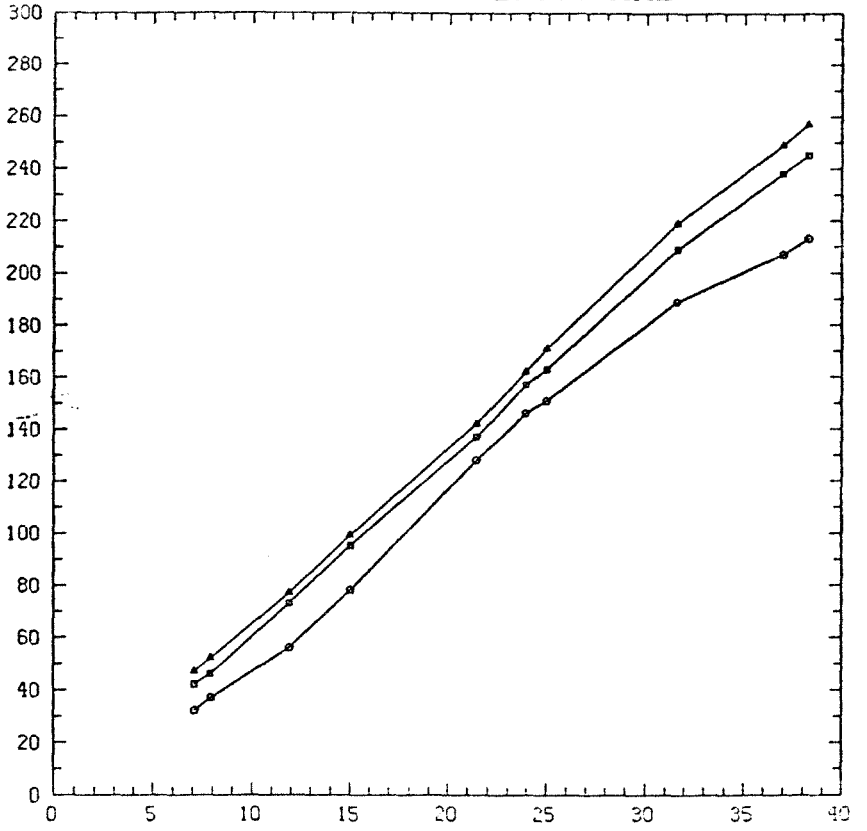

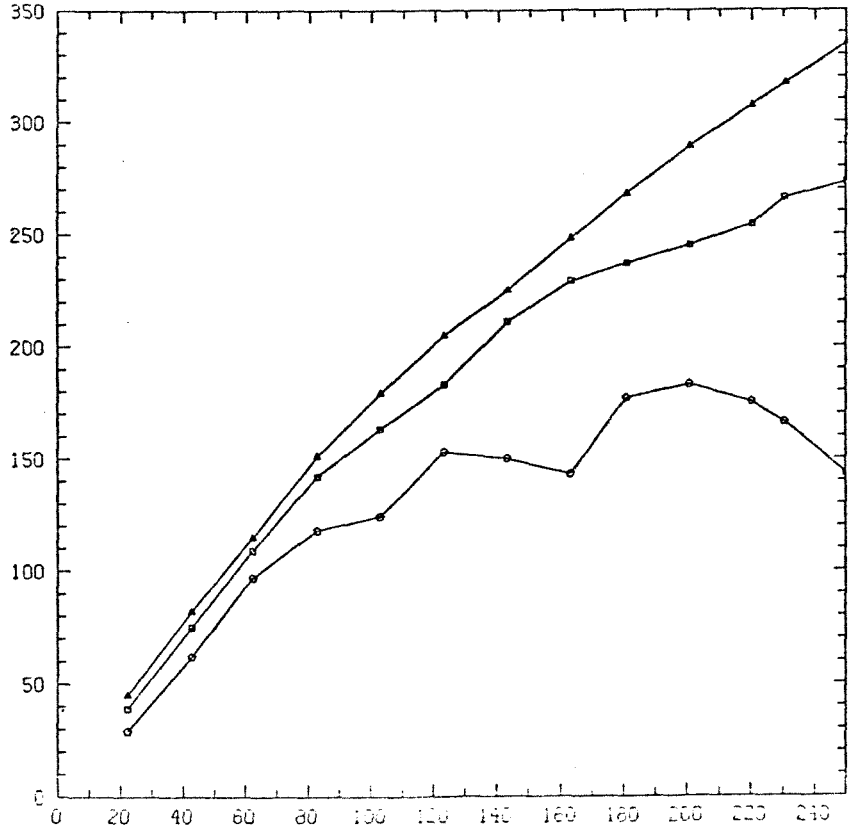

Figure 7

DENSITY

Figure 8

VELOCITY

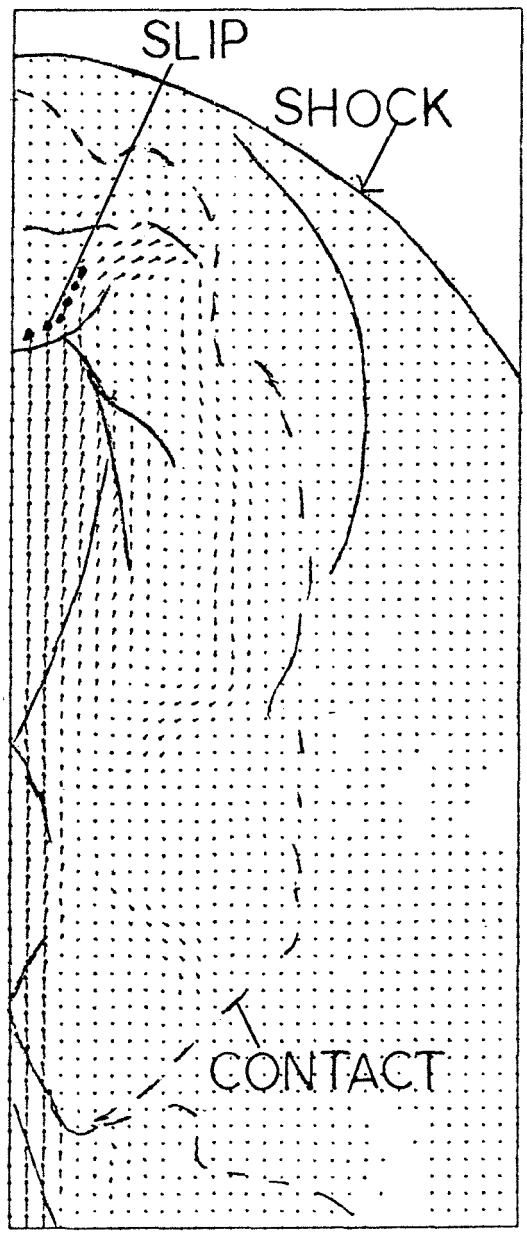

Figure 9

VELOCITY

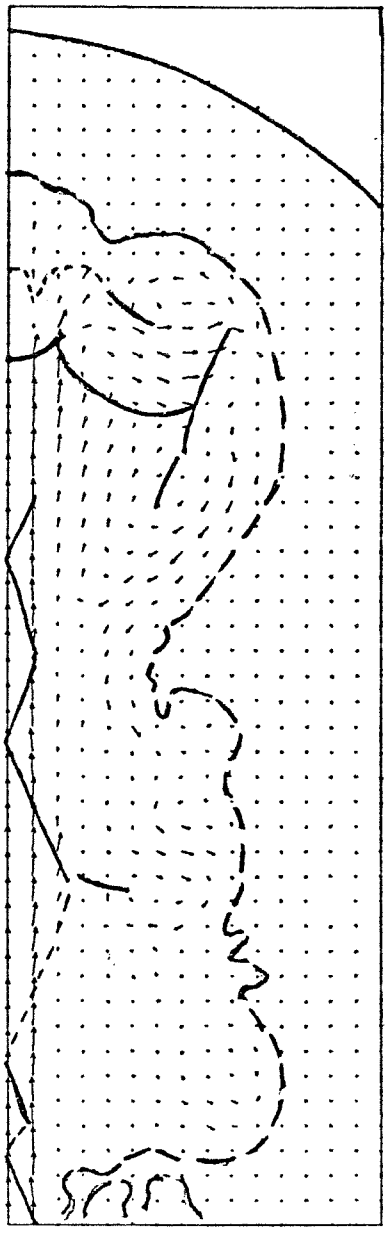

Figure 10

DENSITY DENSITY

Figure 11

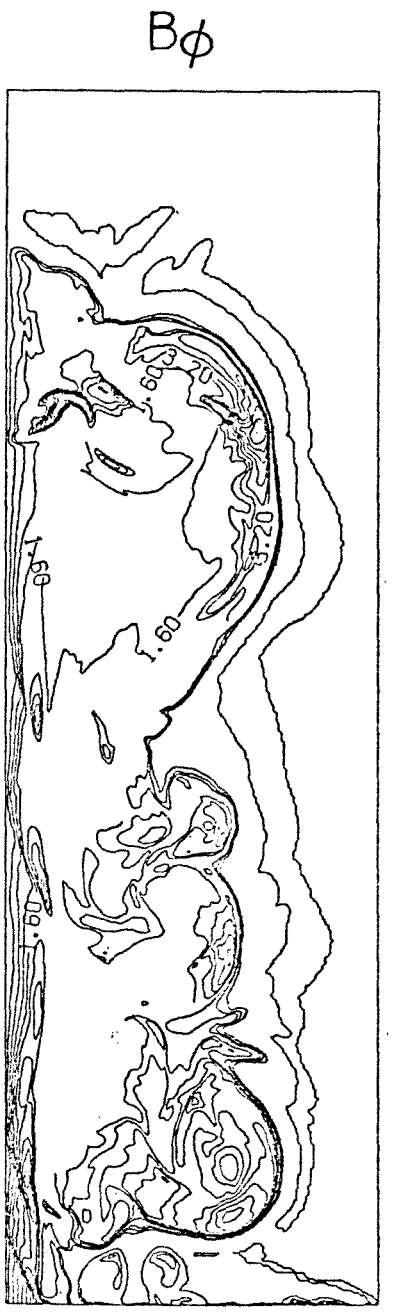

Figure 12

GAS PRESSURE

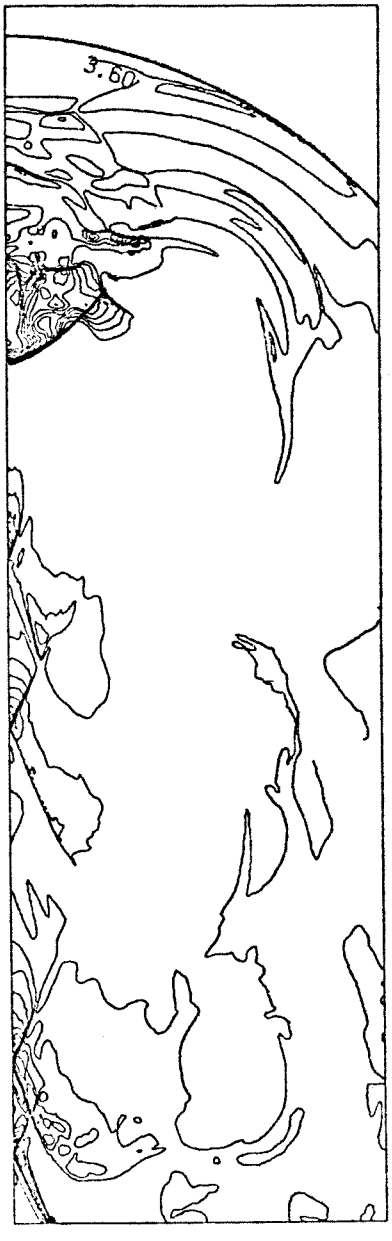

Figure 13

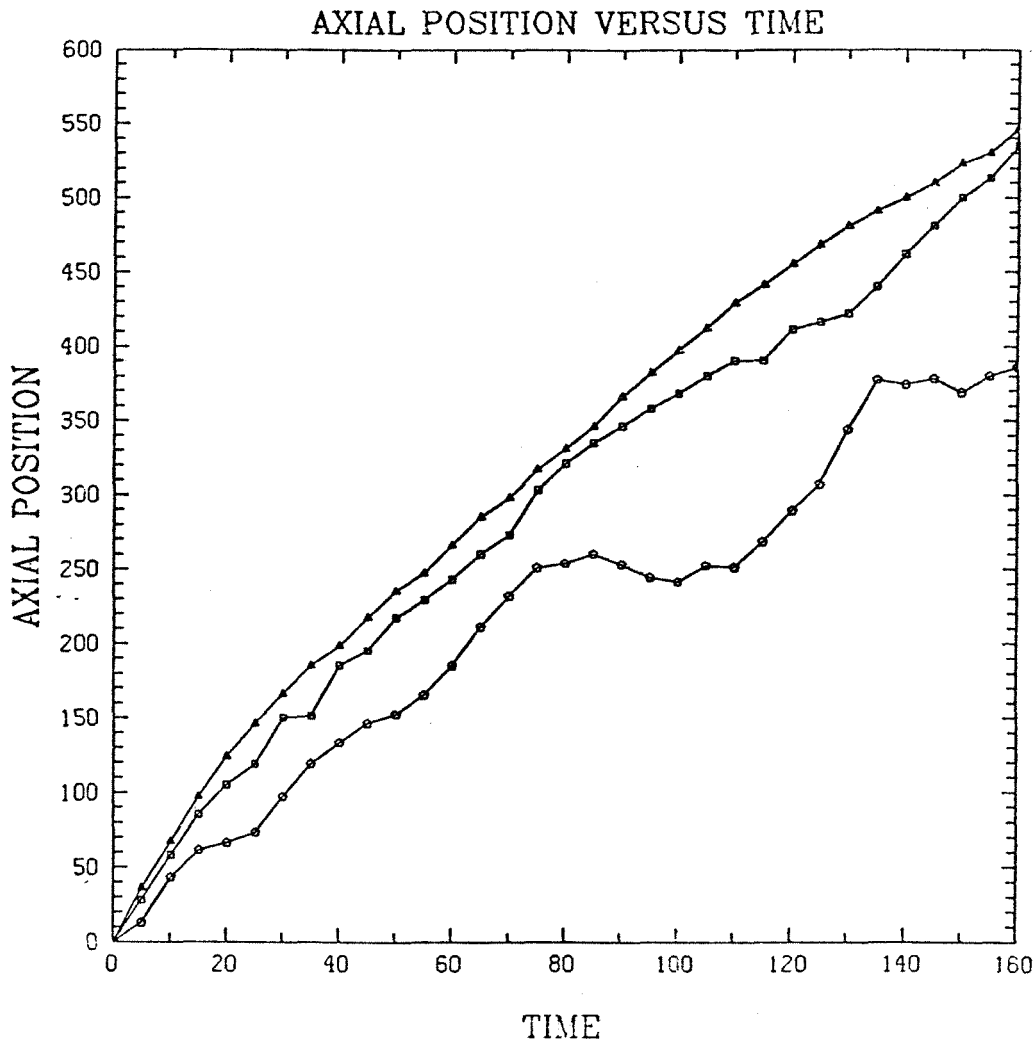
AXIAL POSITION VERSUS TIME
AXIAL POSITION
TIME
600
550
500
450
400
350
300
250
200
150
100
50
0
0
20
40
60
80
100
120
140
160

Figure 14

GAS PRESSURE

Figure 15

VELOCITY

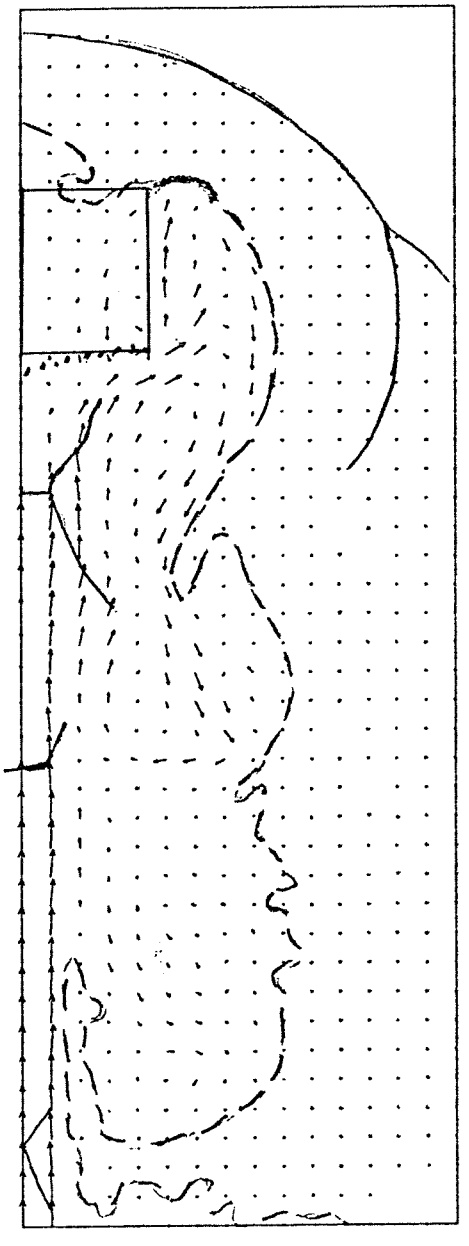

Figure 16

VELOCITY

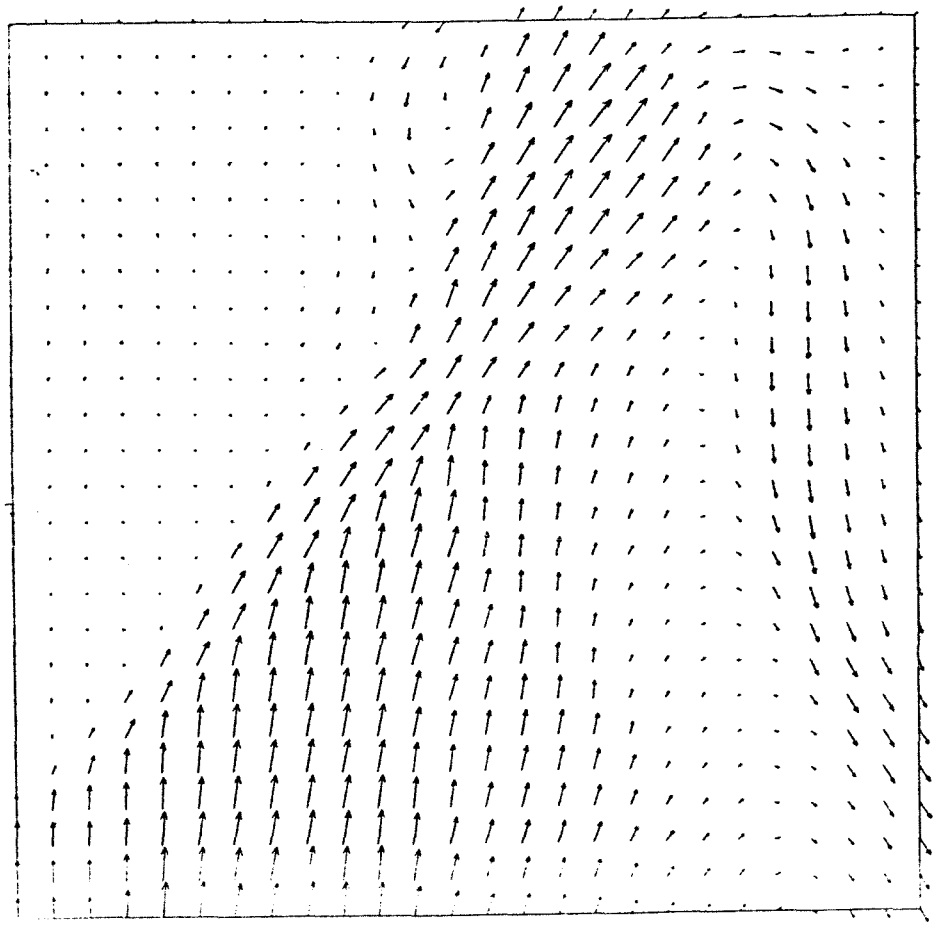

Figure 17

TOROIDAL MAGNETIC FIELD

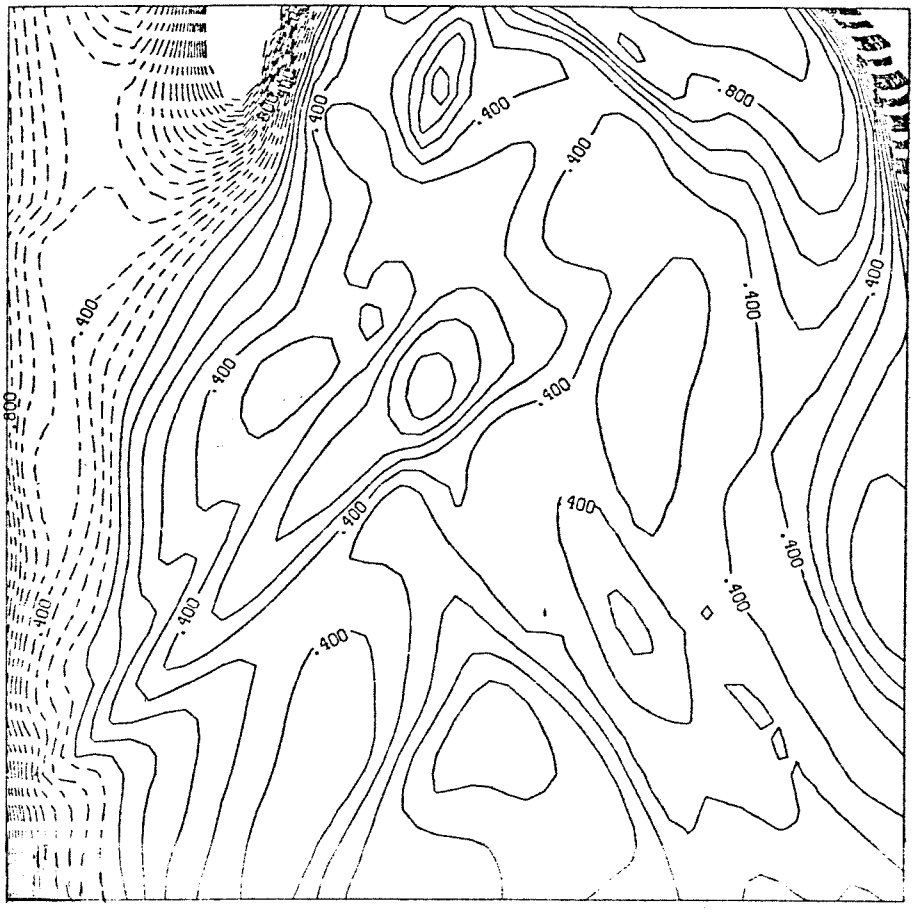

Figure 18

VELOCITY DIVERGENCE

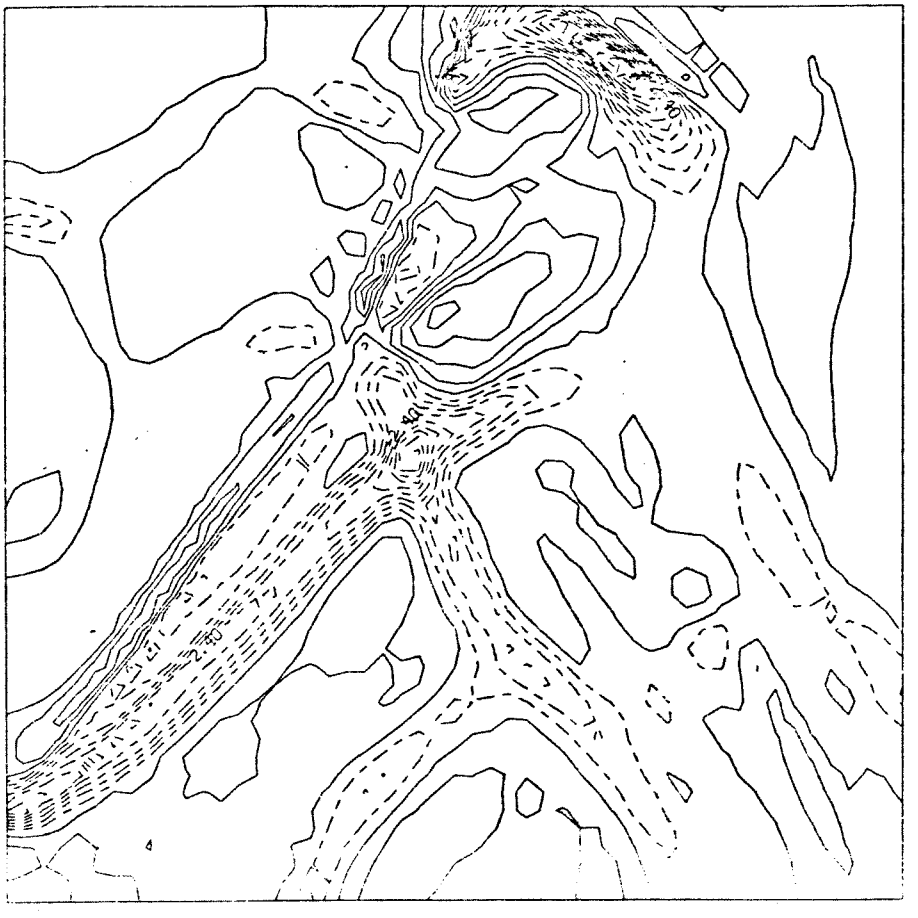

Figure 19

VELOCITY

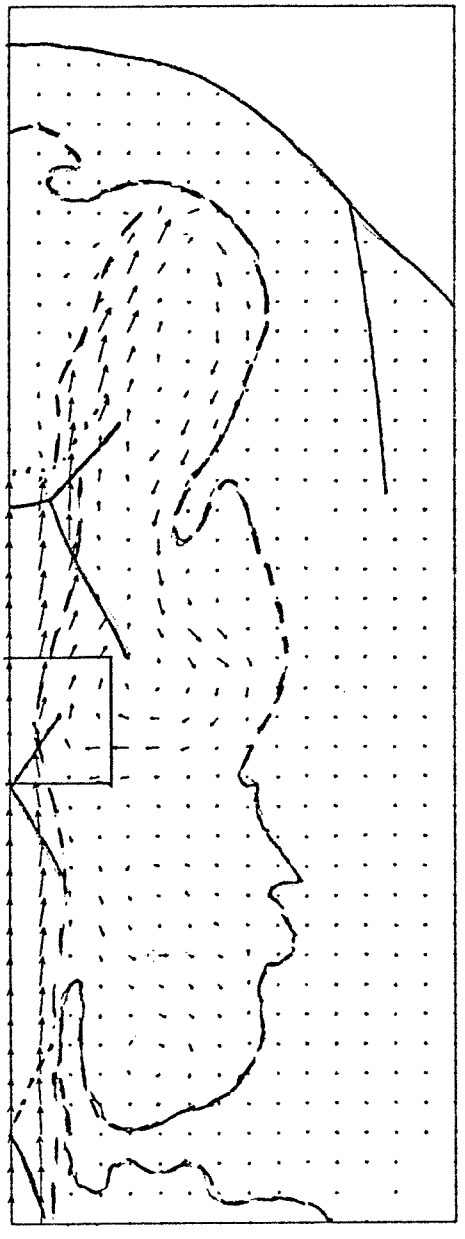

Figure 20

$\nabla \cdot \underset{\sim}{V}$

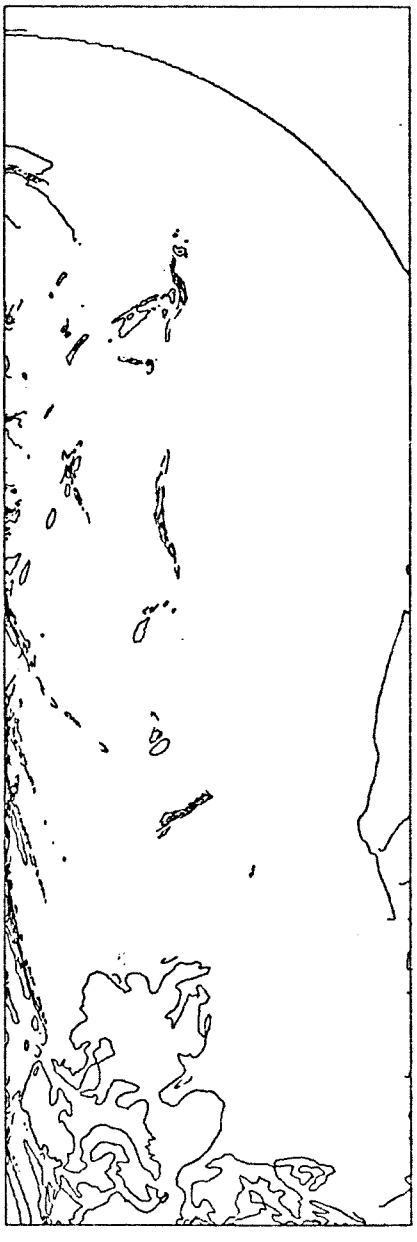

Figure 21

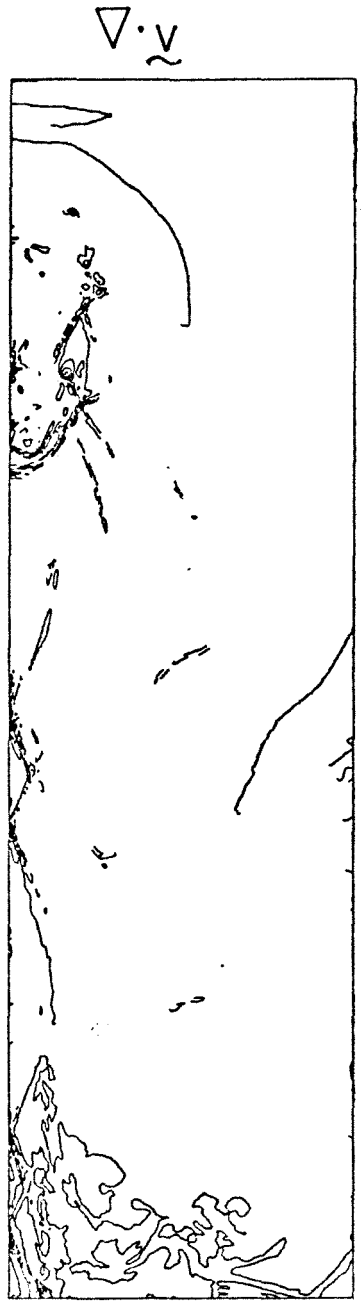

Figure 22

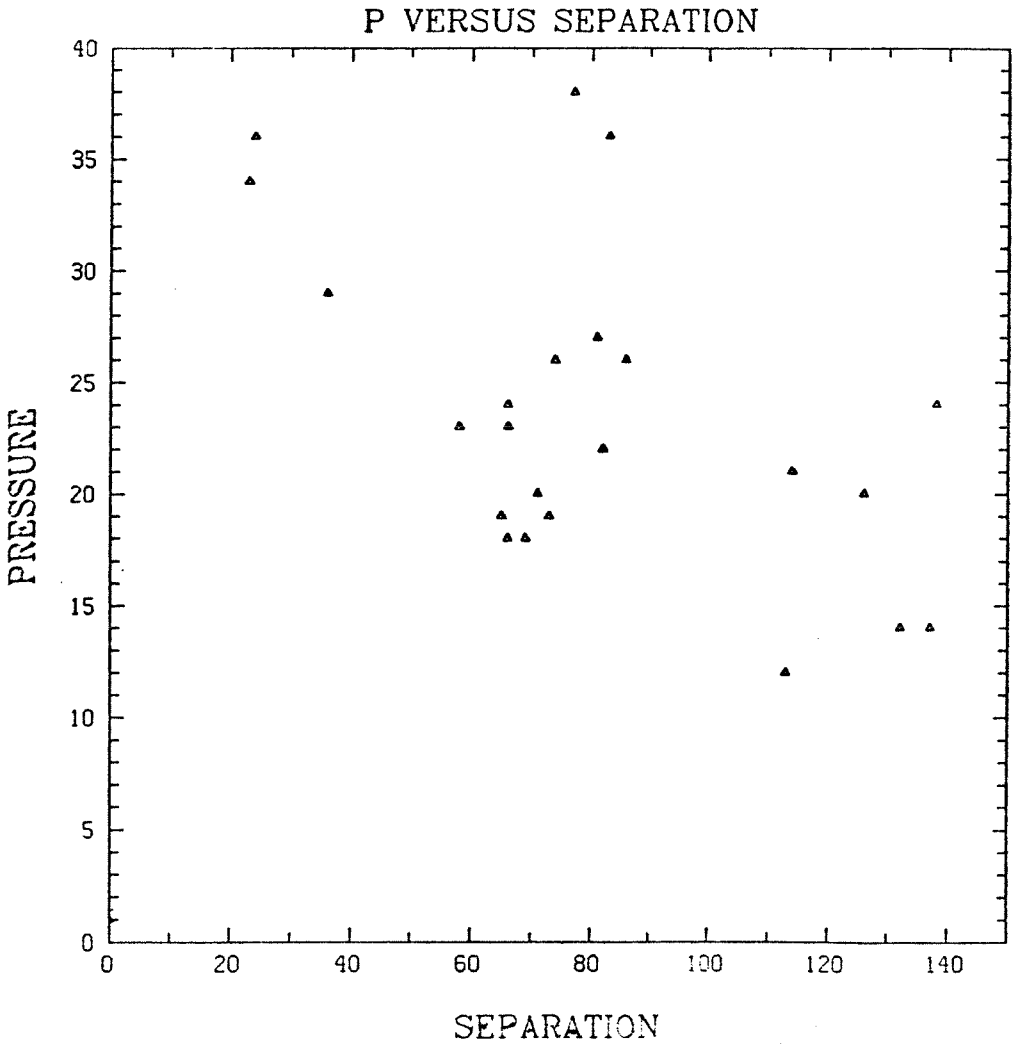
P VERSUS SEPARATION
PRESSURE
SEPARATION
0
5
10
15
20
25
30
35
40
0
20
40
60
80
100
120
140

Figure 23

VELOCITY

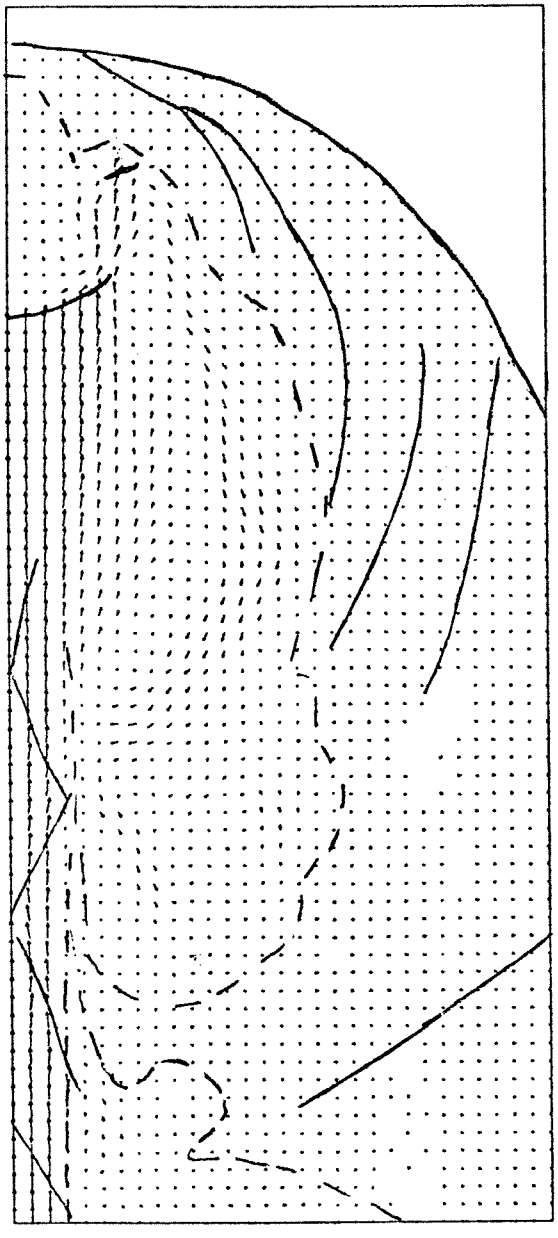

Figure 24

VELOCITY

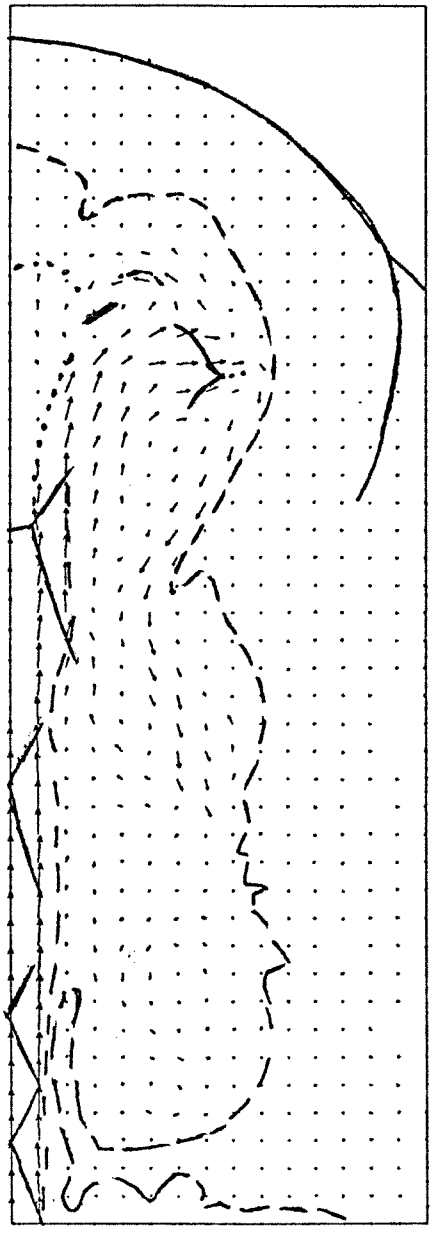

Figure 25

VELOCITY

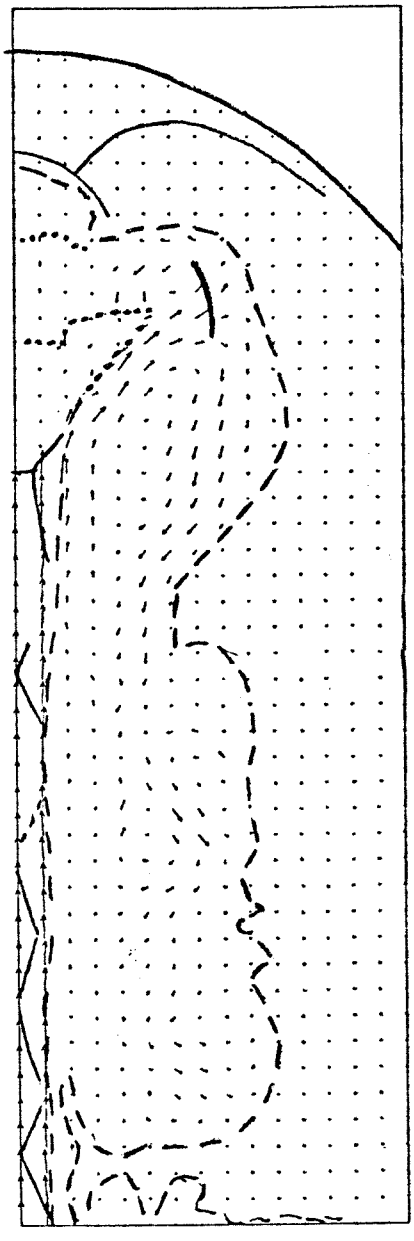

Figure 26

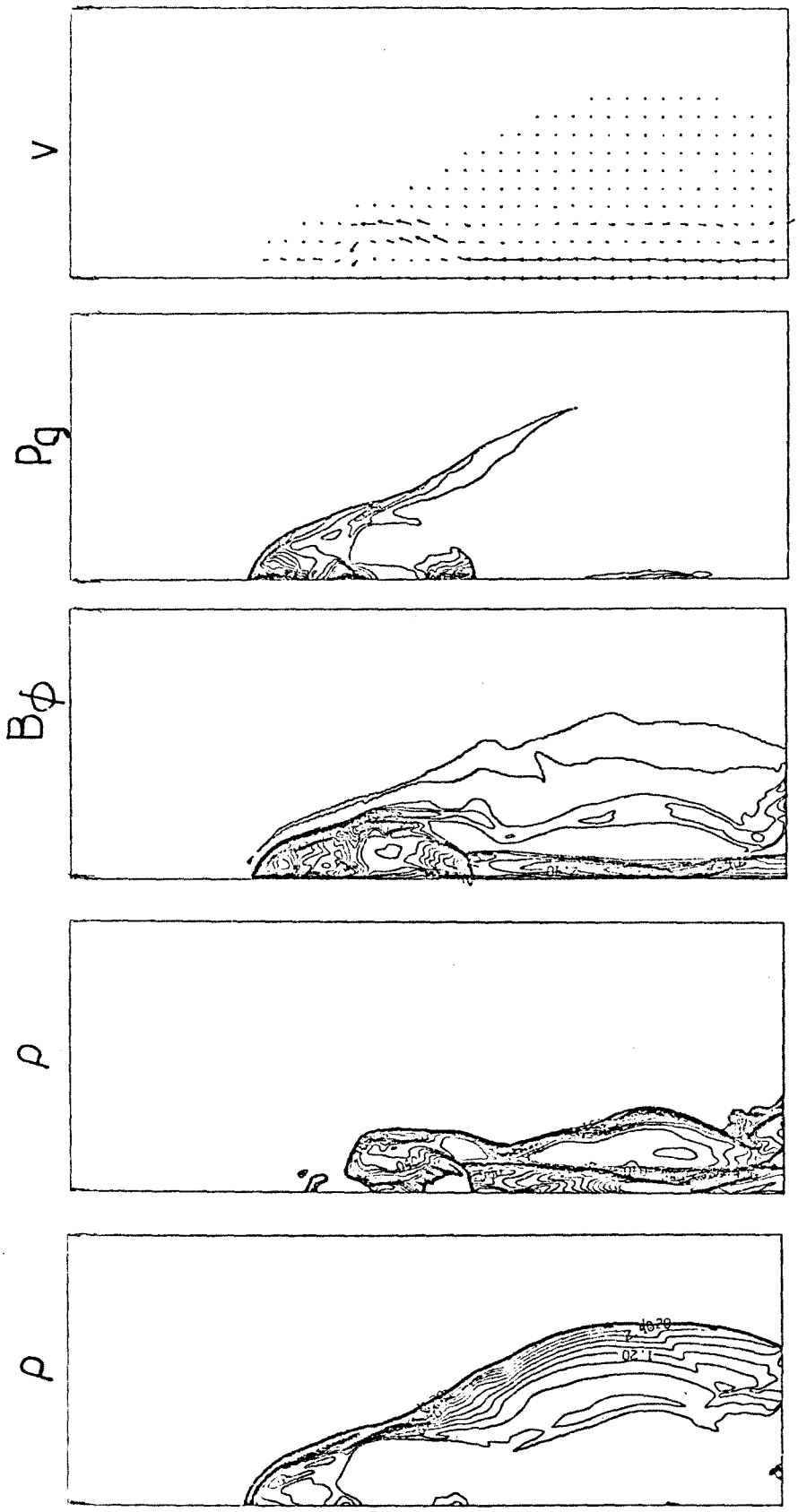

Figure 27

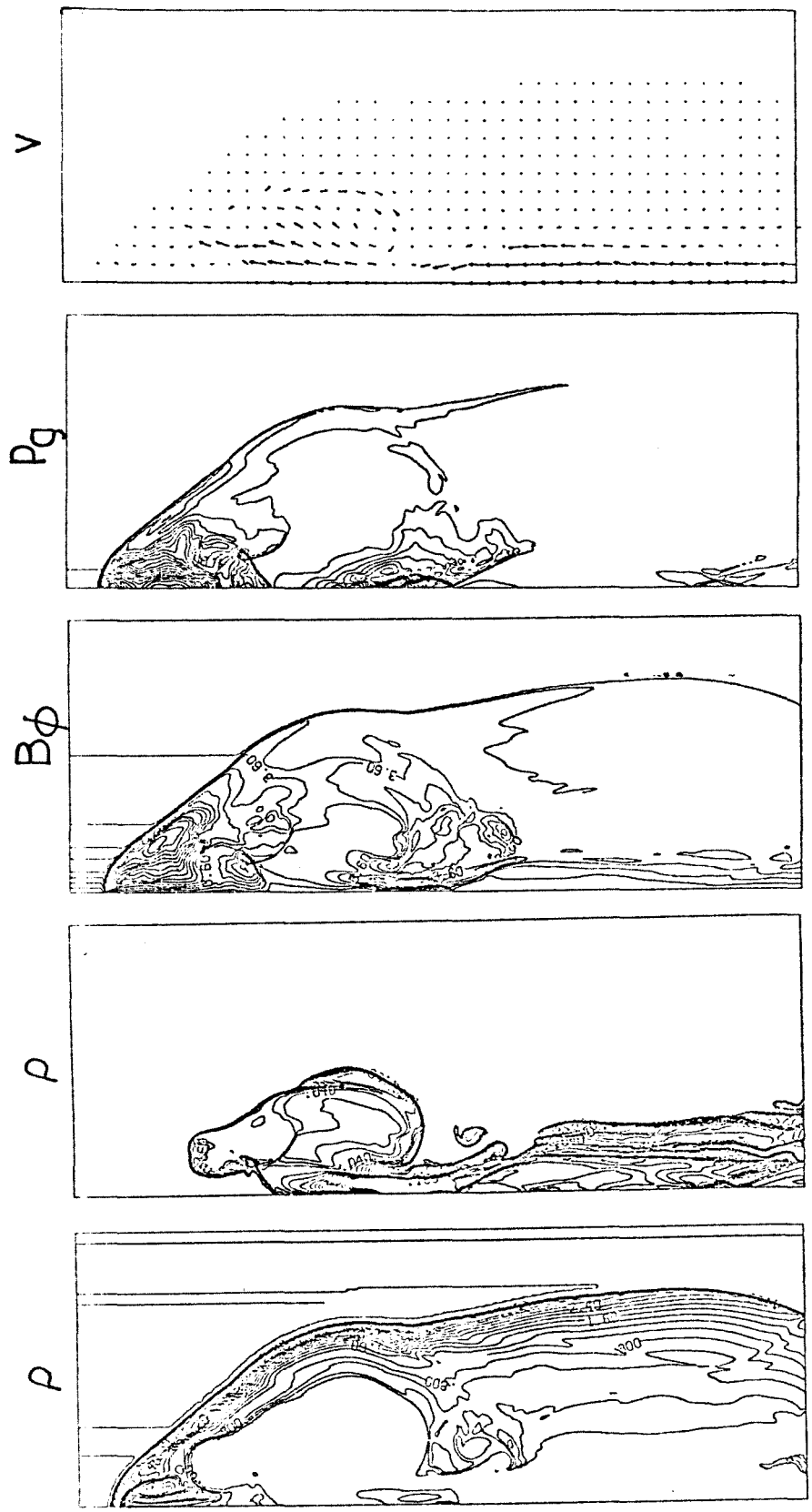

Figure 28

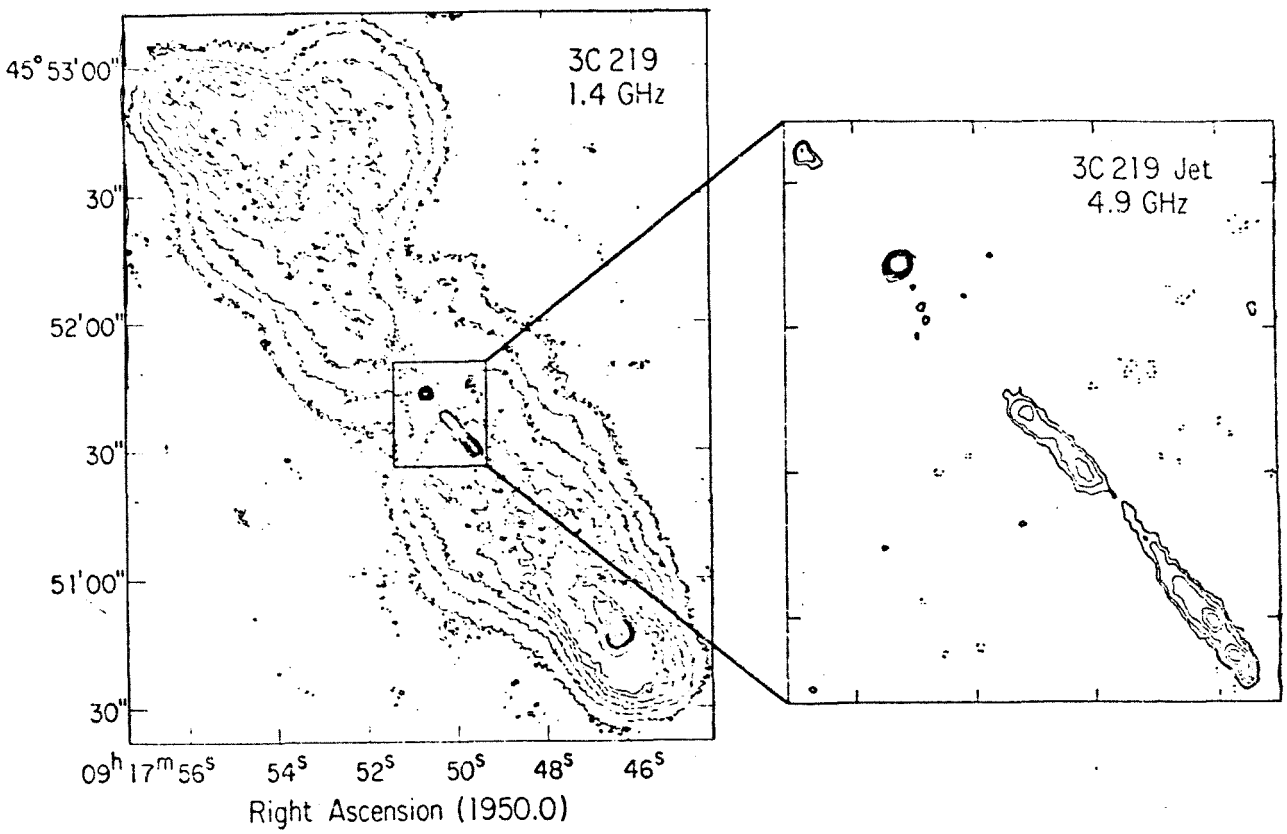
3C 219
1.4 GHz
3C 219 Jet
4.9 GHz
45° 53' 00"
30"
52' 00"
30"
51' 00"
30"
09h 17m 56s
54s
52s
50s
48s
46s
Right Ascension (1950.0)

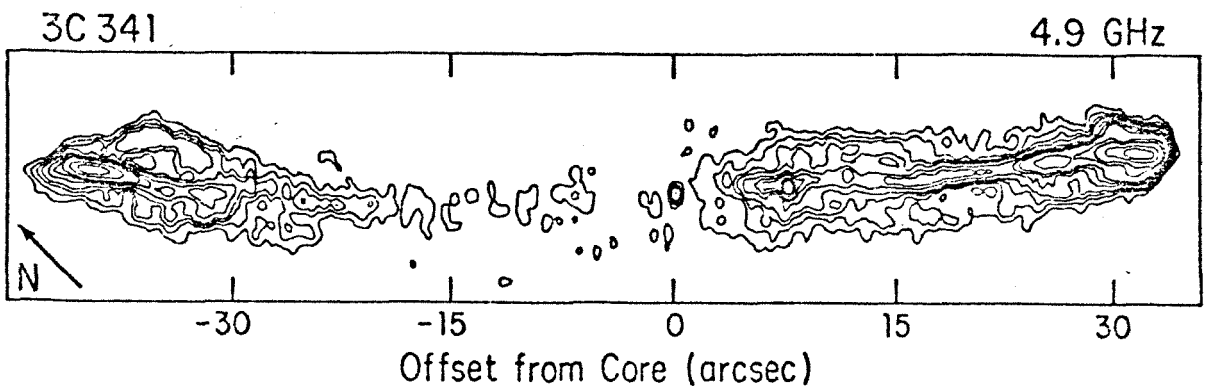
3C 341
4.9 GHz
N
-30
-15
0
15
30
Offset from Core (arcsec)

Figure 29